NATIONAL TECHNICAL UNIVERSITY OF ATHENS
(NTUA)

SCHOOL OF RURAL, SURVEYING AND
GEOINFORMATICS ENGINEERING

Methodology for orbit determination using DORIS RINEX data

PhD dissertation

Xanthos Papanikolaou

supervised by
Dr. Maria TSAKIRI, Prof. NTUA

Athens, May, 2023

NATIONAL TECHNICAL UNIVERSITY OF ATHENS
(NTUA)

SCHOOL OF RURAL, SURVEYING AND
GEOINFORMATICS ENGINEERING

Methodology for orbit determination using DORIS RINEX data

Xanthos Papanikolaou

ADVISORY COMMITEE
Maria Tsakiri, Professor NTUA (supervisor)
Demitris Paradissis, Emeritus Professor, NTUA
Samuel Nahmani, Research Fellow Space Geodesy, IGN/IPGP, France

EXAMINATION COMMITEE
Maria Tsakiri, Professor NTUA (supervisor)
Demitris Paradissis, Emeritus Professor, NTUA
Samuel Nahmani, Research Fellow Space Geodesy, IGN/IPGP, France
Dimitris Tsoulis, Professor AUT
George Vergos, Professor AUT
Dimitris Anastasiou, Assistant Professor NTUA
Arnaud Pollet, Research Fellow Space Geodesy, IGN/IPGP, France

Athens, May, 2023

Acknowledgments

The current text is the result of my PhD studies. The academic process has taken place in Dionysos Satellite Observatory, at the School of Rural, Surveying and Geoinformatics Engineering, of the National Technical University of Athens (NTUA).

Firstly, I would like to express my sincere gratitude to my supervisor, Prof. Maria Tsakiri. Her guidance, support and assistance, not only on technical matters, has been of major importance during the course of my PhD. Without her endorsement, i would have never concluded this task. Furthermore, my gratitude goes to Emeritus Prof. Demitris Paradissis. Since my graduation, Prof. Paradissis has been a scientific mentor to me and has lavishly shared his knowledge and understanding throughout the nearly 15 years of out collaboration.

I would like to thank all of my friends and colleagues at Dionysos Satellite Observatory; Jordan Galanis, Thanasis Zisopoulos and Kostas Raptakis. Way to often have they transformed dull working hours in times to be remembered. Special thanks goes to Vangelis Zacharis, who apart from supporting me and sharing his expertise, has always been ungrudgingly listening to my mumbling about bugs and km-level errors that shouldn't be there. The same goes for Dr. Pol Kolokousis, who pretty much taught me how computers work.

It has been with great pleasure that throughout this journey I have been standing along my good friend Prof. Demitris Anastasiou. His hard work, commitment and progress have been a joy to watch and an example to strive for. His help and support were simply overwhelming.

A big thank-you is in due to Dr. Samuel Nahmani and Dr. Arnaud Pollet. They showed no glimpse of fear (!) when a few years back I showed up to them proposing an overreaching, pretty "crazy" (to be honest) idea. Since then, they have provided crucial feedback and support.

Abstract

Geodesy has greatly advanced since the introduction of artificial, Earth orbiting satellites. A new era has emerged, where satellite-based data dominate the field, providing results for a wide range of geodesy-related fields. The use of artificial satellites in geosciences however requires a comprehensive knowledge of the satellite motion under the influence of all acting forces as well as the description of the satellite trajectory in suitable reference frames. Thus exploitation of satellite-based observations is inherently coupled with the complex problem of orbit determination, a problem that lies in the core of satellite geodesy since its inception.

To-date, Precise Orbit Determination (POD) is dominated by three space geodetic techniques, namely Satellite Laser Ranging (SLR), Global Navigation Satellite System (GNSS) and Détermination d'Orbite et Radiopositionnement Intégré par Satellite (Doppler Orbitography and Radiopositioning Integrated by Satellite) (DORIS), which additionally, via the corresponding Technique Centers, provide the input data time series of station positions and Earth Orientation Parameters (EOP) for the realization of the International Terrestrial Reference Frame (ITRF).

Despite its prominence and significance in the field of satellite geodesy, DORIS has failed to allure a dedicated scientific audience comparable in size to the other techniques. The shortage of dedicated IDS analysis centers, is indicative of the limited availability of dedicated software solutions designed to handle DORIS data, particularly for the purpose of orbit determination.

In the framework of the current Thesis, the scarcity of dedicated DORIS analysis tools for orbit determination is targeted, with the aim of creating a high quality, scientific software solution. Specifically, the software package is *non-proprietary* and *open-source*, *adaptable* and *extensible* to meet the demands of scientific community, implements state-of-the-art *algorithms* and *methodologies* and is designed using *modern programming patterns* and paradigms.

The software is built in a modular fashion. The various components are organized in different, independent, moderate-sized libraries, targeting well defined problems. Various different implementations are put to the test and robust algorithmic approaches are constructed based on criteria of accuracy and efficiency (computing speed and resources).

Given the complexity of the problem and the inherent limitations of a thesis, both in terms of time and resources, the objective of the current study is not to attain the highest possible accuracy achievable by the IDS Analysis Centers. Instead, the focus is on developing a brand-new toolset from scratch, which can serve as a foundational component towards achieving that goal. The envisioned toolset, with some additional fine refinements, has the potential to form the backbone of a state-of-the-art, DORIS POD analysis pipeline.

Using the toolset developed, an orbit determination analysis scheme was designed and tested using the Joint Altimetry Satellite Oceanography Network (JASON)-3 satellite mission, using a high quality reference orbit for validation. Position differences range within a few meters for one day, while velocity discrepancies are in the order of a few millimeters per second.

These results show that the software package developed can serve as a building block for a high quality DORIS analysis software solution. Conclusions and recommendations for further enhancements and refinements are supplied to eventually reach the goal set.

Περίληψη

Η επιστήμη της Γεωδαισίας έχει κάνει μεγάλα άλματα προόδου μετά την εισαγωγή των τεχνητών δορυφόρων που βρίσκονται σε τροχιά γύρω από τη Γη. Σε αυτή τη 'νέα εποχή', τα δεδομένα που προέρχονται από δορυφορικές αποστολές παίζουν σημαίνοντα ρόλο στο ευρύτερο γνωστικό πεδίο, προσφέροντας σημαντικά αποτελέσματα σε ένα ευρύ φάσμα γεωεπιστημών. Η χρήση όμως τέτοιων δεδομένων, είναι συχνά συνυφασμένη με την περιγραφή της δορυφορικής κίνησης και των δυνάμεων που την επηρεάζουν, σε κατάλληλα, υψηλής ακρίβειας χωρικά και χρονικά συστήματα αναφοράς. Συνεπώς, η εκτίμηση των δορυφορικών τροχιών αποτελεί ένα θεμελιώδες πρόβλημα στην σύγχρονη γεωδαισία.

Η εκτίμηση υψηλής ακρίβειας δορυφορικών τροχιών, γίνεται κυρίως με χρήση τριών συστημάτων και συγκεκριμένα του SLR, του GNSS και του DORIS. Οι τεχνικές αυτές, συμβάλουν καταλυτικά και στην υλοποίηση των σύγχρονων παγκόσμιων συστημάτων αναφοράς (π.χ. ITRF).

Παρά τη σημαντική συμβολή και την εξέχουσα θέση που καταλαμβάνει τις τελευταίες δεκαετίες, το σύστημα DORIS δεν έχει έως τώρα προσελκύσει το ανάλογο επιστημονικό κοινό και συνεπώς μια κατάλληλη υπολογιστική πλατφόρμα λογισμικού για την εκμετάλλευση των δυνατοτήτων που μπορεί να προσφέρει. Ενδεικτικός είναι ο μικρός αριθμός εξειδικευμένων κέντρων ανάλυσης, ειδικά σε σχέση με τις λοιπές τεχνικές προσδιορισμού τροχιών.

Με αφορμή την έλλειψη αυτή, στο πλαίσιο της παρούσας Διδακτορικής Διατριβής, επιχειρείται ο σχεδιασμός και η ανάπτυξη μια δέσμης λογισμικών εργαλείων επιστημονικής ποιότητας, για την επεξεργασία δεδομένων DORIS και δη για τη χρήση δεδομένων καταγραφής του συστήματος για την εκτίμηση δορυφορικών τροχιών. Τα υπολογιστικά εργαλεία που αναπτύχθηκαν είναι ελεύθερα διαθέσιμα στην επιστημονική κοινότητα, ακολουθώντας την πολιτική του 'ανοιχτού κώδικα', προσαρμόσιμα και επεκτάσιμα για να ανταποκρίνονται σε ερευνητικές απαιτήσεις υψηλής ακρίβειας, περιλαμβάνοντας τους πλέον σύγχρονους αλγορίθμους και μεθοδολογίες. Ο σχεδι-

ασμός και η υλοποίηση ακολουθεί και υιοθετεί σύγχρονα προγραμματιστικά πρότυπα.

Η διάρθρωση της εργαλειοθήκης που αναπτύχθηκε, αποτελείται από ανεξάρτητα 'πακέτα' (ή βιβλιοθήκες), καθένα εκ των οποίων έχει σαφώς καθορισμένη στόχευση. Με τον τρόπο αυτό, τα ξεχωριστά κομμάτια συγκρατούνται σε εύκολα διαχειρίσιμα μεγέθη, καθιστώντας το πακέτο ιδανικό για χρήση από την επιστημονική κοινότητα σε ένα ευρύ φάσμα εφαρμογών.

Τα τρέχοντα διεθνή, υψηλής ακρίβειας πρότυπα μοντελοποίησης έχουν ακολουθηθεί αυστηρά, σε μία σειρά προβλημάτων που αφορούν ενδεικτικά: τις δυνάμεις που επιδρούν σε τεχνητούς δορυφόρους γύρω από τη γη, την ίδια κίνηση της γης, τα χωρικά και χρονικά συστήματα αναφοράς, την αριθμητική επίλυση διαφορικών εξισώσεων. Όπου χρειάστηκε, δοκιμάστηκαν και αξιολογήθηκαν διαφορετικές μέθοδοι και εν συνεχεία προσαρμόστηκαν και επεκτάθηκαν με βάση κριτήρια ακρίβειας και υπολογιστικού φόρτου. Αξίζει να σημειωθεί ότι το λογισμικό εστιάζει σε μία μοντέρνα, καινοφανή προσέγγιση επεξεργασίας δεδομένων DORIS υποστηρίζοντας τις τελευταίες εξελίξεις τις τεχνικής όπως π.χ. η υιοθέτηση του μορφότυπου ανταλλαγής δεδομένων DORIS RINEX, η διαχείριση δεδομένων φέροντος κύματος (carrier phase) καθώς και η δυνατότητα επεξεργασίας δεδομένων σε σχεδόν πραγματικό χρόνο.

Δεδομένης της πολυπλοκότητας του προβλήματος και των περιορισμών που τίθενται σε μία Διδακτορική Διατριβή, ο σκοπός της παρούσας δεν είναι η ανάπτυξη ενός λογισμικού που θα φτάσει τα επίπεδα ποιότητας που αυτή τη στιγμή πετυχαίνουν κέντρα ανάλυσης εγνωσμένης αξίας, με δεκαετίες εμπειρίας και μεγάλες ερευνητικές ομάδες υποστήριξης (IDS). Ο στόχος που τέθηκε είναι η δημιουργία μιας καινούριας, σύγχρονης εργαλειοθήκης που θα μπορεί να παίζει το ρόλο του θεμελιώδους δομικού στοιχείου για την επίτευξη τέτοιων ακριβειών στο άμεσο μέλλον. Με μικρές, σαφώς ορισμένες βελτιώσεις, εκτιμάται ότι το πακέτο που σχεδιάστηκε για την παρούσα Διατριβή μπορεί να υπηρετήσει το ρόλο αυτό.

Για τον έλεγχο της ποιότητας του πακέτου που σχεδιάστηκε, αναπτύχθηκε ένα πρόγραμμα για τον προσδιορισμό της τροχιάς της δορυφορικής αποστολής JASON-3. Οι εκτιμήσεις θέσης και ταχύτητας του δορυφόρου που προέκυψαν, για μία ημέρα ενδεικτικά, συγκρίθηκαν με αντίστοιχα αποτελέσματα της υψηλότερης δυνατής ακρίβειας από την CNES/SSALTO. Οι διαφορές που προέκυψαν είναι της τάξης των λίγων μέτρων και των λίγων χιλιοστών ανά μέτρο για την θέση και την ταχύτητα αντίστοιχα.

Τα αποτελέσματα υποδεικνύουν ότι η εργαλειοθήκη που σχεδιάστηκε και αναπτύχθηκε μπορεί να αποτελέσει το κύριο δομικό στοιχείο ενός προγράμματος επεξεργασίας δεδομένων doris, ποιότητας εφάμιλλης των κέντρων ανάλυσης της τεχνικής.

Contents

List of Figures

List of Tables

Nomenclature

Physics constants

$\mu_\oplus$ Gravitational constant times Earth's mass

$\mu_\mathbb{C}$ Gravitational constant times Moon's mass

$\mu_\odot$ Gravitational constant times Sun's mass

c Speed of light in a vacuum

G Gravitational constant

$M_\oplus$ Earth's mass

$M_\mathbb{C}$ Moon's mass

$M_\odot$ Sun's mass

$R_\oplus$ Earth's equatorial radius

$R_\mathbb{C}$ Moon's radius

$R_\odot$ Sun's radius

Acronyms

ANTEX Antenna Exchange Format.

ARP Antenna Reference Point.

BCRS Barycentric Celestial Reference System.

CATR Compact Antenna Test Range.

CDDIS Crustal Dynamics Data Information System.

CIO Celestial Intermediate Origin.

CIP Celestial Intermediate Pole.

CIRS Celestial Intermediate Reference System.

CLS Collecte Localisation Satellites.

CNES Centre National d'Etudes Spatiales (National Centre for Space Studies).

DORIS Détermination d'Orbite et Radiopositionnement Intégré par Satellite (Doppler Orbitography and Radiopositioning Integrated by Satellite).

ECEF Earth Centered Earth Fixed.

EOP Earth Orientation Parameters.

ERA Earth Rotation Angle.

EUMETSAT European Organisation for the Exploitation of Meteorological Satellites.

FCN Free Core Nutation.

GCRF Geocentric Celestial Reference Frame.

GCRS Geocentric Celestial Reference System.

GGOS Global Geodetic Observation System.

GMST Greenwich Mean Sidereal Time.

GNSS Global Navigation Satellite System.

GOCE Gravity Field and Steady-State Ocean Circulation Explorer.

GPS Global Positioning System.

GRACE Gravity Recovery and Climate Experiment.

GRGS Groupe de Recherche en Géodésie Spatiale.

GSFC Goddard Space Flight Center.

GST Greenwich Sidereal Time.

IAG International Association of Geodesy.

IAU International Astronomical Union.

ICGEM International Centre for Global Earth Models.

ICRF International Celestial Reference Frame.

ICRS International Celestial Reference System.

IDS International DORIS Service.

IERS International Earth Rotation and Reference Systems Service.

IGFS International Gravity Field Service.

IGN Institut Géographique National.

IGS International GNSS Service.

ILRS International Laser Ranging Service.

ITRF International Terrestrial Reference Frame.

ITRS International Terrestrial Reference System.

IUGG International Union of Geodesy and Geophysics.

IVS International VLBI Service for Geodesy and Astronomy.

JASON Joint Altimetry Satellite Oceanography Network.

JD Julian Date.

JPL Jet Propulsion Laboratory.

LEO Low Earth Orbit.

MJD Modified Julian Date.

NASA National Aeronautics and Space Administration.

NOAA National Oceanic and Atmospheric Administration.

ODE Ordinary Differential Equation.

PCO Phase Center Offset.

PCV Phase Center Variations.

PECE Predictor-Corrector.

POD Precise Orbit Determination.

SAA South Atlantic Anomaly.

SLR Satellite Laser Ranging.

SOFA Standards Of Fundamental Astronomy.

TAI International Atomic Time.

TCB Barycentric Coordinate Time.

TCG Geocentric Coordinate Time.

TDB Barycentric Dynamical Time.

TGP Tide Generating Potential.

TIO Terrestrial Intermediate Origin.

TIRS Terrestrial Intermediate Reference System.

TT Terestrial Time.

TVG Time Variable Gravity.

USO Ultra Stable Oscillator.

UT1 Universal Time.

UTC Coordinated Universal Time.

VLBI Very Long Baseline Interferometry.

Chapter 1

Introduction

1.1 Review and Motivation

Geodesy has greatly advanced since the introduction of artificial, Earth orbiting satellites. A new era has emerged, where satellite-based data dominate the field, providing results for a wide range of geodesy-related fields, including but not limited to positioning, reference frames, altimetry and gravity field determination. Nowadays, space geodetic techniques, provide a unique opportunity to monitor and, therefore, understand the processes and feedback mechanisms of the Earth system with unparalleled precision and resolution.

The use of artificial satellites in geosciences has some prerequisites though; these are basically a comprehensive knowledge of the satellite motion under the influence of all acting forces as well as the description of the satellite trajectory and ground stations in suitable reference frames, both spatial and temporal. Thus exploitation of satellite-based observations is inherently coupled with the complex problem of orbit determination, a problem that lies in the core of satellite geodesy since its inception.

Satellite orbit determination is the process by which knowledge of the satellite's motion relative to the center of mass of the Earth in a specified coordinate system can be obtained (Tapley et al. 2004b). Its contribution can be broadly grouped in a twofold role:

As a product (i.e. tabulated satellite coordinates and/or velocity) it is needed

1

for most spaced-based applications. Knowledge of satellite position (or state) is a prerequisite for most applications and in general dictates the quality of the application's outcome. It should be noted that despite the extended demand for accurate satellite coordinates in recent years (mainly due to GNSS), the product list is by no means exhausted here; several other estimates constitute orbit determination products, as are e.g. earth orientation parameters, crucial for reference frame studies.

As a field of study , it enables the testing, validation and improvement of models and theoretical aspects for various scientific disciplines, geodesy being the first and foremost beneficiary.

Orbit determination is by no means a homogeneous, non-deviating pattern; satellite dynamics, orbit characteristics, parameter quality and product latency as well as observation method/system, all play a significant role in making key strategic choices. On top of that, one must make optimal decisions between models and methodologies, design and implementation, in an ever-upgrading, multi-discipline field.

To-date, POD is dominated by three space geodetic techniques, namely SLR, GNSS and DORIS, which additionally, via the corresponding Technique Centers, provide the input data time series of station positions and EOP for the realization of the ITRF [1]. Along with Very Long Baseline Interferometry (VLBI), these techniques constitute the fundamental pillars of modern satellite geodesy.

DORIS is a technique whereby satellites receive the broadcasted signal transmitted by ground beacons. Using the measured Doppler shift, DORIS can accurately determine the orbit of the satellite, Earth rotation and station coordinates that can be used in different geodetic applications (e.g. Lemoine et al. 2016, Gambis 2006 and Kur et al. 2022). State-of-the-art POD analysis, can deliver accuracies in the centimeter level in the radial direction (Rudenko et al. 2023).

DORIS has played a crucial role in expanding geodetic knowledge and enhancing our understanding of the Earth's dynamics since its introduction in the late 1980s. The technique is anticipated to continue to enhance its significant role in the field of satellite geodesy through endeavors such as the Surface Water and Ocean Topography (SWOT) and GENERIS missions. The SWOT mission, launched in December 2022, aims to carry out the first-ever global survey of Earth's surface water (Biancamaria et al. 2016). Additionally, the GENESIS platform, employing "space-ties," is expected to solve inconsistencies and biases between different

---

[1]ITRF2020, https://itrf.ign.fr/en/solutions/ITRF2020

geodetic techniques, ultimately improving TRF accuracy and stability (Delva et al. 2023).

1.2 Problem Statement and Objective

Despite the DORIS prominence and significance in the field of satellite geodesy, it has failed to allure a dedicated scientific audience comparable in size to the other two techniques. For the most recent realization of ITRF, the International Laser Ranging Service (ILRS) contributed data from 7 Analysis Centers (Pavlis et al. 2023), International GNSS Service (IGS) from 10 (Rebischung 2021), while at the same time the IDS's contribution was derived from only 4 Analysis Centers (Moreaux et al. 2022). This shortage of dedicated IDS analysis centers, is indicative of the limited availability of dedicated software solutions designed to handle DORIS data, particularly for the purpose of orbit determination.

POD is a very challenging task, requiring multi-scientific expertise, coupled with efficient engineering. Building a software tool to perform POD matching the highest accuracy levels assumes expertise, a dedicated scientific group and years of development. Most, if not all, of the currently available software packages to perform POD using DORIS data (e.g. GEODYN (Beal 2015, GINS (CNES 2013) and Bernese (Štěpánek et al. 2010)) have evolved over decades of continuous development. Important issues though come into play:

- These packages are either not free and/or not open souce; hence it is not easy, if possible at all, for the scientific community to use them.

- They are not easily adaptable and/or extensible to meet user needs (e.g. due to not being open source, or due to their sheer codebase size).

- They do not comply with modern programming patterns and paradigms. Maturity often comes at a price, and in this case this is having to comply with legacy codebase.

In the framework of the current Thesis, the scarcity of dedicated DORIS analysis tools for orbit determination is targeted, with the aim of creating a high quality, scientific software solution. Designing for extensibility, reusability and adaptability, and adhering to a free and open source policy, an as large as possible impact is sought for in the scientific community. Coupled with recent advancements in the

technique (e.g. adoption of the RINEX format, dissemination of non-preprocessed data including carrier phase observables, introduction of next generation receivers and beacons) all of which are incorporated in the software built, we hope to spur further, renewed interest in this fundamental area of satellite geodesy.

Given the complexity of the problem and the inherent limitations of a thesis, both in terms of time and resources, the objective of the current study is not to attain the highest possible accuracy achievable by the IDS Analysis Centers. Instead, the focus is on developing a brand-new toolset from scratch, which can serve as a foundational component towards achieving that goal. The envisioned toolset, with some additional fine refinements, has the potential to form the backbone of a state-of-the-art, DORIS POD analysis pipeline.

Since DORIS receivers are on-board Low Earth Orbit (LEO) satellites (e.g. altimetry oriented missions), focus is placed in implementing models and methodologies targeted towards LEO satellites. However, care is taken to not place unneeded constraints on the software, so that later enhancements can easily broaden the application range to other trajectories.

Furthermore, the software should be designed in a manner that could easily accommodate a near-real-time processing scheme, since it is currently possible to to acquire DORIS data with a latency of a few hours[2] (see e.g. Wang et al. 2022). Hence, algorithmic design and implementation, as well as efficiency and resource awareness are all topics to be considered.

1.3   Methodology and Implementation

To accomplish the Thesis objectives, a brand new software toolset was designed and implemented from scratch. The software is built in a modular fashion. The various components are organized in different, independent, moderate-sized libraries, targeting well defined problems. This scheme allows for extensive and thorough testing and validation of the different parts of the package, a vital part of modern software design (e.g. Oberkampf and Roy 2010, Meyer 2008). Additionally, it enables customization according to user needs and accommodates extensibility and maintainability. The aforementioned attributes are crucial when targeting an analysis tool that meets the demanding accuracy requirements of IDS, as such software packages are constantly evolving to incorporate the most recent and cutting-edge

---

[2]IDS Working Group "NRT DORIS data" https://ids-doris.org/organization/working-group-nrt-doris-data.html

scientific advancements.

In practical terms, this design approach facilitates the development of straightforward, customizable, and easy to reason about source code, tailored to the specific application requirements, without necessitating a comprehensive understanding of the entire codebase's intricacies. For example, the source code for orbit determination using daily RINEX files for JASON-3 presented in section 6.6, is only a few hundreds of lines long. Adapting the scheme to process data from a different LEO satellite would only consist in adding the respective macromodel and attitude determination options.

Changing the Earth's gravity model, e.g. for testing or validation purposes, would only incur a change in the respective line of the configuration file (given that a corresponding data file is available via International Centre for Global Earth Models (ICGEM), a condition met by all modern models).

State-of-the-art models and methodologies are used, adhering to the latest standards and recommendations (e.g. International DORIS Service 2020, Petit and Luzum 2010). Extensions and modifications are derived and applied where needed. Various different implementations are put to the test and robust algorithmic approaches are constructed based on criteria of accuracy and efficiency (computing speed and resources).

Implementing sophisticated and complex models poses a significant challenge, requiring a rigorous comprehension of the theoretical implications on one hand, and robust engineering practices on the other. The path taken here, is to follow modern software design patterns, including principles of *data-oriented* design (Fabian 2018), coupled with the well established *object-oriented* pattern, while also taking advantage of modern features such as generic programming via *template metaprogramming* (e.g. Gawlik et al. 2018). Given that most scientific software packages were built a few decades back, this design constitutes a novel approach in software tools for the given problem set.

Multi-threading and parallel processing techniques are used, taking advantage of "standard libraries", hence no external tool is needed, minimizing dependencies, third-party limitations and compliance constraints.

Near-real-time processing capabilities are embedded into the software through meticulous design. To accommodate such possibility, care is taken during the design and implementation phases to proceed in an iterative fashion, and not consume any resources further than the ones needed at the current step. Data pre-processing requirements are limited down to minimum. Data files, which pose

a serious challenge due to their size, are incrementally mapped to memory (resembling in essence a streaming process) so that only the information relating to the current time interval is needed at each step.

1.4 Significance and Novelties

This Thesis addresses a fundamental problem in satellite geodesy that is crucial for utilizing Earth-orbiting satellites to study the Earth system. In doing so, it introduces novel approaches and validates state-of-the-art methodologies. Accurate knowledge of satellite position is critical for space-based applications, making orbit determination a problem of utmost significance.

Building a software tool for a fundamental yet not too popular amongst the scientific community technique such as DORIS, the aim is to create a brand new, modern toolset, to spur further interest and explore further the system's capabilities and limitations. The prominence of the technique is evident by its involvement in some of the most ambitious space geodesy missions to come (e.g. SWOT and GENESIS), thus dedicated analysis packages will play a major role in years to come.

Adopting a free and open-source policy, can create a new, extended, high-expertise user base, which in turn will push for further technique enhancements.

Focal points addressed and novelties introduced in this Thesis, are the following:

- Processing of the newly established DORIS RINEX data. This new format replaces the older doris.v2.2 file format, enabling the dissemination of new observation types and products. Effort has been made to accommodate the complete parsing of all available observation types. Additionally, linear combinations and corresponding antenna reference point eccentricities are (optionally) constructed and used for the formulation of observation equations. This generic design (in which no certain linear combination and reference point is hard-coded within the software) enables user flexibility and accommodates novel processing approaches.

- Capability of processing carrier phase measurements (instead of the current practice in which only Doppler counts are used). Currently, this constitutes

an experimental approach within the DORIS technique (e.g. Mercier et al. 2010).

- A modern view on software design and software engineering principles applied. This includes the emerging, so called data-oriented design paradigm, usage of generic template metaprogramming techniques, and adoption of well established programming tools in the scientific community, including the `C++` and `Python3` programming languages (e.g. also adopted for the development of GipsyX/RTGx, see Bertiger et al. 2020).

- Capacity to process DORIS data in a near-real-time fashion. To the author's best knowledge, no Analysis Center is currently performing near-real-time analysis (except for the operational on-board receiver systems).

- Implementation of in-house strategies and techniques to tackle intricate issues and methodologies. Two examples are orbit integration (section 3.4), where state-of-the-art methods were adapted and rigorously implemented to fit current needs and computation of Earth's gravity acceleration (section 2.2.3), where numeric and analytic derivations were performed to implement an efficient yet accurate computation algorithm.

- Adoption of a free and open-source policy, developing source code in the public domain and making it instantly and unambiguously available to any interested party.

1.5 Organization of the Thesis

The layout of the Thesis, includes seven chapters. The second chapter (chapter 2) serves to introduce fundamental concepts in astrodynamics that are necessary for understanding the subject matter. Perturbed satellite motion is discussed and state-of-the-art approaches for modeling perturbation forces acting on Earth orbiting satellites are presented along with implementation details. Spatial and temporal reference frames are then introduced, to efficiently describe orbital motion.

Chapter three (chapter 3), provides a comprehensive review on orbit integration , focusing on numerical integration of orbital motion using the *special perturbations* approach. An efficient yet robust integrator is derived, to be used in a POD analysis scheme.

In Chapter four (chapter 4), an overview of POD concepts is given, with special attention on the *Extended Kalman Filter* and the linearization of the (non-linear)

perturbed orbital trajectory model. Consequently, efficient representation and formulation of the *variational equation* system is discussed, a fundamental yet complex problem for high accuracy orbit determination.

The DORIS technique is introduced in Chapter five (chapter 5). The technique's principle is presented, along with the instrumentation used and details on the ground segment, including the tracking network. Derivation of the observation equation model, theoretical implications, error sources and mitigation are also discussed. Implementation details and considerations conclude this chapter.

Chapter six (chapter 6) commences by outlining the software developed specifically for this Thesis. The subsequent sections of the chapter detail the rigorous testing and validation process undertaken for the tools constructed, utilizing actual DORIS data collected during the JASON-3 satellite mission over a duration of one day. Results obtained are checked against high-quality reference results. Differences with respect to the reference solution are thoroughly examined and reasoned about.

The last Chapter (chapter 7) of the Thesis discusses conclusions drawn from the work performed and recommendations for further research activities and refinements of the software tools built.

The Thesis also includes two appendices; the first discusses a formulation of the system of variational equations, while the second provides a short introduction in the concept of quaternions focused on their usage for attitude representation.

Chapter 2

Fundamental Astrodynamics

2.1 Introduction

Orbital motion for Earth orbiting satellites, is dominated by the Earth's attraction on the space vehicle. In the absence of all other forces, and assuming point-like gravitational attraction the trajectory would follow a *Keplerian orbit*. While this approximation is the starting point for orbital mechanics, it does not suffice for modern requirements of POD.

The complex force model acting on satellites must be efficiently modeled to derive robust results required for geodetic studies. The growing number of satellite missions, the technological advance coupled with an ever increasing quantity and quality of data sets available, and the quest for understanding complicated dynamics and underlying processes (e.g. density variations in high atmosphere) affecting and describing satellite motion, have resulted in sophisticated, high accuracy models.

Describing (in mathematical terms) and computing trajectories assumes the introduction of spatial and temporal reference systems, ones that are defined and realized in a precision level appropriate to accommodate modern day POD analysis. Transforming back and forth between such frames to fit computation and modeling requirements is frequent within a POD analysis chain, hence such transformation should be efficient and precise.

In an effective POD analysis, such models have to be carefully considered and implemented, a task that raises both analytical and engineering challenges.

9

2.1.1 Goals of the Chapter

In this chapter the fundamental concepts of celestial mechanics are presented, in an approach oriented towards POD for LEO satellites. Starting from fundamental Keplerian motion, orbital perturbations are introduced, as well as the underlying perturbing forces. State-of-the-art models for computing induced accelerations are discussed and their design, implementation and validation are given in detail. Through a thorough examination of the perturbing forces, especially those relevant to geodesy (e.g. Earth's gravity field, Earth tides, etc) recent developments in the field are reviewed as well as their weaknesses, limitations and strengths.

The goal of this discussion, is to derive efficient and robust algorithms, for computing perturbing accelerations, using the most recent models, altering, adapting and re-formulating on the way according to application needs and problem constraints.

A presentation of the spatial and temporal reference systems and their realizations follows, based on the most recent, international standards. Since orbital motion has to be expressed in an inertial reference frame, but a number of modeling techniques (e.g. spherical harmonics expansions) usually assume a reference system co-rotating with the Earth, transforming between systems is customary in POD. The latest International Astronomical Union (IAU) standards for such transformations are presented, with the aim of deriving algorithmic implementations serving efficiency and robustness.

2.2 Orbital Mechanics

2.2.1 The Two-Body Problem

The main features of the motion of artificial satellites can be described by a reasonably simple approximation, due to the fact that the force induced by the Earth's gravity field outrules all other forces by several orders of magnitude. Assume that the masses are spherically symmetrical, thus acting like point masses, and isolated, so the only force acting is gravitational attraction along the line joining the centers. The problem of predicting the orbit of the masses, given the described setup, is usually referred to as the *Two-Body Problem* (or *Kepler Problem* since the attracting force is gravity) and lies in the core of celestial mechanics. The solution can be expressed as a *Kepler orbit*, using six *orbital elements* (see subsection 2.2.2).

In the case of an Earth orbiting satellite, it can safely be assumed that the mass of the satellite m, is insignificant compared to Earth's mass $M_\oplus$, i.e. $m \ll M_\oplus$, (thus considering what is often called a *central-force problem*). The acceleration of the satellite $\ddot{\boldsymbol{r}}$ is given by Newton's law of gravitational attraction

$$\ddot{\boldsymbol{r}} = -\frac{GM_\oplus}{r^3}\boldsymbol{r} \tag{2.1}$$

A full treatment of the Two-Body Problem is beyond the scope of this Thesis and well documented in e.g. Curtis 2014 and Chobotov 2002. It can be shown that the path of the satellite, relative to the Earth, is a conic section (ellipse) whose shape is determined by the *eccentricity*. Using the laws of conservation of angular momentum and energy, the period of the elliptic orbit can also be deduced (see e.g. Curtis 2014).

The Two-Body Problem results in what is called the *Keplerian orbit*. In this ideal case, a set of six parameters is required to uniquely identify a specific orbit. This parameter set in not unique (there are different ways to mathematically describe the same orbit), but the most oftenly used set is the *Keplerian elements* (see subsection 2.2.2).

2.2.2 Orbital Elements

A total of six independent parameters are needed to unambiguously define an arbitrary and unperturbed orbit at some instant t in time. Two parameters, eccentricity e and angular momentum h (or alternatively the semi-major axis, α) define the form of the orbit. To locate a point on the orbit we need a third parameter, the true anomaly θ. Describing the orientation of the orbit in three dimensions requires three additional parameters, inclination i, argument of perigee ω and right ascension of the ascending node, Ω. These six parameters are called the *orbital* or *Keplerian elements*[1] (see Figure 2.1 and Figure 2.2).

α : the *semi-major axis* (sometimes h, the specific *angular momentum* is used instead),

i : *inclination*,

Ω : *right ascension of the ascending node*,

---

[1]There exist alternate sets of (six) parameters that can uniquely define the orbit, but this set is by far the most widely used in celestial mechanics.
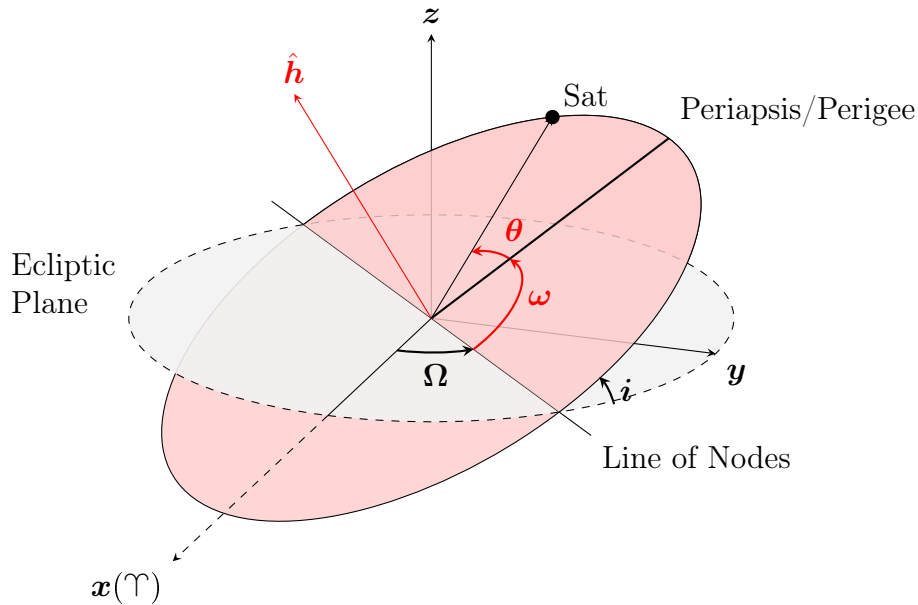
Figure 2.1: Geometry of orbital elements.

e : *eccentricity*,

ω : *argument of perigee*,

θ [2].: *true anomaly* (sometimes $\boldsymbol{M}$, the *mean anomaly* is used instead)

Ω, ω and i, which define the orientation of the orbit in space, are sometimes called *Euler angles*. Given these six elements, it is always possible to uniquely calculate the *state vector*, that is the three spatial dimensions defining the position $\begin{pmatrix} x & y & z \end{pmatrix}$ in a Cartesian coordinate system, and their corresponding velocities $\begin{pmatrix} \dot{x} & \dot{y} & \dot{z} \end{pmatrix}$.

A real orbit and its elements change over time due to various perturbations (see subsection 2.2.3). A Kepler orbit is an idealized, mathematical approximation of the orbit at a particular time. To avoid confusion, we are going to adopt the distinction of orbital elements sets proposed by Vallado 2001 and distinguish between the following cases:

two-body elements are the elements derived from or used with the two-body equations of motion,

---

[2]True anomaly is often designated with the letter ν of f, but here we are following the notation θ
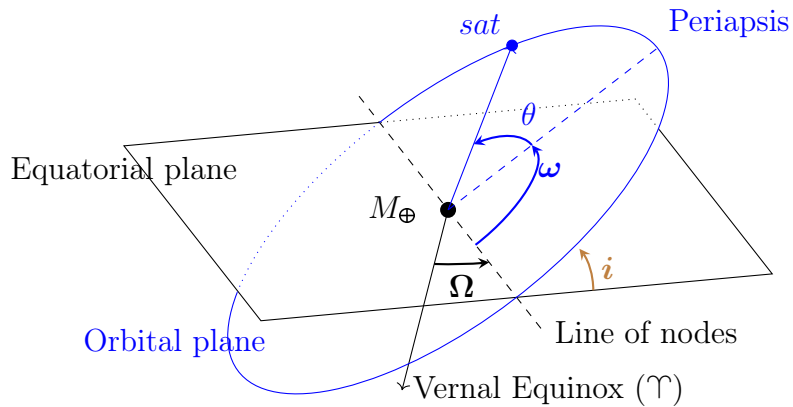
Figure 2.2: Orbital Elements Ω, ω and i

osculating elements are the *instantaneous* elements, under the influence of perturbations, and

mean elements are the elements obtained when averaging the effect of perturbations over a specified time interval

Mathematical formulae to transform between state vector and orbital elements can be found in relevant literature. In the software developed for this Thesis, the methodology described in Montenbruck and Gill 2000 is adopted and implemented.

2.2.3 Perturbed Motion

The Two-Body problem (subsection 2.2.1) is the basis for most trajectory problems, due to (Hintz 2016):

1. the relative two-body problem can be solved analytically,

2. it is often a good approximation to the real solution (central body gravitational force is dominant compared to perturbing forces),

3. provides a clear and illustrative picture of the situation, and

4. it can be used as a reference trajectory for precise orbit determination techniques

In real world, a satellite orbiting the Earth departs from the Two-Body problem scenario; neither is the system isolated, acting only on mutual gravitational attraction, nor can the gravitational attraction of the Earth be attributed to a point-like mass. The force field acting on the satellite in this case, has to be augmented to account for forces other than the ones considered in the Two-Body problem. As a result, satellite orbits are *perturbed* away from Keplerian orbits, making the actual motion follow a complex, "disturbed" trajectory. In POD, effects other than a spherical Earth central gravitational attraction are treated as perturbations of the hypothetical unperturbed motion of the satellite around the Earth.

A perturbing force can either be *conservative* (e.g. third body attraction) or *non-conservative* (e.g. atmospheric drag). Systems driven by conservative forces have a constant total energy (kinetic and potential), whereas in the non-conservative case, energy may be gained or lost mainly through heat exchange (friction) or external sources (thrust). Conservative forces are derivable from a scalar function

$$\boldsymbol{F} = -\nabla U(\boldsymbol{r}) \tag{2.2}$$

a fact that will be used later on, when dealing with perturbing forces.

The fundamental problem in perturbation analysis is orbit propagation. Unlike the Two-Body case, the most accurate way to analyze perturbations is numerically (Vallado 2001). In general, solution techniques for the perturbation problem fall into two categories

Special perturbation techniques where numerical integration of the equations of motion is performed, including all necessary perturbing accelerations, and

General perturbation techniques where analytical approximation and integration s considered, over some time interval

In this Thesis, the problem of perturbed orbit motion will be approximated using special perturbation techniques. This approach is more recent (compared to the general perturbation approach), since it requires significant computational power. To-date, with the limitations on computing power pretty much raised, a new era in analyzing perturbations has emerged. A drawback of this technique, is its specificity; new data means new integration, which can add lengthy computing times. Additionally, as most numerical methods, it suffers from errors that build up with truncation and round-off due to floating point arithmetic. These errors build up with the lengthening of integration intervals, and can cause a degradation of the solution accuracy. Even so however, they offer significantly better accuracy than the analytical approach. A nice overview of both approaches is given in ibid.

In the following, the *Force Model* acting on an Earth orbiting satellite is discussed, departing from the Two-Body problem.

Geopotential

In the two-body problem (subsection 2.2.1) a radially symmetric gravity force was assumed, acting like a point mass. For POD however, this assumption needs to be replaced by a model closer to a real world scenario. As known, the Earth is not a perfect sphere, but rather resembles an oblate spheroid, with different equatorial and polar diameter. To derive a more realistic model, it is convenient to use an equivalent representation involving the gradient of the corresponding gravity potential U (Montenbruck and Gill 2000):

$$\ddot{\boldsymbol{r}} = \nabla U \text{ where } U = GM_{\oplus}\frac{1}{r} \qquad (2.3)$$

so that $\boldsymbol{F} = \left(\frac{\partial U}{\partial x} \quad \frac{\partial U}{\partial y} \quad \frac{\partial U}{\partial z}\right)$ This formulation enables the replacement of the three components of the vector $\boldsymbol{F}$ by a single function U, thus simplifying notation and further developments. The geopotential is widely used in geodesy (see e.g. Hofmann-Wellenhof et al. 2005).

Given an arbitrary mass distribution, the individual elementary mass contributions $dm = \rho(\boldsymbol{s})d^3s$ can be summed, and thus the potential be expressed as:

$$U = G \int \frac{\rho(\boldsymbol{s})}{\|\boldsymbol{r} - \boldsymbol{s}\|} d^3s \qquad (2.4)$$

where $\boldsymbol{r}$ is the vector from the mass center to the attracted body (i.e. satellite) and $\boldsymbol{s}$ is the geocentric vector the elementary mass dm.

For any point $\boldsymbol{r}$ outside the mass, $r > s$, the inverse of the distance can be expanded using a series of *Legendre polynomials*, as

$$\frac{1}{\|\boldsymbol{r} - \boldsymbol{s}\|} = \frac{1}{r} \sum_{n=0}^{\infty} \left(\frac{s}{r}\right)^n P_n(\cos\gamma) \qquad (2.5)$$

where $\cos\gamma = \frac{\boldsymbol{r}\cdot\boldsymbol{s}}{rs}$ (the angle between $\boldsymbol{r}$ and $\boldsymbol{s}$) and $P_n(u)$ is the Legendre polynomial of degree n. Making use of the addition theorem of Legendre polynomials (Montenbruck and Gill 2000):

$$P_n(\cos\gamma) = \sum_{m=0}^{n} (2 - \delta_{0m}) P_{nm}(\sin\phi)P_{nm}(\sin\phi') \cos m (\lambda - \lambda') \qquad (2.6)$$

15

with P_{nm} the *associated Legendre polynomials* of degree n and order m and $\begin{pmatrix} \phi & \lambda \end{pmatrix}$ and $\begin{pmatrix} \phi' & \lambda' \end{pmatrix}$ being the longitude and geocentric latitudes of points $\boldsymbol{r}$ and $\boldsymbol{s}$ respectively.

The Earth's gravity potential can now be written as:

$$U(r, \phi, \lambda) = \frac{GM_\oplus}{r} \sum_{n=0}^{\infty} \sum_{m=0}^{n} \left(\frac{R_\oplus}{r} \right)^n P_{nm}(\sin\phi) \left(C_{nm} \cos m\lambda + S_{nm} \sin m\lambda \right) \quad (2.7)$$

with coefficients:

$$
\begin{aligned}
C_{nm} &= \frac{2 - \delta_{0m}}{M_\oplus} \frac{(n-m)!}{(n+m)!} \int \left(\frac{s}{R_\oplus} \right)^n P_{nm}(\sin\phi') \cos m\lambda' \rho(\boldsymbol{s}) \, d^3s \\
S_{nm} &= \frac{2 - \delta_{0m}}{M_\oplus} \frac{(n-m)!}{(n+m)!} \int \left(\frac{s}{R_\oplus} \right)^n P_{nm}(\sin\phi') \sin m\lambda' \rho(\boldsymbol{s}) \, d^3s
\end{aligned}
\quad (2.8)
$$

which describe the dependence on the Earth's internal mass distribution. In geodetic applications, the *normalized* geopotential coefficients $\bar{C}_{nm}$ and $\bar{S}_{nm}$, are most often used, and defined as

$$\begin{Bmatrix} \bar{C}_{nm} \\ \bar{S}_{nm} \end{Bmatrix} = \sqrt{\frac{(n+m)!}{(2 - \delta_{0m})(2n+1)(n-m)!}} \begin{Bmatrix} C_{nm} \\ S_{nm} \end{Bmatrix} \quad (2.9)$$

which are much more uniform in magnitude, thus helping reduce round-off errors. Note that the coefficients C_{nm} and S_{nm} are often called *Stokes' coefficients*, e.g. Barthelmes 2018.

The acceleration due to the Earth's gravity potential can now be written as (Montenbruck and Gill 2000)

$$\ddot{\boldsymbol{r}}(r, \phi, \lambda) = \nabla \frac{GM_\oplus}{r} \sum_{n=0}^{\infty} \sum_{m=0}^{n} \left(\frac{R_\oplus}{r} \right)^n \bar{P}_{nm}(\sin\phi) \left(\bar{C}_{nm} \cos m\lambda + \bar{S}_{nm} \sin m\lambda \right)$$

$$(2.10)$$

where the *normalized* associated Legendre functions are used

$$\bar{P}_{nm} = \sqrt{\frac{(2 - \delta_{0m})(2n+1)(n-m)!}{(n+m)!}} P_{nm} \quad (2.11)$$

Gravity Models Earth gravity models, contain the potential coefficients $\bar{C}_{nm}$ and $\bar{S}_{nm}$ up to a given degree n and order m (with $m \leqslant n$) and the parameters $GM_\oplus$ and $R_\oplus$ via which one can compute the geopotential or the induced acceleration on an orbiting satellite, given its position vector $\boldsymbol{r}$. Gravity models are derived from:

Satellite data , making use of the fact that the Earth's gravity field can produce perturbations "seen" in satellite orbits via POD. It is worth noting that since GRACE (Tapley et al. 2004a) was launched in March 2002, satellite gravimetry has brought a new era of studying global mass variation and redistribution through measuring the time-variable gravity field with unprecedented accuracy (see e.g. Chen et al. 2022 and Jäggi et al. 2023). This progress was further enhanced with the launch of Gravity Field and Steady-State Ocean Circulation Explorer (GOCE) (Johannessen et al. 2003) in 2009.

Terrestrial observations (surface gravimetry), providing precise local and regional (short-wavelength) information on the gravity field. Due to their inhomogeneous distribution though, deriving a global gravity model is quite challenging.

Altimeter data , which provide detailed information about the form of the geoid, which may in turn be used to derive geopotential coefficients.

Combinations of the above methods/data.

Recent advantages in gravity models and estimation, have enabled temporal modeling of the geopotential coefficients. Thus, the parameters $\bar{C}_{nm}$ and $\bar{S}_{nm}$ are not constant but slightly varying with time. Most often, the parametrization of the coefficients consists of two parts,

- a *linear* part, including terms for a "bias" and a drift coefficient, pertaining to a given validity interval; normally, the bias and drift are in general coherent so that the result is a piece wise linear function, except in the case of earthquakes. E.g., for the case of *CNES/GRGS RL04* (Lemoine et al. 2019), three major earthquakes have been introduced in the modelling: Sumatra on 2004/12/26, Concepcion on 2010/02/27 and Sendai on 2011/03/11.

- a *harmonic* part, usually including two annual and two semi-annual coefficients for each year (in- and out-of-phase).

In these Time Variable Gravity (TVG) models, the normalized Stoke's coeffi-

cients are given by:

$$\bar{C}_{nm}(t) = \bar{C}_{nm}|_{t_0,k} + V_{\bar{C}_{nm},k} \cdot (t - t_0) + \sum_{j=0}^{N} \left(A_{\bar{C}_{nm},j} \sin\left(\frac{2\pi}{T}\delta t\right) + B_{\bar{C}_{nm},j} \cos\left(\frac{2\pi}{T}\delta t\right) \right)$$

$$\bar{S}_{nm}(t) = \bar{S}_{nm}|_{t_0,k} + V_{\bar{S}_{nm},k} \cdot (t - t_0) + \sum_{j=0}^{N} \left(A_{\bar{S}_{nm},j} \sin\left(\frac{2\pi}{T}\delta t\right) + B_{\bar{S}_{nm},j} \cos\left(\frac{2\pi}{T}\delta t\right) \right)$$

(2.12)

for each validity interval k valid within the period t_{start}, t_{end}, where $t_{start} < t < t_{end}$ and

$\bar{C}_{nm}|_{t_0}$ and $\bar{S}_{nm}|_{t_0}$ are the constant, "bias" terms for the given interval and degree/order coefficient (n,m),

$V_{\bar{C}_{nm}}$ and $V_{\bar{S}_{nm}}$ are the drift terms for the given interval and degree/order coefficient (n,m),

j is the number of harmonics signals (frequencies) included in the model,

$A_{\bar{C}_{nm},j}$ and $A_{\bar{S}_{nm},j}$ are the in-phase amplitudes of the frequency j, for the degree/order coefficient (n,m) coefficient,

$B_{\bar{C}_{nm},j}$ and $B_{\bar{S}_{nm},j}$ are the out-of-phase amplitudes of the frequency j, for the degree/order coefficient (n,m) coefficient,

t_0 is the reference epoch for the given validity interval,

δt is the difference between the epoch t and the start of the current year (in years)

The ICGEM ICGEM (Sinem et al. 2019) is one of five services coordinated by the International Gravity Field Service (IGFS) of the International Association of Geodesy (IAG). Among other services, ICGEM collects and archives all existing global gravity field models and provides a web interface for getting access to them.

Gravity models are published in what is called the *ICGEM-format* (Barthelmes and Förste 2011), an effort to standardize the distribution of such models, that is gaining evermore attention in recent years. This format offers great advantages since it is standardized, well documented, generic and can be used to publish and/or parse (with slight extensions) coefficients other than gravity models (e.g. ocean tides).

Implementation For the purposes of the current Thesis, software has been designed and developed to handle the modeling of the Earth's gravity models. Highlights of the software are:

- Handling (parsing) of gravity models published in the *ICGEM-format* (see section 2.2.3). This approach enables genericity, since any (recently published) gravity model can be used as input to compute satellite acceleration (see e.g. the listed models published in the ICGEM site http://icgem.gfz-potsdam.de/tom_longtime). This important feature, makes the software highly suitable for scientific studies.

- Handling of both static and TVG models; for the latter, the formulation Equation 2.12 is used, to account for temporal modelling of the Stoke's coefficients.

- Efficient memory handling and introduction of special data structures to store and retrieve coefficients, directly targeting and exploiting their intrinsic characteristics (e.g. $\bar{S}_{0m}$ are not stored).

- Direct retrieval and usage of the data structures to compute acceleration, as well as partials (i.e. $\frac{\partial \ddot{r}}{\partial r}$), in one step.

- Algorithmic design to account for efficiency, yet with as close as possible minimal loss of precision due to truncation errors (e.g. employ a *Kahan summation* algorithm, Klein 2006).

In the current Thesis, two gravity models are used, namely *EIGEN-6C4* (Förste et al. 2014) and *CNES/GRGS RL04*. The former is mainly used for validation purposes (see section 2.2.3). The latter is the most recent recommendation of the IDS (see Lemoine and Štěpánek 2019, Štěpánek et al. 2022) used in the latest processing campaign for ITRF2020. Note though, that the software is designed in a generic way, allowing the introduction of any gravity field model structured in the *ICGEM-format*.

Computing Gravity Acceleration

The acceleration of an Earth orbiting satellite due to the Earth's gravity field, can be computed using the potential U (see Equation 2.3)

$$\ddot{r} = \begin{pmatrix} \ddot{x} & \ddot{y} & \ddot{z} \end{pmatrix} = \nabla U \tag{2.13}$$

19

The classical formulation of the gravitational acceleration derived from the spherical harmonics expansion (see Equation 2.10) employs the geocentric spherical coordinate representation. This approach can result in singularities at the north and south poles (Atallah et al. 2022). To avoid this problem, the implementation adopted for this Thesis employs a computation algorithm based on a development using Cartesian components, which is singularity-free. The method was introduced by Cunningham 1970 and also presented in Montenbruck and Gill 2000. The derivation and results described therein use the un-normalized form; an equivalent, normalized form was derived and implemented, taking into account Atallah et al. 2022. In the following, the algorithmic approach adopted in the design of the software built for the current Thesis is derived.

Defining

$$\bar{V}_{nm} = \bar{M}_{nm} + i\bar{W}_{nm} = \left(\frac{R_\oplus}{r}\right)^{n+1} \bar{P}_{nm}(\sin\phi)\left(\cos(m\lambda) + i\sin(m\lambda)\right) \qquad (2.14)$$

the potential (see Equation 2.7) can be written as

$$U = \Re\left(\frac{GM_\oplus}{R_\oplus} \sum_{n=0}^{\infty} \sum_{m=0}^{n} \left(\bar{C}_{nm} - i\bar{S}_{nm}\right)\bar{V}_{nm}\right) \qquad (2.15)$$

using normalized coefficients, so that the acceleration is given by

$$\ddot{\boldsymbol{r}} = \Re\left(\frac{GM_\oplus}{R_\oplus} \sum_{n=0}^{\infty} \sum_{m=0}^{n} \left(\bar{C}_{nm} - i\bar{S}_{nm}\right)\nabla\bar{V}_{nm}\right) \qquad (2.16)$$

Omitting intermediate results (see e.g. ibid.), the recurrence relations can be written as:

$$\bar{V}_{nm} = B_{nm}\frac{z}{r}\frac{R_\oplus}{r}\bar{V}_{n-1,m} - (n+m-1)\frac{B_{nm}}{B_{n-1,m}}\left(\frac{R_\oplus}{r}\right)^2 \bar{V}_{n-2,m}$$

$$\bar{M}_{nm} = B_{nm}\frac{zR_\oplus}{r^2}\bar{M}_{n-1,m} - \frac{B_{nm}}{B_{n-1,m}}\left(\frac{R_\oplus}{r}\right)^2 \bar{M}_{n-2,m} \qquad (2.17)$$

$$\bar{W}_{nm} = B_{nm}\frac{zR_\oplus}{r^2}\bar{W}_{n-1,m} - \frac{B_{nm}}{B_{n-1,m}}\left(\frac{R_\oplus}{r}\right)^2 \bar{W}_{n-2,m}$$

where

$$B_{nm} = \sqrt{\frac{(2n+1)(2n-1)}{(n+m)(n-m)}} \qquad (2.18)$$

and for the $n = m$ cases, we have

$$
\begin{aligned}
\bar{V}_{mm} &= \sqrt{\frac{2m+1}{2m}} \frac{(x+iy)}{r^2} \bar{V}_{m-1,m-1} \\
\bar{M}_{mm} &= \sqrt{\frac{2m+1}{2m}} \left(\frac{xR_\oplus}{r^2} \bar{M}_{m-1,m-1} - \frac{yR_\oplus}{r^2} \bar{W}_{m-1,m-1} \right) \\
\bar{W}_{mm} &= \sqrt{\frac{2m+1}{2m}} \left(\frac{xR_\oplus}{r^2} \bar{W}_{m-1,m-1} + \frac{yR_\oplus}{r^2} \bar{M}_{m-1,m-1} \right)
\end{aligned}
\tag{2.19}
$$

The recurrence starts with initial conditions

$$
\begin{aligned}
\bar{M}_{00} &= \frac{R_\oplus}{r} \text{ and } \bar{M}_{10} = \sqrt{3}\frac{z}{r^2}\bar{M}_{00} \\
\bar{W}_{00} &= 0 \text{ and } \bar{W}_{10} = 0
\end{aligned}
\tag{2.20}
$$

$\bar{M}_{nm}$ and $\bar{W}_{nm}$ can now be used to compute the Cartesian acceleration components via

$$
\begin{aligned}
\ddot{x} &= \sum_{n=0}^{\infty} \sum_{m=0}^{n} \ddot{x}_{nm} \\
\ddot{y} &= \sum_{n=0}^{\infty} \sum_{m=0}^{n} \ddot{y}_{nm} \\
\ddot{z} &= \sum_{n=0}^{\infty} \sum_{m=0}^{n} \ddot{z}_{nm}
\end{aligned}
\tag{2.21}
$$

where for $m = 0$

$$
\begin{aligned}
\ddot{x}_{n0} &= -\frac{GM_\oplus}{R_\oplus^2} \frac{N_{n,0}}{N_{n+1,1}} \bar{C}_{n0} \bar{M}_{n+1,1} \\
\ddot{y}_{n0} &= -\frac{GM_\oplus}{R_\oplus^2} \frac{N_{n,0}}{N_{n+1,1}} \bar{C}_{n0} \bar{W}_{n+1,1} \\
\ddot{z}_{n0} &= -\frac{GM_\oplus}{R_\oplus^2} \frac{N_{n,0}}{N_{n+1,1}} (n+1) \bar{C}_{n0} \bar{M}_{n+1,0}
\end{aligned}
\tag{2.22}
$$

21

and for $m > 0$

$$
\begin{aligned}
\ddot{x}_{nm} &= \frac{GM_\oplus}{2R_\oplus^2} \Big(\frac{N_{n,m}}{N_{n+1,m+1}} \left(-\bar{C}_{n,m}\bar{M}_{n+1,m+1} + \bar{S}_{n,m}\bar{W}_{n+1,m+1} \right) \\
&\quad + \frac{(n-m+2)!}{(n-m)!} \frac{N_{n,m}}{N_{n+1,m-1}} \left(-\bar{C}_{n,m}\bar{M}_{n+1,m-1} + \bar{S}_{n,m}\bar{W}_{n+1,m-1} \right) \Big) \\
\ddot{y}_{nm} &= \frac{GM_\oplus}{2R_\oplus^2} \Big(\frac{N_{n,m}}{N_{n+1,m+1}} \left(-\bar{C}_{n,m}\bar{W}_{n+1,m+1} + \bar{S}_{n,m}\bar{M}_{n+1,m+1} \right) \\
&\quad + \frac{(n-m+2)!}{(n-m)!} \frac{N_{n,m}}{N_{n+1,m-1}} \left(-\bar{C}_{n,m}\bar{W}_{n+1,m-1} + \bar{S}_{n,m}\bar{M}_{n+1,m-1} \right) \Big) \\
\ddot{z}_{nm} &= \frac{GM_\oplus}{R_\oplus^2} \frac{N_{n,m}}{N_{n+1,m}} \left((n-m+1) \left(-\bar{C}_{n,m}\bar{W}_{n+1,m+1} + \bar{S}_{n,m}\bar{M}_{n+1,m+1} \right) \right)
\end{aligned}
\tag{2.23}
$$

where N_{nm} is the normalization factor for degree n and order m

$$
N_{nm} = \sqrt{\frac{(n-m)!(2n+1)(2-\delta_{0m})}{(n+m)!}} \tag{2.24}
$$

Derivative of Acceleration Partial derivatives of the acceleration need to be computed, with respect to the satellite state vector, $\frac{\partial \ddot{r}}{\partial r}$ for the variational equations. For the central term

$$
\ddot{r} = -\frac{GM_\oplus}{r^3} r \tag{2.25}
$$

and using the relation

$$
\frac{\partial r^n}{\partial r} = \frac{\partial \left(x^2 + y^2 + z^2 \right)}{\partial r} = n \cdot r^{n-2} \cdot r^T \tag{2.26}
$$

if follows that

$$
\begin{aligned}
\frac{\partial \ddot{r}}{\partial r} &= -GM_\oplus \frac{\partial}{\partial r} \left(r \frac{1}{r^3} \right) = -GM_\oplus \left(\frac{1}{r^3} I_{3\times3} - 3r \frac{r^T}{r^5} \right) \\
&= \frac{-GM_\oplus}{r^5} \begin{pmatrix} 3x^2 - r^2 & 3xy & 3xz \\ 3yx & 3y^2 - r^2 & 3yz \\ 3zx & 3zy & 3z^2 - r^2 \end{pmatrix}
\end{aligned}
\tag{2.27}
$$

which shows that the gravity gradient is symmetric and with a zero trace. The same result can be deduced considering Earth's gravitational potential expressed as Equation 2.4 (see Montenbruck and Gill 2000). The two properties reduce the number of independent components that have to be considered in the computation from nine to five.

22

Deriving the partials is quite tedious and requires analytical work. For the derivation of the formulae, the development presented in section 2.2.3 can act as reference, following a normalized version of the algorithm presented in Cunningham 1970 and Montenbruck and Gill 2000. The partials $\frac{\partial \ddot{x}_{nm}}{\partial x}$, $\frac{\partial \ddot{x}_{nm}}{\partial y}$, $\frac{\partial \ddot{x}_{nm}}{\partial z}$, $\frac{\partial \ddot{y}_{nm}}{\partial z}$ and $\frac{\partial \ddot{z}_{nm}}{\partial z}$ are needed to compute $\frac{\partial \ddot{r}}{\partial r}$, taking into account the symmetric nature and zero trace of the matrix.

Earth Rotation   Formulae presented in the current section, section 2.2.3, are valid in an ECEF frame, that is ignoring Earth's rotation (aka r is the satellite's position vector in ECEF coordinates). Letting $r_{ef} \equiv r$ and introducing r_{sf} to denote the corresponding celestial, "space-fixed" vector, with

$$r_{ef} = R \cdot r_{sf} \tag{2.28}$$

where R is the terrestrial-to-celestial transformation matrix (see subsection 2.3.3). The partial derivatives $\frac{\partial \ddot{r}}{\partial r}$ is the "space-fixed" frame, would then be given by

$$\left(\frac{\partial \ddot{r}}{\partial r} \right)_{sf} = R^T \left(\frac{\partial \ddot{r}}{\partial r} \right)_{ef} R \tag{2.29}$$

and for the acceleration

$$\ddot{r}_{sf} = R^T \cdot \ddot{r}_{ef} \tag{2.30}$$

Validation   The acceleration induced to an earth orbiting satellite by the Earth's gravity field, is by far the largest in magnitude, hence it should be computed with utmost precision. To test the implementation, results obtained were checked against the `COST-G` benchmark test. Input data for the test is a one-day orbital arc of GRACE, paired with the earth gravity model `EIGEN-6C4`. Acceleration is evaluated from degree and order 2 to 180 (i.e. leaving out the largest in magnitude central term). According to Lasser 2023, accelerations should be consistent to at least $1 \times 10^{-12}\,\mathrm{m/s^2}$. The discrepancies between our implementation and the benchmark test are depicted in Figure 2.3 and Table 2.1. It is clear that results obtained lie within the accuracy demands of the benchmark test.

Third Body Attraction

The presence of other bodies in the gravitational field exerted by a main central body (Earth), makes the problem of orbit determination a N-body problem, which
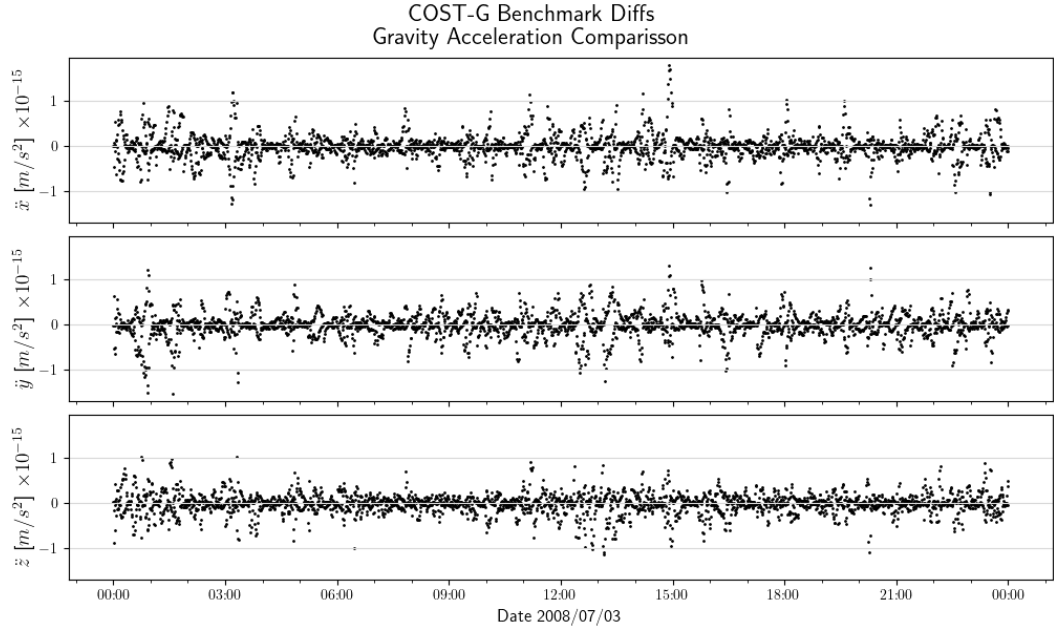
Figure 2.3: Earth gravity acceleration discrepancies against the COST-G benchmark test. Gravity model is EIGEN-6C4 from degree and order 2 to 180. Comparing results for a one-day orbit arc of GRACE in ITRF.

Component	Min	Max	Mean	Std. Deviation
			m/s^2	
$\ddot{x}$	-1.28e-15	+1.79e-15	-1.00e-18	2.64e-16
$\ddot{y}$	-1.52e-15	+1.32e-15	-3.43e-18	2.58e-16
$\ddot{z}$	-1.14e-15	+1.00e-15	-5.81e-18	2.19e-16

Table 2.1: Earth gravity acceleration discrepancies against the COST-G benchmark test.

however, as known, cannot be solved analytically. In the case of artificial satellites orbiting the Earth at low altitudes, the gravitational force due to the Earth is by far larger than those exerted by the Moon, Sun or planets. Therefore, the problem can be solved by using the methods of perturbation theory. In this approach, the computation of the perturbing acceleration can be simplified when considering the third or *perturbing body* as a point mass. Third body perturbing acceleration from Sun and Moon, are often called *Direct Tides*.

Introducing vectors $\boldsymbol{r}$ and $\boldsymbol{s}$, to describe the geocentric coordinates of the satellite and the third-body respectively, then according to Newton's law, the acceleration of the satellite by the third-body (or *perturbing body*), considered as a point mass, is (the subscript pb denotes the perturbing body)

$$\ddot{\boldsymbol{r}} = GM_{pb}\frac{\boldsymbol{s} - \boldsymbol{r}}{\|\boldsymbol{s} - \boldsymbol{r}\|^3} \tag{2.31}$$

where Earth's acceleration due to the perturbing body should also be account for, hence

$$\ddot{\boldsymbol{r}} = GM_{pb}\left(\frac{\boldsymbol{s} - \boldsymbol{r}}{\|\boldsymbol{s} - \boldsymbol{r}\|^3} - \frac{\boldsymbol{s}}{\|\boldsymbol{s}\|^3}\right) \tag{2.32}$$

For the current Thesis, third body perturbations from Moon and Sun are considered. In a similar fashion using the software developed, third body attraction can be computed for all planets, though their effect can be safely neglected for LEO satellites.

Jet Propulsion Laboratory (JPL) Ephemerides To compute third body perturbations, as evident from Equation 2.32, coordinates of the perturbing bodies at a given instant t need to be known. For high precision applications, Sun, Moon and planetary ephemerides are used and interpolated for the requested epoch.

JPL Development Ephemeris (abbreviated `JPL DE(number)`) designates one of a series of mathematical models of the Solar System produced at the JPL for use in spacecraft navigation and astronomy. The models consist of numeric representations of positions, velocities and accelerations of major Solar System bodies, tabulated at equally spaced intervals of time, covering a specified span of years. Further information and a description of available ephemerides, can be found at the JPL Planetary and Lunar Ephemerides website.

For the purposes of this Thesis, software was developed to interact with the JPL DE files, generic enough to handle all versions of the ephemerides. An interface to the JPL-provided Observation Geometry System for Space Science Missions
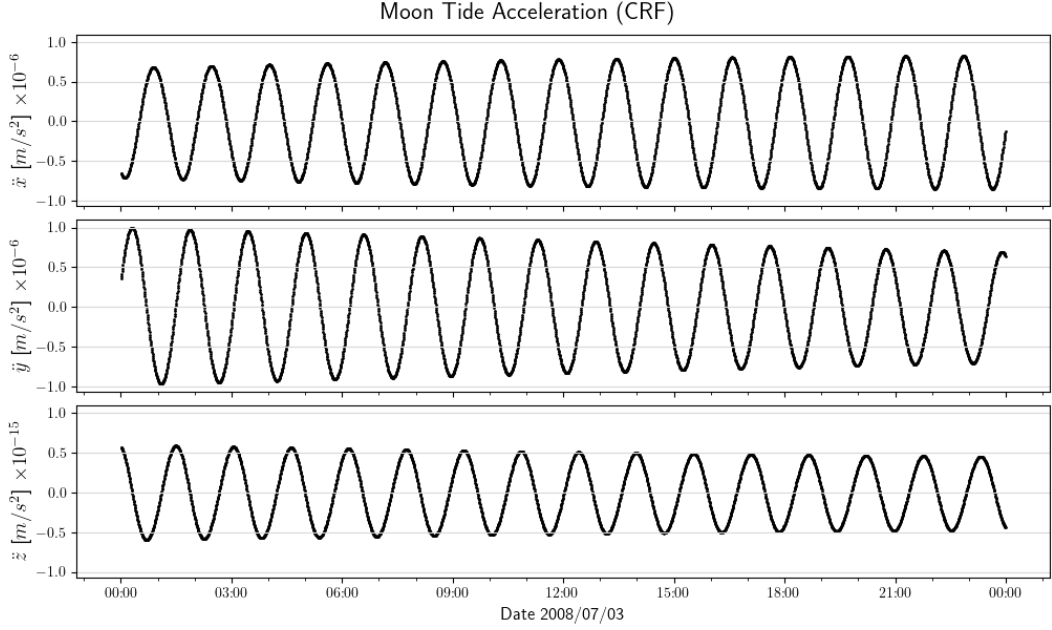
Figure 2.4: Third body acceleration from Moon on GRACE for a one-day arc in ICRF. GRACE orbit is extracted from the COST-G benchmark test. Moon ephemerides extracted from DE421.

(SPICE) software library [3] was designed to extract Sun, Moon and planet coordinates, and respective constants. Tests and validation are performed using the DE421 ephemerides (Folkner et al. 2009).

Partial Derivatives of Third Body Perturbations   As can be shown from Equation 2.32, the partial derivative of the third body perturbation w.r.t to the satellite state vector $\boldsymbol{x} = \begin{pmatrix} \boldsymbol{r} & \boldsymbol{v} \end{pmatrix}^T$ is given by

$$
\begin{aligned}
\frac{\partial \ddot{\boldsymbol{r}}}{\partial \boldsymbol{r}} &= -GM_{pb} \left(\frac{1}{\|\boldsymbol{r} - \boldsymbol{s}\|^3} \boldsymbol{I}_{3 \times 3} - 3 \left(\boldsymbol{r} - \boldsymbol{s} \right) \frac{\left(\boldsymbol{r} - \boldsymbol{s} \right)^T}{\|\boldsymbol{r} - \boldsymbol{s}\|^5} \right) \\
\frac{\partial \ddot{\boldsymbol{r}}}{\partial \boldsymbol{v}} &= \boldsymbol{0}
\end{aligned}
\tag{2.33}
$$

Validation   To test the implementation, results were checked against the COST-G benchmark test, considering third body perturbing accelerations both from Moon and Sun. Input data for the test is a one-day orbit arc of GRACE in ICRF and

---

[3] Based on the C version of the Navigation and Ancillary Information Facilty (NAIF)

26

Component	Min	Max	Mean	Std. Deviation
			m/s^2	
$\ddot{x}_{Moon}$	-1.72e-16	+1.80e-16	-1.02e-18	7.20e-17
$\ddot{y}_{Moon}$	-2.25e-16	+2.45e-16	4.14e-18	1.31e-16
$\ddot{z}_{Moon}$	-1.27e-16	+1.39e-16	2.32e-18	7.17e-17
$\ddot{x}_{Sun}$	-5.34e-18	+4.59e-18	3.95e-20	2.03e-18
$\ddot{x}_{Sun}$	-9.95e-18	+1.05e-17	2.39e-20	3.65e-18
$\ddot{x}_{Sun}$	-4.21e-18	+4.70e-18	8.50e-21	1.59e-18

Table 2.2: Moon & Sun direct tide acceleration differences against the COST-G benchmark test.

the DE ephemeris file DE421 (see section 2.2.3). The differences are depicted in Figure 2.5 and Figure 2.6 and information is tabulated in Table 2.2. Figure 2.5 and Figure 2.6 reveal a harmonic behavior of the differences, but since the values are close to machine precision, no safe conclusion can be drawn.

Solid Earth Tide

Apart from the direct force third bodies (Moon and Sun) induce on earth orbiting satellites (see section 2.2.3), they also have an effect on the body of the Earth, resulting in *tidal* phenomena. The latter produce small periodic deformations of the solid body of the Earth called *earth tides* or *solid earth tides*, which lead to periodic variations in the Earth's gravity field. These tidal perturbations have to be addressed in the case of POD. Note that his section is centered on the effect of solid Earth tides on the geopotential; tidal forces though, via the deformation they cause on the Earth's crust, result in site displacements (e.g. on instrumentation sites) that often have to be addressed when processing observations from Earth to satellites.

Solid earth tide effects, include the direct attraction of the tide generating potential, as well as deformations and associated geopotential changes arising from oceanic loading (which cause a loading of the crust) and wobbles of the mantle and the core regions (causing incremental centrifugal potentials). More information on tidal theory can be found in Wilhelm et al. 1997, Petit and Luzum 2010 and references therein.

The perturbations of satellite orbits from the lunisolar solid Earth tides are derived by an expansion of the tidal-induced gravity potential using spherical har-

27
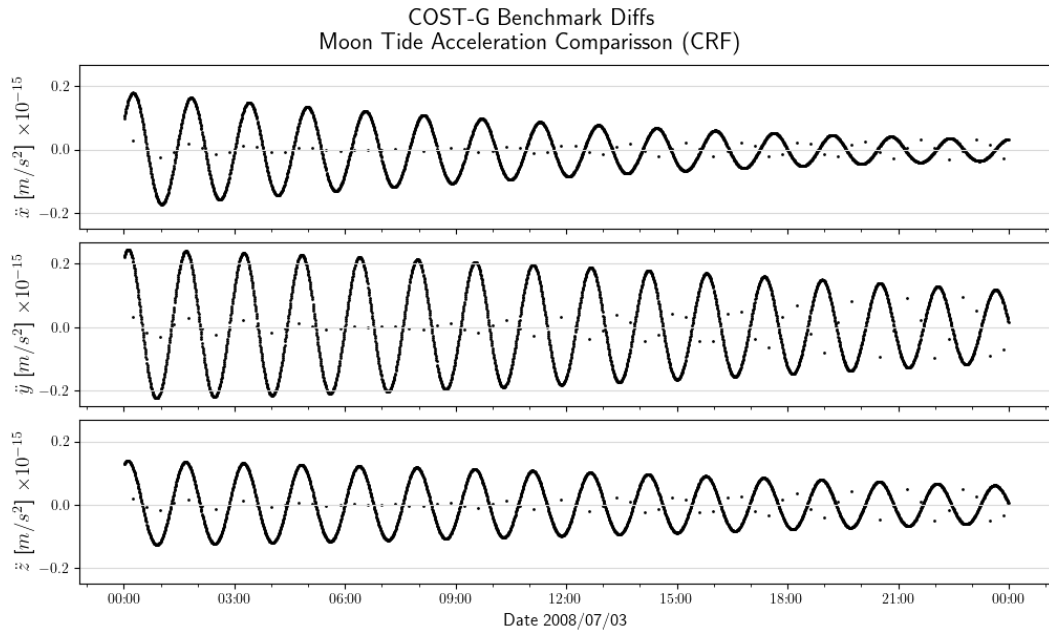
Figure 2.5: Third body acceleration induced by Moon on GRACE; descripancies against the COST-G benchmark test. Moon ephemerides extracted from DE421. Comparing results for a one day orbit arc of GRACE in ICRF.
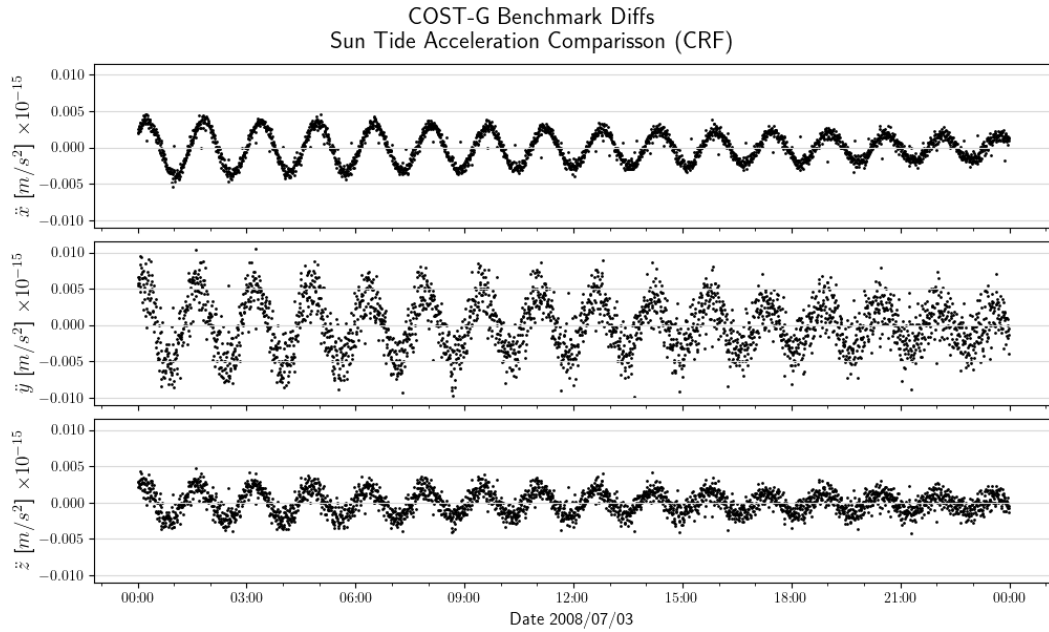
Figure 2.6: Third body acceleration induced by Sun on GRACE; descripancies against the COST-G benchmark test. Sun ephemerides extracted from DE421. Comparing results for a one-day orbit arc of GRACE in ICRF.

28

monics in a similar way as for the "static" gravity field of the Earth (Montenbruck and Gill 2000). The contributions ΔC_{nm} and ΔS_{nm} from the tides are expressible in terms of the *Love* number k (two k parameters are needed for $n = 2$ namely $k_{nm}^{(0)}$ and $k_{nm}^{(+)}$, while three such parameters are needed for $n \neq 2$, namely $k_{nm}^{(0)}$, $k_{nm}^{(+)}$ and $k_{nm}^{(-)}$, the latter being 0 in the case of $n = 2$). These parameters include a small imaginary part, due to the mantle's anelasticity (reflecting a phase lag in the deformational response of the Earth to tidal forces) Petit and Luzum 2010.

Hereafter, the treatment of earth tides as described in ibid. is adopted. Practically, the computation of the tidal contributions to the geopotential coefficients is most efficiently done by a three-step procedure. In the following, a summary of the process for computing the contributions ΔC_{nm} and ΔS_{nm}, as performed in the software developed for this Thesis is presented; further information can be found in ibid. Results for a one-day arc of GRACE are given in Figure 2.7; dataset was chosen to match the COST-G benchmark test.

Step 1 Corrections   In Step 1, the $(2m)$ part of the tidal potential is evaluated in the time domain for each m using lunar and solar ephemerides, and the corresponding changes $\Delta \bar{C}_{2m}$ and $\Delta \bar{S}_{2m}$ are computed using frequency independent nominal values k_{2m} for the respective $k_{2m}^{(0)}$. The contributions of the degree 3 tides to $\bar{C}_{3m}$ and $\bar{S}_{3m}$ through $k_{3m}^{(0)}$ and also of those of the degree 2 tides to $\bar{C}_{4m}$ and $\bar{S}_{4m}$ through $k_{2m}^{(+)}$ may be computed by a similar procedure.

With frequency-independent values k_{nm}, changes induced by the (nm) part of the Tide Generating Potential (TGP) in the *normalized* geopotentials coefficients of the same degree and order (nm), are given in the time domain by (ibid.):

$$\Delta \bar{C}_{nm} - i \Delta \bar{S}_{nm} = \frac{k_{nm}}{2n+1} \sum_{j=2}^{3} \frac{GM_j}{GM_\oplus} \left(\frac{R_e}{r_j} \right)^{n+1} \bar{P}_{nm} \left(\sin \Phi_j \right) e^{-im\lambda_j} \qquad (2.34)$$

where:

k_{nm}[4] is the nominal Love number for degree n and order m,

---

[4] Tables of relevant Love numbers are listed in Petit and Luzum 2010, Table 6.3. Note that in the $n = 2$ case, k_{2m} have a non-zero imaginary part $k_{2m} = \Re(k_{2m}) + i\Im(k_{2m})$, hence Equation 2.34 expands to

$$\begin{Bmatrix} \Delta \bar{C}_{nm} \\ \Delta \bar{S}_{nm} \end{Bmatrix} = \frac{1}{5} \frac{GM_j}{GM_\oplus} \left(\frac{R_e}{r_j} \right)^3 \bar{P}_{2m} \begin{Bmatrix} \Re(k_{2m}) \cos m\lambda_j + \Im(k_{2m}) \sin m\lambda_j \\ \Re(k_{2m}) \sin m\lambda_j - \Im(k_{2m}) \cos m\lambda_j \end{Bmatrix} \qquad (2.35)$$

R_e and $GM_{\oplus}$ are the equatorial radius and the gravitational parameter of the Earth,

GM_j is the gravitational parameter of the Moon and Sun, for $j = 2$ and $j = 3$ respectively,

Φ_j is the body-fixed geocentric latitude of the Moon and Sun (j indexes as above), and

λ_j is the body-fixed (east) longitude of the Moon and Sun (j indexes as above)

For $n = 4$, formula Equation 2.34 becomes (Petit and Luzum 2010):

$$\Delta \bar{C}_{4m} - i\Delta \bar{S}_{4m} = \frac{k_{nm}}{5} \sum_{j=2}^{3} \frac{GM_j}{GM_{\oplus}} \left(\frac{R_e}{r_j}\right)^3 \bar{P}_{2m}(\sin \Phi_j) e^{-im\lambda_j} \text{ for } m = 0, 1, 2 \quad (2.36)$$

to account for the changes in the degree 4 coefficients produced by the degree 2 tides.

In summary, via Step 1, corrections for

$$\Delta \bar{C}_{nm}, \Delta \bar{S}_{nm} \text{ for } \begin{cases} n = 2 & m = 0, 1, 2 \\ n = 3 & m = 0, 1, 2, 3 \\ n = 4 & m = 0, 1, 2 \end{cases} \quad (2.37)$$

are computed.

Step 2 Corrections   In Step 2, corrections for the deviations of the $k_{21}^{(0)}$ from the constant nominal value k_{21} assumed (for this band) in the first step are computed. Similar corrections need to be applied to a few of the constituents of the other two bands also.

The contribution to $\Delta \bar{C}_{20}$ from the long period tidal constituents, each with a frequency f, can be computed by (ibid.):

$$\Re\left\{\sum_{f(2,0)} (A_0 \delta k_f H_f) e^{i\theta_f}\right\} = \sum_{f(2,0)} \left[\left(A_0 H_h \delta k_f^{\Re}\right) \cos \theta_f - \left(A_0 H_h \delta k_f^{\Im}\right) \sin \theta_f\right] \quad (2.38)$$

Furthermore, computation of the contribution for $(nm) = (21)$ from the diurnal tidal constituents and to (22) from the semidiurnal can be computed using (ibid.):

$$\Delta \bar{C}_{2m} - i\Delta \bar{C}_{2m} = \eta_m \cdot \sum_{f(2,m)} (A_m \delta k_f H_f) e^{i\theta_f} \text{ for } m = 1, 2 \quad (2.39)$$

where

$\delta k_f = \delta k_f^{\Re} + i \delta k_f^{\Im}$ is the difference between k_f defined as $k_{2m}^{(0)}$ at frequency f and the nominal value $(k_f - k_{2m})$, plus a contribution from ocean loading. Values of the imaginary and real part, $\delta k_f^{\Re}$ and $\delta k_f^{\Im}$ respectively, can be found in ibid., Tables 6.5a through 6.5c. Note however, that in the computation we use the amplitude values for the in-phase and out-of-phase components ($A_{in-phase} = \left(A_m H_f \delta k_f^{\Re} \right)$ and $A_{out-of-phase} = \left(A_m H_f \delta k_f^{\Im} \right)$) directly, recorded in the same tables.

H_f is the amplitude (in meters) of the term at frequency f

θ_f is given by

$$\theta_f = m \cdot (\theta_g + \pi) - \sum_{j=1}^{5} N_j F_j \tag{2.40}$$

where θ_g is the Greenwich Mean Sidereal Time (GMST) expressed in angle units. Here we use the expression based on the expansion using the *Fundamental Arguments*. For alternate formulations, e.g. using the *Doodson* arguments, see ibid., Sec. 6.2.1.

The terms η_m and A_m, are given by:

$$\eta_m = \begin{cases} -i, m = 1 \\ 1, m = 2 \end{cases} \tag{2.41}$$

and

$$A_m = \begin{cases} \frac{1}{R_\oplus \sqrt{4\pi}}, m = 0 \\ \frac{(-1)^m}{R_\oplus \sqrt{8\pi}}, m \neq 0 \end{cases} \tag{2.42}$$

As with the $\delta k_f^{\Re}$ and $\delta k_f^{\Im}$ terms explicit computation of A_m is not needed if the amplitude terms $A_{in-phase}$ and $A_{out-of-phase}$ are used from ibid. Tables 6.5a through 6.5c.

Steps 1 and 2 can be used to compute the total tidal contribution, including the time independent (permanent) contribution to the geopotential coefficient $\bar{C}_{20}$, which is adequate for a "conventional tide free" model. When using a "zero tide" model, this permanent part should not be counted twice.

31
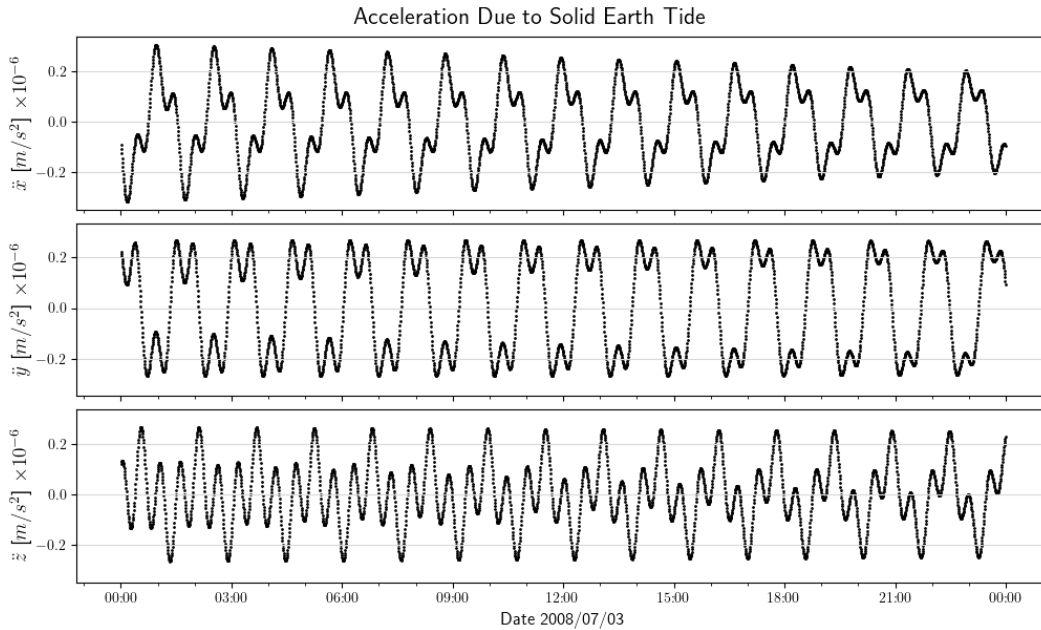
Figure 2.7: Acceleration due to solid Earth tide computed on a one-day arc of GRACE.

Implementation & Validation The above described procedure was implemented in the software build for this Thesis. It is clear from the above, that the computations involved are rather complicated and cumbersome; the problem is further perplexed by the fact that the magnitude of the computed geopotential coefficient corrections is very small, while computations involve values spanning a wide range of orders of magnitude, thus making the computations susceptible to round-off errors.

To test the implementation developed for this Thesis, results were checked against the `COST-G` benchmark test. Input data for the test is a one-day orbit arc of GRACE along with the Sun and Moon ephemerides, extracted from `DE 421`. The discrepancies between our implementation and the benchmark test are depicted in Figure 2.8 and Table 2.3. It should be noted here that the benchmark test considered, involves a number of steps in which different software implementations can produce slightly different results, as are e.g. computation of Sun and Moon position, handling of datetimes and ICRF-to- ITRF transformations.
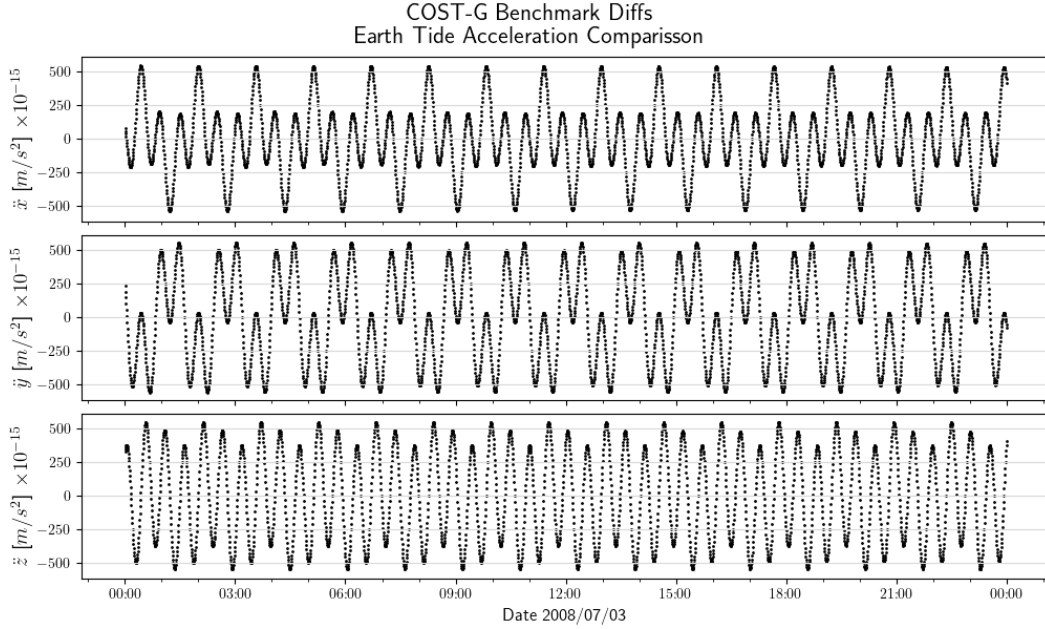
Figure 2.8: Discrepancies with the COST-G benchmark test for the acceleration due to solid Earth tide, computed on a one-day arc of GRACE.

Component	Min	Max	Mean	Std. Deviation
			m/s^2	
$\ddot{x}$	-5.36e-13	+5.45e-13	3.51e+00	2.71e-13
$\ddot{y}$	-5.56e-13	+5.56e-13	-4.58e+00	3.39e-13
$\ddot{z}$	-5.43e-13	+5.47e-13	-9.51e-01	3.39e-13

Table 2.3: Earth tide acceleration discrepancies against the COST-G benchmark test.

33

Ocean Tide

As in the case of Earth tides (see section 2.2.3), the dynamical effects of ocean tides can be modeled as periodic variations in the Stoke's coefficients $\Delta \bar{C}_{nm}$ and $\Delta \bar{S}_{nm}$ (for degree n and order m). To compute these values, the prograde and retrograde geopotential harmonic amplitudes $\mathcal{C}^{\pm}$ and $\mathcal{S}^{\pm}$ for $\mathcal{C}$ and $\mathcal{S}$ respectively are needed, for each tidal constituent f involved. Adopting the development presented in Petit and Luzum 2010, we can compute the variations from

$$\left(\Delta \bar{C}_{nm} - i \Delta \bar{S}_{nm}\right)(t) = \sum_f \overline{\sum_+} \left(\mathcal{C}^{\pm}_{f,nm} \mp \mathcal{S}^{\pm}_{f,nm}\right) e^{\pm i \theta_f(t)} \tag{2.43}$$

where

f is a given tidal constituent,

$\theta_f(t)$ is the argument of the constituent f at epoch t, and

$\mathcal{C}^{\pm}_{f,nm}$ and $\mathcal{S}^{\pm}_{f,nm}$ are the geopotential harmonic amplitudes

Note that not all of the available ocean loading models are published in the form of $\mathcal{C}^{\pm}_{f,nm}$ and $\mathcal{S}^{\pm}_{f,nm}$ coefficients Typically, most are developed and distributed as gridded maps of tide height amplitudes. These models provide in-phase and quadrature amplitudes of tide heights for selected, main tidal frequencies (or main tidal waves), on a variable grid spacing over the oceans (ibid.). However, using spherical harmonic decomposition and with the use of an Earth loading model, the maps of ocean tide height amplitudes have been converted to spherical harmonic coefficients for use in Equation 2.43. The procedure is outlined in e.g. ibid.

Typically, ocean tide models provide maps for only the largest tides or "main waves". Interpolation from the main waves to the smaller, "secondary waves" can be performed, using an assumption of linear variation of tidal admittance between closely spaced tidal frequencies. Through this method, the spectrum of tidal geopotential perturbations can be completed to the requested degree. For a secondary wave f, the needed coefficients can be computed as

$$
\begin{aligned}
\mathcal{C}^{\pm}_{f,nm} &= \frac{\dot{\theta}_f - \dot{\theta}_1}{\dot{\theta}_2 - \dot{\theta}_1} \frac{H_f}{H_2} \mathcal{C}^{\pm}_{2,nm} + \frac{\dot{\theta}_2 - \dot{\theta}_f}{\dot{\theta}_2 - \dot{\theta}_1} \frac{H_f}{H_1} \mathcal{C}^{\pm}_{1,nm} \\
\mathcal{S}^{\pm}_{f,nm} &= \frac{\dot{\theta}_f - \dot{\theta}_1}{\dot{\theta}_2 - \dot{\theta}_1} \frac{H_f}{H_2} \mathcal{S}^{\pm}_{2,nm} + \frac{\dot{\theta}_2 - \dot{\theta}_f}{\dot{\theta}_2 - \dot{\theta}_1} \frac{H_f}{H_1} \mathcal{S}^{\pm}_{1,nm}
\end{aligned}
\tag{2.44}
$$

```
Coefficients to compute variations in normalized Stokes coefficients (unit = 10^-11)
Ocean tide model: FES2014b up to (180,180)
Doodson Darw  l   m    DelC+     DelS+      DelC-      DelS-
055.565 om1   1   0  -0.84987   0.00000   -0.84987    0.00000
055.565 om1   2   0   2.55417  -0.00000    2.55417   -0.00000
055.565 om1   3   0   0.02827  -0.00000    0.02827   -0.00000
055.565 om1   4   0  -0.25307   0.00000   -0.25307    0.00000
055.565 om1   5   0   0.34383  -0.00000    0.34383   -0.00000

...
055.575 om2   1   0   0.00830   0.00000    0.00830    0.00000
055.575 om2   2   0  -0.02493   0.00000   -0.02493    0.00000
055.575 om2   3   0  -0.00028   0.00000   -0.00028    0.00000
055.575 om2   4   0   0.00247   0.00000    0.00247    0.00000
055.575 om2   5   0  -0.00336   0.00000   -0.00336    0.00000
```

Figure 2.9: Part of `FES2014b` geopotential harmonic amplitudes $\mathcal{C}_{f,nm}^{\pm}$ and $\mathcal{S}_{f,nm}^{\pm}$ for tidal constituents 055.565 and 055.575. File retrieved from the `COST-G` benchmark test repository, ftp://ftp.tugraz.at/outgoing/ITSG/COST-G/.

where the subscript 1 and 2 denote the two nearby main lines, or *pivot waves* and H is the astronomic amplitude of the considered wave.

As in the case of solid Earth tides (section 2.2.3), ocean loading can induce deformation on the Earth's crust and thus displacements on instrumentation sites.

Ocean Tide Models   Ocean tide models are defined using an underlying tide height model, and further include the maximum degree and order of the expansion and identification of the main, pivot waves. Since the mid-1990s, a series of `FES` (finite element solution) global ocean tidal atlases has been produced and released with the primary objective to provide altimetry missions with tidal de-aliasing correction at the best possible accuracy. In this Thesis, the latest model in this series, labeled `FES2014` (Lyard et al. 2021) is used, since it is the one suggested from the IDS for the ITRF2020 processing campaign. Table 2.4 lists the tidal constituents contained within the aforementioned data file.

Implementation   Design and implementation of the procedure outlined above for the computation of variations in the Stoke's coefficients $\Delta \bar{C}_{nm}$ and $\Delta \bar{S}_{nm}$, poses a series of challenges. First off, a decision must be made to allow for the distinction between different tidal waves. This allows for efficiency, adaptability, extensibility and ease of use. To that end, a generic class was designed to represent different waves, based on the Doodson number; this approach offers several advantages, as well as the ability to compute arguments of the tide constituents (e.g. θ in

Doodson Number	Darwin Symbol	Description
055.565	Ω_1	Lunar Saros
055.575	Ω_2	
056.554	S_a	Solar annual
057.555	S_{sa}	Solar semiannual
065.455	M_m	Lunar monthly
075.555	M_f	Lunisolar fortnightly
085.455	M_{tm}	
093.555	M_{sqm}	
135.655	Q_1	Larger lunar elliptic diurnal
145.555	O_1	Principal lunar declinational
163.555	P_1	Principal solar declination
164.555		
165.555	K_1	Lunisolar diurnal
175.455	J_1	Smaller lunar elliptic diurnal
227.655	ϵ_2	
235.755	$2N_2$	Lunar elliptical semidiurnal second-order
237.555	μ_2	Variational
245.655	N_2	Larger lunar elliptic semidiurnal
247.455	ν_2	Larger lunar evectional
255.555	M_2	Principal lunar semidiurnal
263.655	λ_2	Smaller lunar evectional
265.455	L_2	Smaller lunar elliptic semidiurnal
272.556	T_2	
273.555	S_2	Principal solar semidiurnal
274.554	R_2	
275.555	K_2	Lunisolar semidiurnal
355.555	M_3	Lunar terdiurnal
435.755		
445.655	M_{N4}	Shallow water quarter diurnal
455.555	M_4	Shallow water overtides of principal lunar
473.555	M_{s4}	Shallow water quarter diurnal
491.555	S_4	Shallow water overtides of principal solar
655.555	M_6	Shallow water overtides of principal lunar
855.555	M_8	Shallow water eighth diurnal

Table 2.4: List of "main" tidal constituents contained listed in `FES2014b`; published file via `COST-G`. Description is extracted from Beauducel 2023.

Equation 2.43), via the Doodson multipliers, which are in turn obtained through the computation of the fundamental arguments of nutation theory or *Delaunay variables* l, l_0, F, D and Ω, augmented by the GMST. These values are computed using the latest formulations (Petit and Luzum 2010).

Next, efficient mapping/loading of the coefficients $\mathcal{C}_{f,nm}^{\pm}$ and $\mathcal{S}_{f,nm}^{\pm}$ must be developed. Note that four such coefficients per tidal wave, and for every combination of degree and order (n, m) have to be considered; as can be seen in Figure 2.9, the maximum degree and order in this case is 180; that amounts to a huge number of floating point numerics that need to be stored and loaded to/from memory. The software developed, uses efficient data structures and contiguous memory chunks to speed-up computations and only allocate the memory needed.

Computation of $\Delta\bar{C}_{nm}$ and $\Delta\bar{S}_{nm}$ values follows Equation 2.43. When needed, interpolation through tidal admittance (see Equation 2.44) is also handled in the software, per user/application needs.

Atmospheric Drag

For LEO satellites, the largest non-gravitational force is the atmospheric drag. Despite its significance though, accurate modeling of aerodynamic forces is a very complex problem, requiring knowledge of the physical properties of the (upper) atmosphere, interaction of neutral gas and charged particles with the satellite's surfaces and precise knowledge of attitude with respect to atmospheric particle flux (Montenbruck and Gill 2000).

Drag is a decelerating force, directed opposite to the velocity of the satellite with respect to atmospheric flux. Minor contributions, including lift and binormal forces, can be safely ignored. A simple derivation of the acceleration induced to a satellite due to atmospheric drag can be found in ibid.; following this formulation, drag induced acceleration can be computed from

$$\ddot{\boldsymbol{r}} = -\frac{1}{2}C_d\frac{A}{m}\rho v_r^2\hat{\boldsymbol{e}}_v \tag{2.45}$$

where

ρ is the atmospheric density at the location of the satellite,

A is the satellite's cross-sectional area,

v_r is the velocity of the satellite relative to the atmosphere,

$\hat{\boldsymbol{e}}_v = \boldsymbol{v}_r/\|\boldsymbol{v}_r\|$ is the unit vector in the direction of v_r

C_d is the *drag coefficient*, a dimensionless quantity describing the interaction of the atmosphere with the satellite's surface material. This parameter is normally estimated during POD procedure.

With the assumption that the atmosphere co-rotates with the Earth (thus partly ignoring the complex atmosphere dynamics), the relative velocity of the satellite with respect to the atmosphere, $\boldsymbol{v}_r$, is given by

$$\boldsymbol{v}_r = \boldsymbol{v} - \boldsymbol{\omega}_\oplus \times \boldsymbol{r} \tag{2.46}$$

which is a very good approximation even for POD applications. According to Montenbruck and Gill 2000, the maximum observed deviations from this assumption lead to uncertainties in the drag force of less than 5%. $\boldsymbol{v}$ and $\boldsymbol{r}$ are the inertial satellite velocity and position vectors, while $\boldsymbol{\omega}_\oplus$ is the Earth's angular velocity vector.

In the ideal case of a spherical spacecraft, the projected area A would not change. For all other shapes however, A needs to be computed using the space vehicle's attitude. It is typical to model such complex geometries using a collection of flat plates (macromodel), each with an area A_i and outward normal unit vector $\hat{\boldsymbol{n}}_i$, expressed in the spacecraft body-fixed coordinate system.

The inclination of the ith plate to the relative velocity $\boldsymbol{v}_r$, is given by:

$$\cos\theta_i = \left(\mathcal{R}^T \hat{\boldsymbol{n}}_i\right)^T \left(\frac{\boldsymbol{v}_r}{\|\boldsymbol{v}_r\|}\right) \tag{2.47}$$

where $\mathcal{R}$ is the attitude matrix that rotates the GCRF frame to the spacecraft body-fixed frame. Using this formulation, the projected area A can be computed as the collection of the N macromodel plates, i.e.

$$A = \sum_{i=1}^{N} A_i \cdot \begin{cases} \cos\theta_i, & \text{if } \cos\theta_i > 0 \text{ or} \\ 0, & \text{if } \cos\theta_i < 0 \end{cases} \tag{2.48}$$

Partial Derivatives Differentiation of Equation 2.45 with respect to the C_d parameter, yields

$$\frac{\partial \ddot{\boldsymbol{r}}}{\partial C_d} = -\frac{1}{2}\frac{A}{m}\rho\|v_r\|\boldsymbol{v_r} \tag{2.49}$$

From Equation 2.45 and Equation 2.46, one can analytically derive the partials of the acceleration with respect to the satellite velocity vector

$$\frac{\partial \ddot{r}}{\partial v} = -\frac{1}{2}C_d\frac{A}{m}\rho\left(\frac{v_r v_r^T}{\|v_r\|} + \|v_r\| \cdot I_{3\times3}\right) \tag{2.50}$$

Correspondingly, the partial of the acceleration with respect to the satellite position vector, is given by

$$\begin{aligned}\frac{\partial \ddot{r}}{\partial r} &= -\frac{1}{2}C_d\frac{A}{m}\|v_r\|v_r\frac{\partial\rho}{\partial r} - \frac{1}{2}C_d\frac{A}{m}\rho\left(\frac{v_r v_r^T}{\|v_r\|} + \|v_r\| \cdot I_{3\times3}\right)\frac{\partial v_r}{\partial r} \\ &= -\frac{1}{2}C_d\frac{A}{m}\rho\|v_r\|v_r\frac{\partial\rho}{\partial r} - \frac{\partial \ddot{r}}{\partial v}\omega\end{aligned} \tag{2.51}$$

In Equation 2.51, the $\frac{\partial\rho}{\partial r}$ term describes the dependence of atmospheric density on satellite position. Analytical derivation of this term is nearly impossible, due to the complexity of the atmospheric model used. Therefore, a numerical approach is followed to derive the density gradient, using the *Difference Quotient Approximation*. Thus, the formula

$$\begin{aligned}\frac{\partial\rho}{\partial r}(r,t) &= \frac{\rho(r + \delta r, t)}{\delta r} \\ &= \left(\frac{\rho(r+\delta r_x)}{\|\delta r_x\|} \quad \frac{\rho(r+\delta r_y)}{\|\delta r_y\|} \quad \frac{\rho(r+\delta r_z)}{\|\delta r_z\|}\right)^T\end{aligned} \tag{2.52}$$

is used, where δr_x, δr_y and δr_z are vectors along the x, y and z axis respectively, and r is the satellite's position vector at instant t. The values of the vector components along the three axis, should be small enough to approximate the derivative (or more precisely the gradient) at the given point. Using unit vectors (of length $1\,\mathrm{m}$ per component, i.e $\delta r_x = \hat{x}$), should yield realistic results; this is the default value used in our implementation. It should be noted that here it is implicitly assumed that the density function ρ is differentiable within the given interval. In reality this means that no "abrupt" changes should occur within the spatial/temporal span considered.

Atmospheric Models   The most challenging term in Equation 2.45, is the atmospheric density ρ (at the location of satellite). This requires the modeling of complex properties and dynamics of the Earth's atmosphere. The latter is a highly demanding task, and a number of models have been introduced (often including empirical data) to target the question. In the upper atmosphere ($> 100\,\mathrm{km}$), apart

from spatial and temporal variances, the density also depends on solar soft x-ray and extreme ultraviolet (EUV) output, as well as the geomagnetic activity. Hence, the density is considered as a function of altitude, solar ten-centimetre flux ($F10.7$) and the geomagnetic activity index (A_p).

Different (upper) atmospheric models are available (for comparison and overview, see e.g. Doornbos et al. 2009, Yang et al. 2022 and Vallado and Finkleman 2014) varying in methodology, input data, application criteria and demands, complexity and efficiency. In this Thesis, two atmospheric models were implemented, namely:

NRLMSISE-00 model (Picone et al. 2002), which is an empirical atmospheric model that extends from the ground to the exobase and describes the average observed behavior of temperature, various species densities, and mass density via a parametric analytic formulation. The model inputs are location, date and time, solar activity, and geomagnetic activity. It was developed by researchers in the US Naval Research Laboratory.

DTM-2020 model (Bruinsma and Boniface 2021), a semi-empirical Drag Temperature Model (DTM) to predict the Earth's thermosphere's temperature, density, and composition, especially for orbit computation purposes. This model comes in two variations, the "operational" version, driven by the trusted and established $F10.7$ and A_p indices for solar and geomagnetic activity and the "research" alternative which is based on space weather observations not yet accredited operationally. Hence, in the Thesis, the first, "operational" version is used.

In order to use the `NRLMSISE-00` and `DTM-2020` models, space weather data is needed, including an 81-day average of F10.7 flux[5] (centered on day), daily F10.7 solar flux for previous day and daily magnetic index. This data can be obtained via the "Space Weather Data" records archived by CelesTrack (Vallado and Kelso 2013).

Implementation Implementing the atmospheric density models described above, is a challenging task. Not only due to model complexity and the large number of computations involved, but also because it needs to be paired with space weather

---

[5]The solar radio flux at 10.7 cm (2800 MHz) is an excellent indicator of solar activity. Often called the F10.7 index, it is one of the longest running records of solar activity, reported in "solar flux units". The F10.7 Index has proven very valuable in specifying and forecasting space weather, and tracks well with Extreme UltraViolet (EUV) emissions that impact the ionosphere and modify the upper atmosphere

data spanning various time intervals (e.g. an 81-day average of $F10.7$ is needed at each epoch, as well as values of A_p per 3-hour intervals). Obviously, the complete scheme must be efficient and robust, since computing atmospheric density is performed hundreds of times in a POD process spanning considerable arcs.

Source code for implementing the above has been designed and implemented from scratch, for the purpose of this Thesis. It has undergone extensive testing for correctness and efficiency. The final design, is one that allows the incremental parsing of needed data, via a "hunting process" (i.e. storing current stream positions and using indexes for searching onward) and a one-time mapping of input file streams.

Acceleration (see Equation 2.45 and Equation 2.46) and derivatives (see discussion in section 2.2.3) with respect to the parameters considered are also implemented in source code.

Solar Radiation Pressure

An Earth orbiting satellite exposed to solar radiation, experiences a small force arising from the absorption or reflection of photons. The effect depends on the satellite's mass and surface area. The primary radiation source to be considered in satellite geodesy is the Sun. The radiation pressure due to the direct solar radiation is also referred to as *direct radiation pressure*. Other sources of radiation are the Earth, which reflects and/or re-emits the radiation received by the Sun, or to a much lesser extent, the Moon, reflecting the solar radiation. Radiation pressure is the dominating non-gravitational perturbation above heights of about $600 \, \text{km}$ (Beutler 2005).

The radiation field due to the direct solar radiation may be considered as parallel to the direction $Sun \rightarrow Satellite$. This implies that for the computation of solar radiation pressure, the surface of the cross section of the satellite normal to the direction $Sun \rightarrow Satellite$ needs to be known.

Assuming rotational symmetry of the satellite w.r.t. the axis $Sun \rightarrow Satellite$, the acceleration due to the direct solar radiation may be written as (ibid.)

$$\ddot{\boldsymbol{r}} = -P_\odot C_R \frac{A}{m} \frac{\boldsymbol{r} - \boldsymbol{r}_\odot}{\|\boldsymbol{r} - \boldsymbol{r}_\odot\|^3} 1 \, \text{au}^2 \tag{2.53}$$

where:

41

$P_\odot$ is the Sun's solar flux at a distance of $1\,\mathrm{au}$, $P_\odot \approx 4.56 \times 10^{-6}\,\mathrm{N/m^2}$

C_R is the *radiation pressure coefficient* depending on the *refractivity* ε of the satellite,

$\boldsymbol{r}$ is the geocentric position vector of the satellite,

$\boldsymbol{r}_\odot$ is the geocentric position vector of the Sun,

au is the Astronomical Unit,

m is the mass of the satellite, and

A is the cross section of the satellite normal to the direction $Sun \rightarrow Satellite$

C_R is usually estimated during a POD process. While Equation 2.53 constitutes a good approximation, more sophisticated methods are often used in a POD process to obtain more accurate estimates of solar radiation pressure, if detailed knowledge of the vehicle is available. In such a case, the total force (or acceleration) is decomposed into contributions due to *specular* reflection, *diffuse* reflection *absorption* and *emission*, modeling the spacecraft's surface as a collection of N flat plates, each of area A_i.

To use such complex model, the spacecraft's attitude must be known at each request epoch. Using $\mathcal{R}$ as the attitude matrix that rotates the GCRF frame to the spacecraft body-fixed frame and $\hat{\boldsymbol{e}}_\odot$ to denote the unit vector directed from the space vehicle to the center of the Sun, the inclination of the ith plate to the spacecraft-to-Sun vector is given by:

$$\cos\theta_i = \left(\mathcal{R}^T \hat{\boldsymbol{n}}_i\right)^T \hat{\boldsymbol{e}}_\odot \tag{2.54}$$

where $\hat{\boldsymbol{n}}_i$ is the outward normal of the ith plate, expressed in the spacecraft body-fixed coordinate system.

The individual contribution of each plate can now be be expressed as (Markley and Crassidis 2019)

$$\sum_{i=1}^{N} A_i \cos\theta_i \left(2\left(\frac{R_i^{diff}}{3} + R_i^{spec} \cos\theta_i \right) \left(\mathcal{R}^T \hat{\boldsymbol{n}}_i\right)^T + (1 - R_i^{spec}) \hat{\boldsymbol{e}}_\odot \right) \tag{2.55}$$

where the summation is performed on all plates for which $\cos\theta_i > 0$ holds, and

R_i^{diff} is the diffuse reflection coefficient for the ith plate, and

R_i^{spec} is the specular reflection coefficient for the ith plate,

Equation 2.55 is used in this Thesis to compute individual plate contributions. It should be noted that *albedo* effects, i.e. radiation pressure from reflected light from the Earth and/or Moon, is not considered here, as is the force of thermal radiation emitted from the spacecraft.

Partial Derivatives Starting from 2.53, the acceleration due to solar radiation pressure varies with the satellite position in the same way as the gravitational attraction of the Sun, with derivatives given by:

$$\frac{\partial \ddot{\boldsymbol{r}}}{\partial \boldsymbol{r}} = P_\odot C \frac{A}{m} AU^2 \left(\frac{1}{\|\boldsymbol{r} - \boldsymbol{r}_\odot\|^3} \boldsymbol{I}_{3\times3} - 3 \left(\boldsymbol{r} - \boldsymbol{r}_\odot \right) \frac{\left(\boldsymbol{r} - \boldsymbol{r}_\odot \right)^T}{\|\boldsymbol{r} - \boldsymbol{r}_\odot\|^5} \right) \tag{2.56}$$

Due to the fact that the radiation pressure coefficient C is usually estimated during orbit determination, the derivative of the acceleration w.r.t C must be calculated. The respective partials are:

$$\frac{\partial \ddot{\boldsymbol{r}}}{\partial C} = \frac{1}{C} \ddot{\boldsymbol{r}} = -P_\odot \frac{A}{m} \frac{\boldsymbol{r} - \boldsymbol{r}_\odot}{\|\boldsymbol{r} - \boldsymbol{r}_\odot\|^3} AU^2 \tag{2.57}$$

required to compute the influence of variations in the radiation pressure coefficient on the satellite trajectory.

Radiation pressure obviously is "turned off" if the radiation is blocked by an "obstacle", i.e the Moon or Earth, between the Sun and the satellite.

Satellite Eclispes and Earth Shadow Satellites routinely enter eclipse periods during their orbits, resulting in fluctuations in the experienced solar radiation pressure. When a satellite enters the *umbra* or the *penumbra* area of an occulting body (e.g., the Earth or the Moon), a satellite shadow function model is used to estimate the occultation degree. For the purposes of this Thesis, the so called *conical model* is used (R. Zhang et al. 2019) to compute occulatation factor.

For the conical model and using the Earth as an occulting body, the following

angles are defined:

$$\theta_{\oplus} = \arcsin\left(\frac{R_{\oplus}}{\|\boldsymbol{r}\|}\right) \tag{2.58}$$

$$\theta_{\odot} = \arcsin\left(\frac{R_{\odot}}{\|\boldsymbol{r}_{\odot} - \boldsymbol{r}\|}\right) \tag{2.59}$$

$$\theta = \arccos\left(\frac{-\boldsymbol{r}^T\left(\boldsymbol{r}_{\odot} - \boldsymbol{r}\right)}{\|\boldsymbol{r}\|\|\boldsymbol{r}_{\odot} - \boldsymbol{r}\|}\right) \tag{2.60}$$

When $\theta \geqslant \theta_{\oplus} + \theta_{\odot}$ occultation does not take place. If $\theta \leqslant \theta_{\oplus} - \theta_{\odot}$ occultation is total. Partial occultation takes place if $\|\theta_{\oplus} - \theta_{\odot}\| < \theta < \theta_{\oplus} + \theta_{\odot}$. In this latter case, an occultation factor is computed, as

$$F = 1 - \frac{S}{\pi\theta_{\odot}^2} \tag{2.61}$$

where S is the occulted area. Shadow models considering the Earth's oblateness and the atmospheric effec can be found in e.g. Y. Zhang et al. 2022.

2.3 The Celestial Reference Frame

2.3.1 International Celestial Reference Frame

A reference system is a theoretical concept of coordinates, and includes the time and the standards necessary to specify the bases for giving positions and motions in the system (Gurfil and Seidelmann 2018). There are celestial and terrestrial reference systems.

The International Celestial Reference System (ICRS) is based on the theory of relativity, observations of distant extragalactic radio sources, and a fixed origin, thus it is essentially "fixed" in space (since there is no apparent motion of distant sources). Two distinct systems are defined, the Barycentric Celestial Reference System (BCRS), centered at the barycenter of the solar system and the GCRS, centered at the geocenter. The GCRS is defined such that its spatial coordinates are not kinematically rotating with respect to the BCRS (ibid.). The axes of the GCRS are considered non-rotating in the Newtonian absolute sense, but the geocenter is accelerated within the solar system, thus this system is in reallity a "quasi-inertial" system.

The ICRS is materialized by a celestial reference frame called the ICRF, consisting of the precise coordinates of extragalactic objects, mostly quasars. The necessity of keeping the reference directions fixed and the continuing improvement in the source coordinates requires regular maintenance of the frame.

The IERS Earth Orientation Parameters provide the permanent tie of the ICRF to the ITRF. They describe the orientation of the Celestial Intermediate Pole (CIP) in the terrestrial system and in the celestial system (polar coordinates x, y; celestial pole offsets $\delta\psi$, $\delta\epsilon$) and the orientation of the Earth around this axis (UT1-UTC), as a function of time (Petit and Luzum 2010). This tie is available daily with an accuracy of ± 0.1 mas in the IERS publications.

2.3.2   Kinematics of the Earth

Earth attitude is complicated by earth kinematics, including precession and nutation of the axes of rotation, the motion of the pole of rotation within the Earth (polar motion), and the variability of the rate of rotation of the Earth (resulting in variations in the length of day). While the first two phenomena (precession and nutation) can be predicted quite accurately, the latter two have to be observed. To connect observations performed on the Earth's surface in a local coordinate system to a celestial system, these effects have to be considered.

Precession, which consists of the *precession of the equator* and *precession of the ecliptic*, is the motion of the equator with respect to the ecliptic. Nutation is the oscillations in the motion of the Earth's pole due to torques from external gravitational forces, limited to motions with periods longer than two days (Gurfil and Seidelmann 2018). Polar Motion is the motion of the Earth's pole of rotation with respect to the Earth's solid body, that is the angular excursion of the CIP from the ITRS z-axis.

Earth kinematics, including all the aforementioned phenomena, plays a crucial role in relating the ICRF and ITRF, a task needed in POD since the equations of motions of an Earth orbiting satellite need to be formulated in an inertial frame. Description of these variations and the related adopted models can be found in detail in e.g. ibid. and Urban and Seidelmann 2013. In this thesis, the nomenclature and resolutions adopted in the framework of the IAU 2000/2006 resolutions (see Petit and Luzum 2010 and references therein) will be used.

2.3.3 Terrestrial to Celestial Transformation

The definition of the GCRS and ITRS and the procedures for the ITRS to GCRS transformation that are provided in this section comply with the IAU 2000/2006 resolutions (see Capitaine et al. 2006 and IAU Division 1 Working Group n.d.). It should be noted that this section is not an extensive study or presentation of the concepts and models involved to relate terrestrial and celestial reference systems (and/or frames). It is rather meant to act as a guideline for the work performed in the framework of the current Thesis, centered on the design patterns, algorithms and methodologies adopted for the implementation of relevant software.

The transformation used to relate the ITRS to the GCRS at the date t of an observation can be written as (Petit and Luzum 2010)

$$\boldsymbol{r}_{gcrs} = \boldsymbol{Q}(t)\boldsymbol{R}(t)\boldsymbol{W}(t)\boldsymbol{r}_{itrs} \qquad (2.62)$$

where

$\boldsymbol{Q}(t)$ is the transformation matrix due to the motion of the celestial pole in the celestial reference system

$\boldsymbol{R}(t)$ is the transformation matrix due to the rotation of the Earth around the axis associated with the pole, and

$\boldsymbol{W}(t)$ is the transformation matrix due to polar motion

t is the time parameter in the Terestrial Time (TT) time-scale, and given by:

$$t = (\text{TT} - 2000 \text{ January 1d 12h TT})\text{d}/36525 \qquad (2.63)$$

involving J2000.0, defined at the geocenter and at the date 2000 January 1.5 TT = Julian Date 2451545.0 TT.

Note that Equation 2.62 uses the theoretical formulation of a reference "system". In reality, it should be clear that the numerical implementation of this formula involves the IAU/International Union of Geodesy and Geophysics (IUGG) adopted realization of those reference systems, i.e. the ITRF and ICRF.

Equation 2.62 can be implemented in two distinct procedures, differing only on the adopted origin of the CIP equator, i.e. either using the equinox, thus resulting in an *equinox based* transformation, or the CIO, which in turn results in the so-called *CIO based* transformation. In both cases, the matrix $\boldsymbol{W}(t)$ is identical, while $\boldsymbol{Q}(t)$ and $\boldsymbol{R}(t)$ will differ. The CIO based procedure, contrary to the equinox based, is in agreement with IAU 2000 Resolution B1.8, which:

requires the use of the "non-rotating origin" in both the GCRS and the ITRS as well as the position of the CIP in the GCRS and in the ITRS

(ibid.). Hence, for this Thesis we have adopted the *CIO based* implementation of the transformation Equation 2.62.

Schematically, the CIO-based procedure, implies (see also Figure 2.10):

- realization of the Terrestrial Intermediate Reference System (TIRS) via applying matrix $\boldsymbol{W}(t)$ on an ITRS vector $\boldsymbol{r}$; the TIRS uses the CIP as its z-axis and the Terrestrial Intermediate Origin (TIO) as its x-axis

- realization of the Celestial Intermediate Reference System (CIRS), that uses the CIP as its z-axis and the CIO as its x-axis, via the rotation matrix $\boldsymbol{R}$ with the Earth Rotation Angle (ERA) as its argument, and the matrix $\boldsymbol{Q}$ using the two coordinates of the CIP. Note that the position of the CIP both in the ITRS and GCRS is provided by the x and y components of the CIP unit vector. These components are called "coordinates", and their numerical expressions are multiplied by the factor $129\,600\,000''/2\pi$ in order to represent the approximate values in arcseconds of the corresponding "angles" (strictly their sines) with respect to the z-axis of the reference system (ibid.).

Polar Motion Matrix $W(t)$ The rotation of the Earth is represented by the diurnal rotation around a reference axis, called the CIP. The CIP does not coincide with the axis of figure of the Earth, but slowly moves (in a terrestrial reference frame) (Urban and Seidelmann 2013). This motion of the terrestrial reference frame with respect to the CIP is known as *polar motion*. Note that the CIP is not the instantaneous axis of rotation but the axis around which the diurnal rotation of earth is applied (in the celestial to terrestrial transformation). Polar motion is typically determined from VLBI observation, as except from the principal periods of 365 days (annual wobble) and 428 days (Chandler wobble), it is also affected by unpredictable geophysical forces.

According to IAU 2006 Resolution B2, the system at date t as realized from the ITRS by applying the transformation $\boldsymbol{W}(t)$ is the TIRS. It uses the CIP as its z-axis and the TIO as its x-axis (Petit and Luzum 2010). This matrix gives the position of the terrestrial reference frame with respect to the TIO.

The $\boldsymbol{W}$ matrix can be expressed as (ibid.):

$$\boldsymbol{W}(t) = \boldsymbol{R}_z(-s') \cdot \boldsymbol{R}_y(x_p) \cdot \boldsymbol{R}(y_p) \tag{2.64}$$

Interpolate IERS C04 file to get x_p, y_p, ΔUT, δX and δY at given t, see 2.12

Geocentric Celestial Reference System (GCRS)

compute IAU 2006/2000A X, Y from series (2.71 and 2.72)
compute s
apply corrections δX and δY
compute & apply matrix $\boldsymbol{Q}(t)$, see 2.3.3

Celestial Intermediate Reference System (CIRS)

apply matrix $\boldsymbol{R}(t)$, using the ERA and ΔUT
$\boldsymbol{R}(t) = R_3(ERA)$, see 2.3.3

Terrestrial Intermediate Reference System (TIRS)

compute s' and use x_p and y_p to
apply matrix $\boldsymbol{W}(t)$, see 2.3.3

International Terrestrial Reference System (ITRS)

Figure 2.10: Schematic representation of the "CIO-based" procedure to transform between the GCRS and ITRS.

48

where s' is the "TIO locator" and x_p, y_p are the "polar coordinates" of the CIP in the ITRS. The latter values, if not estimated, should be the ones published by the IERS, corrected for the effect of ocean tides and forced terms (aka "libration"), with periods less than two days in space (Petit and Luzum 2010), see subsection 2.3.4.

The TIO locator s', positioning the TIO on the equator of the CIP, is necessary to provide an exact realization of the "instantaneous prime meridian", designated by "TIO meridian" (ibid.). s' is obtained from polar motion observations by numerical integration, and so is in essence unpredictable. However, it is dominated by a secular drift of about $47\,\mu\text{as/century}$. The latter is used to actually compute s' in Equation 2.64. using the function:

$$s' = -47\,\mu\text{as} \cdot t \tag{2.65}$$

obtained from C04 data (Lambert and Bizouard 2002).

Earth Rotation Matrix $R(t)$ The rotation of the Earth around the axis of the CIP (i.e. relating TIRS and CIRS), can be expressed as (Petit and Luzum 2010):

$$\boldsymbol{R}(t) = \boldsymbol{R}_z(-ERA) \tag{2.66}$$

where ERA is the ERA between the CIO and the TIO at date t on the equator of the CIP, which is the rigorous definition of the sidereal rotation of the Earth. Working with respect to the CIO (rather than the equinox) sweeps away sidereal time's complexities and opportunities for error. The Earth rotation angle, the CIO based counterpart of Greenwich Sidereal Time (GST), is simply a conventional linear transformation of Universal Time (UT1) (IAU SOFA Board 2021c):

$$\begin{aligned}
ERA(T_u) = 2\pi(&\text{UT1 Julian day fraction} \\
&+ 0.7790572732640 + 0.00273781191135448 \cdot T_u)
\end{aligned} \tag{2.67}$$

where $T_u = (\text{Julian UT1 date } - 2451545.0)$ and $UT1 = UTC + (UT1 - UTC)$.

Similarly to polar motion, additional components should be added to the values published by IERS for ΔUT to account for the effects of ocean tides and libration, see subsection 2.3.4.

Celestial Motion Matrix $Q(t)$ The CIO based transformation matrix arising from the motion of the CIP in the GCRS (i.e. relating CIRS and GCRS), can be expressed as (Petit and Luzum 2010):

$$\boldsymbol{Q}(t) = \boldsymbol{R}_z(-E) \cdot \boldsymbol{R}_y(-d) \cdot \boldsymbol{R}_z(E) \cdot \boldsymbol{R}_Z(s) \tag{2.68}$$

49

where s is the "CIO locator" and E and d being such that the coordinates of the CIP in the GCRS are:

$$X = \sin d \cos E$$
$$Y = \sin d \sin E \qquad (2.69)$$
$$Z = \cos d$$

Equation 2.68 can be given in an equivalent form directly involving X and Y as (Petit and Luzum 2010):

$$\boldsymbol{Q}(t) = \begin{pmatrix} 1 - \alpha X^2 & -\alpha XY & X \\ -\alpha XY & 1 - \alpha Y^2 & Y \\ -X & -Y & 1 - \alpha(X^2 + Y^2) \end{pmatrix} \cdot \boldsymbol{R}_Z(s) \qquad (2.70)$$

with $\alpha = 1/(1 + \cos d)$, which can also be written, with an accuracy of $1\,\mu as$ as $\alpha = 1/2 + 1/8(X^2 + Y^2)$.

X and Y coordinates can be given by developments as function of time in the μas level, based on the IAU 2006 precession and IAU 2000A nutation (Capitaine and Wallace 2006). The IAU 2006/2000A developments are as follows (Petit and Luzum 2010):

$$\begin{aligned} X = {} & -0.016\,617\,00'' + 2004.191\,898\,00''t - 0.429\,782\,900''t^2 \\ & - 0.198\,618\,340\,0''t^3 + 0.000\,007\,578\,00''t^4 + 0.000\,005\,928\,500''t^5 \\ & + \sum_i \left[(a_{s,0})_i \sin\theta + (a_{c,0})_i \cos\theta \right] \\ & + \sum_i \left[(a_{s,1})_i t \sin\theta + (a_{c,1})_i t \cos\theta \right] \\ & + \sum_i \left[(a_{s,2})_i t^2 \sin\theta + (a_{c,2})_i t^2 \cos\theta \right] \\ & + \cdots \end{aligned} \qquad (2.71)$$

and

$$\begin{aligned} Y = {} & -0.006\,951\,00'' - 0.025\,896\,00''t - 22.407\,274\,700''t^2 \\ & + 0.001\,900\,590\,0''t^3 + 0.001\,112\,526\,00''t^4 + 0.000\,000\,135\,800''t^5 \\ & + \sum_i \left[(b_{s,0})_i \sin\theta + (b_{c,0})_i \cos\theta \right] \\ & + \sum_i \left[(b_{s,1})_i t \sin\theta + (b_{c,1})_i t \cos\theta \right] \\ & + \sum_i \left[(b_{s,2})_i t^2 \sin\theta + (b_{c,2})_i t^2 \cos\theta \right] \\ & + \cdots \end{aligned} \qquad (2.72)$$

50

where θ is a function of the fundamental lunisolar and planetary arguments. Further information and computation formulas for the fundamental arguments, can be found in ibid. Complete list of coefficients for Equation 2.71 and Equation 2.72 is provided by IERS.

VLBI observations have shown that there are deficiencies in the IAU 2006/2000A precession-nutation model of the order of 0.2 mas, mainly due to the fact that the free core nutation (Free Core Nutation (FCN)) is not part of the model, IERS publish observed estimates of the corrections to the IAU precession-nutation model. The observed differences with respect to the conventional celestial pole position defined by the models are monitored and reported by the IERSas "celestial pole offsets". Such time-dependent offsets from the direction of the pole of the GCRS must be provided as corrections δX and δY to the X and Y coordinates (ibid.). Using these offsets, the corrected celestial position of the CIP is given by (ibid.):

$$
\begin{aligned}
X &= X_{\text{IAU 2006/2000}} + \delta X \\
Y &= Y_{\text{IAU 2006/2000}} + \delta Y
\end{aligned}
\tag{2.73}
$$

thus enabling to re-write Equation 2.70 as:

$$
\tilde{\boldsymbol{Q}}(t) = \begin{pmatrix} 1 & 0 & \delta X \\ 0 & 1 & \delta Y \\ -\delta X & -\delta Y & 1 \end{pmatrix} \cdot \boldsymbol{Q}_{IAU}
\tag{2.74}
$$

where $\boldsymbol{Q}_{IAU}$ represents the $\boldsymbol{Q}(t)$ matrix based on the IAU 2006/2000 precession-nutation model.

The "CIO locator" s, providing the position of the CIO in the GCRS can also be computed using a development described in Capitaine et al. 2003.

2.3.4 Earth Orientation Parameters Information And Interpolation

EOP information for formulating the Celestial-to-Terrestrial transformation matrix, is extracted from the IERS C04 files (Bizouard et al. 2019). These files contain tabulated EOP values (x_p, y_p, $\delta UT1$, LOD and the celestial pole offsets δX and δY) at 0^{h} Coordinated Universal Time (UTC). LOD and celestial pole offsets contain the most dramatic variation over time, while the pole coordinates and time offset parameters exhibit much smoother variations.

In general, the tabulated pole coordinates, $\delta UT1$ and LOD values must first be interpolated to the appropriate time and then corrected for ocean tide and

libration effects. The ocean tide corrections, include diurnal and semi-diurnal variations caused by ocean tides for polar motion, $\delta UT1$ and LOD. Libration effects, include diurnal and semi-diurnal nutations that originate from the direct effect of the external (mainly luni-solar) torque on the non-axisymmetric part of the Earth (Petit and Luzum 2010 and references therein) and like ocean tide corrections, have an effect on pole coordinates as well as $\delta UT1$ and LOD. The variations of these effects have to be accounted for when using the published values for EOP parameters.

Especially for $\delta UT1$ and LOD, according to Bradley et al. 2016, prior to their interpolation, "the tabulated values should be smoothed through regularization to enhance the interpolation accuracy". Regularization is the removal of zonal tidal variations with frequencies ranging from 5 days to 18.6 years. This "regularization" is implemented in the EOP interpolation process.

For the current Thesis, the process described above was designed and implemented, for extracting EOP information from C04 files, storing values in efficiently designed data structures, and performing the interpolation along with the corrections described above. A schematic representation is given in Figure 2.12. As shown in Figure 2.11, including the ocean tide and libration effects, allows for the introduction of diurnal and semi-diurnal signals.

For the polar motion EOP, x_p and y_p,

$$\begin{pmatrix} x_p & y_p \end{pmatrix} = \begin{pmatrix} x & y \end{pmatrix}_{IERS} + \begin{pmatrix} \Delta x & \Delta y \end{pmatrix}_{ocean\ tides} + \begin{pmatrix} \Delta x & \Delta y \end{pmatrix}_{libration} \qquad (2.75)$$

where $\begin{pmatrix} \Delta x & \Delta y \end{pmatrix}_{ocean\ tides}$ and $\begin{pmatrix} \Delta x & \Delta y \end{pmatrix}_{libration}$ are computed as outlined in Petit and Luzum 2010; the former is achieved by a software routine designed on the basis of the ORTHO_EOP[6] to compute the diurnal and semidiurnal variations in the Earth orientation, while the latter is based on PMSDNUT2[7] to compute the diurnal lunisolar effect on polar motion, see Figure 2.12.

Similarly, for the $\delta UT1$ and LOD values,

$$\begin{pmatrix} \delta UT1 & LOD \end{pmatrix} = \begin{pmatrix} x & y \end{pmatrix}_{IERS} + \begin{pmatrix} \delta UT1 & LOD \end{pmatrix}_{ocean\ tides} + \begin{pmatrix} \delta UT1 & LOD \end{pmatrix}_{libration}$$
$$(2.76)$$

where again $\begin{pmatrix} \delta UT1 & LOD \end{pmatrix}_{ocean\ tides}$ are computed using the same procedure as above, while $\begin{pmatrix} \delta UT1 & LOD \end{pmatrix}_{libration}$ are computed using a software routine designed

---

[6]Available from the IERS Conventions Centre at https://iers-conventions.obspm.fr/content/chapter8/software/ORTHO_EOP.F, provided by R. Eanes.

[7]Available from the IERS Conventions Centre at https://iers-conventions.obspm.fr/content/chapter5/software/PMSDNUT2.F, provided by A. Brzezinski.
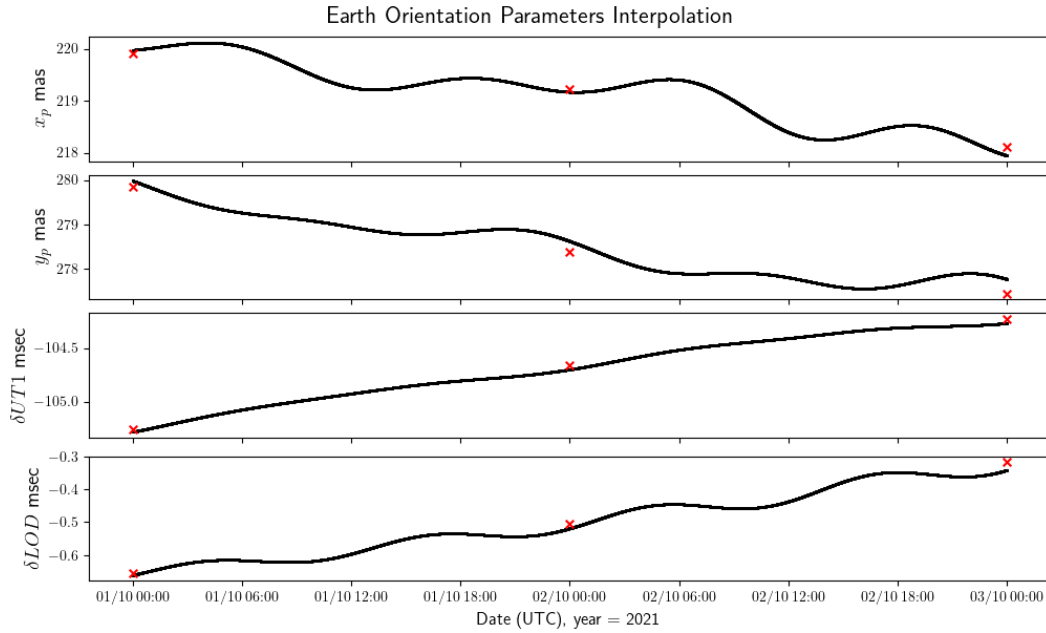
Figure 2.11: Interpolation of EOP parameters x_p, y_p, $\delta UT1$ and LOD performed by the software developed, following 2.12. Red crosses represent the input, reference EOP values.

on the basis of the IERS-published `UTLIBR`[8] to account for the subdiurnal librations.

The linear interpolation is based on a Lagrangian interpolation scheme, generic enough to perform interpolation of any order (given enough data). For POD, a 5-order interpolation procedure is performed, based on results from Bradley et al. 2016.

Optionally, users can perform the "regularization" of $\delta UT1$ and LOD values. In this case, prior to the interpolation the tabulated values are smoothed through regularization to enhance the interpolation accuracy. After regularization and interpolation, the zonal tide value should be added back at the time of interpolation. At this point, the ocean tide corrections should be computed and added to the interpolated values. The zonal tide effects are based on models recommended by the IERS Conventions and the distributed `RG_ZONT2`

---

[8]Available from the IERS Conventions Centre at https://iers-conventions.obspm.fr/content/chapter5/software/UTLIBR.F, provided by A. Brzezinski.
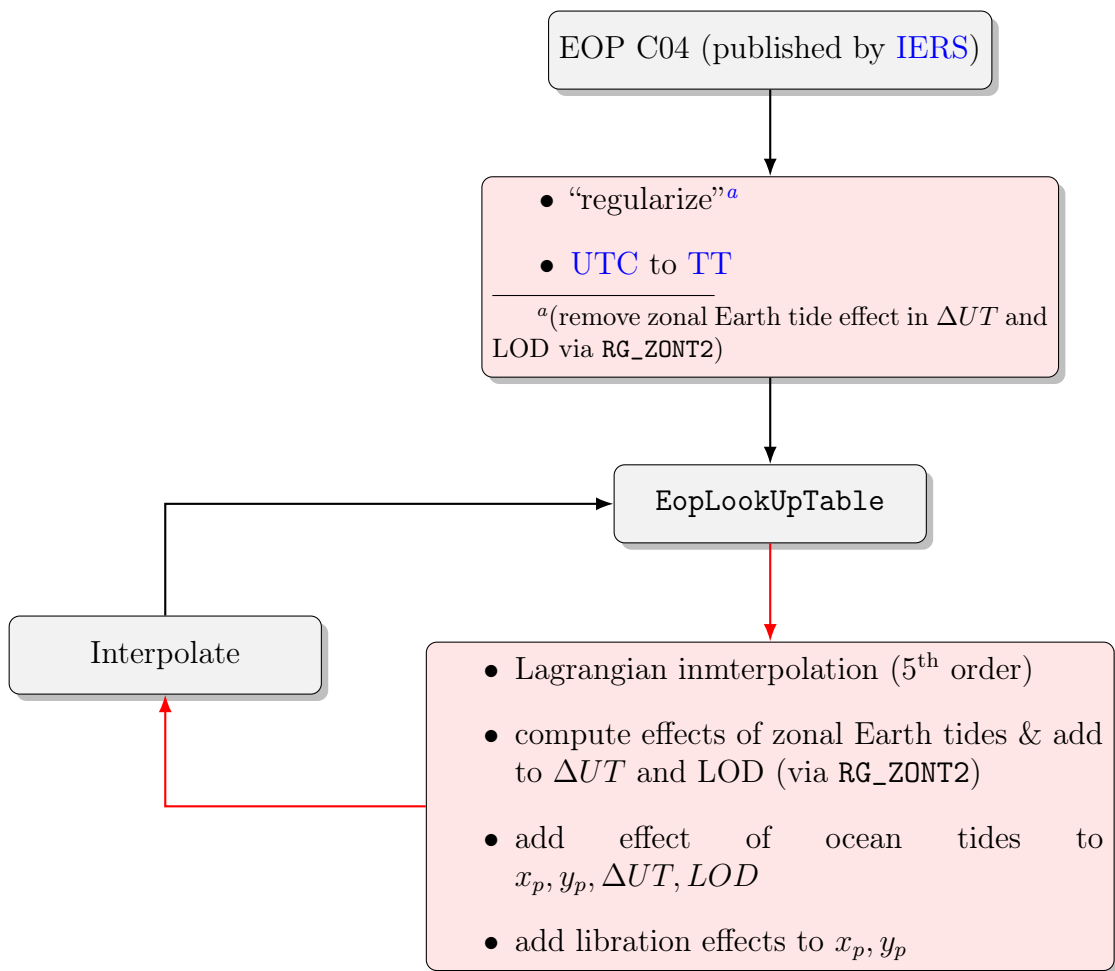
Figure 2.12: Extracting EOP information from IERS C04 data files.

2.4 Time Systems and Scales

2.4.1 A Short Introduction to Time Scales

This section only touches upon the fundamentals of time scales used in Satellite Geodesy (see Table 2.5) and relevant transformation algorithms, as applied in the software designed for the purposes of this Thesis. An extensive discussion on the subject can be found in i.e. Urban and Seidelmann 2013 and IAU SOFA Board 2021b.

Historically, solar time was the basis of time keeping, based on the diurnal rotation of the Earth. However, with the discovery of the variability of the rate of rotation of the Earth and later on the development of atomic clocks, ans the SI second different time systems and scales have been introduced to match the ever growing precision demands.

Time Scale	Usage	Type
International Atomic Time (TAI)	the official timekeeping standard	Atomic
UTC	the basis of civil time	Atomic/Solar hybrid
UT1	based on Earth rotation	Solar
TT	used for solar system ephemeris look-up	Dynamical
Geocentric Coordinate Time (TCG)	used for calculations centered on the Earth in space	Dynamical
Barycentric Coordinate Time (TCB)	used for calculations beyond Earth orbit	Dynamical
Barycentric Dynamical Time (TDB)	a scaled form of TCB that keeps in step with TT on the average	Dynamical

Table 2.5: Fundamental time scales used in Geodesy and Astronomy.

TAI The unit of TAI is the SI second, defined as "the duration of 9,192,631,770 periods of the radiation corresponding to the transition between the two hyperfine levels of the ground state of the caesium 133 atom". TAI is a laboratory time scale, independent of astronomical phenomena apart from having been synchronized to

solar time when first introduced. It is realized via a weighted average of a number of high-precision atomic clocks held around the world. It is close to proper time for an observer on the geoid, and is an appropriate choice for terrestrial applications (IAU SOFA Board 2021b).

UTC UTC is a compromise between the demands of precise timekeeping and the desire to maintain the current relationship between civil time and daylight. Until 1972, rate changes were introduced to keep UTC roughly in step with UT1; since then, adjustments have been made by occasionally inserting a whole second, called a *leap second*, a procedure that can be thought of as stopping the UTC clock for a second to let the Earth catch up (ibid.). Leap seconds are introduced as necessary to keep UT1-UTC in the range ±0.9 s. The difference between UT1 and UTC is usually designated as ΔAT.

UT1 UT1 is the modern equivalent of mean solar time. In a physical sense, it is an angle rather than actual time, and is defined through its relationship with Earth rotation angle. Because of the variability of Earth's rotation, UT1 second is not precisely matched to the SI second. The difference between UT1 and TT is normally designated as ΔT, and can be written out as

$$\Delta T = TT - UT1 = 32.184 \, \text{s} + \Delta AT - \Delta UT1 \tag{2.77}$$

The Dynamical Time Scales TCG, TCB & TDB The coordinate time scales TCG, TCB and TDB are the independent variable in General Relativity based theories which describe the motions of bodies in the vicinity of the Earth (TCG) and in the solar system (TCB, TDB). TT and TDB are close to each other (less than 2 ms) and run at the same rate as TAI (exactly in the case of TT). TCG and TCB, used in theoretical work, run at different rates and so have long term drifts relative to TAI (ibid.). TCG and TCB are the time coordinates of two IAU spacetime metrics called, respectively, the geocentric and barycentric celestial reference systems (GCRS and BCRS). TCG, is appropriate for theoretical studies of geocentric ephemerides. Its relationship with TT is this conventional linear transformation:

$$TCG = TT + L_G \times (JD_{TT} - TT_0) \tag{2.78}$$

where $TT_0 = 2443144.5003725$ (i.e. TT at 1977 January 1.0 TAI) and $LG = 6.969290134 \times 10 - 10$. The rate change LG means that TCG gains about 2.2 s per century with respect to TT or TAI; this represents the combined effect on the

terrestrial clock of the gravitational potential from the Earth and the observatory's diurnal speed (ibid.).

TT TT, is the theoretical time scale for clocks at sea-level (on the geoid): for practical purposes it is tied to TAI through

$$TT = TAI + 32.184\,\mathrm{s} \qquad (2.79)$$

Note that UTC has to be expressed as hours, minutes and seconds (or at least in seconds in a given day) if leap seconds are to be taken into account in the correct manner. In particular, it is inappropriate to express UTC as a Julian Date, because there will be an ambiguity during a leap second—so that for example 1994 June 30 23h 59m 60s.0 and 1994 July 1 00h 00m 00s.0 would both come out as MJD 49534.00000—and because subtracting two such JDs would not yield the correct interval in cases that contain leap seconds.

2.4.2   Implementing Time Scales

Designing and implementing software for handling dates, time scales and related transformations is a rather challenging task. The complexity is evident, considering:

- The long list of different time-scales involved in Satellite Geodesy and Astronomy (see 2.4.1)

- The different representation conventions (e.g. Julian Date (JD), Modified Julian Date (MJD), year/month/day and hour/minute/seconds)

- The accuracy required when transforming between different time scales

- The heavy usage of dates and time in a POD process (i.e. efficiency)

All of the above must be taken into account in software design, making the "datetime" problem a field of continuous investigation. Despite the fact that there are a few datetime libraries, (some languages have even relevant implementations in their standard libraries), none complies with the accuracy and complexity involved in Satellite Geodesy. The exception is the official IAU implementation of Fundamental Astronomy, i.e. the Standards Of Fundamental Astronomy (SOFA)

library (IAU SOFA Board 2021a). However, SOFA is implemented in the FOR-TRAN (and C) programming languages and has to reserve a level of "backwards compatibility", thus its design paradigm is rather outdated (e.g. no Object Oriented Design). Additionally, the package provides core functionality, hence one should implement various utility functions (e.g. parsers) to interact with this functions.

For all the above, a decision was taken to design and implement a new software library, from scratch, to address the "datetime" problem. The design follows recent developments and paradigms in Software Engineering, such as Template Metaprogramming (Vandevoorde et al. 2017). The library is open and free for any interested user.

A "datetime" or *epoch* within the library is represented as an MJD, where the integral and fractional part of day are stored separately, to preserve precision. In the special case of UTC dates, the epoch can be stored in the Year Month Date plus Hours Minutes Seconds (YMD/HMS) format. Depending on the user/application needs, the fractional part of the day can be stored as either a floating point numeric value, or the accumulated number of s, ms, μs or ns, since the beginning of the day. Both implementations are supported by individual "classes"; the latter is achieved via heavy template usage.

While storing the fractional part of day as a floating point number is intuitive and straightforward, it suffers from roundoff errors. This is avoided in the case where the fraction of day is stored as an integer numeric value (i.e. accumulated second submultiple); however, in this case, precision is limited by the chosen submultiple and non-integer division will also introduce truncation. It is up to the user to choose the suitable representation to meet application demands.

The components of the library have been extensively tested using the SOFA results as reference, as well as the relevant (limited) standard library functions. The software is developed as a stand-alone library, complying with the latest C++ standards (C++17 & C++20) and include ≈5000 lines of source code (including test suits).

Chapter 3

Orbit Integration

3.1 Introduction

The equations of motion governing the orbital path followed by an Earth orbiting satellite, constitute a system of Ordinary Differential Equations (ODEs). To "propagate" the orbit, we need to solve this system, using a reference trajectory at a given instant $t = t_0$ as *initial conditions*. The high accuracy that is nowadays required for POD applications, can only be achieved via numerical methods (Montenbruck and Gill 2000). Although there are many types of numerical integrators developed for solving ODE problems, only a few of them are suitable for POD due to their limited numerical precision and stability (Nie et al. 2020).

A variety of methods have been successfully applied to the problem of orbit propagation, each with its own drawbacks, limitations and advantages (see e.g. Somodi and Földváry 2011 and Atallah et al. 2020.) Thus, in general, it is not possible to simply select one method as best suited for the prediction of satellite motion.

In this Thesis, two different techniques of numerical integration are investigated, namely:

Runge—Kutta methods, that have the advantage of being well established and easy to implement, and

multistep methods, that a high efficiency and accuracy at a cost of increased implementation complexity

Both of these techniques, are further subdivided into more specialized algorithms, depending on problem constraints, choice of parameters and algorithmic approach. Typically, application needs indicate the appropriate methodology.

A comparisson of different integration techniques considering a simple, Keplerian orbit is discussed in Montenbruck 1992, where the highly flexible, variable order and step size multistep methods are shown to be ideal candidates for use in general satellite orbit prediction and determination systems. A more realistic scenario is studied in Somodi and Földváry 2011, where again the efficiency and robustness of the *Adams* methods is shown. Papanikolaou and Tsoulis 2016, compare integration techniques (including direct 2nd-order integrators such as *Gauss-Jackson* methods) in the frame of the GRACE and GOCE satellite missions; the efficiency of the Adams PECE algorithm compared to *Runge-Kutta* methods is evident, even though only constant-step implementations are considered. A comprehensive study of the precision and efficiency of different *Runge-Kutta* methods (among others) is presented in Atallah et al. 2020.

It should be noted that the equations of motions considered, constitute a system of ODEs of seconds degree. Even though methods for direct integration of such equations exist, they will not be considered here, since such methods assume that forces acting on a satellite do not depend on its velocity (an assumption not fulfilled in the POD case considered here, see e.g. section 2.2.3). For a more detailed and general discussion on numerical methods for ODEs, see Hairer et al. 2009 and Hairer and Wanner 2010.

A first order system of ODEs can always be obtained from a respective second order, by combining the position $\boldsymbol{r}$ and velocity $\dot{\boldsymbol{r}}$ vectors into the 6-dimensional *state vector* $\boldsymbol{y}$

$$\boldsymbol{y} = \begin{pmatrix} \boldsymbol{r} \\ \dot{\boldsymbol{r}} \end{pmatrix} \tag{3.1}$$

with

$$\dot{\boldsymbol{y}} = \boldsymbol{f}(t, \boldsymbol{y}) = \begin{pmatrix} \dot{\boldsymbol{r}} \\ \boldsymbol{a}(t, \boldsymbol{r}, \dot{\boldsymbol{r}}) \end{pmatrix} \tag{3.2}$$

so that the original system

$$\ddot{\boldsymbol{r}} = \boldsymbol{a}(t, \boldsymbol{r}, \dot{\boldsymbol{r}}) \tag{3.3}$$

can be written in the general form

$$\dot{\boldsymbol{y}} = \boldsymbol{f}(t, \boldsymbol{y}), \ \text{with} \ \boldsymbol{y}, \dot{\boldsymbol{y}}, \boldsymbol{f} \in \Re \tag{3.4}$$

3.1.1 Goals of Current Chapter

Orbit integration plays a major role in POD as it can be used to "connect" the trajectory between observation epochs. Nowadays, the increasingly enhanced ground and space-borne geodetic observation techniques have put forward even higher requirements on the precision of numerical orbit integration. Efficiency constraints and computational resources have to be thoroughly considered in such an integration process, as the computational burden it incurs is significant.

In this chapter a quick overview of the most widely used ODE solution techniques, as applied to the orbit determination problem, is presented. Focus is placed on *multistep* methods, and more specifically the *Adams* PECE family of algorithms, as they represent state-of-the-art integration schemes.

Unfortunately, there is a lack of relevant software or software availability; well established, scientific packages performing POD are mostly either not freely available or not open-source. Hence, the decision was made to design and implement an efficient, robust integrator from scratch within the framework of this Thesis. The *Adams* PECE method was adopted as the algorithm of choice, due to the advantages it offers both in terms of precision and efficiency. The implemented scheme follows a *variable step*, *variable order* approach, based on the theoretical groundwork laid by Shampine and Gordon 1975.

The implementation details of the software built to address orbit integration, are discussed in section 3.4. Elaborate mathematical formulations are employed to allow for as much efficiency as possible; variable, but not rapidly changing step sizes and orders of the integrator are sought for in every individual step, to accommodate robustness and precision and limit computational burden.

The integrator constitutes a big part of the software package built for this Thesis. As such, it pertains to the overall philosophy of free and open-source software, adopting a modern, generic design and accommodating reusability and adaptability (see subsection 3.4.4).

3.2 Runge-Kutta Methods

In the *Runge-Kutta* methods, a weighted average of the slopes ($\boldsymbol{f}$) of the solution computed at nearby points is used to determine the solution at $t = t_{n+1}$ from that at $t = t_n$. Typically, Runge-Kutta methods are further divided in *explicit* and

implicit methods; the latter are more complicated but allow for higher order and improved stability (see Griffiths and Higham 2010).

The general s-stage Runge-Kutta methods, may be written in the form

$$y_{n+1} = y_n + h \sum_{i=1}^{s} b_i k_i \tag{3.5}$$

where the k_i terms can be computed from the function f

$$k_i = f\left(t_n + c_i h, y_n + h \sum_{j=1}^{s} a_{i,j} k_j\right) \text{ with } i = 1, 2, \ldots s \tag{3.6}$$

Typically, we impose the condition

$$c_i = \sum_{j=1}^{s} a_{i,j} \tag{3.7}$$

Thus, given a value of s, the method depends on $s^2 + s$ parameters $a_{i,j}$ and b_j. These can be conveniently displayed in a tableau known as the *Butcher array* (see e.g. Butcher 2016).

c_1	$a_{1,1}$	$a_{1,2}$	$\ldots$	$a_{1,s}$
c_2	$a_{2,1}$	$a_{2,2}$	$\ldots$	$a_{2,s}$
$\vdots$	$\vdots$	$\vdots$		$\vdots$
c_s	$a_{s,1}$	$a_{s,2}$	$\ldots$	$a_{s,s}$
	b_1	b_2	$\ldots$	b_s

Table 3.1: The Butcher array for a full (implicit) RK method

0	0	0	$\ldots$	0	0
c_2	$a_{2,1}$	0	$\ldots$	0	0
c_3	$a_{3,1}$	$a_{3,2}$	$\ldots$	0	0
$\vdots$	$\vdots$	$\vdots$	$\ddots$	0	0
c_s	$a_{s,1}$	$a_{s,2}$	$\ldots$	$a_{s,s-1}$	0
	b_1	b_2	$\ldots$	b_{s-1}	b_s

Table 3.2: The Butcher array for an explicit RK method. Zeros are often omitted.

Equation 3.6 constitutes a nonlinear equation system of size s, that can be used to determine k_i; once found, they can be substituted into Equation 3.5 to determine y_{n+1}. Thus, a general Runge-Kutta method is implicit (Griffiths and Higham 2010). The form of the Butcher array for an implicit Runge-Kutta method is shown in Equation 3.2. Although early studies were devoted entirely to explicit Runge-Kutta methods, interest has now moved to include implicit methods, which have become recognized as appropriate for the solution of stiff differential equations (Butcher 2016).

If the coefficients $a_{i,j}$ can be placed in a lower triangular matrix, i.e. $a_{i,j} = 0$ for all $j \geqslant i$, the k_i terms can be computed directly (from Equation 3.6) without the need to solve any nonlinear equations. These are the methods most often used, and are called explicit. In this case, the general form of the associated Butcher array is depicted in Table 3.2.

The *Local Truncation Error* of a Runge-Kutta method T_{n+1}, is defined to be the difference between the exact and the numerical solution at $t = t_{n+1}$ (Griffiths and Higham 2010)

$$T_{n+1} = x(t_{n+1}) - x_{n+1} \tag{3.8}$$

with $y_n = y(t_n)$. If $T_{n+1} = \mathcal{O}(h^{p+1})(p > 0)$ the method is said to be of *order* p. In practice, two related Runge-Kutta methods are used, one of order p and another of order $p + 1$, to approximate the value of the local truncation error via $T_{n+1} = y_{n+1}^{p+1} - y_{n+1}^p$, where the T_{n+1} estimate is for the lowest order method p. To perform the calculation in an efficient way, the values of ks for the lowest degree method, are chosen so that they are a subset of the higher degree method coefficients. Such methods of neighboring orders are often called *embedded* Runge-Kutta methods.

While for $s < 4$ there are always Runge-Kutta methods where $s = q$, this is not the case for methods of stages higher than four. The number of stages necessary for a given order is known up to order 8, but there are no precise results for higher orders (ibid.).

3.2.1 Adaptive Step Size

The step size h is a crucial parameter in the integration methods; it dictates the number of steps required to integrate over a given interval, and the accuracy of the results obtained. Small step sizes (in general) improve accuracy but comes with an efficiency cost. To that end, *step size control* can be used, to compute a value h_n for step n, to obtain the same accuracy with fewer steps or better accuracy with the same number of steps. In *adaptive* step size control, the step size in each step is adapted to local conditions, so as to take short steps when the solution varies rapidly and longer steps when there is relatively little activity. Obviously, computing such variable step sizes, should be automatic and inexpensive. A thorough discussion on implementing sophisticated adaptive step size control, fit for computer programs, is given in the classic text by Shampine and Gordon 1975.

3.3 Multistep Methods

3.3.1 Adams Method(s)

Each step in the integration process in the *Runge-Kutta* method (see section 3.2) is completely independent and is discarded once used for computation (this is why they are often referred to as *single-step* methods). To cut down on the number of function calls *multi-step* methods have been introduced to allow for efficiency. These store previous step values and reuse them in the subsequent steps, so that to generate an approximation for the next step, the previously computed y and $\dot{y}$ values computed at the previous k steps are combined.

In general, starting with the ODE $\dot{\boldsymbol{y}} = \boldsymbol{f}(t, \boldsymbol{y})$, and integrating both sides for the interval t_i to t_{i+j} the following expression is obtained

$$\boldsymbol{y}(t_{i+1}) = \boldsymbol{y}(t_i) + \int_{t_i}^{t_{i+1}} \boldsymbol{f}(t, \boldsymbol{y}(t)) \, dt \tag{3.9}$$

In multistep methods, the integrand is replaced by a polynomial $p(t)$, that interpolates a subset of the already available approximate values $\boldsymbol{\eta}_j$ of the solutions $\boldsymbol{y}(t_j)$, such that

$$\boldsymbol{f}_j = \boldsymbol{f}(t_j, \boldsymbol{\eta}_j) \tag{3.10}$$

Hence, if $\boldsymbol{\eta}_{i+1}$ is the approximate solution at the next step to be taken,

$$\boldsymbol{\eta}_{i+1} = \boldsymbol{\eta}_i + \int_{t_i}^{t_{i+h}} p(t) \, dt \tag{3.11}$$

and the increment function of a multistep method is therefore given by

$$\boldsymbol{\Phi} = \frac{1}{h} \int_{t_i}^{t_{i+h}} p(t) \, dt \tag{3.12}$$

Finally, the solution approximation at $t = t_{i+1}$ can be approximated by

$$\boldsymbol{y}(t_{i+1}) = \boldsymbol{y}(t_i) + h \left(b_1 \boldsymbol{f}_i + b_2 \boldsymbol{f}_{i-1} + \cdots + b_k \boldsymbol{f}_{i-k+1} \right) \tag{3.13}$$

Methods of this form are known as *Adams-Bashforth* methods. Coefficients for the representation Equation 3.13 for up to 4th degree are available in e.g. Butcher 2016.

Multistep methods are typically derived by using an interpolating polynomial in either of two ways. The first is to use an interpolating polynomial through

$t_i, t_{i-1}, \ldots, t_{i-k+1}$ for $\boldsymbol{f}(t, \boldsymbol{\eta})$ and then integrate the equation (as discussed above). The second method consists in using an interpolating polynomial (again through $t_i, t_{i-1}, \ldots, t_{i-k+1}$) to approximate $\boldsymbol{y}(t)$ and then differentiate it, evaluate at t_{i+1} for an implicit method and set it equal to the given slope ($\boldsymbol{f}(t, \boldsymbol{\eta})$) at that point to obtain the difference equation. This gives rise to a family of implicit methods called *backward difference formulas*. In the latter case, the polynomial is given by the expression (Montenbruck and Gill 2000)

$$p_m^i(t) = p_m^i(t_i + \sigma h) = \sum_{j=0}^{m-1} (-1)^j \binom{-\sigma}{j} \nabla^j \boldsymbol{f}_i \qquad (3.14)$$

where the binomial coefficient is used

$$\binom{-\sigma}{j} = \begin{cases} \frac{(-\sigma)(-\sigma-1)\ldots(-\sigma-j-1)}{j!} & \text{, if } j > 0 \text{ and} \\ 1 & \text{, if } j = 0 \end{cases} \qquad (3.15)$$

The ∇^i operator here denotes the backward difference operator, which is recursively defined by (see Table 3.3)

$$\begin{aligned} \nabla^0 \boldsymbol{f}_i &= \boldsymbol{f}_i \\ \nabla^1 \boldsymbol{f}_i &= \boldsymbol{f}_i - \boldsymbol{f}_{i-1} \\ \nabla^n \boldsymbol{f}_i &= \nabla^{n-1} \boldsymbol{f}_i - \nabla^{n-1} \boldsymbol{f}_{i-1} \end{aligned} \qquad (3.16)$$

Using Equation 3.12 the increment function of the mth-order Adams-Bashforth methods, can be written as

$$\boldsymbol{\Phi} = \frac{1}{h} \int_{t_i}^{t_i+h} p_m^i(t) \, dt = \sum_{j=0}^{m-1} \gamma_j \nabla^j \boldsymbol{f}_i \qquad (3.17)$$

with

$$\gamma_j = (-1)^j \int_0^1 \binom{-\sigma}{j} \, d\sigma \qquad (3.18)$$

γ_j coefficients can be found in e.g. Butcher 2016 up to 7th order.

The local truncation error of the Adams-Bashforth method decreases with the order m and may be estimated by comparing two methods of order m and $m + 1$ (Montenbruck and Gill 2000)

$$T_m = \|\boldsymbol{y}(t_i + h) - \eta_m\| \approx \|\eta_{m+1} - \eta_m\| = h\|\gamma_m \nabla^m \boldsymbol{f}_i\| \qquad (3.19)$$

$$
\begin{array}{llllll}
\boldsymbol{f}_{i-4} & \cdots & & & & \\
& \searrow & & & & \\
\boldsymbol{f}_{i-3} & \rightarrow & \nabla^1 \boldsymbol{f}_{i-3} & \cdots & & \\
& \searrow & & \searrow & & \\
\boldsymbol{f}_{i-2} & \rightarrow & \nabla^1 \boldsymbol{f}_{i-2} & \rightarrow & \nabla^2 \boldsymbol{f}_{i-2} & \cdots \\
& \searrow & & \searrow & & \searrow \\
\boldsymbol{f}_{i-1} & \rightarrow & \nabla^1 \boldsymbol{f}_{i-1} & \rightarrow & \nabla^2 \boldsymbol{f}_{i-1} & \rightarrow & \nabla^3 \boldsymbol{f}_{i-1} & \cdots \\
& \searrow & & \searrow & & \searrow & & \searrow \\
\boldsymbol{f}_i & \rightarrow & \nabla^1 \boldsymbol{f}_i & \rightarrow & \nabla^2 \boldsymbol{f}_i & \rightarrow & \nabla^3 \boldsymbol{f}_i & \rightarrow & \nabla^4 \boldsymbol{f}_i & \cdots
\end{array}
$$
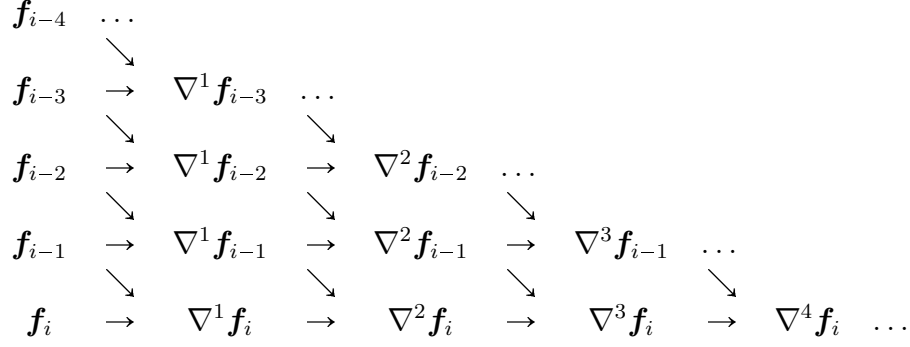
Table 3.3: Schematic representation of backward differences for polynomial interpolation, Montenbruck and Gill 2000.

which can be approximated by

$$
T_m \approx h^{m+1} \| \gamma_m \boldsymbol{f}_i^{(m)} \| = h^{m+1} \| \gamma_m \boldsymbol{y}_i^{(m+1)} \| \tag{3.20}
$$

which shows that the order of the Adams-Bashforth method is equal to the number m of nodes $t_{i-m+1}, \ldots, t_i$.

The method of backward differences has two major advantages:

1. it allows a straightforward estimation of the local truncation error, and

2. the order can be changed in-between integration steps

Note that the polynomial p (Equation 3.13) is defined by m function values, up to and including $\boldsymbol{f}_i$ at time t_i, but the integration Equation 3.12 is performed over the subsequent interval $t_i, \ldots, t_{i+1}$. Instead of Equation 3.13, a slightly different polynomial can be chosen

$$
\boldsymbol{y}(t_{i+1}) = \boldsymbol{y}(t_i) + h \left(b_0 \boldsymbol{f}_{i+1} b_1 \boldsymbol{f}_i + b_2 \boldsymbol{f}_{i-1} + \cdots + b_k \boldsymbol{f}_{i-k+1} \right) \tag{3.21}
$$

(that is, include a term for the t_{i+1}), which leads to the *Adams-Moulton* method. For order m in this case, the interpolating polynomial is (compare to Equation 3.14)

$$
p_m^{i+1}(t) = p_m^{i+1}(t_i + \sigma h) = \sum_{j=0}^{m-1} (-1)^j \binom{-\sigma + 1}{j} \nabla^j \boldsymbol{f}_{i+1} \tag{3.22}
$$

which yields the increment function

$$
\boldsymbol{\Phi} = \frac{1}{h} \int_{t_i}^{t_i+h} p_m^{i+1}(t) \, dt = \sum_{j=0}^{m-1} \bar{\gamma}_j \nabla^j \boldsymbol{f}_{i+1} \tag{3.23}
$$

with coefficients

$$\bar{\gamma}_j = (-1)^j \int_0^1 \binom{-\sigma+1}{j} d\sigma \tag{3.24}$$

The local truncation error in this case, is given by (Montenbruck and Gill 2000)

$$T_m \approx h^{m+1}\|\hat{\gamma}_m \boldsymbol{y}_i^{(m+1)}\| \tag{3.25}$$

and since in general $\hat{\gamma}_m < \gamma_m$, it is smaller that the respective T_m value for an Adams-Bashforth method of equal size.

3.3.2 Predictor-Corrector Method

Since the increment function Equation 3.23 depends on $\boldsymbol{f}_{i+1} \equiv \boldsymbol{f}(t_{i+1}, \boldsymbol{\eta}_{i+1})$, it is not possible to calculate an explicit solution at t_{i+1} from Equation 3.21, making this method an *implicit* method. To surpass this difficulty, a combination of the Adams-Bashforth and Adams-Moulton methods can be used, in what is called a PECE scheme (Figure 3.1). At a first step, an Adams-Bashforth of order m is used to compute an approximate solution $\boldsymbol{\eta}_{t_{i+1}}^{(p)}$, using the already computed values $\boldsymbol{f}_i, \boldsymbol{f}_{i-1}, \ldots, \boldsymbol{f}_{i-m+1}$. This *predicted* value $(\boldsymbol{\eta}_{t_{i+1}}^{(p)})$, can then be used to obtain a *predicted* function value at $t_{i=1}$, $\boldsymbol{f}_{i+1}^{(p)}(t_{i+1}, \boldsymbol{\eta}_{t_{i+1}}^{(p)})$ and proceed to the *corrector* step, where an updated, improved solution $\boldsymbol{\eta}_{t_{i+1}}$ is computed, via an Adams-Moulton method of order m or $m = 1$. The "final" function value at t_{i+1}, $\boldsymbol{f}_{i+1}^{(p)}(t_{i+1}, \boldsymbol{\eta}_{t_{i+1}}^{(p)})$ can be evaluated for the next integration step.

Even though the PECE algorithms are complicated and difficult to implement, they offer increased stability, especially at large stepsizes (ibid.). Low-order methods are generally more stable even for large stepsizes.

3.4 Integrator implementation

In this section a brief outline of the integrator designed and implemented for the current Thesis is given. The method used, is a *variable step*, *variable order* Adams-Bashforth-Moulton PECE algorithm. The implementation is based on the developments of Shampine and Gordon 1975, which up to date constitute one of the most robust ODE solvers solvers, given the problem constraints (non stiff
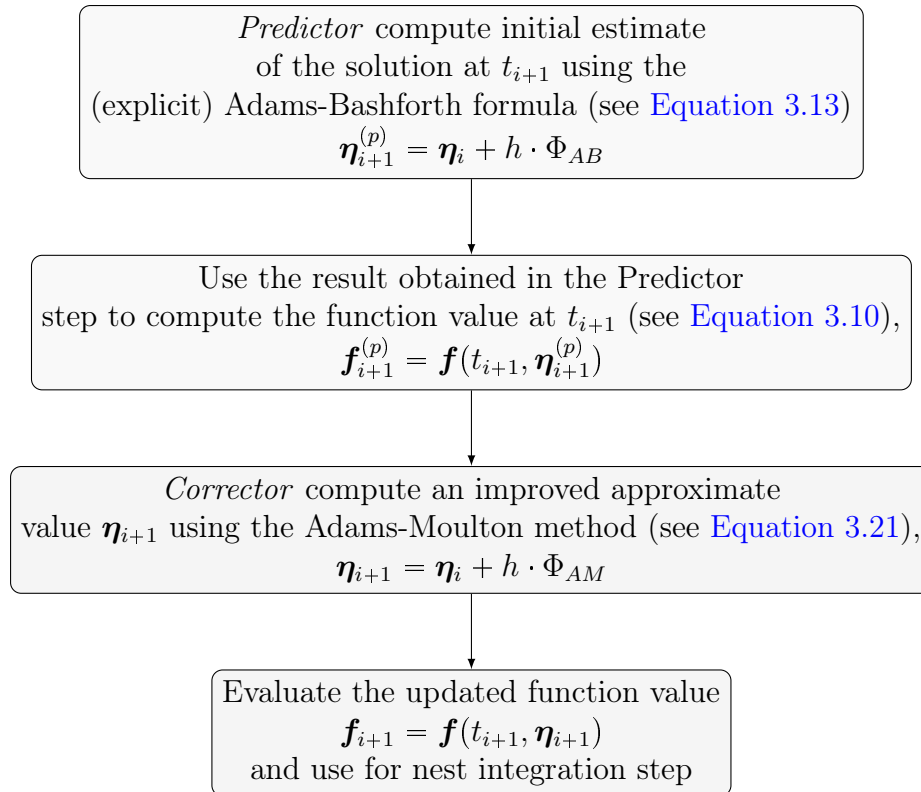
Figure 3.1: Schematic representation of the *Predictor-Corrector* algorithm using the Adams-Bashforth and Adams-Moulton methods.

ODE systems of 1st order). An overview of the implemented schema is depicted in Figure 3.2.

According to Shampine and Gordon 1975, use of Adams methods are most advantageous for problems in which:

- function evaluations are expensive,

- moderate to high accuracy is requested,

- many output points are required

In the case of POD, at least the first two points above hold; function evaluations are expensive in terms of computational time and resources. Computation of the force model (see subsection 2.2.3) and respective accelerations are resource demanding tasks, especially in view of the high accuracy standards expected to be met in a POD process.

It is worth noting that major scientific software packages used for POD, such as GINS, developed by CNES and Groupe de Recherche en Géodésie Spatiale (GRGS) (CNES 2013) and GEODYN developed by Goddard Space Flight Center (GSFC) (Beal 2015) use *multi-step* methods for the numerical integration. The algorithm implementation was written from scratch requiring many difficult steps, as explained in the preceding sections. Exisiting libraries were not preferred (when available) as were developed with reduced analytical capabilities for modern computing systems. An overview of the integrator designed for this Thesis, is given in Figure 3.2.

In POD, the cost of calling the derivative function $\boldsymbol{f}(t, \boldsymbol{y}(t))$ is quite heavy and repeated calls can make the integrator inefficient. Hence, care must be taken to limit such computations. The Adams methods, when carefully used, are more efficient in this respect than any other method being used today to solve general ODE (Shampine and Gordon 1975). This incurs an additional overhead, however, because making such decisions necessitates estimating the errors that are, or would be, incurred for various step sizes and orders. To address this issue, most steps are performed in groups with constant step size and order.

For a varying step size, a wise choice of stored variables and coefficients should be made to accommodate efficiency. Since, the algorithm will be using divided and backward differences, this choice includes the variables
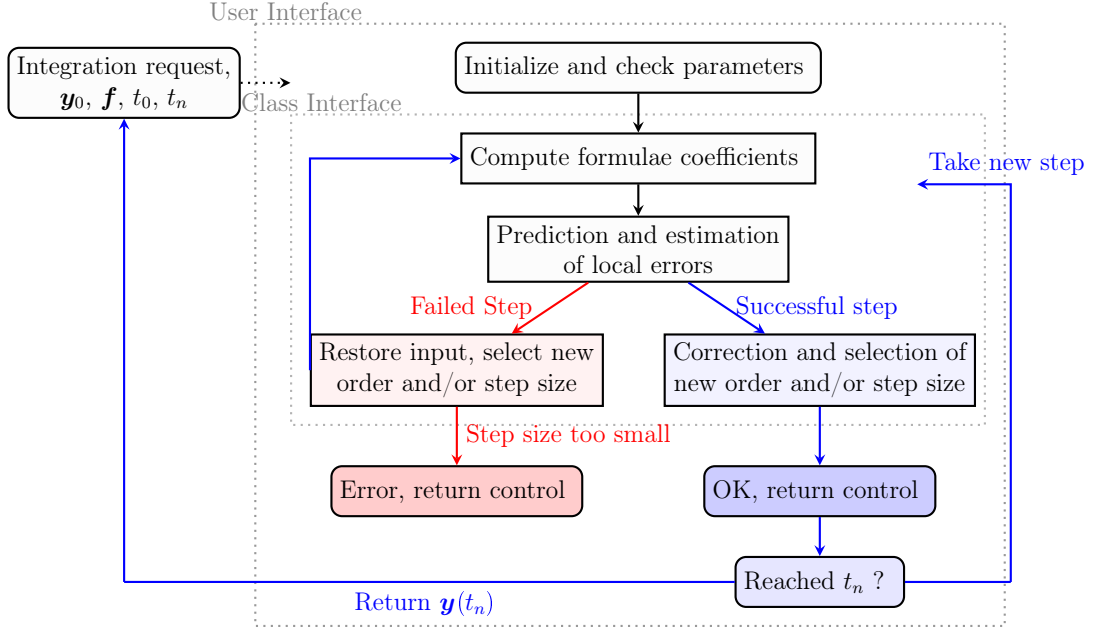
Figure 3.2: Flow chart of the implemented PECE integrator, based on Shampine and Gordon 1975.

$$h_i = x_i - x_{i-1}, \tag{3.26}$$

$$s = \frac{x - x_n}{h_{n+1}}, \tag{3.27}$$

$$\psi_i(n+1) = h_{n+1} + h_n + \cdots + h_{n+2-i} \ i \geqslant 1, \tag{3.28}$$

$$\alpha_i(n+1) = \frac{h_{n+1}}{\psi_i(n+1)} \ i \geqslant 1, \tag{3.29}$$

$$\beta_1(n+1) = 1, \tag{3.30}$$

$$\beta_i(n+1) = \frac{\psi_1(n+1)\psi_2(n+1)\ldots\psi_{i-1}(n+1)}{\psi_1(n)\psi_2(n)\ldots\psi_{i-1}(n)} \ i > 1, \tag{3.31}$$

$$\phi_1(n) = f[x_n] = f_n, \tag{3.32}$$

$$\phi_i(n) = \psi_1(n)\psi_2(n)\ldots\psi_{i-1}(n)f[x_n, x_{n-1}, \ldots, x_{n-i+1}], \ i > 1 \tag{3.33}$$

where h_i are the step size, $\psi_i(n+1) = h_{n+1} + h_n + \cdots + h_{n+2-i} = x_{n+1} - xn + 1 - i$ are the sums of the step sizes, $\phi_i(n)$ are the modified divided differences (which reduce to backward differences for constant step sizes), s is a normalized variable taking value in the range $[0,1]$ as x runs from x_n to x_{n+1} and α_i and β_i are intermediate coefficients used for the computations.

70

Through Equation 3.26 to Equation 3.33, a change from value n to $n+1$ can be performed via the recursion for $i = 2, 3, \ldots$

$$\psi_i(n+1) = \psi_{i-1}(n) + h_{n+1}$$
$$\beta_i(n+1) = \beta_{i-1}(n+1)\frac{\psi_{i-1}(n+1)}{\psi_{i-1}(n)}$$

(3.34)

with initial conditions for $i = 1$

$$\psi_1(n+1) = h_{n+1}$$
$$\beta_1(n+1) = 1$$

(3.35)

It is worth noting that if the step size is constant, Equation 3.26 through Equation 3.33 are simplified to

$$s = \frac{x - x_n}{h_{n+1}},$$

(3.36)

$$\psi_i(n+1) = ih$$

(3.37)

$$\alpha_i(n+1) = \frac{1}{i}$$

(3.38)

$$\beta_i(n+1) = 1$$

(3.39)

$$\phi_i(n) = \nabla^{i-1}f_n,$$

(3.40)

The expression of the polynomial $P_{k,n}(x)$ in Equation 3.52 and Equation 3.53 can be written as

$$P_{k,n}(t) = \sum_{i=1}^{k} c_{i,n}(s)\phi_i^*(n)$$

(3.41)

where

$$c_{i,n}(s) = \begin{cases} 1 & i = 1 \\ \frac{sh_{n+1}}{\psi_1(n+1)} = s & i = 2 \\ \left(\frac{sh_{n+1}}{\psi_1(n+1)}\right)\left(\frac{sh_{n+1}+\psi_1(n)}{\psi_2(n+1)}\right)\cdots\left(\frac{sh_{n+1}+\psi_{i-2}(n)}{\psi_{i-1}(n+1)}\right) & i \geqslant 3 \end{cases}$$

(3.42)

$$\phi_i^*(n) = \beta_i(n+1)\phi_i(n)$$

(3.43)

The derivative in Equation 3.53, is then

$$P_{k,n}(t_{n+1}) = p'_{n+1} = \sum_{i=1}^{k} \phi_i^*(n)$$

(3.44)

71

and the (approximate) solution at t_{n+1}, Equation 3.52 is

$$p_{n+1} = y_n + h_{n+1} \sum_{i=1}^{k} \phi_i^*(n) \int_0^1 c_{i,n}(s)\, ds \qquad (3.45)$$

As already shown, for constant step size h, Equation 3.45 reduces to

$$p_{n+1} = y_n + h \sum_{i=1}^{k} \gamma_{i-1} \nabla^{i-1} f_n \qquad (3.46)$$

To compute the integral in Equation 3.45, the quantity $g_{i,q}$ is introduced, defined as $g_{i,q} = (q-1)! c_{i,n}^{(-q)}(1)$. According to Shampine and Gordon 1975, the integral can now be evaluated via the formula

$$\int_0^1 c_{i,n}(s)\, ds = \sum_{i=1}^{k} g_{i,1} \phi_i^*(n) \qquad (3.47)$$

so that Equation 3.45 can be numerically computed from

$$p_{n+1} = y_n + h_{n+1} \sum_{i=1}^{k} g_{i,1} \phi_i^*(n) \qquad (3.48)$$

The coefficients $g_{i,q}$ follow the recursion formulas

$$g_{i,q} = \begin{cases} \frac{1}{q} & i = 1 \\ \frac{1}{q(q+1)} & i = 2 \\ g_{i-1,q} - \alpha_{i-1}(n+1) g_{i-1,q+1} & i \geqslant 3 \end{cases} \qquad (3.49)$$

In the formulas presented here, a series of simplifications can be made if a constant step size h is considered. These are implemented in the source code for the integrator. The interested reader can find details in ibid.

3.4.1   The Predictor

The predictor part of the PECE integrator follows the Adams-Bashforth method (see subsection 3.3.1). In general, a kth order Adams-Bashforth predictor at t_n is defined by the expression

$$y_n + \int_{t_n}^{t} P_{k,n}(t)\, dt \qquad (3.50)$$

where $P_{k,n}(t)$ satisfies the interpolation conditions

$$P_{k,n}(t_{n+1-j}) = \boldsymbol{f}_{n+1-j} \text{ for } j = 1, \ldots, k \tag{3.51}$$

Equation 3.50 is used to predict both the solution and its derivative at t_{n+1}

$$p_{n+1} = y_n + \int_{t_n}^{t_{n+1}} P_{k,n}(t) \, dt \tag{3.52}$$

$$p'_{n+1} = P_{n,k}(t_{n+1}) \tag{3.53}$$

The implementation computes the above values using Equation 3.48 and Equation 3.44 using a series of intermediate variables and coefficients (as described in section 3.4). To promote efficiency, these coefficients are stacked in contiguous memory, divided in blocks based on their usage in the algorithm, to minimize as much as possible cache misses.

3.4.2 The Corrector

The corrector part of the PECE integrator is based on the Adams-Moulton algorithm. In this step, p_{n+1} is "corrected" and all relevant values needed for the next step are computed and stored. The corrector implemented here, is one order higher than the predictor. In general, the solution and its derivative, using an Adams-Moulton method, is given by

$$y_{n+1} = y_n + \int_{t_n}^{t_{n+1}} P^*_{k+1,n}(t) \, dt \tag{3.54}$$

and

$$f_{n+1} = f(t_{n+1}, y_{n+1}) \tag{3.55}$$

where

$$P^*_{k+1,n}(t_{n+1-j}) = f_{n+1-j} \text{ for } j = 1, 2, \ldots, k \tag{3.56}$$

$$P^*_{k+1,n}(t_{n+1}) = f^p_{n+1} = f(t_{n+1}, p_{n+1}) \tag{3.57}$$

The corrector polynomial interpolates the same set of values as the predictor, plus the additional value f^p_{n+1}. Using the divided differences formulation, $P^*_{k+1,n}$ can be computed from $P_{k,n}$ using one extra term. Using the notation introduced in section 3.4, the polynomial can be given by

$$P^*_{k+1,n}(t) = P_{n,k}(t) + c_{k+1,n}(s)\phi^p_{k+1}(n+1) \tag{3.58}$$

73

and after integration, the solution and derivative function can be shown to be (Shampine and Gordon 1975)

$$y_{n+1} = p_{n+1} + h_{n+1}g_{k+1,1}\phi_{k+1}^p(n+1) \tag{3.59}$$

$$f_{n+1} = f(t_{n+1}, y_{n+1}) \tag{3.60}$$

Equation 3.59 allows the computation of the "corrected" solution using the work done at the corrector phase, plus the term $g_{k+1,1}$; the latter is computed along with the $g_{i,1}$, needed in the prediction (see Equation 3.48). Note also that changing the term $g_{k+1,1}$ to $g_{k,1}$, yields the solution of order k (ibid.), a fact used to assist the estimation of the error (here the notation $y_{n+1}(k)$ is used to distinguish between the order k and solution the order $k+1$ as given in Equation 3.59)

$$y_{n+1}(k) = p_{n+1} + h_{n+1}g_{k,1}\phi_{k+1}^p(n+1) \tag{3.61}$$

In the case of constant step size h, Equation 3.59 and Equation 3.61 reduce to

$$y_{n+1} = p_{n+1} + h\gamma_k \nabla^k f_{n+1}^p \tag{3.62}$$

$$y_{n+1}(k) = p_{n+1} + h\gamma_{k-1} \nabla^k f_{n+1}^p \tag{3.63}$$

The terms $\phi_i^p(n+1)$ and $\phi_i(n+1)$ can be computed via recursion, given that the divided difference approach is followed, from (ibid.)

$$\phi_{i+1}^p(n+1) = \phi_i^p(n+1) - \phi_i^*(n) \text{ for } i = 1, 2, \ldots, k \tag{3.64}$$

$$\phi_{i+1}(n+1) = \phi_i(n+1) - \phi_i^*(n) \text{ for } i = 1, 2, \ldots, k \tag{3.65}$$

with initial conditions

$$\phi_1^p(n+1) = f_{n+1}^p \tag{3.66}$$

$$\phi_1(n+1) = f_{n+1} \tag{3.67}$$

According to ibid., despite the straightforwardness of these recursive relations, they lack storage efficiency. This can be corrected using an alternate way to compute these terms. Introducing the modified divided differences ϕ_i^e, that make us of the value p'_{n+1} at t_{n+1} (that is extend the differences $\phi_i(n)$ based on the sequence $x_n, x_{n-1}, \ldots$ to the values at $x_{n+1}, x_n, x_{n-1} \ldots$)

$$\phi_i^e(n+1) = \phi_{i+1}^e(n+1) + \phi_i^*(n) \tag{3.68}$$

which can be used to generate the $\phi_i^e(n+1)$ terms in the sequence $i = k, k-1, \ldots, 1$. Now, Equation 3.64 and Equation 3.65 can be written as

$$\phi_i^p(n+1) = \phi_i^e(n+1) - \left(f_{n+1}^p - \phi_1^e(n+1)\right) \tag{3.69}$$

$$\phi_i(n+1) = \phi_i^e(n+1) - \left(f_{n+1}^p - \phi_1^e(n+1)\right) \tag{3.70}$$

The combined predictor-corrector step phase is depicted in Figure 3.3.

Compute $g_{i,1}$ for $i = 1, 2, \ldots, k + 1$, see Equation 3.49

Prediction Step
compute $\phi_i^*(n)$ via Equation 3.43, for $i = 1, 2, \ldots, k$
compute p_{n+1} via Equation 3.48
set $\phi_{k+1}^e(n + 1) = 0$
compute $\phi_i^e(n + 1)$ via Equation 3.68, for $i = k, k - 1, \ldots, 1$

Evaluation Step
compute $f_{n+1}^p = f(x_{n+1}, p_{n+1})$

Correction Step
compute $y_{n+1} = p_{n+1} + h_{n+1} g_{k+1,1} \left(f_{n+1}^p - \phi_1^e(n + 1) \right)$

Evaluation Step
compute $f_{n+1} = f(x_{n+1}, y_{n+1})$
compute $\phi_{k+1}(n + 1) = f_{n+1} - \phi_1^e(n + 1)$ and
compute $\phi_i(n + 1) = \phi_i^e(n + 1) + \phi_{k+1}(n + 1)$ for $i = k, k - 1, \ldots, 1$
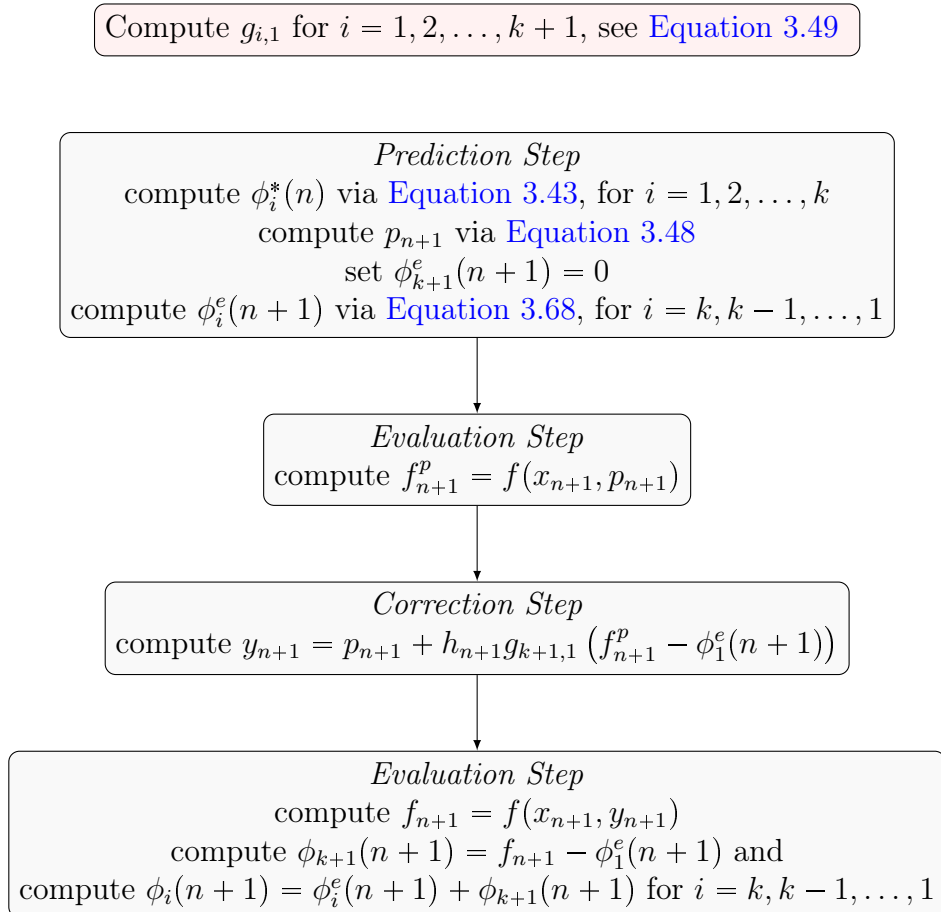
Figure 3.3: Schematic representation of the Adams PECE integrator, based on Shampine and Gordon 1975.

3.4.3 Error Estimation, Order and Step Size

Error estimation in the integration process plays a crucial role, since it allows the algorithm to adjust the step size and order accordingly, so as to preserve efficiency and accuracy. Local error can be computed before the final step of the PECE algorithm, aka after the corrector, for orders $k-2$, $k-1$, k and $k+1$. Hence, if the step is unsuccessful, the final evaluation is not performed, and a change of the order is examined.

In the source code the quantity ERK is used to make decisions on the step size. This quantity was introduced by Shampine and Gordon 1975 and is given by

$$ERK = \|h\left(g_{k+1,1} - g_{k,1}\right)\sigma_{k+1}(n+1)\phi_{k+1}^p(n+1)\| \tag{3.71}$$

In reality, ERK estimates what the local error at x_{n+1} would have been, had the preceding steps been of constant size h. Given a successful step, the next step (to x_{n+2}) of size rh, will have a local error of $r^{k+1}ERK$. If on contrary the step were to be repeated with a step size of rh, then again its error estimate would be $r^{k+1}ERK$.

For order selection, three further quantities are introduced, based on ibid.

$$ERKM1 = \|h\left(g_{k+1,1} - g_{k,1}\right)\sigma_k(n+1)\phi_k^p(n+1)\| \tag{3.72}$$

$$ERKM2 = \|h\left(g_{k+1,1} - g_{k,1}\right)\sigma_{k-1}(n+1)\phi_{k-1}^p(n+1)\| \tag{3.73}$$

$$ERKP1 = \|h\left(g_{k+1,1} - g_{k,1}\right)\phi_{k+2}(n+1)\| \tag{3.74}$$

The first two, estimate what the local error would have been at x_{n+1} had these steps be taken with an order of $k-1$ and $k-2$ respectively. $ERKP1$ is an estimate of the local error at x_{n+2}. All of the estimates assume a step size h. The philosophy of the order selection is to change the order only if the predicted error is reduced and if there is a trend in the terms. In general, lower order formulas have better stability properties (ibid.), and the algorithm is so designed as to prefer lower orders. The maximum order limit within the algorithm is 12.

After the order selection, the algorithm tries to select the optimal step size rh. The value of r is initially estimated by

$$r = \left(\frac{0.5\epsilon}{ERK}\right)^{\frac{1}{k+1}} \tag{3.75}$$

and restrict increase of r to factors of two. Hence, if the inequality $0.5\epsilon \geqslant 2^{k+1}ERK$, holds, the step size is doubled. If this is not possible, then the inequality $0.5\epsilon \geqslant ERK$ is checked, to see if a constant step size can be retained.

Keeping a constant step size (when a factor of two increase is not feasible) offers efficiency, simplicity, stability and a more realistic error estimation. If however the latter inequality demands so, a decrease of step size is performed by a factor in between 0.5 to 0.9, computed via Equation 3.75. The value of ϵ is user defined.

3.4.4 Design Considerations

An efficient and precise solution of the orbit integration problem plays a key role in POD applications. The algorithm described above is a state-of-the-art integrator, which allows for a robust treatment of the problem at hand. A few design consideration are discussed here, which enable further enhancements of the algorithm's efficiency based on its architectural design.

The whole algorithm is encapsulated in an *object-oriented* design; this provides easy and user-friendly interaction with the integration process and eliminates in as much as possible errors incurred by user misusage. One additional benefit is that the user (or the user application) does not need to know the very complex background and methods that are implemented within the algorithm. One only needs to specify the initial conditions of the ODE and if needed the tolerance values (see subsection 3.4.3). The algorithm will then seek for the optimal way (i.e. stepsize and order) to handle the problem.

Additionally, the object oriented design implemented enables the integrator instance (i.e. a data structure of integrator type) to have *state*. Users can query this state and find out information about the process, a fact that enables a clear and unambiguous interaction between the instance and the caller.

Memory allocations are handled using the *Resource Acquisition Is Initialization* (RAII) programming technique (https://en.cppreference.com/w/cpp/language/raii) and users are free of any obligation regarding allocating/freeing memory. Special care is taken so that only no excess memory is allocated and most importantly, that memory blocks are allocated in a contiguous manner, minimizing cache misses.

Part of the source code uses the `eigen` (Guennebaud and Jacob 2010) library, which supports vectorization (*Single Instruction, Multiple Data* (SIMD) instructions) including the widely used *Advanced Vector Extensions* AVX, AVX2 and AVX512.

3.4.5 Integrator Validation

Checking and validating integrator results is not a straight-forward process, since the computation of the complex force field acting on the satellite is required (see subsection 2.2.3). Some of these forces further depend on satellite-specific characteristics (e.g. atmospheric drag, solar radiation pressure). Additionally, validation of trajectory extrapolation requires a "reference" orbit (i.e. reference state results), which may have been computed using a non identical set of models, reference frames and algorithms.

To test the integrator designed and implemented for this Thesis, IDS-published (Willis et al. 2016b) `sp3` files were acquired and used as "reference" orbits. These orbits are the accumulated results for the satellite state, tabulated at equidistant epochs, of the individual analysis centers contributing to the service. Hence, they represent state-of-the-art POD results using the DORIS satellite system.

The test devised to check the integrator proceed as follows:

1. Read a state vector off from the sp3 file for an epoch t

2. Extrapolate the state to a later time t_i (prior to the end of sp3 records)

3. Read the state off from the sp3 file for the epoch t_i and compare with the results obtained from the integrator. Go to (1) and repeat the process.

The force model used within the integrator, does not contain contributions of the solar radiation pressure and atmospheric drag. Ocean tidal loading effects on the geopotential, are limited to the 11 major tides. All other contributions, are computed as described in subsection 2.2.3. Handling of the transformation between the ITRF and GCRF is described in section 2.3.

The validation test is performed for a time interval of approximately one week, starting on 26/08/2022. The satellite mission picked for the test is Jason-3 (Bannoura et al. 2011), since this is the mission used later on, to test the integrated POD process.

Normally, in a POD process using the DORIS system, there is no need to extrapolate an orbit further than some seconds, after it has been adjusted by the inclusion of observations (see chapter 4). Two distinct measurements are made every 10 sec and the ground network is dense enough so that at least one ground

Figure 3.4: Integration results of satellite state compared to respective IDS-distributed sp3 file records. Extrapolation is performed for an interval of 1 min.

stations is nearly always visible by any DORIS-equipped satellite. For the validation process, extrapolation is tested up to time intervals of 15 min to gain a thorough view on the robustness of the implemented algorithm (Figure 3.4).

Figure 3.4 depicts the differences in the state vector $\boldsymbol{y} = \begin{pmatrix} \boldsymbol{r} & \boldsymbol{v} \end{pmatrix}^T$ between the reference values obtained by the sp3 file and the ones computed using the integrator with an extrapolation interval of 1 min. Differences in the position range between -2 to 2 mm while for the velocity components the differences are within -1×10^{-5} to 1×10^{-5} m/s. A diurnal signal seems to be present in the latter case, which could be due to unmodeled effects of

- (remaining) ocean tidal constituents,

- solid earth pole tides and ocean pole tides,

- solar radiation pressure acting on the satellite,

- atmospheric drag

Figure 3.5 depicts the differences in the state vector when the integration interval is expanded to 3 min. Differences in position range between -5 to 5 mm
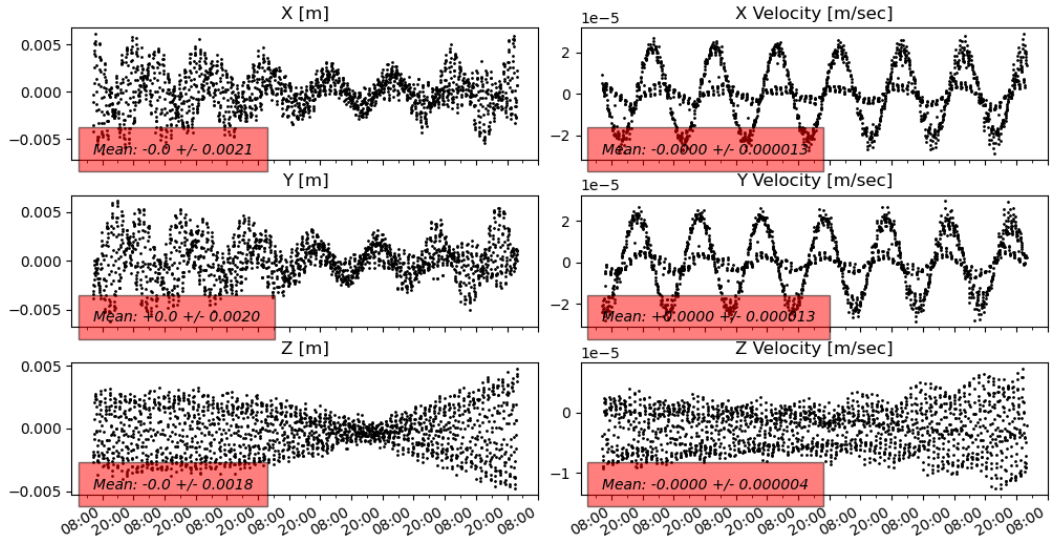
Figure 3.5: Integration results of satellite state compared to respective IDS-distributed sp3 file records. Extrapolation is performed for an interval of 3 min.

while for the velocity components the differences are within -2×10^{-5} to 2×10^{-5} m/s. As in the case of 1 min extrapolation (see Figure 3.4), velocity differences are dominated by a harmonic, diurnal signal and the same can be told for the position discrepancies.

Differences when extrapolating for an interval of 15 min are depicted in Figure 3.6. In this case, differences in position range between -5 to 5 cm while for the velocity components the range is -0.1 to 0.1 mm/s

In general, due to the very small magnitude in the discrepancies computed for the extrapolated vs the "reference" state (see Figure 3.4, Figure 3.5 and Figure 3.6), the design of the algorithm and its implementation seem to be robust, while the discrepancies are attributed to either mismodelled, or unmodelled effects.
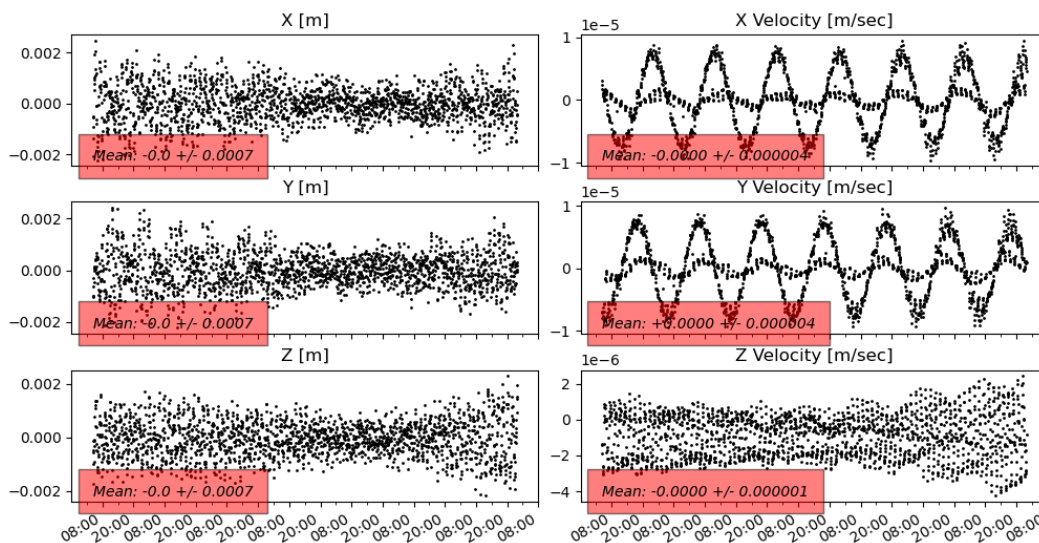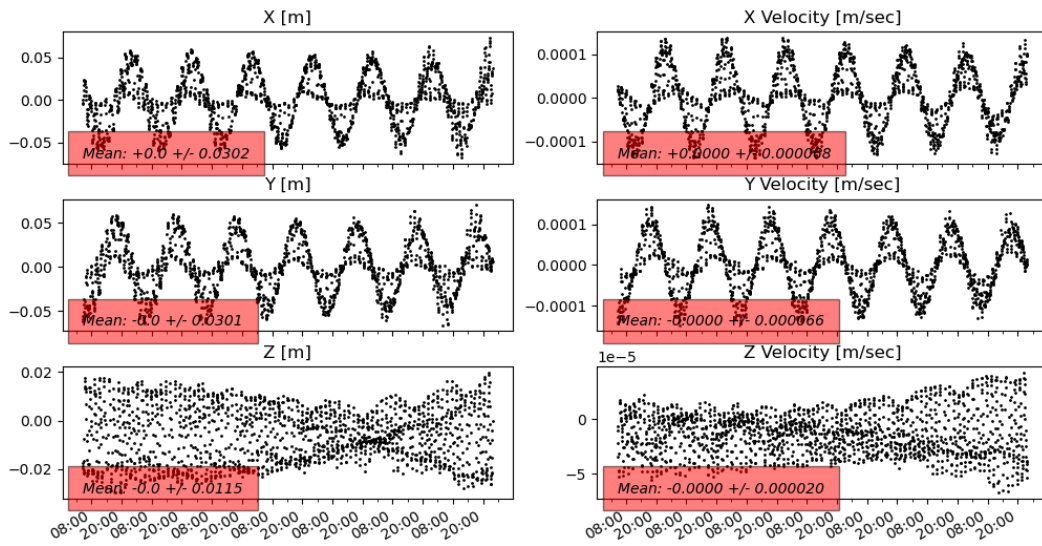
Figure 3.6: Integration results of satellite state compared to respective IDS-distributed sp3 file records. Extrapolation is performed for an interval of 15 min.

Chapter 4

Precise Orbit Determination

4.1   Introduction

Orbit determination of artificial satellites began in essence in the 1960s. However, it was not until the 1980s that great advancements were made, facilitated by a better modeling of the Earth's gravity field and its variations (e.g. tides) and the large increase in computing capabilities. This enabled orbit determination accuracy to increase to the tens-of-centimeter level. This improvement was motivated and further pushed by the ever-increasing demands of scientists in the oceanographic and geodetic communities, in search for centimeter-level accuracy in global ocean topography obtained from altimetric satellites (Tapley et al. 2004b). To-date, POD can yield results in the few-centimeter level.

Orbit determination can be viewed as a special case of a parameter estimation problem, where the parameters characterizing the orbit of an Earth orbiting satellite have to be determined from observations. Observations are themselfes values of nonlinear functions (the so-called *observed functions*, Beutler 2005), thus for the solution of the problem, initial approximate parameter values are needed (a problem often called *initial orbit determination*). Such approximate starting values can be obtained in a number of ways (see e.g. Vallado 2001), including published values of preliminary solutions, and will not be considered here. Hence, the POD process is in essence an *orbit improvement* problem.

Apart from the orbital elements or equivalently the state vector, a number of different parameters have to be considered in a POD problem, including

- dynamical parameters characterizing the force model, necessary to describe the orbital motion of the satellites,

- coordinates of the observing sites in an ECEF system,

- motion of the observing sites (e.g. crustal deformation),

- Earth rotation and Earth orientation parameters,

- atmosphere parameters defining the tropospheric refraction correction,

- parameters defining the ionospheric refraction correction,

- technique-specific, hardware and (possibly site-specific) instrumentation bias parameters

All of these parameters have to be considered and dealt-with (either estimated or introduced) in a POD analysis scheme. In this Thesis, a "restricted" problem is addressed, often labeled *pure orbit determination*, where coordinates of reference observation sites are assumed to known (via their ECEF position vector).

It is not always possible to describe the entire time period covered by observations by one set of initial conditions and dynamic parameters (Beutler 2005). Thus, the period can be split into consecutive *orbital arcs*; an orbital arc is thought of as contiguous, limited part of the satellite's trajectory, described by exactly one initial state vector and the dynamical parameters. Using short arcs, modeling deficiencies can be mitigated (absorbed by the initial state vectors), but rapidly increases the number of arc-specific parameters, a fact that could lead to a considerably weakened solution (ibid.). To overcome this problem, an alternate method can be used, in which stochastic accelerations are introduced (added to the parameter list), with known mean values and variance-covariance matrices. Not only observation noise but also system noise has to be introduced, and each *deterministic* parameter is replaced by a stochastic process (see e.g. Jäggi et al. 2005b and Jäggi et al. 2005a for a least-squares approach).

4.1.1   Goals of Current Chapter

In this section the fundamentals of orbit determination are discussed, focusing on two of the most crucial problems:

- the derivation, computation and solution of the so called *variational equations*, and
- efficient, robust and precise parameter estimation via a variation of the Kalman filter, labeled *Extended Kalman Filter*

Variational equations are a set of differential equations that describe how small changes (i.e. perturbations) in initial conditions propagate over time and thus play a important role in predicting the satellite's trajectory. For the derivation of these equations, a linearization of the (non-linear) equations of motion is needed. Solution of the variational equations is coupled with the computation of the *state transition matrix*, which relates the perturbed state at one epoch to a perturbed state at a later time and can be used to propagate the covariance matrix. Propagating the latter forward in time, a prediction can be made of the evolution of uncertainty in the estimate of the satellite's state. Formulae and numerical recipes for the linearization, as well as the differential equations of the state transition matrix and variational equations are presented. The discussion focuses on a hands-on approach, limiting analytical derivations which can be found in relevant literature. Equations are presented in matrix form, to enable an as much as possible easy translation to source code, and special care is taken to single out and exploit features, equations and particularities that can be used to derive a more efficient and/or robust algorithmic design.

Subsequently, the problem of parameter estimation is considered. There are two major methodologies that come into play in POD problems, the method of *Least Squares* and the extended family of filters called *Kalman filters* and variations. For the current thesis, the latter methodology was used and more specifically the *Extended Kalman filter* to derive a robust estimator. Computational aspects of the methodology and the implementation are discussed, as well as advantages and shortcomings.

Since a discussion on the input data for the POD problem considered in this Thesis is not yet touched upon, the computation of *observation equations* (needed in the estimation process) is not thoroughly presented here; this issue will be revisited once the basics of the DORIS system are presented (see chapter chapter 5).

4.2 Linearization

In a POD problem, both the dynamics and the measurements involve significant nonlinear relationships. For both the trajectory and the observation models, a

large number of partial derivatives have to be computed for a rigorous linearization. These, according to Montenbruck and Gill 2000 can be divided into four different categories:

The State Transition Matrix $\Phi(t, t_0)$, which maps deviations in the state vector from an epoch t_0 to a later time t, and is given by

$$\Phi(t, t_0) = \left(\frac{\partial \boldsymbol{y}(t)}{\partial \boldsymbol{y}(t_0)} \right)_{(6 \times 6)} \tag{4.1}$$

The Sensitivity Matrix $\boldsymbol{S}(t)$, which describes the dependence of the orbit on the dynamical parameters p_i with $i = 1, 2, \ldots, n_p$ and is formed by the respective partial derivatives of the state with respect to the force model,

$$\boldsymbol{S}(t) = \left(\frac{\partial \boldsymbol{y}(t)}{\partial \boldsymbol{p}} \right)_{(6 \times n_p)} = \begin{pmatrix} \frac{\partial x(t)}{\partial p_1} & \frac{\partial x(t)}{\partial p_2} & \cdots & \frac{\partial x(t)}{\partial p_n} \\ \frac{\partial y(t)}{\partial p_1} & \frac{\partial y(t)}{\partial p_2} & \cdots & \frac{\partial y(t)}{\partial p_n} \\ \frac{\partial z(t)}{\partial p_1} & \frac{\partial z(t)}{\partial p_2} & \cdots & \frac{\partial z(t)}{\partial p_n} \\ \frac{\partial \dot{x}(t)}{\partial p_1} & \frac{\partial \dot{x}(t)}{\partial p_2} & \cdots & \frac{\partial \dot{x}(t)}{\partial p_n} \\ \frac{\partial \dot{y}(t)}{\partial p_1} & \frac{\partial \dot{y}(t)}{\partial p_2} & \cdots & \frac{\partial \dot{y}(t)}{\partial p_n} \\ \frac{\partial \dot{z}(t)}{\partial p_1} & \frac{\partial \dot{z}(t)}{\partial p_2} & \cdots & \frac{\partial \dot{z}(t)}{\partial p_n} \end{pmatrix} \tag{4.2}$$

Partials of the measurements with respect to the state vector, which given an observation z at some instant t, is given by

$$\left(\frac{\partial z}{\partial \boldsymbol{y}(t)} \right)_{(1 \times 6)} \tag{4.3}$$

, and

Partials with respect to measurement model parameters, which given the observation model parameters q_i for $i = 1, 2, \ldots, n_q$, given by

$$\left(\frac{\partial z}{\partial \boldsymbol{q}} \right)_{(1 \times n_q)} \tag{4.4}$$

Note that from Equation 4.1, the dependence of an individual observation z on the initial state $\boldsymbol{y}(t_0)$ is

$$\frac{\partial z}{\partial \boldsymbol{y}(t_0)} = \frac{\partial z}{\partial \boldsymbol{y}(t)} \frac{\partial \boldsymbol{y}(t)}{\partial \boldsymbol{y}(t_0)} = \frac{\partial z}{\partial \boldsymbol{y}(t)} \Phi(t, t_0) \tag{4.5}$$

and from Equation 4.2

$$\frac{\partial z}{\partial \boldsymbol{p}} = \frac{\partial z}{\partial \boldsymbol{y}(t)} \frac{\partial \boldsymbol{y}(t)}{\partial \boldsymbol{p}} = \frac{\partial z}{\partial \boldsymbol{y}(t)} \boldsymbol{S}(t) \tag{4.6}$$

Analytical computation of the partial derivatives is tedious, cumbersome and an error prone procedure. However, it constitutes an essential part of orbit determination and have a noticeable impact on the achieved performance and convergence speed (Montenbruck and Gill 2000).

The orbit determination problem, can in the general case be described by the 1$^{\text{st}}$ order ODE system for the dynamics accompanied with the observation functions

$$\dot{\boldsymbol{Y}} = \boldsymbol{F}(t, \boldsymbol{Y}) \tag{4.7}$$
$$\boldsymbol{Z}_i = G(t_i, \boldsymbol{Y}_i) + \boldsymbol{\epsilon}_i \tag{4.8}$$

where $\boldsymbol{y}$ is the state vector and $\boldsymbol{z}_i$ is a $p-$dimensional set of observations, for $i = 1, 2, \ldots, l$. If a sufficiently precise reference (initial) trajectory $\boldsymbol{y}^*$ is available, then the actual, "true" trajector $\boldsymbol{y}$ can be expanded in a Taylor series about this reference trajectory at each point in time. Truncating higher order terms, the deviation in state from the reference trajectory can be described by a set of linear differential equations with time-dependent coefficients. The same procedure can be used in Equation 4.8 to obtain a linear relation between the observation deviation and the state deviation. In this way, the original, non-linear orbit determination problem is transformed to a linear problem, in which the deviation from some reference solution must be determined. If $\boldsymbol{y}$ denotes the state deviation vector and $\boldsymbol{z}$ the observation deviation vector, then

$$\begin{aligned} \boldsymbol{\delta y}(t) &= \boldsymbol{y}(t) - \boldsymbol{y}^*(t) \\ \boldsymbol{\delta z}(t) &= \boldsymbol{z}(t) - \boldsymbol{z}^*(t) \end{aligned} \tag{4.9}$$

so that

$$\boldsymbol{\dot{\delta y}}(t) = \dot{\boldsymbol{y}}(t) - \dot{\boldsymbol{y}}^*(t) \tag{4.10}$$

Expanding Equation 4.7 and Equation 4.8 in a Taylor's series about the reference trajectory, leads to (Tapley et al. 2004b)

$$\begin{aligned} \dot{\boldsymbol{y}}(t) &= \boldsymbol{f}(t, \boldsymbol{y}) \\ &= \boldsymbol{f}(t, \boldsymbol{y}^*) + \frac{\partial \boldsymbol{f}(t, \boldsymbol{y})}{\partial \boldsymbol{y}^*(t)} \left(\boldsymbol{y}(t) - \boldsymbol{y}^*(t)\right) + \mathcal{O}\left(\boldsymbol{y}(t) - \boldsymbol{y}^*(t)\right) \end{aligned} \tag{4.11}$$

and

$$\begin{aligned} \boldsymbol{z}_i &= \boldsymbol{g}(t_i, \boldsymbol{y}_i) + \epsilon_i \\ &= \boldsymbol{g}(t, \boldsymbol{y}_i^*, t_i) + \frac{\partial \boldsymbol{g}}{\partial \boldsymbol{y}^*}|_i \left(\boldsymbol{y}(t_i) - \boldsymbol{y}^*(t_i)\right) + \mathcal{O}\left(\boldsymbol{y}(t_i) - \boldsymbol{y}^*(t_i)\right) + \epsilon_i \end{aligned} \tag{4.12}$$

where the partials are evaluated on the reference solution, $\boldsymbol{y}^*(t)$ can be obtained by integrating Equation 4.7 and $\mathcal{O}$ indicate terms containing products of the difference $\boldsymbol{y}(t) - \boldsymbol{y}^*(t)$ higher than the first term. Given that these terms are sufficiently small to be neglecting and using $\dot{\boldsymbol{y}}^* = \boldsymbol{f}(t, \boldsymbol{y}^*)$, Equation 4.11 and Equation 4.12 can be written as

$$\dot{\boldsymbol{\delta y}}(t) = A(t)\delta\boldsymbol{y}(t) \tag{4.13}$$

$$\boldsymbol{\delta z}_i = H_i \delta\boldsymbol{y}_i + \epsilon_i \tag{4.14}$$

where

$$A(t) = \frac{\partial f(t)}{\partial \boldsymbol{y}(t)}\big|_{\boldsymbol{y}^*} \text{ and } H_i = \frac{\partial g}{\partial \boldsymbol{y}}\big|_{\boldsymbol{y}_i^*} \tag{4.15}$$

Hence the original non-linear problem describe by the equations Equation 4.7 and Equation 4.8 is replaced by the linear Equation 4.13 and Equation 4.14.

4.2.1 State Transition Matrix

Equation 4.13 represents a system of linear differential equations with time-dependent coefficients (notice that the matrix A in Equation 4.15 is derived from a particular solution of $\dot{\boldsymbol{y}} = \boldsymbol{f}(t, \boldsymbol{y})$, generated with the initial conditions $\boldsymbol{y}(t_0) = \boldsymbol{y}_0^*$). The general solution for this system can be expressed as

$$\delta\boldsymbol{y}(t) = \Phi(t, t_k)\delta\boldsymbol{y}_k \tag{4.16}$$

with $\delta\boldsymbol{y}_k \equiv \delta\boldsymbol{y}(t_k)$ Differentiating Equation 4.16 and noting that $\delta\boldsymbol{y}_k$ is constant, gives

$$\delta\dot{\boldsymbol{y}}(t) = \dot{\Phi}(t, t_k)\delta\boldsymbol{y}_k \tag{4.17}$$

and using Equation 4.13 and Equation 4.16, the ODE system

$$\dot{\Phi}(t, t_k) = A(t)\Phi(t, t_k)$$
$$\Phi(t_k, t_k) = \boldsymbol{I} \tag{4.18}$$

The great advantage of this formulation, is that it allows the solution $\delta\boldsymbol{y}(t)$ to be expressed in terms of the unknown initial state $\delta\boldsymbol{y}_k$. Hence, the state transition matrix enables relating observations made at different times.

The ODE system for the state transition matrix Equation 4.17 is prefered against a direct solution of $\delta\boldsymbol{y}(t)$ from the system Equation 4.13 for computational reasons, ibid.

Montenbruck and Gill 2000 give the formulae for forming the state transition matrix using orbital elements and the associated partials with respect to the state vector. Battin 1999 uses the fact that Φ is a *sympletic* matrix, to obtain an analyticaly its inverse.

4.2.2 The Observation Equations

Equation 4.14 involves an unknown state vector $\delta\boldsymbol{y}_i$ related to the observation set $\boldsymbol{z}_i$. The state transition matrix can be used to relate all observation with the state at a single epoch. For each set, Equation 4.14 ($\boldsymbol{\delta z}_i = H_i\delta\boldsymbol{y}_i + \epsilon_i$) can be written as

$$\boldsymbol{\delta z}_i = H_i\Phi(t_i, t_k)\delta\boldsymbol{y}_k + \epsilon_i \tag{4.19}$$

where Equation 4.16 was used, and subsequently in matrix form

$$\boldsymbol{\delta z} = \bar{H}\delta\boldsymbol{y}_k + \boldsymbol{\epsilon} \tag{4.20}$$

with

$$\boldsymbol{\delta z} \equiv \begin{pmatrix} \boldsymbol{\delta z}_1 \\ \boldsymbol{\delta z}_2 \\ \vdots \\ \boldsymbol{\delta z}_l \end{pmatrix}, \ \bar{H} \equiv \begin{pmatrix} H_1\Phi(t_1, t_k) \\ H_2\Phi(t_2, t_k) \\ \vdots \\ H_l\Phi(t_l, t_k) \end{pmatrix} \text{ and } \boldsymbol{\delta z} \equiv \begin{pmatrix} \boldsymbol{\epsilon}_1 \\ \boldsymbol{\epsilon}_2 \\ \vdots \\ \boldsymbol{\epsilon}_l \end{pmatrix} \tag{4.21}$$

4.3 The Kalman Filter

In this section, the sequential estimation algorithm referred to as the *Kalman filter* is discussed, with emphasis on its application on the orbit determination problem. A more thorough discussion on the sequential estimation techniques can be found at Gelb et al. 1974, while Montenbruck and Gill 2000 and Tapley et al. 2004b describe the filter's application and variations thereof for POD. One important advantage of the Kalman filter is that the matrix to be inverted will be of the same dimension as the observation vector, which means that given that the observations can be processed one at a time, only scalar divisions will be required to obtain the estimate of $\delta\boldsymbol{y}(t_k)$. For the rest of this section, the notation $\boldsymbol{y}_k$ will be used to denote the value $\delta\boldsymbol{y}(t_k)$ to reduce complexity and follow relevant literature in the field.

Given that an estimate $\hat{\boldsymbol{y}}_j$ and the associated covariance matrix $\boldsymbol{P}_j$ are available at a given epoch t_j, the state and its variance-covariance matrix can be propagated according to

$$\begin{aligned}
\bar{\boldsymbol{y}}_k &= \phi(t_k, t_j)\hat{\boldsymbol{y}}_j \\
\bar{\boldsymbol{P}}_k &= \phi(t_k, t_j)\boldsymbol{P}_j\phi^T(t_k, t_j)
\end{aligned} \qquad (4.22)$$

This step of the algorithm, is often called the *time update* step. Assuming that an observation is available at t_k

$$\boldsymbol{z}_k = \tilde{H}_k\boldsymbol{y}_k + \boldsymbol{\epsilon}_k \qquad (4.23)$$

with $E[\boldsymbol{\epsilon}_k] = \mathbf{0}$ and $E[\boldsymbol{\epsilon}_k\boldsymbol{\epsilon}_k^T] = \boldsymbol{R}_k\delta_{kj}$, it can be shown (see ibid.) that:

$$K_k = \bar{\boldsymbol{P}}_k\tilde{H}_k^T \left(\tilde{H}_k\bar{\boldsymbol{P}}_k\tilde{H}_k^T + \boldsymbol{R}_k\right)^{-1} \qquad (4.24)$$

$$\boldsymbol{P}_k = \left(\boldsymbol{I} - \boldsymbol{K}_k\tilde{H}_k\right)\bar{\boldsymbol{P}}_k \qquad (4.25)$$

$$\hat{\boldsymbol{y}}_k = \bar{\boldsymbol{y}}_k + \boldsymbol{K}_k\left(\boldsymbol{z}_k - \tilde{H}_k\bar{\boldsymbol{y}}_k\right) \qquad (4.26)$$

Equation 4.24, Equation 4.25 and Equation 4.26 are collectively labeled the *measurement update* step. The matrix $\boldsymbol{K}$ is called the *(Kalman) gain matrix*. The above equations can be used in a recursive fashion to compute the estimate of $\hat{\boldsymbol{y}}_k$, incorporating the observation $\boldsymbol{z}_k$. A flowchart of the process is depicted in Figure 4.1.

Note that the differential equations for the state transition matrix are reinitialized at each observation epoch. If observations are introduced as scalars, and more than one measurements are available at each epoch, $\Phi(t_i, t_i)$ would be set to the unity matrix $\Phi(t_i, t_i) = \boldsymbol{I}$ after processing the first observation in the epoch, and $\boldsymbol{P}$ and $\hat{\boldsymbol{y}}$ would only be time updated at the next observation epoch $i+1$.

4.3.1 Filter Shortcomings

One disadvantage of the sequential algorithm presented here, lies in the fact that if the true state and the reference state are not close together then the linearization assumption leading to Equation 4.13 may not be valid and the estimation process may diverge (ibid.). To overcome this problem, the *Extended Kalman Filter* algorithm (section 4.4) was used in this Thesis.

Yet another disadvantage is that the state estimation error covariance matrix may approach zero as the number as the number of observations becomes large.
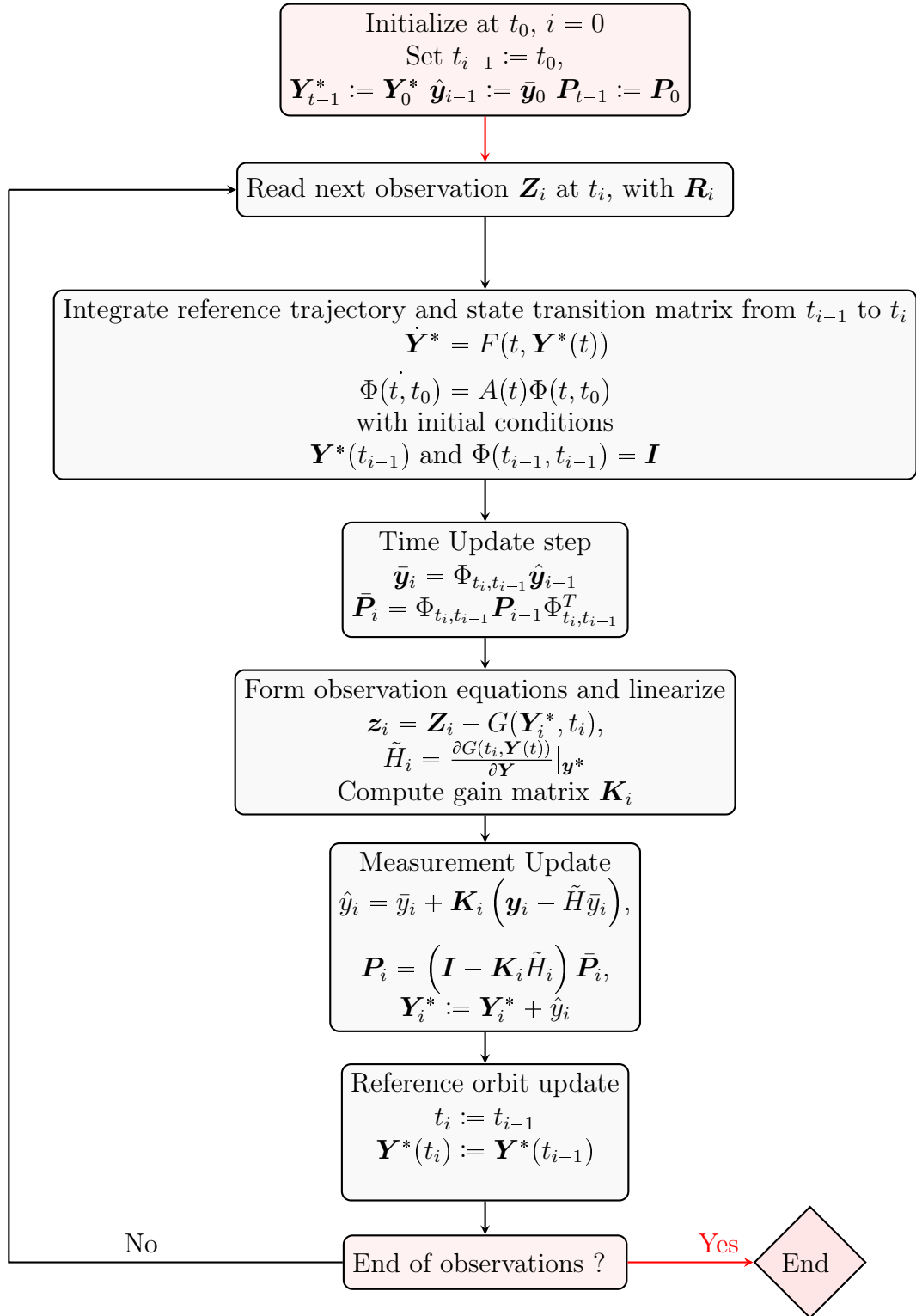
Figure 4.1: Flowchart of the Kalman filter algorithm for orbit determination.

As $\boldsymbol{P}_k \to \boldsymbol{0}$, gain also approaches zero $\boldsymbol{K} \to \boldsymbol{0}$, and the estimation procedure will become insensitive to further observations. Consequently, the estimate will diverge due to either errors introduced in the linearization procedure, computational errors, or errors due to an incomplete mathematical model. To overcome this problem, process noise often is added to the state propagation equations (Tapley et al. 2004b).

In addition to these two problems, the Kalman filter may diverge because of numerical difficulties associated with the covariance measurement update, given by Equation 4.25 (ibid.). This can be the case if the covariance matrix loses its properties of symmetry and become non-positive definite due to roundoff error (this pitfall is especially possible when a large a-priori covariance is reduced by the incorporation of very accurate observation data). An alternative equation to Equation 4.25 is to use the more numerically stable formula introduced by *Bucy* and *Joseph*, which reads

$$\boldsymbol{P}_k = \left(\boldsymbol{I} - \boldsymbol{K}_k \tilde{\boldsymbol{H}} \right) \bar{\boldsymbol{P}}_k \left(\boldsymbol{I} - \boldsymbol{K}_k \tilde{\boldsymbol{H}} \right)^T + \boldsymbol{K}_k \boldsymbol{R}_k \boldsymbol{K}_k^T \tag{4.27}$$

More information and a detailed discussion on the stability of relevant approaches can be found in Bierman 1977.

4.4 The Extended Kalman Filter

To address the problem of growing the errors due to higher order terms that are ignored in the sequential Kalman filter (see subsection 4.3.1), an extended form of the algorithm can be used, labeled the *Extended Kalman Filter*. The advantage of this approach is that convergence (to the best estimate) is accelerated because of the reduced linearization errors. The major disadvantage of the extended sequential algorithm is that the differential equations for the reference trajectory must be reinitialized after each observation is processed. The concept of this filter involves the notion that the true state is sufficiently close to the estimated state (Markley and Crassidis 2019). A flowchart of the algorithm is depicted in Figure 4.2.

The primary difference between the classic formulation and the extended algorithm is that the reference trajectory for the extended Kalman filter is updated after each observation to reflect the best estimate of the true trajectory. E.g., after processing the kth observation, the computed best estimate is used to provide a new initial condition for the reference orbit,

$$\boldsymbol{y}_{k,new}^* = \hat{\boldsymbol{y}}_k = \boldsymbol{y}_k^* + \hat{\delta \boldsymbol{y}}_k \tag{4.28}$$

Note that using $\hat{\boldsymbol{y}}_k$ as the reference orbit, implies that $\hat{\delta\boldsymbol{y}}_k = \boldsymbol{0}$ and thus $\bar{\delta\boldsymbol{y}}_{k+1} = \boldsymbol{0}$. The integration for the reference trajectory and the state transition matrix is reinitialized at each observation epoch, and the equations are integrated forward from t_k to t_{k+1}. After the time update step, the best estimate can be computed as

$$\hat{\delta\boldsymbol{y}}_{k+1} = K_{k+1}\boldsymbol{y}_{k+1} \tag{4.29}$$

with K_{k+1} and $\boldsymbol{y}_{k+1}$ computed based on the updated reference orbit. The process of incorporating the estimate at each observation point into the reference trajectory for propagating to the next observation epoch leads to the reference trajectory being the prediction of the estimate of the nonlinear state (Tapley et al. 2004b), e.g. $\boldsymbol{y}_t^* = \hat{\boldsymbol{y}}(t)$.

When implementing the extended Kalman filter for applications demanding high accuracy, care must be taken when updating the reference orbit at the beginning of the processing. Often, the update is omitted for the first few observations, especially if these contain significant noise. After a few observations have been processed, the estimates of $\hat{\delta\boldsymbol{y}}$ will stabilize, and the trajectory update step can be added to the process (ibid.).

4.5 Variational Equations

For application with high accuracy demands, the state transition matrix should include terms at least the major perturbations. That is, the initial value problem should be expanded to include differential equations to account for perturbed motion. An analytical solution of this problem is close to impossible, thus this extended formulation should be solved for numerically. The added differential equations (to the state transition matrix system) are labeled *variational equations*. Aside from the increased accuracy that may be obtained by accounting for perturbations, the concept of the variational equations offers the advantage that it is not limited to the computation of the state transition matrix, but may also be extended to the treatment of partial derivatives with respect to force model parameters (Montenbruck and Gill 2000).

4.5.1 Differential Equations for the State Transition Matrix

Denoting the state vector as $\boldsymbol{y}(t) = \begin{pmatrix} \boldsymbol{r}(t) & \boldsymbol{v}(t) \end{pmatrix}^T$, the differential equation, which describes the change of the state transition matrix with time in a first-order ODE

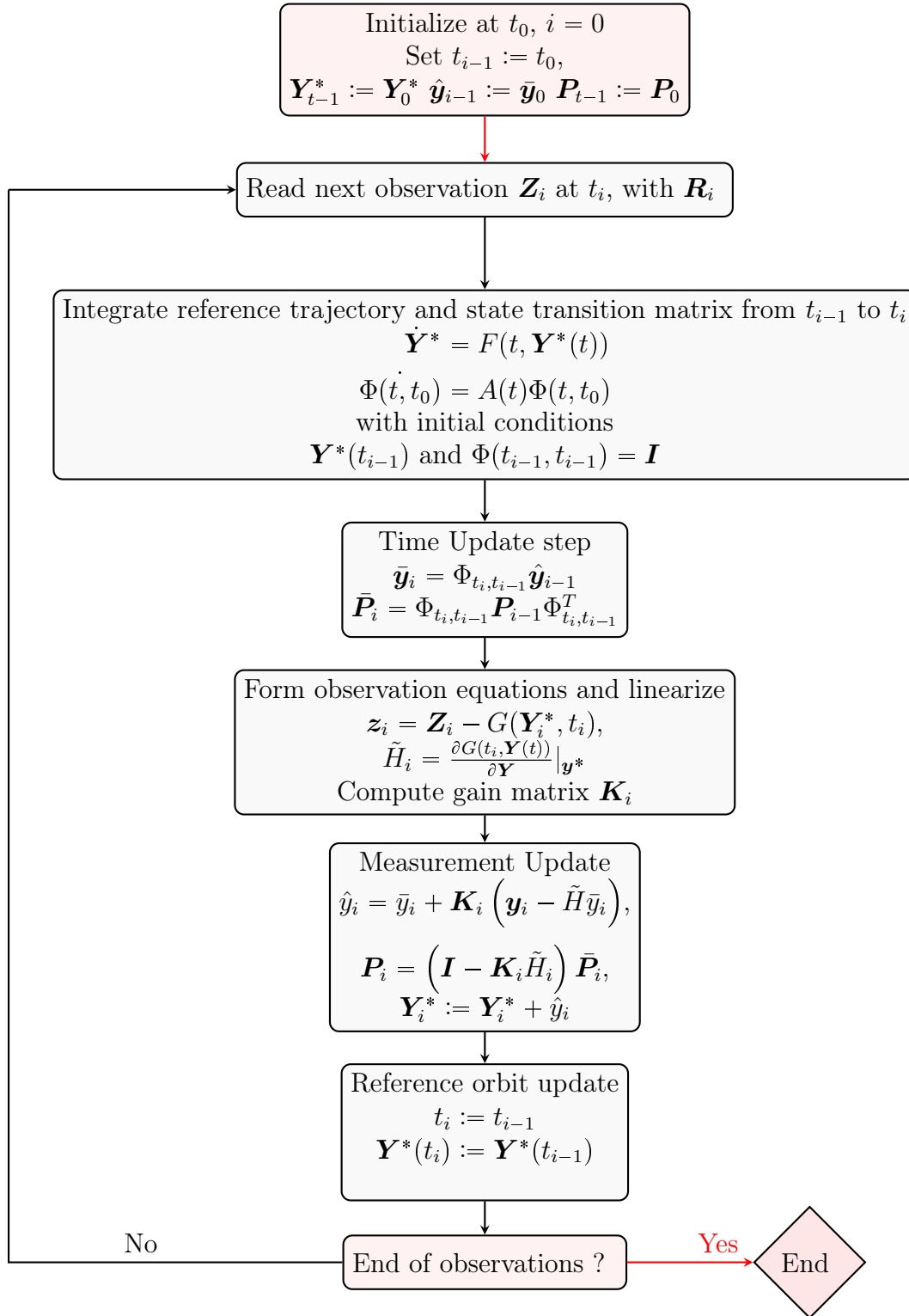Figure 4.2: Flowchart of the Extended Kalman filter algorithm for orbit determination.

$$\frac{d\boldsymbol{y}(t)}{dt} = \boldsymbol{f}(t, \boldsymbol{y}(t)) = \begin{pmatrix} \boldsymbol{v}(t) \\ \boldsymbol{a}(t, \boldsymbol{r}, \boldsymbol{v}) \end{pmatrix} \tag{4.30}$$

An differentiating with respect to $\boldsymbol{y}(t_0)$ gives

$$\frac{\partial}{\partial \boldsymbol{y}(t_0)} \left(\frac{d\boldsymbol{y}(t)}{dt} \right) = \frac{\partial \boldsymbol{f}(t, \boldsymbol{y}(t))}{\partial \boldsymbol{y}(t_0)} = \frac{\partial \boldsymbol{f}(t, \boldsymbol{y}(t))}{\partial \boldsymbol{y}(t)} \frac{\partial \boldsymbol{y}(t)}{\partial \boldsymbol{y}(t_0)} \tag{4.31}$$

Since the state transition matrix $\Phi(t, t_0)$ is given by

$$\Phi(t, t_0) = \frac{\partial \boldsymbol{y}(t)}{\partial \boldsymbol{y}(t_0)} \tag{4.32}$$

its derivative can be computed from

$$\begin{aligned} \frac{d}{dt} \Phi(t, t_0) &= \frac{\partial \boldsymbol{f}(t, \boldsymbol{y}(t))}{\partial \boldsymbol{y}(t)} \Phi(t, t_0) \\ &= \begin{pmatrix} \frac{\partial \boldsymbol{v}(t, \boldsymbol{r}, \boldsymbol{v})}{\partial \boldsymbol{r}(t)} & \frac{\partial \boldsymbol{v}(t, \boldsymbol{r}, \boldsymbol{v})}{\partial \boldsymbol{v}(t)} \\ \frac{\partial \boldsymbol{a}(t, \boldsymbol{r}, \boldsymbol{v})}{\partial \boldsymbol{r}(t)} & \frac{\partial \boldsymbol{a}(t, \boldsymbol{r}, \boldsymbol{v})}{\partial \boldsymbol{v}(t)} \end{pmatrix} \Phi(t, t_0) \\ &= \begin{pmatrix} \boldsymbol{0}_{3\times 3} & \boldsymbol{I}_{3\times 3} \\ \frac{\partial \boldsymbol{a}(t, \boldsymbol{r}, \boldsymbol{v})}{\partial \boldsymbol{r}(t)} & \frac{\partial \boldsymbol{a}(t, \boldsymbol{r}, \boldsymbol{v})}{\partial \boldsymbol{v}(t)} \end{pmatrix} \Phi(t, t_0) \end{aligned} \tag{4.33}$$

Paired with the initial condition $\Phi(t_0, t_0) = \boldsymbol{I}_{6\times 6}$, Equation 4.33 can be solved for as an initial value problem, using numerical integration.

4.5.2   Differential Equations for the Sensitivity Matrix

To form the variational equations, the partial derivatives of the state with respect to the n_p dynamical, or force model parameters p_i are needed. Taking the time derivatives

$$\frac{d}{dt} \frac{\partial \boldsymbol{y}(t)}{\partial \boldsymbol{p}} = \frac{\partial \boldsymbol{f}(t, \boldsymbol{y}(t), \boldsymbol{p})}{\partial \boldsymbol{y}(t)} \frac{\partial \boldsymbol{y}(t)}{\partial \boldsymbol{p}} + \frac{\partial \boldsymbol{f}(t, \boldsymbol{y}(t), \boldsymbol{p})}{\partial \boldsymbol{p}} \tag{4.34}$$

and hence using the sensitivity matrix defined in section 4.2,

$$\frac{d}{dt} \boldsymbol{S}(t) = \begin{pmatrix} \boldsymbol{0}_{3\times 3} & \boldsymbol{I}_{3\times 3} \\ \frac{\partial \boldsymbol{a}(t, \boldsymbol{r}, \boldsymbol{v}, \boldsymbol{p})}{\partial \boldsymbol{r}(t)} & \frac{\partial \boldsymbol{a}(t, \boldsymbol{r}, \boldsymbol{v}, \boldsymbol{p})}{\partial \boldsymbol{v}(t)} \end{pmatrix}_{6\times 6} \boldsymbol{S}(t) + \begin{pmatrix} \boldsymbol{0}_{3\times n_p} \\ \frac{\partial \boldsymbol{a}(t, \boldsymbol{r}, \boldsymbol{v}, \boldsymbol{p})}{\partial \boldsymbol{p}} \end{pmatrix}_{6\times n_p} \tag{4.35}$$

The initial condition for the above system is $\boldsymbol{S}(t_0) = \boldsymbol{0}$, since the state vector at t_0 does not depend on the force model parameters.

4.5.3 Solving the Variational Equations

Combining the differential equation systems formed above for the state transition matrix (subsection 4.5.1) and the sensitivity matrix (subsection 4.5.2), the full system of variational equations is formed, which reads

$$
\frac{d}{dt} \begin{pmatrix} \Phi & \boldsymbol{S} \end{pmatrix} == \begin{pmatrix} \boldsymbol{0}_{3\times3} & \boldsymbol{I}_{3\times3} \\ \frac{\partial \boldsymbol{a}}{\partial \boldsymbol{r}} & \frac{\partial \boldsymbol{a}}{\partial \boldsymbol{v}} \end{pmatrix}_{6\times6} \begin{pmatrix} \Phi & \boldsymbol{S} \end{pmatrix} + \begin{pmatrix} \boldsymbol{0}_{3\times6} & \boldsymbol{0}_{3\times n_p} \\ \boldsymbol{0}_{3\times6} & \frac{\partial \boldsymbol{a}}{\partial \boldsymbol{p}} \end{pmatrix}_{6\times n_p} \tag{4.36}
$$

Given also the initial conditions (described in subsection 4.5.1 and subsection 4.5.2)

$$
\begin{pmatrix} \Phi(t_0, t_0)_{6\times6} & \boldsymbol{S}(t_0) \end{pmatrix} \begin{pmatrix} \boldsymbol{I}_{6\times6} & \boldsymbol{0}_{6\times n_p} \end{pmatrix} \tag{4.37}
$$

an initial value problem of 1st degree is formed, which can be solved for by methods of numerical integration (see chapter 3). A slightly different approach is presented in section A, starting from the state-space representation.

It is important to note that the variational equations have to be integrated simultaneously with the state vector. Otherwise the position and velocity of the satellite, which are required to evaluate the acceleration partials (right-hand side of the variational equations), would be unknown.

4.6 Implementation

4.6.1 Solution of Variational Equations

The computation of the differential equation system comprisig the variational equations and its subsequent solution is a demading task in POD, posing challenges both in efficiency and in precision. A large number of computations must be performed, mainly including evaluation of partial derivatives. Analytic formulas for the latter are rather complicated making their implementation error prone.

Unfortunately, testing and validation of software designed to tackle this problem is cumbersome, and based on trial-and-error. To test the implemetation, a large number of tests was performed, starting from a simple, two-body formulation and gradually increasing complexity, checking each step with respect to the previously estimated solution. The gradual increase of complexity was expected to be paired with a increase in solution accuracy.

The solution of the variational equations is based on numeric integration, via an Adams-Bashforth-Moulton PECE algorithm, with varying step size and order. The fundametals and implementation of this method is already discussed in section 3.3 and section 3.4.

4.6.2   Exteded Kalman Filter Implementation

For the purposes of the current Thesis, a software package was designed and implemented to perform orbit determination using the Extended Kalman Filter algorithm (see section 4.4). This algorithm was chosen due to a number of factors, including

- robust and efficient estimation algorithm,

- the filter's ability to utilize state models for dynamic processing,

- compensation for dynamic model inaccuracy (*process noise*),

- estimation of varying state and easily adaptable to (near) real-time scenarios; Zhou et al. 2020 use an extended Kalman filterig algorithm to determine in real time the orbit of the HY2A LEO, using DORIS and spaceborne Global Positioning System (GPS) observations

- adaptability and fine tuning of statistical properties of process noise, and measurement error to design an "optimal" filter,

- widely used across various engineering fields and under growing progress

To address the issue raised in subsection 4.3.1, concerning the possible divergence of the estimates due to numerical instabilities, the *Bucy* and *Joseph* formula (Equation 4.27) is adopted.

Kalman filtering offers great verstility in handling stochastic and statistical properties of parameters, state and system dynamics. Special care was taken in order to preserve this versatility and transfer it to the user, through the control of relevant options by means of (user) input. Fundamental stochastic properties of the analysis are set via a user-friendly configuration file, including but not limited to a-priori sigmas (standard deviation) for all parameters considered and observation statistics. Numerous tests have been performed with combinations of different values to derive sensible defaults, an option alsoprovided to the user.

The implementation processes one observation at a time, so as to take full advantage of the scalar computations of various formulas included in the previous chapters. This makes the algorithm more efficient and less demading on memory resources.

Filter design is as generic as possible, so as to allow (except from varying user input descussed above) reusage in different parts of the software package, to perform different tasks. E.g. a variant of the same algorithm performs linear regression to estimate relative frequency offsets biases (see chapter 5).

It is worth noting that most state-of-the-art software packages for POD using DORIS observations, use the method of least squares for parameter estimation. This is true e.g. for the Bernese GNSS Software (Dach 2015), GINS (CNES 2013) and GEODYN (Beal 2015), all of which are packages used by Aalysis Centers actively contributing to the IDS. This choice has to do with the fact that at the time these packages were first developed, Least Squares was the prevailing method for parameter estimation, while Kalman filtering had miimum intrusion into the geodetic community. Nevertheless, using alternate but equally robust techniques can provide insight and drive further research and progress both within the DORIS community (via the combination of Analysis Centers individual results) and in the scientific world in general.

Chapter 5

DORIS

5.1   Introduction

Individual components of POD analysis have been discussed in the preceding sections, including the force model, orbit integration, and parameter estimation. This chapter focuses on the one crucial component that is still missing: actual data.

The most widely used satellite observation techniques in geodesy, are SLR, GNSS and DORIS. In this Thesis the latter technique is considered. Since its inception in the late 1980s, DORIS has been constantly evolving, and it is now of critical importance for geodesy, with applications spanning a wide range of related elds, including reference frame maintenance. There is currently an effort underway to deploy 4th generation ground beacons, securing and strengthening the technique's performance and thus its future.

To date, orbital accuracies achieved using DORIS data, can reach the few-centimeter level (see e.g. Rudenko et al. 2023 and Kong et al. 2017), and since most altimetry satellite missions are equipped with onboard DORIS receivers, the technique plays a crucial role in the study of sea level changes and hence, indirectly, in the monitoring of the Earth's climate.

Currently DORIS is not as popular as other satellite geodetic techniques (e.g. GNSS), for a variety of reasons, including the technique's complexity and its limited (if any) commercial usage. This is evident by the number of Analysis Centers contributing to the IDS (according to Moreaux et al. 2022, four Analysis Centers were involved in IDS's contribution to ITRF2020). The current Thesis work aims

to lay the groundwork for a new, state-of-the-art software package that will allow DORIS data analysis in accordance with IDS quality standards.

5.1.1 Goals of Current Chapter

In this chapter emphasis is given on the DORIS satellite system. A short introduction of the system's origins and technological advancements is given first, and a short description of its operation principle follows. Two pillars of the system are introduced:

- the IDS, a service dedicated to facilitating access to DORIS data and products to the scientific community, while at the same time deriving products of the utmost quality to all interested parties, and

- the DORIS network, i.e. the transmitting ground beacons, scattered around the globe in a homogeneous spatial distribution, which along with the instrumentation stability is a key factor in the technique's precision

Subsequently, the geometry of the ground stations is discussed. In applications with high accuracy demands, the signal path between emitter and receiver needs to be referred to the appropriate, yet virtual, exact point of transmission (and reception respectively). Hence, beacon geometry, reference points and related offsets and variations (PCO and Phase Center Variations (PCV)) are presented and discussed, as well as the reductions involved in data analysis.

The theoretical investigation of the measurements obtained via the DORIS technique, namely the relative velocity between the transmitter and the receiver, follows (via Doppler counts). It is crucial to gain a clear view on both the observation model and the measurement conduction by the receiver electronics, to be able to identify discrepancies, error sources and ambiguities that enter the model, measurements and computations. An observation model is developed and extensively discussed in order to match the acquired measurements as precisely as possible. Basic formulas involved, along with theoretical implications are also presented.

Last but not least, a thorough discussion on the implementation of the observation equations, obtained via the DORIS system, follows. Starting from the theoretical background (discussed previously), implementation details and practical aspects of the computations involved are presented, following a hands-on approach. Given that analysis of DORIS observations is not as popular and not as
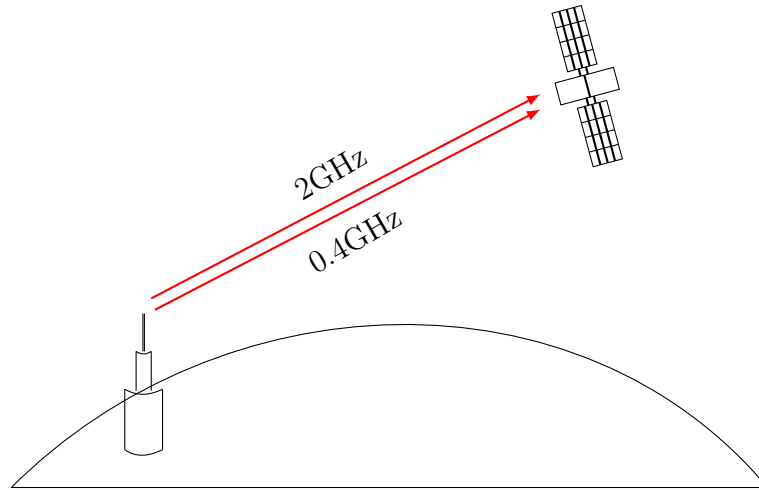
Figure 5.1: DORIS System Description

"standardized" as other techniques (e.g. GNSS), especially since the new, extended DORIS RINEX format was introduced, this section is key in designing a robust processing pipeline.

5.2 Fundamentals of DORIS System

In the late 1980s, CNES, in conjunction with the Institut Géographique National (IGN) and GRGS developed a new geodetic tracking system called DORIS for precise orbit determination of LEO satellites for oceanographic missions. Since then, DORIS has made huge leaps forward, and proved to be an invaluable tool to the scientific community, greatly expanding its application range and significance. This process lead in 2003 to the creation of IDS (Willis et al. 2016b), part of the Global Geodetic Observation System (GGOS) within the IAG (Willis et al. 2006).

DORIS (Barlier 2005) originated during the design phase of the US-French TOPEX/Poseidon mission (Fu et al. 1994), and constitutes a Doppler up-link system, optimized for orbit determination (both in real-time and post-processed). Radio signals are generated from a ground-tracking network, and Doppler measurements are performed on-board the satellite. Since its initialization, the system's technology has greatly improved, and its applications have gradually and logically expanded from orbit determination to gravity-field determination, terrestrial reference frame maintenance and geodynamics. Since TOPEX/Poseidon, an ever-increasing number of LEO satellite missions are equipped with on-board DORIS receivers. Figure 5.2 depicts past, current and future DORIS-equipped satellite missions.
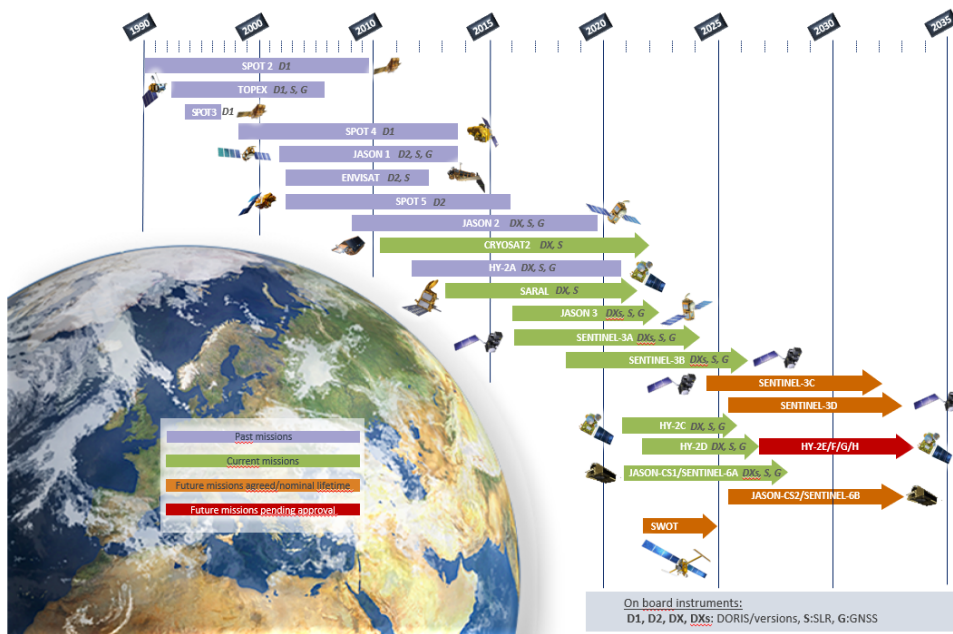
Figure 5.2: DORIS-ecquiped satellites; image courtesy of IDS, source https://ids-doris.org/doris-system/satellites.html

DORIS is based on the accurate measurement of the Doppler shift of radio frequency signals transmitted from ground beacons and received on board the satellite(s) (Figure 5.1). Roughly every 10 s, the on-board receiver accurately measures the Doppler shift of radio-frequencies signals continuously transmitted from beacons at two frequencies: at 2.036 25 GHz for precise Doppler measurement and at 401.25 MHz for correction of the propagation delay trough the ionosphere. The two channels are also used for time-tagging measurements and auxiliary data transmission (Auriol and Tourain 2010).

5.2.1 The DORIS Tracking Network

The tracking network is a key factor in the success of the DORIS system. IGN established and actively maintains this network, which currently (February 2023) has 59 sites (Figure 5.3). It is global, dense and homogeneous, and thus unique among the different techniques that contribute to ITRF. Since its establishment, very few changes of sites and/or instrumentation have been performed, thus enforcing network stability. Furthermore, it is (spatially) dense and well distributed geographically (especially between the Northern and Southern hemispheres). This spatial balance along with several collocations with other space-geodetic tech-

101

niques (Figure 5.4), make the DORIS system an integral part of reference frame maintenance (Moreaux et al. 2022).
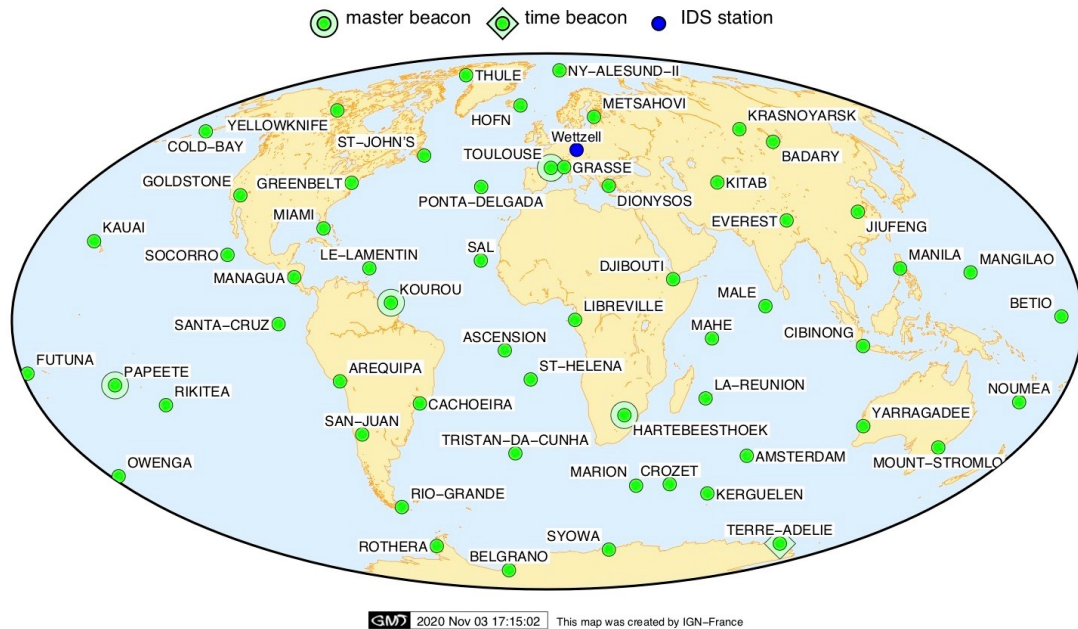
Figure 5.3: The DORIS Network (as of Nov. 2020); image courtesy of IDS, source https://ids-doris.org/doris-system/tracking-network/maps.html

The strengths and advantages of the DORIS tracking network, can be summarized by (Soudarin et al. 2019)

Centralized control and management of the network deployment and evolution, including site instrumentation.

Long operation time ; time-series of current stations span a 21 year period in average, with a median of 26.4 years.

Homogeneous spatial distribution ; half of the stations are located on islands or coastal areas and the network is well balanced between the Northern and Southern hemispheres (Figure 5.3).

Large number of co-locations ; 48 stations are co-located with other techniques (GNSS: 47, SLR: 10, VLBI: 7), plus 28 are co-located with tide gauges (Figure 5.4)
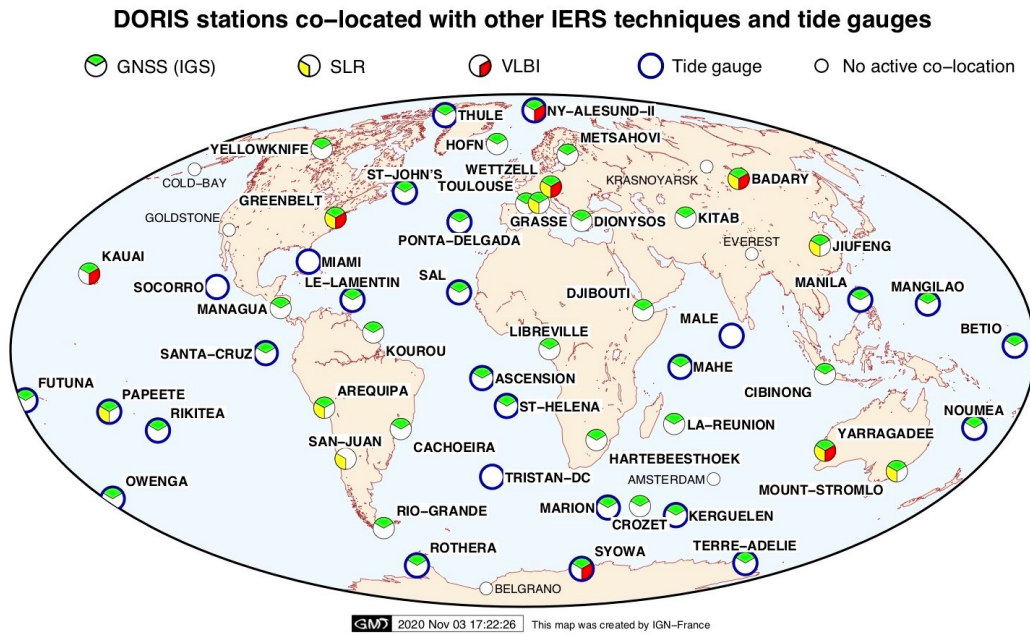
Figure 5.4: DORIS stations co-located with other space-geodetic techniques and tide-gauges (as of Nov. 2020); image courtesy of IDS.

5.2.2 The International DORIS Service

The IDS was established in 2003, with the mission to (ibid.)

- provide support to research activities in geodesy and geophysics, based on DORIS data and derived products, and

- give access to data, products and documents related to the DORIS system

The service is based on international cooperation on a volunteer basis and just like its geodetic counterparts (i.e. IGS, ILRS and International VLBI Service for Geodesy and Astronomy (IVS) for GNSS, SLR and VLBI respectively) plays a crucial role in the development of the technique and most importantly drives and facilitates its usage from the scientific community. Major products published by IDS include times series of the DORIS tracking stations, along with their positions and velocities and time series of geocenter motion and Earth orientation parameters. IDS also coordinates the technique's contribution to the ITRF (see e.g. Moreaux et al. 2022).

IDS's organization chart, includes a Governing Board and a Central Bureau.

The Analysis Centers process the DORIS data available at the IDS Data Centers and generate products with the assistance of the Analysis Center Coordinator. The IDS Combination Center provides regular combination of products of the Analysis Centers and is also in charge of the realization of the so-called DPOD (DORIS extension to the current ITRF for POD) which contains update mean positions and velocities of all the DORIS stations. Last but not least, the IDS Combination Center produces the technique's contribution the ITRF.

5.3 DORIS Ground Segment

Estimation of precise coordinates of both DORIS-equipped satellites and DORIS beacons relies on accurate modeling of the signal path from the ground antenna to the space antenna. It is thus important to have a clear view of the geometry of the respective antennae and reference points of signal transmission and reception. Note that these reference points depend on the frequency (or linear combination of frequencies) used to perform a measurement.

5.3.1 Geometry of Ground Antennae

DORIS observations are referred to the electronic reference points (RP) of the antenna, the points where the DORIS observations are acquired. However, these points are "virtual" and for example may change while using another antenna type, hence they lack the accuracy required for geodetic studies. Observations must therefore be referred to the conventional RP which is defined according to the geometry of the antenna and account for the distance between the electronic RP and the conventional RP of the antenna (Tourain et al. 2016). The ability to get accurate DORIS data relies for one part on the capability of providing accurate models to connect the electronic RP (or electronic *phase center*) and the conventional RP, as well as, PCVs as a function of the elevation angle to the tracking satellite.

Three antenna types are used in the DORIS tracking network, namely `ALCATEL`, `STAREC-B` and `STAREC-C` (Saunier et al. 2016). Table 5.1 records antenna gains per type. ALCATEL is the oldest antenna type, installed throughout the DORIS network at the time of its establishment. These antennas were later replaced by the STAREC-B model, a long-standing effort that ended in 2007 with the replacement of the last station in Toulouse (TLHA) (Štěpánek and Filler 2022).

Zenith Distance	ALCATEL (dBi)		STAREC (dBi)	
	401.25 MHz	2036.25 MHz	401.25 MHz	2036.25 MHz
0°	3.2	2.1	3.5	0
10°	3.5	2.6	3.6	0.4
20°	4	2	3.7	0.5
30°	4.4	4	3.8	1.5
40°	4.6	4.4	3.7	3.2
50°	4.2	4.6	3.2	3.9
60°	2.7	2.7	2.5	4
70°	0.6	-0.1	1	3.2
80°	-2.7	-3.3	-1.3	0.2
90°	-6	-7	-4.2	-5.6

Table 5.1: DORIS ground antennae gains, source: DORIS System Ground Segment Models, (Issue 1.3), https://ids-doris.org/documents/BC/stations/DORIS_System_Ground_Segment_Models.pdf

The type of antenna installed at a particular station, is identified by the 4th character of the beacon mnemonic: letter "A" for the Alcatel type; letter "B" or letter "C" for the Starec B or C type respectively. That is, in the DORIS RINEX field "STATION REFERENCE", the last character of the second column (aka "4-character station code"), defines the ground beacon antenna type; e.g.

```
    51                                          # OF STATIONS
D01  BEMB BELGRANO              66018S002  3   0  STATION REFERENCE
D02  ADHC TERRE ADELIE         91501S005  3   0  STATION REFERENCE
D03  SYQB SYOWA                 66006S005  3   0  STATION REFERENCE
D04  CRQC CROZET                91301S004  4   0  STATION REFERENCE
D05  DIOB DIONYSOS              12602S012  3   0  STATION REFERENCE
```

Phase Center Offsets

Depending on the antenna type, appropriate PCOs need to be applied to the observed quantities for the reduction of the observation vector to the Reference Point (from the respective "virtual" phase center) of the antenna. Table 5.2 lists PCO values for the two fundamental frequencies of the DORIS system per antenna type.

When a linear combination of the observed quantities is used, a respective PCO needs to be computed and applied. E.g., for the case of the ionospheric-free linear

Antenna Type	ALCATEL	STAREC-B & STAREC-C
Δh in mm for $2\,\mathrm{GHz}$	$510\,\mathrm{mm}$	$487\,\mathrm{mm}$
Δh in mm for $400\,\mathrm{MHz}$	$335\,\mathrm{mm}$	$0\,\mathrm{mm}$

Table 5.2: DORIS ground antennae PCOs, source: DORIS System Ground Segment Models, (Issue 1.3), https://ids-doris.org/documents/BC/stations/DORIS_System_Ground_Segment_Models.pdf.

combination, the respective PCO is:

$$\vec{r}_{2GHz,iono-free} = \frac{\vec{r}_{400MHz,2GHz}}{\gamma - 1} \tag{5.1}$$

where $\vec{r}_{2GHz,iono-free}$ is the vector from the $2\,\mathrm{GHz}$ phase center to the iono-free phase center and $\vec{r}_{400MHz,2GHz}$ is the vector from the $400\,\mathrm{MHz}$ to the $2\,\mathrm{GHz}$ phase center. Table 5.2 lists the PCO per antenna type.

The geometry of the DORIS ALCATEL Antenna is depicted in Figure 5.5, with the reference points of interest.

STAREC antennae B and C are identical in terms of design and specification, the difference being about the error budget in phase center position. For STAREC-C, manufacturing process and error budget have been improved (DORIS System Ground Segment Models, (Issue 1.3)). The geometry of these antennae is depicted in Figure 5.6.

Phase Center Variations

According to Tourain et al. 2016, in order to check the consistency of the theoretical characteristics of the STAREC antennae, a measurement campaign was performed by the CNES at the Compact Antenna Test Range (CATR). The CATR is a dedicated facility consisting of an anechoic chamber equipped with several specific devices allowing significant measurement for satellite characterization.

As a result of the campaign, a phase law was established by averaging the estimated phase law values obtained during the CATR characterization. The resulting couple phase center position to phase law correction is provided to the DORIS users in Antenna Exchange Format (ANTEX) (Rothacher and Schmid 2010) format, and made available by IDS (see Figure 5.7).

A similar approach was eventually followed for the ALCATEL antenna type

ALCATEL DORIS Ground Antenna

DORIS reference point
$\begin{bmatrix} x_s y_s z_s \end{bmatrix}^T$ beacon
position in earth reference
frame

phase center 2 GHz

phase center 400 MHz

$h_{2GHz} = 510\,\text{mm}$

$h_{400MHz} = 335\,\text{mm}$

DORIS reference point

DORIS reference plane

local vertical
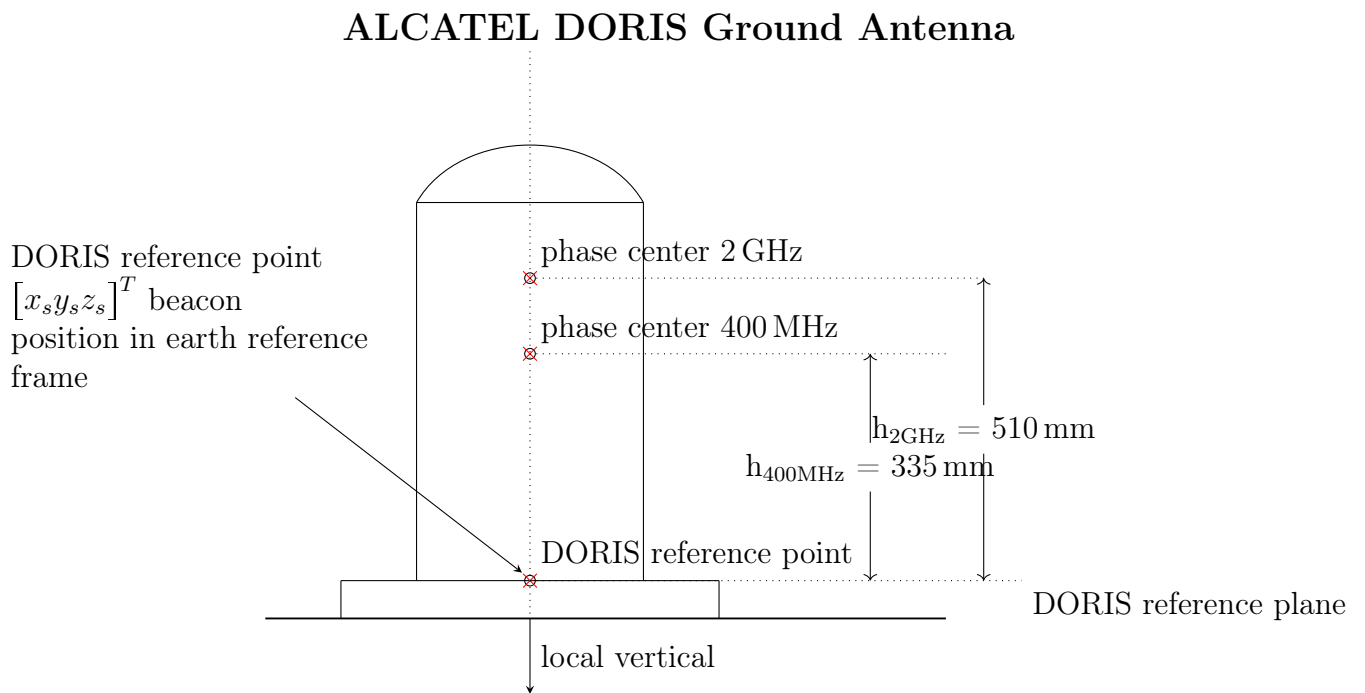
Figure 5.5: Geometry of Alcatel DORIS Ground Antenna/Beacon

STAREC DORIS Ground Antenna

phase center $2\,\mathrm{GHz}$

$\mathrm{h_{2GHz}} = 487\,\mathrm{mm}$

phase center $400\,\mathrm{MHz}$

Painted ring

DORIS reference plane

DORIS reference point
$\begin{bmatrix} x_s y_s z_s \end{bmatrix}^T$ beacon
position in earth reference
frame

local vertical

Figure 5.6: Geometry of Alcatel STAREC Ground Antenna/Beacon
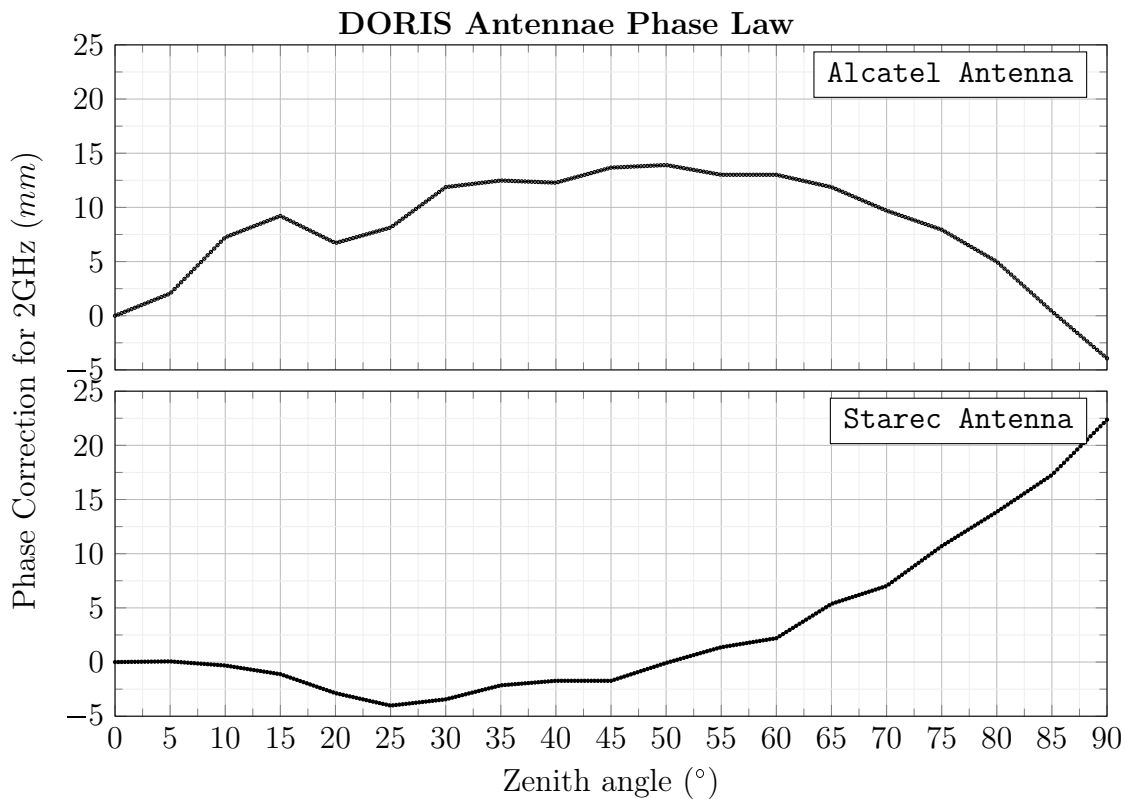
Figure 5.7: DORIS Antennae Phase Law

leading to an elevation-dependent PCV model (see Figure 5.7), conventionally called `PCV2.0`. Štěpánek and Filler 2022 report systematic differences in the estimated station heights of about 15 mm when this model is adopted in the analysis, compared to older PCV values. Note that both PCV models (for ALCATEL and STAREC) do not consider azimuth dependency and have an elevation step of 5°.

5.4 DORIS RINEX

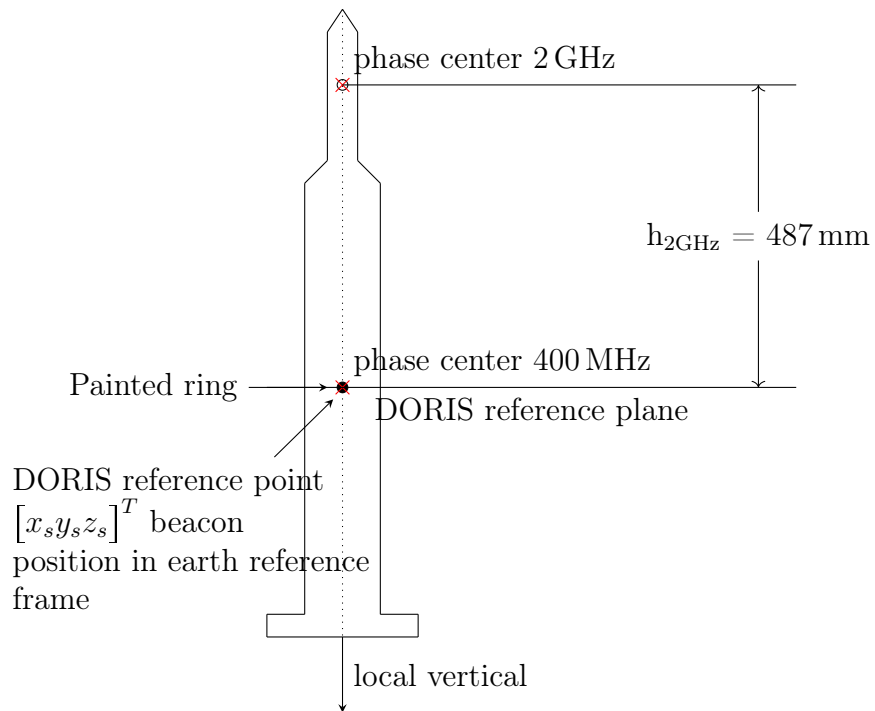With the adoption of the DORIS DGXX receivers, first installed onboard the Jason-2 satellite, signal tracking on seven different channels simultaneously became possible, with synchronous dual frequency phase and pseudo-range measurements (Mercier et al. 2010). This development made it possible for DORIS data to be described in a manner similar to GNSS data, and hence an extension of the RINEX

3.0 format (Romero 2020) was defined and adopted for DORIS observations to be recorded and published in. One major advantage of these new measurement data is that they are available with a very short latency (older data needed to be pre-processed before published). The new data exchange format is expected to further aid analysis development, since it allows each analysis center to be independent from CNES data preprocessing, as users have access to synchronous phase and pseudorange measurements (Cerri and Mercier 2011).

5.4.1 General Format Description

The DORIS RINEX format consists of one ASCII file containing both space based and meteorological data collected at DORIS stations and relayed by satellites. It bears close resemblance to the GNSS RINEX Version 3 (Romero 2020); data files consist of a header section and a data section. The first contains global information for the entire file, while the latter contains the actual observations and a date tag, keeping strict chronological order. Observation types recorded in the DORIS RINEX files are the given in Table 5.3.

DORIS is basically running on its own proper time which is constantly linked to TAI. Time tags are given in instrument time, and clock offset values are provided between instrument time and TAI.

Descriptor	Observation Type	Units
L	carrier phase observation	cycles
C	pseudo-range observation	m
W	power level received at each frequency	dBm
F	relative frequency offset of the receiver's oscillator $\frac{f-f_0}{f_0}$	10^{-11}
P	ground pressure at the station	100 Pa (mbar)
T	ground temperature at the station	°C
H	ground humidity at the station	%

Table 5.3: DORIS RINEX observation types.

A detailed description of the data files, can be found in Lourme et al. 2010.

5.5 DORIS Observation Equation

5.5.1 Theoretical Model of Doppler Observations

A detailed derivation of the Doppler observation equation, as implemented by means of the DORIS system, can be found in Lemoine et al. 2016, including a thorough theoretical discussion. A brief overview is given here, with focus on the measurement model implementation.

To gain a clear view on the model of the measurements, a rigorous distinction of events must be made; four different events can be identified:

beginning of emission of the 1_{st} cycle by the emitter, τ_{e_1} in the proper time scale of the emitter and t_1 in the coordinate time

beginning of reception of the 1_{st} cycle by the receiver, $\tau_{r'_1}$ in the proper time scale of the receiver and $t_{1'}$ in the coordinate time

end of emission of the N_{th} cycle by the emitter, τ_{e_2} in the proper time scale of the emitter and t_2 in the coordinate time

end of reception of the N_{th} cycle by the receiver, $\tau_{r'_2}$ in the proper time scale of the receiver and $t_{2'}$ in the coordinate time

During the proper time interval $\Delta\tau_r = \tau_{r2'} - \tau_{r1'}$, the receiver has received the N_e cycles sent by the emitter, with $N_e = f_e \Delta\tau_e$, f_e being the proper frequency of the emitter. The receiver is also equipped with an oscillator and during the proper time interval $\Delta\tau_r$ has generated a number $N_r = f_r \Delta\tau_r$ of cycles, f_r being the proper frequency of the receiver.

The Doppler measurement is the count, by the receiver electronics, of the number of cycles of difference between N_e and N_r:

$$\begin{aligned} N_{DOP} &= N_e - N_r \\ &= f_e \Delta\tau_e - f_r \Delta\tau_r \end{aligned} \tag{5.2}$$

In the RINEX files, this Doppler count is the difference between two phase measurements done at different time tags in the proper time-scale of the receiver.

After a series of assumptions and simplifications, theoretical formula for the

Doppler count can be written as (Lemoine et al. 2016):

$$
\frac{c}{f_e \Delta \tau_r} N_{DOP} \approx c \frac{f_e - f_r}{f_e}
$$
$$
- (1 - \frac{U_e}{c^2} - \frac{V_e^2}{2c^2}) \frac{\rho_2 - \rho_1}{\Delta \tau_r}
$$
$$
+ \frac{1}{c}(U_r - U_e + \frac{V_r^2 - V_e^2}{2})
$$
$$
+ \frac{2\mu}{c^2 \Delta \tau_r} [\ln (\frac{R_1 + R_{1'} + \rho_1}{R_1 + R_{1'} - \rho_1}) - \ln (\frac{R_2 + R_{2'} + \rho_2}{R_2 + R_{2'} - \rho_2})]
$$

(5.3)

where

c is the velocity of light in vacuum,

f_e and f_r are the emitter's and receiver's proper frequencies,

U_e and U_r are the gravitational potential at the emitter and receiver,

V_e and V_r is the velocity of the clock at the emitter and receiver (in the coordinate reference frame),

ρ_i is the curvlinear trajectory (of the photon(s)) at the event i,

R_i is the geometric distance between the beacon and the satellite at event i

The above equation can be conveniently split into two parts, one containing the "measured" quantities and one with the "theoretical" terms, as

$$
v_{measured} = \frac{c}{f_e}(f_e - f_r - \frac{N_{DOP}}{\Delta \tau_r}) + \Delta u_{REL}
$$

(5.4a)

$$
v_{theo} = \frac{\rho_2 - \rho_1}{\Delta \tau_r}(1 - \frac{U_e}{c^2} - \frac{V_e^2}{2c^2})
$$

(5.4b)

with

$$
\Delta v_{REL} = \frac{1}{c}(U_r - U_e + \frac{V_r^2 - V_e^2}{2})
$$
$$
+ \frac{2\mu}{c^2 \Delta \tau_r} [\ln (\frac{R_1 + R_{1'} + \rho_1}{R_1 + R_{1'} - \rho_1}) - \ln (\frac{R_2 + R_{2'} + \rho_2}{R_2 + R_{2'} - \rho_2})]
$$

(5.5)

It is well known that signals transmitted through the Earth's atmosphere are affected by it (delayed); let Δv_{IONO} and Δv_{TROPO}, be the propagation corrections of the radio electric signal through the ionosphere and troposphere respectively.

112

Additionally, in the actual case (measurements), the nominal frequencies f_e and f_r are not the "true" ones; hence, a relative correction needs to be applied e.g. for the emitter $f_{e_T} = f_{e_N}(1 + \frac{\Delta f_e}{f_{e_N}})$, where the subscript T denotes the "True" frequency and N the nominal one. Thus in Equation 5.4 the terms f_e and f_r need to be substituted by f_{e_T} and f_{r_T} respectively.

Δv_{IONO} and Δv_{REL}, which do not involve adjusted parameters, can be placed on the "measured" part of Equation 5.4 and Δv_{TROPO} and $\frac{\Delta f_e}{f_{e_N}}$ on the "theoretical" part. Furthermore, since $\Delta f_e/f_{e_N} \ll 1$ all terms including $\Delta f_e/f_{e_N}^2$ and $(\Delta f_e/f_{e_N})^2$ can be safely neglected and Equation 5.4 can be rewritten as:

$$v_{measured} = \frac{c}{f_{e_N}}(f_{e_N} - f_{r_T} - \frac{N_{DOP}}{\Delta\tau_r}) + \Delta u_{REL} + \Delta u_{IONO} \tag{5.6a}$$

$$v_{theo} = \frac{\rho_2 - \rho_1}{\Delta\tau_r}(1 - \frac{U_e}{c^2} - \frac{V_e^2}{2c^2}) + \Delta u_{TROPO} - \frac{c(\frac{N_{DOP}}{\Delta\tau_r} + f_{r_T})}{f_{e_N}}\frac{\Delta f_e}{f_{e_N}} \tag{5.6b}$$

where

$v_{measured}$ is the measured relative velocity between the emitter and the receiver between the events 1' and 2', based on the Doppler count N_{DOP}, corrected for the ionospheric and relativistic effects.

v_{theo} is the theoretical (computed) emitter/receiver relative velocity between the events 1' and 2', corrected for the tropospheric effect and for a solved-for frequency bias $\frac{\Delta f_e}{f_{e_N}}$ of the emitter. $f_{r_T} = f_{r_N}(1 + \frac{\Delta f_r}{f_{r_N}})$ is an estimate of the proper frequency of the receiver.

$\Delta v_{REL} = \Delta v_{REL_c} + \Delta v_{REL_r}$ is the relativistic correction, composed of two parts: the clock correction Δv_{REL_c} and the travel correction Δv_{REL_r}

$$\Delta v_{REL_c} = \frac{1}{c}(U_r - U_e + \frac{V_r^2 - V_e^2}{2}) \tag{5.7a}$$

$$\Delta v_{REL_r} = \frac{2\mu}{c^2\Delta\tau_r}\left[\ln\left(\frac{R_1 + R_{1'} + \rho_1}{R_1 + R_{1'} - \rho_1}\right) - \ln\left(\frac{R_2 + R_{2'} + \rho_2}{R_2 + R_{2'} - \rho_2}\right)\right] \tag{5.7b}$$

Note that Equation 5.6a and Equation 5.6b can be further simplified to Equation 5.8a and Equation 5.8b respectively, by omitting small terms (section 5.5.2).

113

5.5.2 Computational Aspects

Small Terms

In Equation 5.6a and Equation 5.6a, the smallest terms are $-U_e/c^2 - V_e^2/2c^2$ and Δv_{REL_T}; in the case of DORIS they amount to 11.0 and 6.0 $10 \times 10^{-6}\,\text{m/s}$ respectively (Lemoine et al. 2016). Furthermore, since the emitters are located on the ground, the term $-U_e/c^2 - V_e^2/2c^2$ is constant per station. This small relativistic offset is absorbed by the adjustment of $\Delta f_e/f_{e_N}$. So it is possibly to further simplify Equation 5.6a and Equation 5.6b to:

$$v_{measured} = \frac{c}{f_{e_N}}(f_{e_N} - f_{r_T} - \frac{N_{DOP}}{\Delta \tau_r}) + \Delta u_{REL_C} + \Delta u_{IONO} \tag{5.8a}$$

$$v_{theo} = \frac{\rho_2 - \rho_1}{\Delta \tau_r} + \Delta u_{TROPO} - \frac{c(\frac{N_{DOP}}{\Delta \tau_r} + f_{r_T})}{f_{e_N}}\frac{\Delta f_e}{f_{e_N}} \tag{5.8b}$$

Correction of Aberration

In Equation 5.6b (or Equation 5.8b), ρ_i is the geometrical distance between the emitter at time t_i and the receiver at time $t_{i'}$ (with $i = 1, 2$). The measurements are made by the receiver electronics, hence the instance t_i is actually unknown. In order to compute accurately t_i and thus the position of the emitter at this instant in time, a *correction of aberration* (ibid.) has to be performed. This correction can be evaluated in an iterative manner: an approximate value of the emitter-receiver distance ρ_i^* is first computed, by evaluating the position of the beacon at time $t_{i'}$. Subsequently, t_i can be found via $t_i = t_{i'} - \rho_i^*/c$. In practice, one iteration is enough.

Geopotential

For a station on the geoid, the potential at the level of the station is the sum of the gravitational potential and the centrifugal potential due to the Earth's rotation: $U_{GEO} = U_e + \frac{V_e^2}{2}$, which is a constant. For a station not located on the geoid, the quantity $U_e + \frac{V_e^2}{2}$ will only depend on the height of the beacon above the geoid.

For the computation of the gravitational potential for LEO satellites, the potential U_r cannot be restricted to the central term only ($GM_\oplus/r$) and the Earth's

oblateness (J_2) effect should also be considered (Larson et al. 2007). Hence, the equation used for computing the potential for a given satellite, reads (Lemoine et al. 2016)

$$U_r = -\frac{GM_\oplus}{r}\left(1 - \left(\frac{R_\oplus}{r}\right)^2 J_2 \frac{3sin^2(\phi) - 1}{2}\right) \tag{5.9}$$

or in Cartesian coordinates (Larson et al. 2007)

$$U_r = -\frac{GM_\oplus}{r}\left(1 - \left(\frac{R_\oplus}{r}\right)^2 J_2 \frac{3z^2 - r^2}{2r^2}\right) \tag{5.10}$$

with $R_\oplus$ the equatorial radius of the earth, r radial distance of the satellite (to the Earth's center), ϕ latitude of the satellite and $J_2 = 1.0826359\dot{1}0^{-3}$ in the zero-tide system (Petit and Luzum 2010).

Nominal Receiver and Emitter Frequencies

In the observation equation model Equation 5.6a and Equation 5.6b, a distinction is made between *nominal* and *true* receiver/emitter frequencies, to account for the fact that in "real world" these two are not actually equal.

Emitter (Beacon) Nominal Frequencies, f_{e_N} RINEX file headers, contain values of the *station frequency shift factor k* for each of the beacons involved (Lourme et al. 2010, Sec. 6.16). These are used to compute the "nominal" frequencies of the beacon/emitter (usually, this shift factor is just 0, but it can be an integer $k \neq 0$). The frequencies are computed as (ibid., Sec. 6.16):

$$L_{2GHz} = 543 \cdot F_0 \left(\frac{3}{4} + \frac{87 \cdot k}{5 \cdot 2^{26}}\right)$$

$$L_{400MHz} = 107 \cdot F_0 \left(\frac{3}{4} + \frac{87 \cdot k}{5 \cdot 2^{26}}\right) \tag{5.11}$$

where $F_0 = 5e6$ Hz the Ultra Stable Oscillator (USO) frequency. These value, are the ones labelled as f_{e_N} in Equation 5.6a and Equation 5.6b.

The *true proper frequency* of the emitter f_{e_T}, can be computed (if needed) from:

$$f_{e_T} = f_{e_N} \cdot \left(1 + \frac{\Delta f_e}{f_{e_N}}\right) \tag{5.12}$$

115

but the quantity $\Delta f_e/f_{e_N}$ is not known a-priori and has to be estimated during the processing.

The quantity $\Delta f_e/f_{e_N}$ can be estimated either as a constant term (bias), or using a linear model (bias ad drift). In the latter case (followed in this Thesis), the model can be written as:

$$\frac{\Delta f_e}{f_{e_N}}\big|_{\tau=\tau_i} = \alpha + \beta \cdot \delta\tau \tag{5.13}$$

For the estimation, the partials of the observation equation Equation 5.6b are needed, with respect to α and β parameters, which are:

$$\begin{aligned}
\frac{\partial v_{theo}}{\partial \alpha} &= \frac{c(\frac{N_{DOP}}{\Delta\tau_r} + f_{r_T})}{f_{e_N}} \\
\frac{\partial v_{theo}}{\partial \beta} &= \frac{c(\frac{N_{DOP}}{\Delta\tau_r} + f_{r_T})}{f_{e_N}} \cdot \delta\tau
\end{aligned} \tag{5.14}$$

Receiver True Proper Frequency f_{r_T} In Equation 5.6a and Equation 5.6b, f_{r_T} is the *true proper frequency of the receiver*, computed as

$$f_{r_T} = f_{r_N} \cdot \left(1 + \frac{\Delta f_r}{f_{r_N}}\right) \tag{5.15}$$

where f_{r_N} is the "nominal" frequency value. The value of the quantity $\Delta f_r/f_{r_N}$, called the *relative frequency offset* of the receiver, can be extracted from the RINEX file, estimated or computed, in one of the following ways (Lemoine et al. 2016)

1. Via the field "F" recorded for every single measurement in the DORIS RINEX file (see section 5.4); not that this estimation is not very smooth, as noticed by Gao et al. 2015 and it is advisable, before using it in Equation 5.6, to perform a linear (or polynomial) regression of these estimates over one or a few days.

2. Obtained from a polynomial regression over the frequency offsets estimated during the passes over the master beacons

3. Estimated as a by-product during a re-computation of the "timetagging" polynomial (see Mercier et al. 2010)

116

Relative frequency offset values, $\frac{\Delta f_r}{f_{r_N}}$, are reported in the RINEX files for each epoch (under the observable tagged F). Note that these values are scaled to 10^{-11} (Lourme et al. 2010, Sec. 6.11), so that for a given epoch t_i, the true frequency is

$$f_{r_T}|_{t=t_i} = f_{r_N} \cdot \left(1 + F_{t_i} \cdot 10^{-11}\right) \tag{5.16}$$

where F_{t_i} is the relative frequency offset value recovered from the RINEX file.

5.5.3 Ionospheric Correction

The basic observation equation Equation 5.6a and Equation 5.6b, is formed for the 2 GHz carrier. For each measurement, the ionospheric path delay has to be corrected for, by computing a correction (in cycles) as (Lemoine et al. 2016, Sec. 2.5.7):

$$\delta_{ION}[2\,\text{GHz cycles}] = \frac{L_{2\,\text{GHz}} - \sqrt{\gamma} \cdot L_{400\,\text{MHz}}}{\gamma - 1} \tag{5.17}$$

which is added to the 2 GHz measurement at time $t = t_i$ (obtained by the RINEX file). Thus, the corrected observation is:

$$L_{2\,\text{GHz},IF}[2\,\text{GHz cycles}] = L_{2\,\text{GHz}} + \delta_{ION} \tag{5.18}$$

Note that after applying Equation 5.18, the measurement is referred to the "Iono-Free" geometrical endpoints of the signal path (and not the 2 GHz endpoints). This means that the respective phase center corrections (i.e. PCO and PCV) both at the satellite and at the beacon have to be applied.

5.6 Implementation of the DORIS Observation Equation

The observation equation formed to process the DORIS data, is based on Equation 5.8a and Equation 5.8b. Consequently, two parts are computed, $v_{measured}$ which represents the "observed" or "measured" relative velocity between the receiver and the transmitter, and v_{theo} which is the "computed" or "theoretical" counterpart. In this way, during the processing phase, all quantities that do not need adjustment can be placed on the "measured" side of the equation (ibid.). A short discussion follows, describing the implementation of the DORIS observation equation in the software designed for this Thesis.

5.6.1 Coordinate and Proper Time

TAI is used as coordinate time; to transform RINEX observation time (given in proper time τ) to coordinate time t, the *receiver clock offset* values are used, extracted from the RINEX file (one value per observation block).

Hence, if an observation block is tagged at proper time τ_i at the RINEX file, and the receiver clock offset for this block is $\Delta\tau_i$ (again from RINEX), then the coordinate time of the event in TAI is computed as

$$t_i^{TAI} = \tau_i + \Delta\tau_i \tag{5.19}$$

According to Lemoine et al. 2016 however, there is no need to make a time conversion for the time interval of the Doppler count, i.e. the term $\Delta\tau_r$ in Equation 5.8a and Equation 5.8b, due to the time-tagging method used in DORIS RINEX.

5.6.2 Receiver Emitter Geometric Distance

The geometric distances between the emitter and the receiver, ρ_1 and ρ_2, when computed, are corrected for the aberration effect, i.e. the slight displacement of the emitter due to Earth's rotation between signal emission and signal reception at the receiver. The algorithm for this correction is described in section 5.5.2. It is worth noting that the checks performed have confirmed that multiple iterations are practically redundant.

5.6.3 Relativistic Correction

Equation 5.8a contains a relativistic correction term, Δu_{REL}. This correction is split into two parts, Δu_{REL_c} the part containing the clock correction and Δu_{REL_r}, containing the effect of the travel path (see Equation 5.7a and Equation 5.7b). In the implementation followed for this Thesis, only the Δu_{REL_c} part is considered (Equation 5.7a).

For the receiver part (with subscripts r), the respective quantities in Equation 5.7a are given by

$$V_r^2 = \|\boldsymbol{v}_{ecef}\|^2$$
$$U_r = \frac{\mu_\oplus}{\|\boldsymbol{r}_{ecef}\|} \cdot \left(1 - \left(\frac{\alpha}{\|\boldsymbol{r}_{ecef}\|}\right)^2 \cdot J_2 \cdot \frac{3 \cdot \sin^2 \phi - 1}{2}\right) \tag{5.20}$$

where $\boldsymbol{r}_{ecef}$ and $\boldsymbol{v}_{ecef}$ are the position and velocity of the satellite at the given instant, in the terrestrial reference frame, aka ITRF. Note that the Earth's oblateness cannot be ignored here (see discussion in section 5.5.2).

For the emitter, potential computation is further simplified. Since $V_e = 0$, the potential is computed as

$$U_e = \frac{\mu_\oplus}{\|\boldsymbol{r}_{ecef}\|} \tag{5.21}$$

where $\boldsymbol{r}_{ecef}$ is the position vector of the beacon in ITRF.

In Equation 5.8a, relativistic corrections must be "differentiated" between two consecutive epochs (used for the Doppler count)

$$
\begin{aligned}
\Delta v_{REL} &= \frac{1}{c} \left(\left[U_r - U_e + \frac{V_r^2 - V_e^2}{2} \right] \Big|_{t=t_i} - \left[U_r - U_e + \frac{V_r^2 - V_e^2}{2} \right] \Big|_{t=t_{i-1}} \right) \\
&= \frac{1}{c} \cdot \left(U_r|_{t_i} - U_r|_{t_{i-1}} + \frac{V_r|_{t_i} - V_r|_{t_{i-1}}}{2} \right) \text{ m/s}
\end{aligned}
\tag{5.22}
$$

5.6.4 Receiver Proper Frequency f_{r_T}

In the implementation, "smoothed" values of RINEX-provided $\Delta f_r/f_{r_N}$ estimates are used to compute the receiver's proper frequency, given by Equation 5.16. In a first RINEX pass, F_{t_i} are used to estimate a linear model spanning the whole RINEX time span. These smoothed values are then used to compute relative frequency offsets at the observation epochs (see discussion in section 5.5.2).

5.6.5 Ionospheric Correction

For each observation in the RINEX file, the ionospheric correction is computed and applied to the 2 GHz measurement (as described in section 5.6.5), thus transforming it to an "iono-free" measurement.

When applied to Equation 5.8a, "differenciation" of the ionospheric delays computed from 5.17 must be performed, affecting two observations (the same ones used to derive the Doppler count). Hence, the term Δv_{IONO} appearing in Equation 5.8a is

$$\Delta v_{IONO}[\text{m/s}] = \frac{c}{f_{e_N}} \cdot \frac{\delta_{ION}\big|_{t=t_{i-1}} - \delta_{ION}\big|_{t=t_i}}{\Delta\tau} \tag{5.23}$$

119

2GHz and Iono-Free Phase Center

When using the transformed, "iono-free" phase measurement, a geometric correction has to be applied to get to the respective beacon (and satellite antenna) phase center. This offset is computed as

$$\boldsymbol{r}_{iono-free} = \boldsymbol{r}_{2\,\text{GHz}} + \frac{\boldsymbol{r}_{2\,\text{GHz}} - \boldsymbol{r}_{400\,\text{MHz}}}{\gamma - 1} \tag{5.24}$$

where $\boldsymbol{r}_{2\,\text{GHz}}$ and $\boldsymbol{r}_{400\,\text{MHz}}$ are the eccentricities for the $2\,\text{GHz}$ and the $400\,\text{MHz}$ carriers respectively from the beacon antenna phase center (given at DORIS System Ground Segment Models, (Issue 1.3), Sec. 5.2.1).

Note that in Equation 5.24, the eccentricity vector $\boldsymbol{r}_{iono-free}$ is in a topocentric reference frame. Hence, to compute the ECEF coordinates of the iono-free phase center, given the (cartesian) ECEF coordinates of the beacon's Antenna Reference Point (ARP) $\boldsymbol{r}_{arp}$

$$\boldsymbol{r}^{ecef}_{iono-free} = \boldsymbol{r}_{arp} + \boldsymbol{R}^T \cdot \boldsymbol{r}_{iono-free} \tag{5.25}$$

where $\boldsymbol{R}$ is the cartesian-to-topocentric rotation matrix, computed at $\boldsymbol{r}_{arp}$.

In accordance to the beacons, a similar geometric reduction must be applied at the satellite's end, to correct for the discrepancy between the $2\,\text{GHz}$ and the "iono-free" phase center

$$\boldsymbol{r}^{satf}_{iono-free} = \boldsymbol{r}^{satf}_{2\,\text{GHz}} + \frac{\boldsymbol{r}^{satf}_{2\,\text{GHz}} - \boldsymbol{r}^{satf}_{400\,\text{MHz}}}{\gamma - 1} \tag{5.26}$$

where the superscript $satf$ denotes the *satellite-fixed* body/reference frame. On-board satellite antenna phase center offset values can be found in Cerri et al. 2022.

5.6.6 Tropospheric Correction

The GPT3/VMF3 (Landskron and Böhm 2018) model is used to handle tropospheric refraction. The hydrostatic zenith delay $zd_{hydrostatic}$, is computed via the "refined" *Saastamoinen* model (Davis et al. 1985 and Saastamoinen 1972). The corresponding value for the wet delay, zd_{wet} is estimated during the analysis, *per beacon and per pass*, using an initial value provided by Askne and Nordius 1987.

Using the mapping function and the zenith delay, the tropospheric delay for an observation at $t = t_i$ is given by

$$\delta_{TRO}[\text{m}] = zd_{hydrostatic} \cdot mf_{hydrostatic} + zd_{wet}|_{t=t_i} \cdot mf_{wet} \tag{5.27}$$

The tropospheric correction term in Equation 5.8b, is actually the "time-differenced" tropospheric delay between two measurements (the same ones used to derive the Doppler count), given in m/s. That is:

$$
\begin{aligned}
\Delta v_{TROPO}[\text{m/s}] &= \left(\delta_{TRO}|_{t=t_{i-1}} - \delta_{TRO}|_{t=t_i} \right) / \Delta\tau \\
&= \left(\left[zd_h \cdot mf_h + zd_w|_{t=t_{i-1}} \cdot mf_w \right] \Big|_{t=t_i} - \left[zd_h \cdot mf_h + zd_w|_{t=t_{i-1}} \cdot mf_w \right] \Big|_{t=t_{i-1}} \right) \Delta\tau
\end{aligned}
$$

(5.28)

Note that in the above equation the same value $zd_w|_{t=t_{i-1}}$ for the wet part of the zenith delay is used, that is the best estimate prior to incorporating the (new) measurement at $t = t_i$.

The parameter zd_w is estimated using no constraints and a simple white noise model (no process noise). Since it is an estimated parameter, the (partial) derivative of the observation equation w.r.t to this parameter, is required

$$
\frac{\partial v_{theo}}{\partial zd_w} = \frac{mf_w|_{t=t_i} - mf_w|_{t=t_{i-1}}}{\Delta\tau}
$$

(5.29)

5.7 Implementation

In the framework of the current Thesis, a software package was designed to analyze DORIS measurements for POD. The practical implementation of the observation equation model is already discussed in section 5.6. In this section, general issues of the algorithmic design are presented.

The first issue that arises when attempting to process DORIS data is the parsing of input files. The decision was made for the software to adhere to the new RINEX format (section 5.4), as suggested by the IDS. For the software created, the decision was made to stick to the new RINEX format (section 5.4), as suggested by the IDS. This decision provides for a wider range of analysis options (compared to the older data format), regarding both the data types available and the subsequent processing options and scheme (e.g. it is possible to parse and process pseudorange measurements). The drawback though, is the complexity of the RINEX format.

A dedicated module of the software package is thus designed to handle parsing of the RINEX files, in a generic way, so that users can extract the observables and meta-data needed for the processing scheme they decide on. Note that recent studies have shown that the phase measurements themselves can be used (instead of

Doppler counts) to effectively process data (see e.g. Mercier et al. 2010, Dettmering et al. 2014 and Zhou et al. 2020), although this method is not yet widely used.

Ground beacon geometry, including PCO and PCV (see section 5.3) information, is hard-coded in the software library. The implementation is based on a *type-safe*, *meta-programming* paradigm (Vandevoorde et al. 2017), so that users can request eccentricities and corrections for any DORIS frequency, including their linear combinations. This design pattern allows for efficiency, safety and versatility.

Site eccentricities are read from the respective *log* files, per beacon. IDS maintains updates log-files for each of the ground beacons included in the DORIS network (see https://ids-doris.org/doris-system/tracking-network/site-logs.html). To that end, a *Python* module has been created that can handle the acquisition, validation and parsing of relevant information off from the site-specific log file. Eccentricities can thus be extracted and sourced into the main processing module. This design was preferred (e.g. to harcoding eccentricity information), as it accommodates an easier adoption of site changes (e.g. instrumentation, of installation).

Once all of the above components are in place, the software can implement the observation model, as described in section 5.6. The processing algorithm applies observation-specific corrections to the extracted measurements, and keeps track (in chronological order) of the previous observations encountered. Thus, it can compute Doppler counts at every new epoch. All available observations can be taken into account, assuming they comply to a number of user-defined criteria:

Observation flags : every observation in a RINEX file is followed by a list of flags, denoting the instrumentation status (see Lourme et al. 2010). Users can define selection criteria based on these flags.

Minimum Elevation : measurements performed on low elevation angles include an increased error budget. Users can define an elevation cut-off angle, under which observations are removed for analysis.

Time Offset : to compute the Doppler count between two consecutive observations, a time distance criterion is set. If the measurements are performed within a time period larger that this interval, then the Doppler count is rest.

Running Statistics : while processing observations, the software computes "running" statistic values (e.g. average and standard deviation). Users can set

boundary values for accepting observations based on these statistics (e.g. a 3-σ statistical test).

The whole analysis can be performed in two "passes" of the RINEX file: the first is performed to model the receiver's proper frequency f_{r_T} (see subsection 5.6.4). In a second pass, the "core" part of the analysis is performed, including parameter estimation. Details on the latter are given in chapter 6.

Chapter 6

Orbit Determination Using DORIS

6.1 Introduction

With the introduction of the DORIS system and the observation model discussed in chapter 5, and using the developments presented earlier in the Thesis, a full orbit determination process can now be put together. The theoretical background and implementation details of the fundamental building blocks of the analysis (discussed above), include:

Astrodynamics and the effective modelling of the *perturbed* motion of an artificial earth orbiting satellite (see section 2.2)

Spatial and Temporal Reference Systems where the equations of motion can be described in, as well as the transformation mechanisms between their realizations (see section 2.3 and section 2.4)

Earth's Attitude , i.e. modelling the Earth's variable rotation and dynamics (see subsection 2.3.2)

Orbit integration for the efficient and precise extrapolation of the satellite's trajectory (see chapter 3),

Orbit estimation or *orbit improvement*, where data are processed in a robust fashion to produce estimates for the satellite's state vector or equivalently orbital elements (see chapter 4)

Data analysis where measurements obtained using the DORIS system are processed using the observation model described in chapter 5, to obtain precise relative velocity values between the emitter and the receiver

6.1.1 Goals of The Current Chapter

In this chapter a software tool to perform DORIS-data analysis is presented, using the models, methods and algorithms already discussed in the previous sections. The program is designed to tackle a "pure orbit determination" problem, or more specifically orbit improvement; that is, given an initial, reference state at some initial epoch, process DORIS observations (in an iterative manner) to compute the "best" estimate of the satellite state.

The problem is labelled "pure" in the sense that it does not consider improvements or estimates for other parameters, as e.g. site coordinates. However, a number of parameters must be included in the filtering process (e.g. drag and radiation coefficients, C_d and C_r respectively, relative frequency offsets for the beacons, $\Delta f_e / f_{e_N}$, and wet zenith tropospheric delay zd_{wet}). The theoretical implications and algorithmic design of the DORIS observation equation has already been discussed in section 5.6 and will be used here to analyze the DORIS measurements.

To test the validity of the estimates, the results are checked against CNES/SSALTO computed trajectories, given in sp3 files. The latter have been computed using a multi-technique approach, using both DORIS and GPS measurements. Differences in the force model and various processing options also exist between the two analysis procedures, that introduce further inconsistencies. However, these sp3 files were the only available in the Crustal Dynamics Data Information System (CDDIS) archive.

6.2 The Software

In the framework of the Thesis, a software package was designed and implemented, to perform orbit determination using the DORIS satellite system. The software was built from scratch, with minimum (external) dependencies. The purpose of the package is to act as the fundamental building block of a state-of-the-art scientific software toolset, utilizing DORIS observations for a wide range of geodetic studies,

including but not limited to POD, reference frame maintenance, earth dynamics and atmospheric studies. A first, imminent step towards this direction, would be for the software to reach IDS standards, a goal not too far-fetched, since the bulk of the work has already been done.

Writing scientific software to meet such high accuracy and efficiency standards is a challenging task. This is evident by the limited number of packages delivering such robust products. A deep understanding of the underlying scientific notions is a prerequisite (including e.g. celestial mechanics, spatial/Temporal reference frames, geodesy and estimation theory) coupled with software engineering skills to match the high volume and high calibre of work needed (about 100000 lines of source code were written for this Thesis, Table 6.1[1]).

Library	Language	Lines of Code	Comment
doris	C++	18286	Including source code for executables
	Python	2068	
iers2010	C++	50000	Python & Fortran mainly used for unit testing
	C	1801	
	Python & Fortran	17120	
sp3	C++	1287	
sinex	C++	1392	
datetime	C++	4432	Mostly header files
	C	136	
geodesy	C++	3755	
	Python	120	
Total		100397	

Table 6.1: Software components of the package designed and implemented for the Thesis.

6.2.1 Policy And Software Philosophy

The software is hosted and developed on the public domain, adopting a *free* and *open*-source policy. Any interested party is free to use and/or adapt the source code, fitting individual needs. It is a strong belief that adhering to such an open-development, open-access paradigm, can prove to be highly beneficial both for

---

[1]Lines of Code counted using `tokei` (https://github.com/XAMPPRocky/tokei) excluding blank and comment lines.
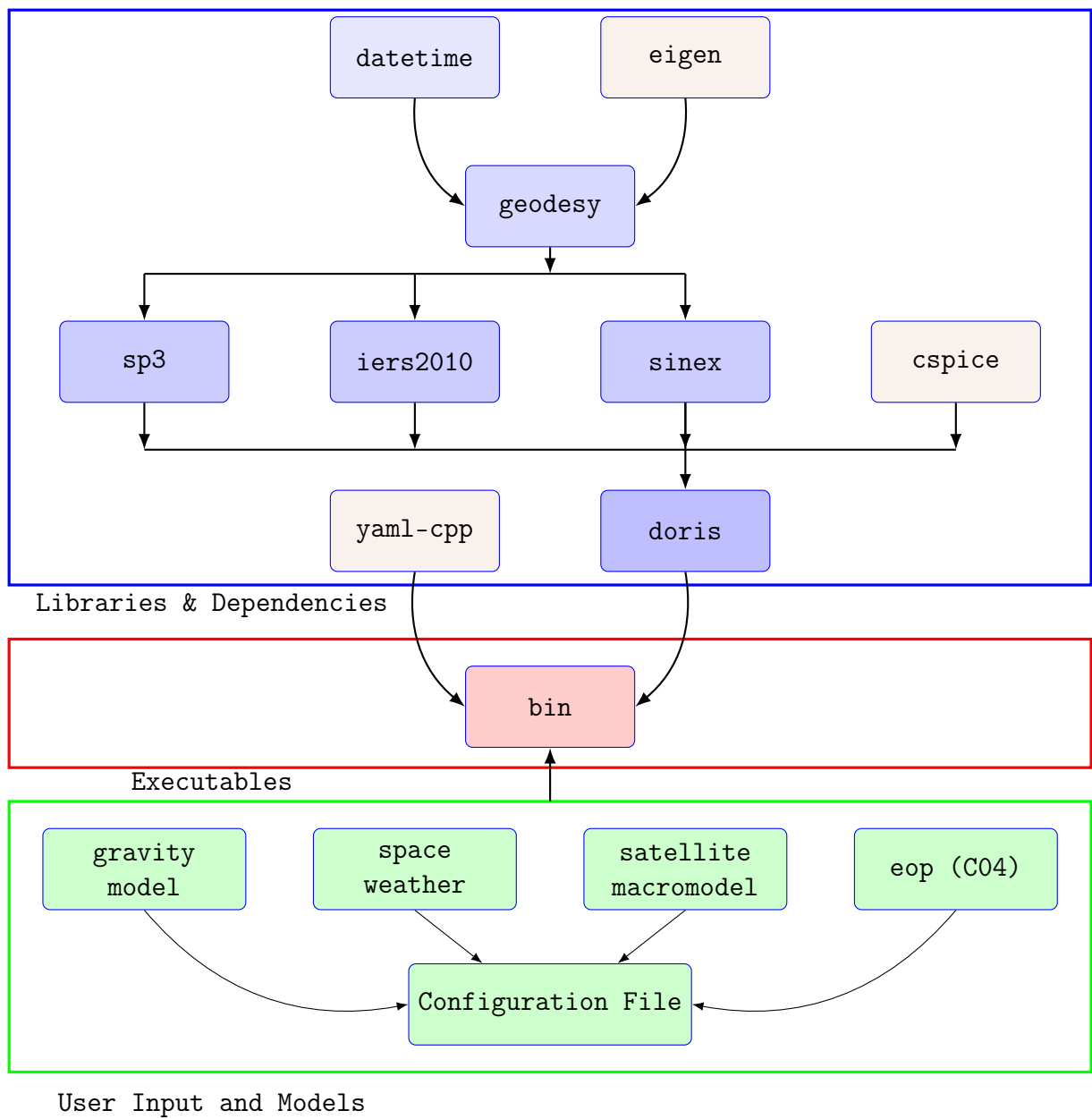
Figure 6.1: Overview of the software structure, dependencies and hierarchy.

the scientific community and for the development team. Already individual modules/libraries built for the Thesis have been "forked" from different users.

6.2.2 Architecture

The general architectural approach followed in designing the software is that of *modular software development*, emphasizing on building simple, compact, clear, modular, and extensible code that can be easily maintained and repurposed by developers other than its creators. This approach favors composability, an attribute greatly valued in scientific programming since it accommodates ease of adoption and expansion. Since the aim of the package is to act as a fundamental building block for an analysis tool matching the highest standards, this design pattern is crucial to its development and further success.

A mixture of the well established *object-oriented design* (OOP) and the newer approach of *data-oriented design* (Fabian 2018) (DOP) is used throughout the codebase. In coarse terms, the former favors code clarity and encapsulation while the latter promotes efficiency. Depending on the problem at hand, the constraints imposed and the abstraction level used, the technique better matching the challenge was chosen.

The language of choice for code development is `C++`, while minor parts are written in `C` and `Python` (see Table 6.1). `C++` is a language supporting OOP, renowned for its speed and efficiency. Via its versatility (especially in handling memory resources) and closeness to the hardware, this programming language is fit for problems posing constraints on computational resources and speed (such as a POD analysis procedure). The source code employs *generic programming* techniques and makes heavy usage of the emerging technique of *template metaprogramming* (Estérie et al. 2014, Gawlik et al. 2018), to get the highest possible performance gains.

The source code is split into different modules/libraries, where each collection serves a well established, individual goal (see Table 6.2). This division favors the overall modularity of the package. Note that the individual repositories can be found online by adding the name at the static path https://github.com/xanthospap/

128

Library	Purpose	Repository Name
libdatetime	A library to handle datetime instances. Includes data structures, operators and transformations between different scales, systems and representations. Facilitates the parsing, formatting and writing of instances in different formats.	datetime
libgeodesy	A library implementing fundamental geodetic concepts and computations. Includes handling of reference systems, reference ellipsoids, and associated geometric operations, as well as transformations between systems and frames.	geodesy
libsp3	Faciliatate the parsing and data extraction and manipulation (e.g. indexing and iterating) of sp3 data files (Hilla 2010).	sp3
libiers2010	Implementation of the IERS-2010 standards, based on Petit and Luzum 2010. Additional material is added (where needed) to handle the convention's updates. To-date model updates are also included, as well as source code to handle data resources in various formats, often encountered when implementing the standards.	iers2010
libsinex	Facilitate the parsing and data extraction and manipulation of SINEX files ("Solution (Software/technique) INdependent EXchange Format Version 2.02" 2006) including additional blocks used by the IDS, see Moreaux 2023. Utilities include reference frame realization, reductions between site and reference points (via eccentricity vectors) and inspection of time interval validity.	sinex
libdoris	A library focused on the DORIS satellite system; includes relevant data handling, implementation of the observation equation model (chapter 5) and its application in POD. Facilitates data retrieval from a wide range of different formats, for various steps of a DORIS data analysis scheme.	libdoris

Table 6.2: Individual libraries (modules) of the package designed and implemented for the Thesis.

6.2.3 External Dependencies

An effort was made while developing the source code, to strive for minimal external dependencies. As a consequence, only three external components are used to build the whole package, namely,

The `SPICE` Toolkit (Acton et al. 2018), release January 3, 2022. This is National Aeronautics and Space Administration (NASA)'s *Observation Geometry System for Space Science Missions*, developed by the Navigation and Ancillary Information Facility (NAIF). This is a multi-purpose toolkit, with a wide range of functionalities, available via a list of dedicated APIs. For the software implemented for this Thesis, `SPICE` is only used to retrieve planetary and lunar ephemeris records. More information on the toolkit are provided in https://naif.jpl.nasa.gov/naif/index.html.

The `eigen` Library (Guennebaud and Jacob 2010), release 3.4. This is an open-source `C++` library for linear algebra, matrix and vector operations, geometrical transformations, numerical solvers and related algorithms. The main use of `eigen` within the implemented software, is to perform matrix/vector operations. More information on the library can be found at http://eigen.tuxfamily.org/.

The `yaml-cpp` Library , developed by Jesse Beder. This is an open-source library, hosted at https://github.com/jbeder/yaml-cpp, that enables efficient parsing of `YAML` (https://yaml.org/) files. This library is only used by the executables (i.e. not needed for any of the libraries) to parse the configuration file(s).

6.3 The COST-G Benchmark Test

The International Combination Service for Time-variable Gravity Fields (COST-G)[2] is a product center of the International Gravity Field Service (IGFS) and is dedicated to the combination of monthly global gravity field models. In the framework of COST-G, gravity field solutions from different analysis centres are combined to provide a consolidated solution of improved quality and robustness to users. To achieve its goal, the individual products must be of utmost accuracy, using state-of-the-art models.

---

[2]https://cost-g.org/

In order to assess the consistency level of the implemented, underlying models from the contributing analysis centers, a benchmark test was devised. A comprehensive dataset containing commonly used forces in orbit and gravity field modeling, such as Earth's gravity field and tides, was compiled and evaluated over a one-day orbit arc of GRACE. Supplementary data were also included to facilitate straightforward comparisons. This benchmark test is intended to be used as a reference data set and provide the opportunity to test the implementation of these models at various institutions involved in orbit and gravity field determination from satellite tracking data. The benchmark test is described in Lasser et al. 2020.

This benchmark test is used throughout this document, to evaluate the implementation of various models and forces used both here and in the analysis performed to derive COST-G products by a series of high quality scientific software packages. Validation of results aimed to comply with the highest standards is hard to achieve, and such tests can provide crucial feedback and help identify and mitigate error and bug that would otherwise pass unnoticed.

6.4 The Jason-3 Satellite Mission

JASON-3 is an international cooperative mission between National Oceanic and Atmospheric Administration (NOAA) CNES, European Organisation for the Exploitation of Meteorological Satellites (EUMETSAT), and NASA. The objective of the mission is to provide a continuation of the TOPEX/Poseidon, JASON-1 and JASON-2 missions and their collection of high accuracy radar altimetry measurements for global ocean circulation and sea surface studies, without any data gaps (Couderc and Zaouche 2015). JASON-3 follows a near-circular and frozen orbit that follows an exact repeating ground track every 127 revolutions in a little less that ten days (see Table 6.3).

Mass and Center of Gravity: Initial values of mass and center of gravity coordinates in satellite reference frame are given in Table 6.4. Actual values of the satellite mass and center of gravity coordinates are obtained by adding the offsets published by the IDS at the dedicated *mass & Center of gravity history* file[3]. Direction of the body-fixed reference frame axis are shown in Figure 6.2 for JASON-1; JASON-3 follows a very similar design (same PROTEUS platform).

---

[3]Available at ftp://ftp.ids-doris.org/pub/ids/satellites/ja3mass.txt

Parameter	Value
Semi-major axis (α)	$7\,714\,431$ m
Eccentricity (e)	9.5×10^{-5}
Inclination (i)	$66.038\,309°$
Argument of periapsis	$90°$
Reference equatorial altitude	1336 km
Cycle duration	$9.915\,64$ d
Number of revolution in a cycle	127 orbits

Table 6.3: Characteristics of JASON-3 orbit, Couderc and Zaouche 2015

Mass	X	Y	Z
kg		m	
509.6	1.0023	0.0000	-0.0021

Table 6.4: Mass and Center of Gravity coordinates in the SV-fixed reference frame for JASON-3, Cerri et al. 2022

DORIS Receiver Phase Center: The position of the 2 GHz and 400 MHz receiver phase centers in the spacecraft-fixed reference frame, are given in Table 6.5.

Frequency	X	Y	Z
		m	
2 GHz	2.4128	-0.1325	0.9235
400 MHz	2.4128	-0.1325	0.7555

Table 6.5: DORIS receiver phase center coordinates in the body-fixed reference frame for JASON-3, Cerri et al. 2022

JASON-3 MacroModel: Macromodel parameters to be used for computing the solar radiation effect (see section 2.2.3) are published by the IDS (Cerri et al. 2022). Details of the macromodel are shown in Table 6.6.

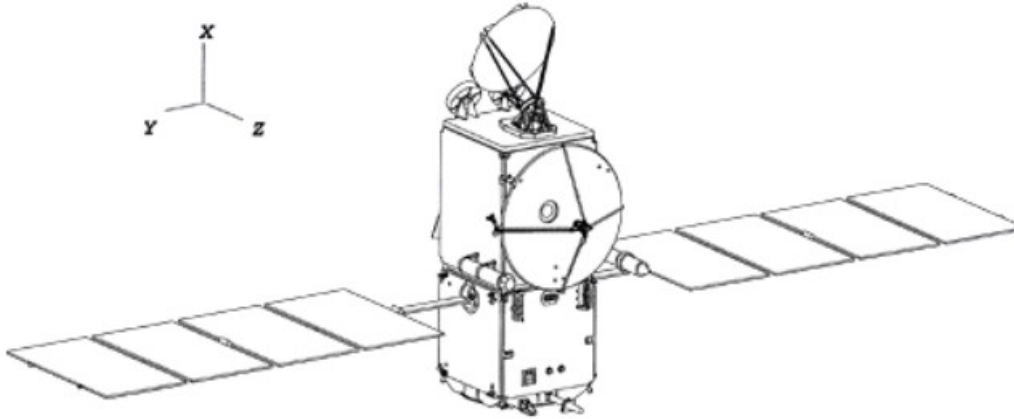Figure 6.2: Image of JASON-1 satellite including the body frame, Cerri et al. 2022.

Surface m^2	Normal in body RF			Optical Properties			Infrared Properties		
	X	**Y**	**Z**	**spec**	**diff**	**abs**	**spec**	**diff**	**abs**
0.783	-1	0	0	0.3410	0.6460	0.0130	0.0000	0.9870	0.0130
0.783	1	0	0	0.1490	0.8510	0.0000	0.0000	1.0000	0.0000
2.040	0	-1	0	0.5730	0.3840	0.0430	0.1040	0.5690	0.3280
2.040	0	1	0	0.5390	0.4240	0.0370	0.0890	0.6270	0.2830
3.105	0	0	-1	0.2460	0.7520	0.0020	0.0050	0.9770	0.0170
3.105	0	0	1	0.2130	0.4530	0.3340	0.0370	0.2870	0.6760
			Solar Array						
9.800	1	0	0	0.0600	0.4070	0.5330	0.0970	0.0980	0.8030
9.800	-1	0	0	0.0040	0.2980	0.6970	0.0350	0.0350	0.9310

Table 6.6: Satellite Macromodel for JASON-3, Cerri et al. 2022.

6.4.1 JASON-3 Attitude

The spacecraft's attitude is needed for various steps in the POD processing pipeline (including e.g. the computation of atmospheric drag (see section 2.2.3) and solar radiation pressure (see section 2.2.3)). Satellite attitude refers to the orientation of the satellite body system in a reference frame, specifically, the coordinate transformation matrix between the latter frame and an Earth-fixed or inertial system. The IDS strongly recommends the use of *measure attitude* if available (International DORIS Service 2020).

To describe the orientation of a satellite in space, a *body-fixed* reference frame

133

$\mathcal{R}_{BF}$ needs to be defined (see Figure 6.3). This frame is permanently tied to the mechanical structure of the satellite and enables the specification of antenna and coordinates relative to the Center of Gravity. The body-fixed frame is likewise required to describe the position and alignment of individual surface elements (Montenbruck et al. 2015). For the JASON-3 satellite, the origin of the body reference system is the center of the launcher interface ring. The $X-$axis points along the satellite's main direction towards the radiometer antenna and the axis $Z-$axis is oriented towards the Earth (nadir pointing). $Y-$axis is parallel to the rotation axis of the solar panels, positively towards the right solar panel (Zeitlhöfler 2019).

The transformation between the body-fixed reference frame and the GCRF is given by the equation:

$$\boldsymbol{r}_{BF} = \mathcal{R}\boldsymbol{r}_{GCRS} \tag{6.1}$$

The transformation denoted here by $\mathcal{R}$ can be represented in different forms (e.g. *Euler Axis/Angle*), one of which is the *quaternion representation*. This way of transforming between the body-fixed and the GCRF frames is adopted and implemented in the software designed for the current Thesis. The quaternion representation expresses the attitude matrix as a homogeneous quadratic function of the elements of the quaternion, requiring no trigonometric or other transcendental function evaluations. Quaternions are more efficient for specifying rotations than the attitude matrix itself, having only four components (instead of nine) and obeying only one constraint, namely that their norm is equal to unity (Markley and Crassidis 2019). Discussions on the use of quaternions for attitude determination and underlying algebraic concepts can be found in Yang 2012 and Markley and Crassidis 2019.

In the case of JASON-3, measured attitude is published by CNES in dedicated data files (Ferrage 2020) by means of quaternions, covering a period of 28 hours (2 overlapping hours between two consecutive files). Data records are retrieved from these files to relate the body-fixed reference frame to the GCRF. Since quaternions are provided in distinct epochs, an interpolation algorithm must be used to estimate the quaternions at the epoch of request. In this Thesis, the *spherical linear interpolation* method (often called *Slerp* in computer graphics) introduced by Shoemake 1985 is used. According to Dam et al. 2000, Slerp is the optimal interpolation curve between two rotations.

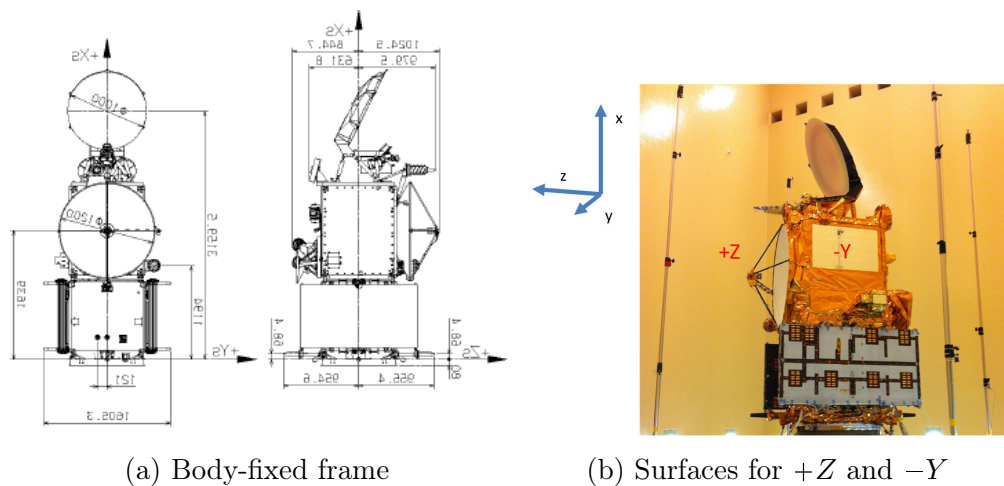Respective solar panel files are also distributed by CNES, containing the angular positions of the solar arrays.

(a) Body-fixed frame

(b) Surfaces for $+Z$ and $-Y$

Figure 6.3: JASON-3 images depicting the satellite and the embeded, body-fixed reference frame, Couderc and Zaouche 2015

6.5 The South Atlantic Anomaly (SAA)

The *Van Allen* radiation belts are toroidal zones around the Earth where high energy particles coming mostly from the solar wind are trapped. Because the inner belt is not symmetrically centered on the Earth, it comes closer to the Earth surface in a region located above South America (Jalabert and Mercier 2018). The SAA is a region of reduced magnetic intensity, where the inner Van Allen radiation belt makes its closest approach to the Earth's surface. This region is centered in southeast South America (see Figure 6.4). Because of the weakened magnetic field, inner radiation belt particles can mirror at lower altitudes increasing the local particle flux. It is thus the region where the inner radiation belt makes its closest approach to the Earth's surface (Anderson et al. 2018). Satellites in low-Earth orbit pass though the SAA periodically, thus being exposed to several minutes of strong radiation each time, creating problems for scientific instruments on-board satellites.

DORIS measurement processing assumes a stable oscillator frequency over the duration of each pass. It also assumes a smooth (i.e. low degree polynomial) evolution of the instrument frequency for both the receiver and the transmitter. The oscillator in the on-board DORIS instrument is an USO which is designed to meet these stability requirements (Jalabert and Mercier 2018). The high radiation level dominating SAA impacts the behavior of on-board oscillators: a rapid change in the frequency can be observed when the satellites fly across this area. This effect
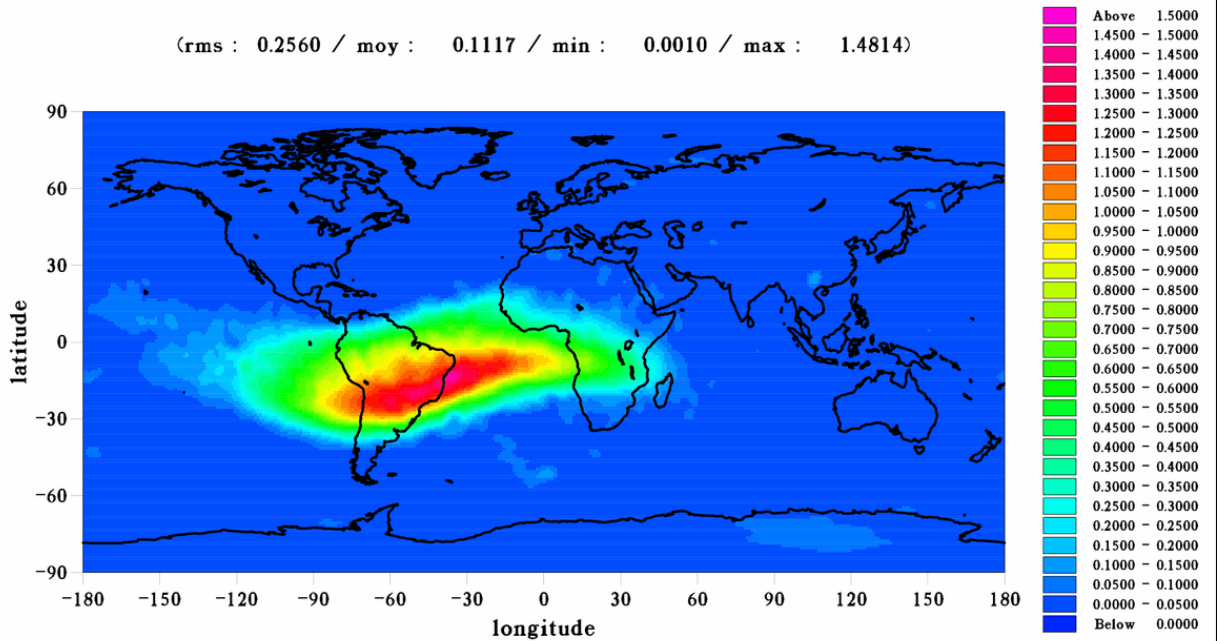
Figure 6.4: JASON-1 exposure to SAA effects, measured on 200-2004 period using the DORIS ultra-stable oscillator. (Credits CNES/CLS, source Aviso https://www.aviso.altimetry.fr/en/news/image-of-the-month/2007/oct-2007-south-atlantic-anomaly-as-seen-by-doris.html)

causes precision degradation in POD and positioning results.

SAA effects on satellites carying DORIS payload have been identified for JA-SON-1 Willis et al. 2003, JASON-2 Willis et al. 2016a, SPOT-5 Štěpánek et al. 2013 and Sentinel-3A Jalabert and Mercier 2018. Capdeville et al. 2016a, show that the JASON-3 satellite is also affected by SAA, evident both in POD and station positioning results. Although corrective models exist for some cases (e.g. for JASON-1 Lemoine and Capdeville 2006 and Capdeville et al. 2016b for SPOT-5), no such model exists in the case of JASON-3. Other possibilities for mitigating the impact include the improved model of the USO frequency to correct the data and the attenuation of the side-effects of the changes in the USO by downweighting or eliminating measurements from beacons placed within the region covered SAA. In this Thesis, the latter method is used.

6.6 Software Tests And Orbit Determination

Using the software designed and implemented in the framework of this Thesis, a fundamental orbit determination processing pipeline was setup, to analyze JASON-3 DORIS measurements. The different, individual parts put together to achieve this task have already been discussed in the previous chapters, including both theoretical implications and implementation details. Table 6.7 lists the models and parameters used for the test suite.

Tacking advantage of the modular design of the software package, made up of different libraries, it is trivial to implement a program targeting a *pure* orbit determination problem using DORIS observables, fitting specific user needs.

JASON-3 was chosen to act as the test bed since it is an on-going, modern satellite mission, extensively documented, and its attitude determination can be performed via quaternions (see subsection 6.4.1). A drawback however, is its USO susceptibility to SAA-induced effects (see section 6.5).

Description	Model Used	Model Parameters
Gravity Model	CNES/GRGS RL04 TVG (Lemoine et al. 2019)	up to 120th degree and order
Third Body	Sun and Moon	Ephemeris DE421 (Folkner et al. 2009)
Solid Earth Tides	IERS2010 (Petit and Luzum 2010)	step-1 and step-2 corrections
Ocean Tide	FES2014 (Lyard et al. 2021)	Only major components included
Atmospheric Drag	According to section 2.2.3, using the NRLMSISE-00 (Picone et al. 2002) model	Flux data from CelesTrack (Vallado and Kelso 2013)
Solar Radiation Pressure	According to section 2.2.3 using the macro-model provided by Cerri et al. 2022	Occultation due to Earth modelled using the conical model (R. Zhang et al. 2019)
Site Positions (Terrestrial RF)	DPOD2020 (Moreaux 2023) realized by the IDS Combination Center	version dpod2020_01; beacon positions and meta-data extracted from SINEX
Celestial/Inertial RF	GCRF (Petit and Luzum 2010 and subsection 2.3.3)	IAU 2000/2006 resolutions, using the CIO-based transformation with full series for the polar motion (IAU 2006 precession and IAU 2000A nutation)
Earth Orientation Parameters	IERS 2020 C04 products (see [4])	interpolated as described in subsection 2.3.4
Orbit Integration	Adams-Bashforth-Moulton, variable step variable order integrator (chapter 3)	Integration performed in TAI; equations of motions solved for including the system of variational equations (section 4.5)
Filtering	Extended Kalman Filter algorithm (section 4.4), no process noise	Parameter set includes: satellite state, atmospheric drag coefficient (1/revolution), solar radiation pressure coefficient (1/revolution), beacon frequency offest (per pass) as bias, per-beacon hydrostatic zenith path delay (per pass)
Troposphere Modelling	GPT3/VMF3 (Landskron and Böhm 2018), see subsection 5.6.6	wet zenith path delay estimated per beacon, per pass

Table 6.7: Processing options used for JASON-3 orbit determination.

```
---
data:
  doris-rinex: data/Jason-3/ja3rx22248.001
  sp3: data/Jason-3/ssaja320.b22238.e22258.DG_.sp3.001
reference-frame:
  station-coordinates: data/dpod2020_01.snx
eop-info:
  eop-file: data/eopc0420.1962-now
gravity:
  model: data/gfc/EIGEN-GRGS.RL04.MEAN-FIELD.gfc2
  degree: 120
  order: 120
troposphere:
  vmf3:
    grid: data/2022248.v3gr_d
force-model:
  atmospheric-drag:
    density-model: nrlmsise00
    atmo-data-csv: data/SW-All.csv
    Cd-apriori: 2e0
  srp:
    Cr-apriori: 1.5e0
...
```

Table 6.8: Configuration file example.

The large number of data and product files to be processed, along with the complexity of the models, corresponding input parameters and user options needed to properly determine the analysis procedure, poses a challenging task. An efficient but on the same time user-friendly way of setting such input parameters must be devised. The solution adopted for the software package described here, is to archive such parameters in *configuration files* using the YAML (https://yaml.org/) format and "feed" them to the program to drive the analysis scheme. YAML is a data serialization language with the important advantage of being human-friendly. An example of such a file is depicted in Table 6.6.

Results of orbit determination are depicted in Figure 6.5, where the state is given in the dpod2020_01 (Moreaux 2023) ECEF reference frame. This frame is suggested by the IDS for POD applications.

The total number of observations per beacon are depicted in Figure 6.6. It is worth noting that:

- observations to beacons ARFB (AREQUIPA, located at Peru) and CADB (CA-CHOEIRA PAULISTA, located at Brazil) were not used, since the corre-

sponding measurements were found to be largely affected by SAA (see section 6.5), giving large residual values

- observations to beacon HOFC (HOFN, installed in Iceland) were not used; this site was installed in September 2020, and no available data based on operational Numerical Weather Model (NWM) were found at the VMF Data Server (VM-Data-Server 2020)
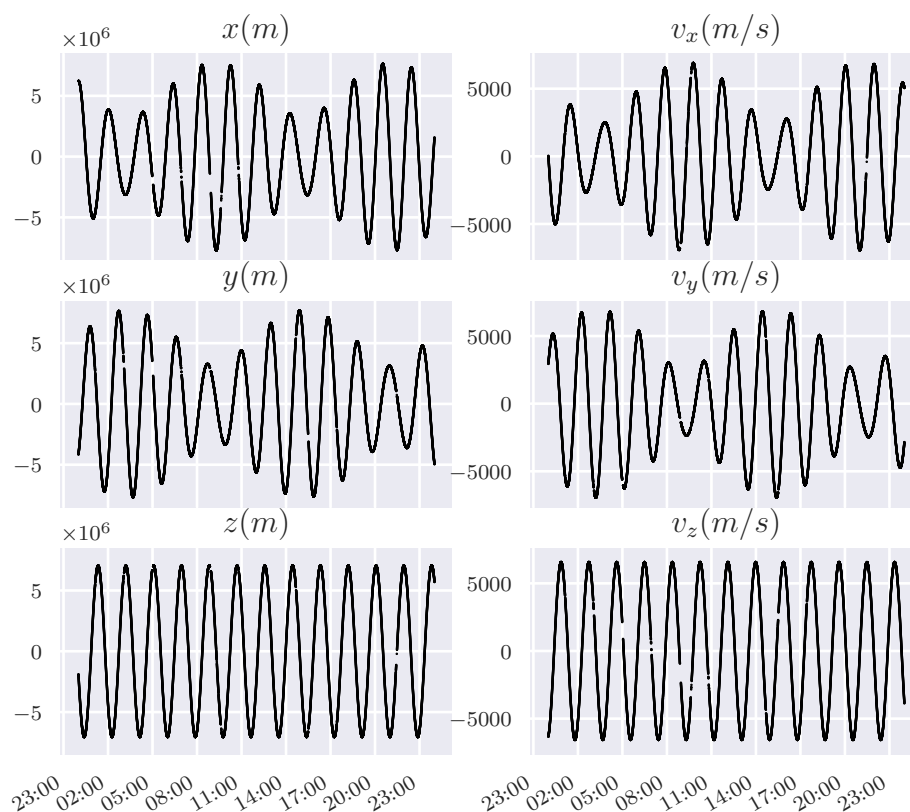

Figure 6.5: Satellite state (in ECEF RF) estimated for one day of JASON-3 orbit

Figure 6.7 depicts the computed acceleration components for the force model considered. Atmospheric drag forces are not included since they are well beyond the targeted precision. For the altitude of JASON-3, solar radiation pressure is several orders of magnitude larger than atmospheric drag, a fact usually inverted for LEO satellites of lower altitude. Identification of dominant accelerations and thereby forces, is crucial for further enhancements of the software since it enables prioritization of further development.

140
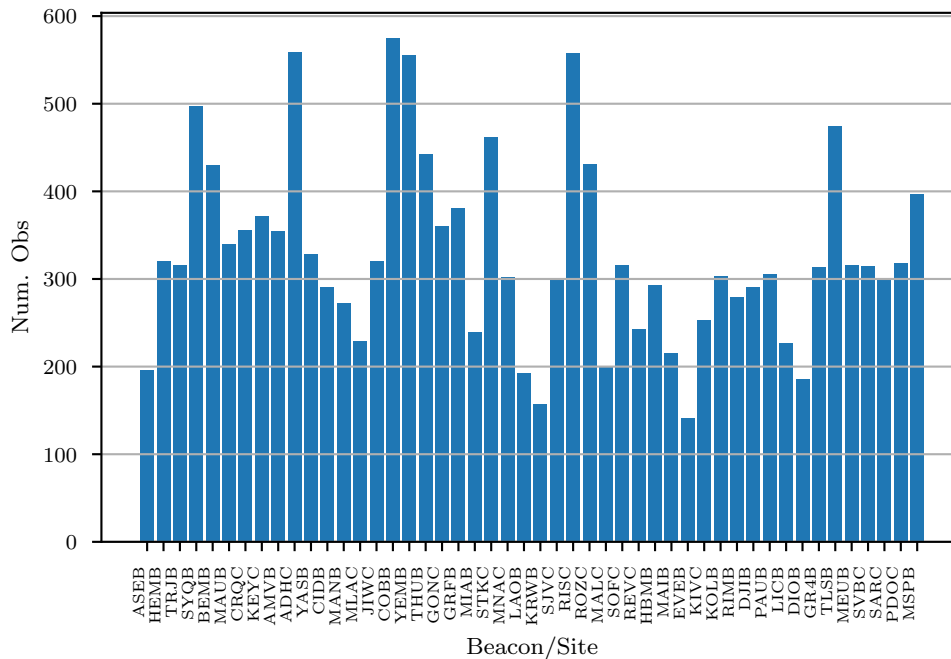
Figure 6.6: Number of measurements performed by the on-board JASON-3 DORIS receiver per ground beacon.

To validate and check the results obtained for the satellite state estimates, JASON-3 sp3 files were retrieved from CDDIS (Noll 2010), recording state (in cartesian components) for the day of interest, with a sampling rate of 1 s. These solutions are computed by CNES's new-generation ground segment called SSALTO[5] and are produced using DORIS and GPS observations. Documentation for the data analysis procedure and the models used therein, is available at `ftp://ftp.ids-doris.org/pub/ids/data/POD_configuration_POEF.pdf`. Note that according to the POD specifications used by SSALTO, a large number of models and options are different from the ones used in the test-suite program listed in Table 6.7. These sp3 files record satellite state of the spacecraft's center of gravity, in ITRF.

Despite the fact that inclusion of GPS data may introduce inconsistencies when compared to a DORIS-only solution, the high sampling rate of these product files makes extrapolation of reference trajectories trivial and only introduces small errors (see subsection 3.4.5). The procedure for computing reference solutions (state estimates) included the following steps:

---

[5]https://www.aviso.altimetry.fr/en/newsletter07/ssalto-a-new-ground-segment-for-a-new-generation-of-altimetry-satellites.html
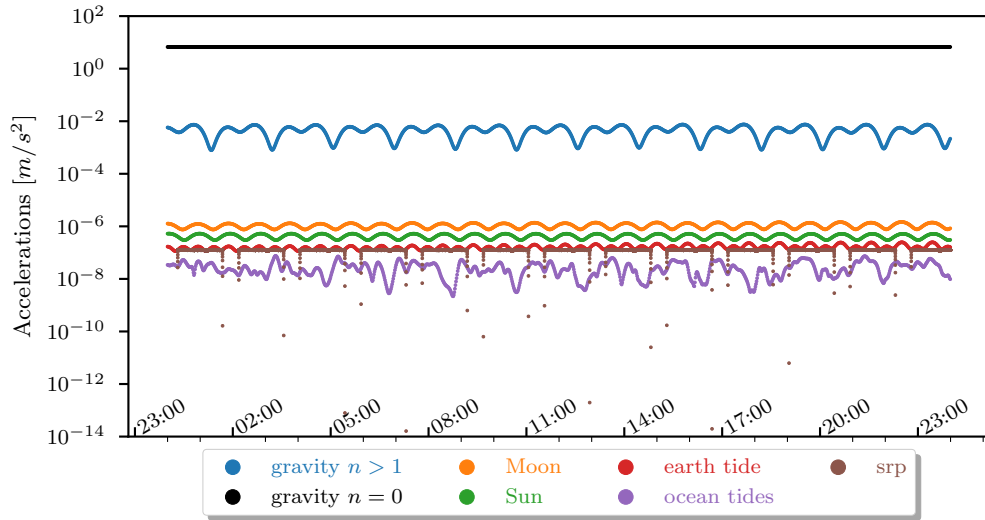
Figure 6.7: Computed accelerations for one day of JASON-3 orbit; $y-$axis in logarithmic scale.

1. get (next) epoch t for which the test-suite has produced a state estimate

2. find the record in the reference sp3 file closest to t, t_0

3. extrapolate the state from t_0 to t; go to item 1 and repeat until a reference state is computed for all t

Results of the comparison are depicted in Figure 6.8 using an ECEF reference frame, and in Figure 6.9 using the celestial GCRF frame. For the latter case, the retrieved sp3 state records were first transformed to the GCRF frame, and then compared to the estimated state.

A description of the differences in the ECEF frame is recorded in Table 6.9. For the position estimates, it is evident that the x and y components are in better agreement with the reference results, with max discrepancies in the order of 2 m (in absolute value). For the z component, max difference reaches a value of 3.5 m (in absolute value). All three component differences seem to be dominated by periodic signal(s), while for the z component case, a trend is also evident, correlating the "worsening" of results with time.

Velocity differences range between -2.2 to 2.3 mm/ sec and, as is the case for position estimates, are worse in the z component direction (see Table 6.9).

Transforming the state estimates and respective reference results to the GCRF
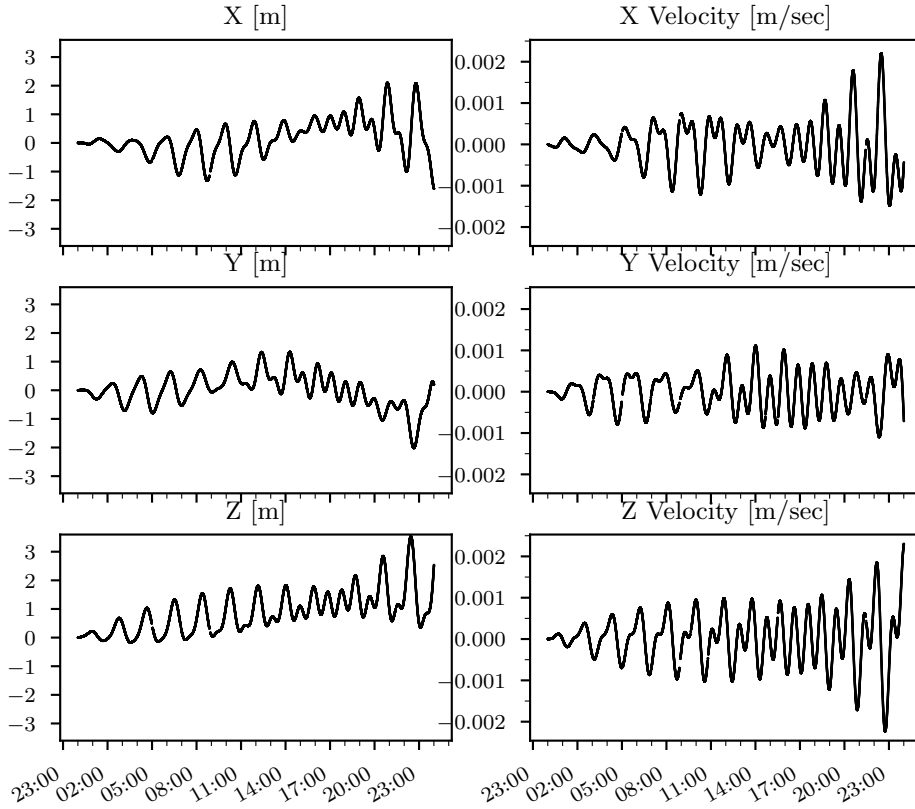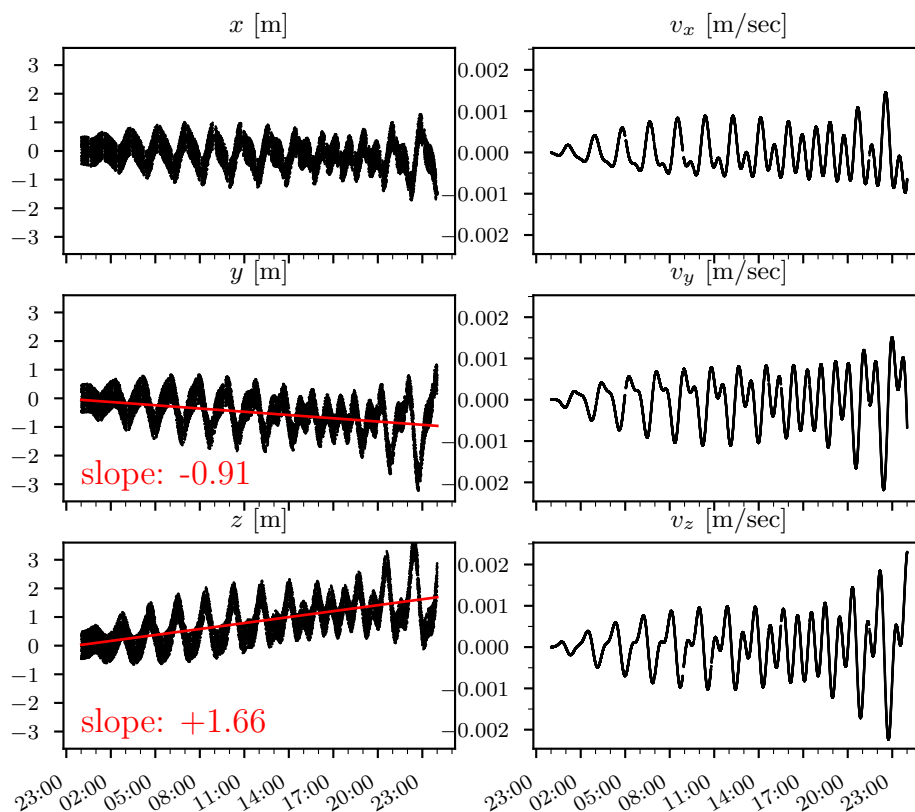
Figure 6.8: Discrepancies of estimated state against the orbits estimated at CNES/AALTO for one day of JASON-3 orbit (in ECEF RF).

Component	Mean	Std. deviation	Max Value	Min Value	Units
x	+0.17	± 0.64	2.09	-1.59	m
y	+0.00	± 0.57	1.33	-2.01	m
z	+0.86	± 0.72	3.52	-0.17	m
v_x	-0.03	± 0.58	2.19	-1.48	mm/s
v_y	+0.01	± 0.44	1.11	-1.09	mm/s
v_z	+0.03	± 0.65	2.29	-2.22	mm/s

Table 6.9: Details of discrepancies between estimated state against the orbits estimated at CNES/AALTO for one day of JASON-3 orbit, depicted in Figure 6.8.

reference frame, absolute values of differences remain the same, though a trend in the y and z directions is more evident, with values of $-0.91\,\mathrm{m/d}$ and $1.66\,\mathrm{m/d}$ respectively. A degradation of velocity estimates with time is also clear in this case (see Figure 6.9).

143

The evident degradation of results over time is a clear indicator of unmodeled effects in the force model applied (e.g. polar tides). This causes the solution of the equations of motion, coupled with the variational equation system, to depart from the "true" state. In turn, this deviation in the results is re-injected into the system of differential equations by means of initial conditions, hence ultimately causing an accumulation of errors. Even though the filtering process adjusts the state according to observation data, this adjustment is not large enough to alleviate shortcomings of the force model.

Figure 6.9: Discrepancies of estimated state against the orbits estimated at CNES/AALTO for one day of JASON-3 orbit (in GCRF).

Since both the GCRF and ECEF state differences seem to include harmonic signals, an analysis of the underlying dominant frequencies was performed to identify the spectral densities of the signal. For this purpose, the *Lomb–Scargle periodogram* (Scargle 1982) was used; this method enables the efficient computation of periodograms for unevenly spaced samples. Since the state differences cover a time span of one day with a sampling rate of $\approx 1\,\text{sec}$, the spectral range was chosen to span the periods 0.1 to 6 h, avoiding aliasing effects (see e.g. VanderPlas

2018). Results are depicted in Figure 6.10 for differences computed in the ECEF reference frame and Figure 6.11 for the GCRF reference frame respectively.
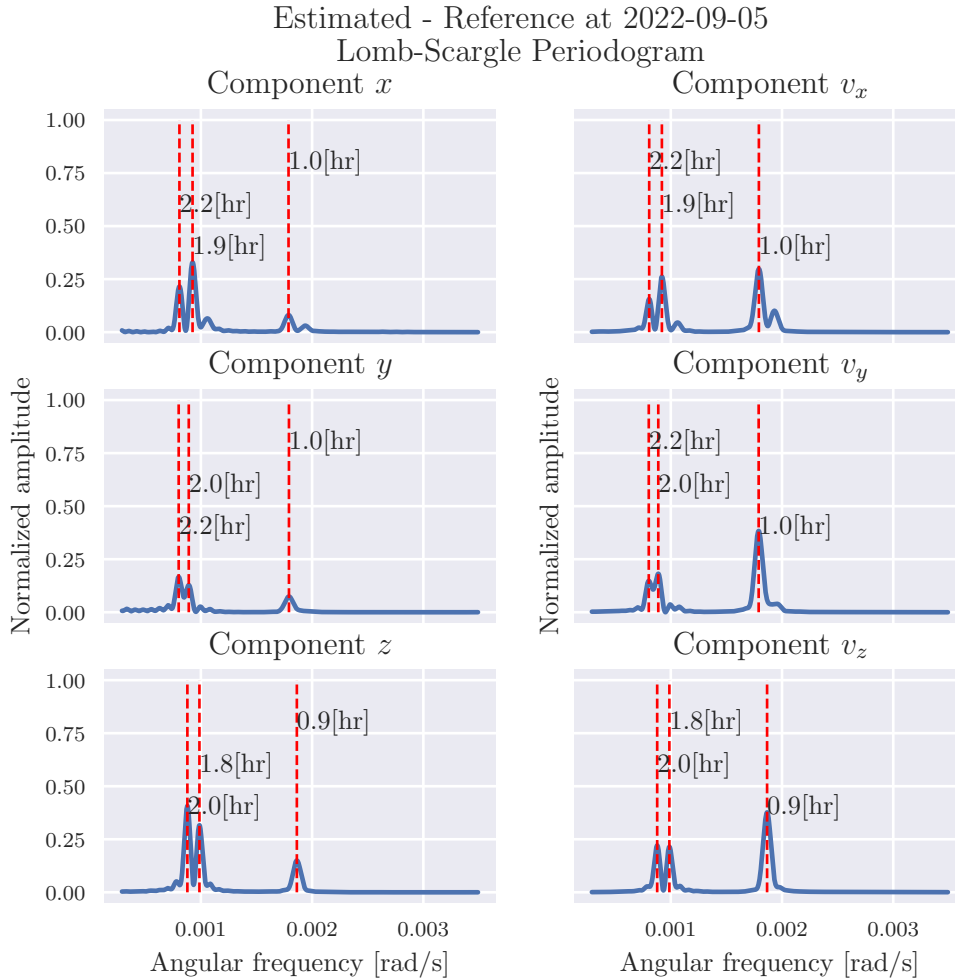

Figure 6.10: Lomb-Scargle periodogram for the differences between estimated and reference results for satellite state in ECEF.

The estimated periodograms show a clear prevalence of two harmonics with periods of $\approx 1\,\mathrm{h}$ and $\approx 2\,\mathrm{h}$. Position estimates are dominated by the second frequency, while velocity estimates by the first. Note that JASON-3 completes a revolution around the Earth in 112.4 min or $\approx 1.9\,\mathrm{h}$. This frequency coincides with the findings of the periodogram for the case of position estimates. The existence of such periodic signals is often attributed to mismodeled radiation forces (e.g. Xia et al. 2022). Given the fact that the force model used does not take into consideration albedo effects and satellite emitted thermal radiation, mismodeled

radiation forces could explain the observed behavior. Apart from modeling enhancements, empirical, once-per-revolution acceleration components can be used to mitigate such effects.

To gain a clearer view on the satellite position differences, discrepancies are often transformed to an "orbital frame", defined by the radial and velocity vectors. The $x-$axis of this frame is the *radial* axis, directed from the unit vector of satellite position. The $y-$axis, labelled *in-track* axis, is in the direction of motion, while the $z-$axis called *cross-track* is directed from the unit vector of normal orbit (Kim et al. 2019). Position differences between estimates and reference results are depicted in Figure 6.12, transformed to the radial, across-track and in-track frame. The in-track component is very smooth, and in good agreement with the reference solution; the maximum difference in this case is $\approx 0.17\,\mathrm{m}$. The radial component is dominated by a periodic harmonic of $\approx 2\,\mathrm{h}$, with a growing amplitude. Max discrepancies in this case are $\approx 1.5\,\mathrm{m}$, at the end of the day. The cross-track component presents the largest fluctuations, and apart from the identified harmonic of $\approx 2\,\mathrm{h}$ seems to follow a parabolic pattern. Details are given in Table 6.10.

Component	Mean	Std. deviation	Max Value	Min Value	Units
radial	-0.03	$\pm\ 0.57$	1.26	-1.46	m
in track	+0.00	$\pm\ 0.06$	0.17	-0.15	m
cross track	-0.19	$\pm\ 1.29$	3.99	-2.11	m

Table 6.10: Details of discrepancies between estimated state against the orbits estimated at CNES/AALTO for one day of JASON-3 orbit, depicted in Figure 6.12.

Figure 6.13 depicts the residuals of the analysis, i.e. the *Observed - Computed* values. Residuals are higher at the beginning of the analysis interval, but quickly converge to smaller values. This effect is due to the unknown a-priori values mainly of the beacon relative frequency offsets (see subsection 5.5.2).

A more enlightening view of the residuals can be obtained in Figure 6.14 and Figure 6.15, where the large starting values are filtered out. The first plot depicts the computed residuals with respect to time, while the latter with respect to elevation angle.

From Figure 6.15 it can be seen that observations at elevation angles that approach the cut-off angle of 10°, have larger residual values, a fact to be expected. There also seems to be a systematic offset of $\approx 8\,\mathrm{mm/s}$ between the computed and the observed values. To check whether this offset has to do with a specific

(ground) antenna type, residual values with respect to antenna type are depicted in Figure 6.16. For the epoch under study, DORIS beacons were equipped with two different antennae, namely STAREC-B and STAREC-C, which share geometric characteristics (see section 5.3). No evident dependence of residual values on antenna type though could be found. Hence, the systematic offset can be attributed to either

- mismodeling of the geometric characteristics of ground antennae (e.g. antenna reference point(s), PCO)

- mismodeling or non-mitigated errors in the observation equation model

Apart from satellite state and beacon-specific parameters, the orbit determination process involves estimation of a number of *dynamic* orbit parameters. For the setup used here, these are the solar radiation pressure coefficient, C_r and the atmospheric drag coefficient C_d. Estimated values for these parameters are depicted in Figure 6.17. While solar radiation pressure coefficient, C_r is stable throughout the time interval analyzed, the atmospheric drag coefficient shows larger discrepancies. This can be attributed to

- an erroneous a-priori value, and

- an "absorption" of mismodeled or remaining errors of the analysis

Since the C_r term is estimated once per revolution, while C_d is estimated for the whole time interval, it is easier for the first to "absorb" remaining errors.
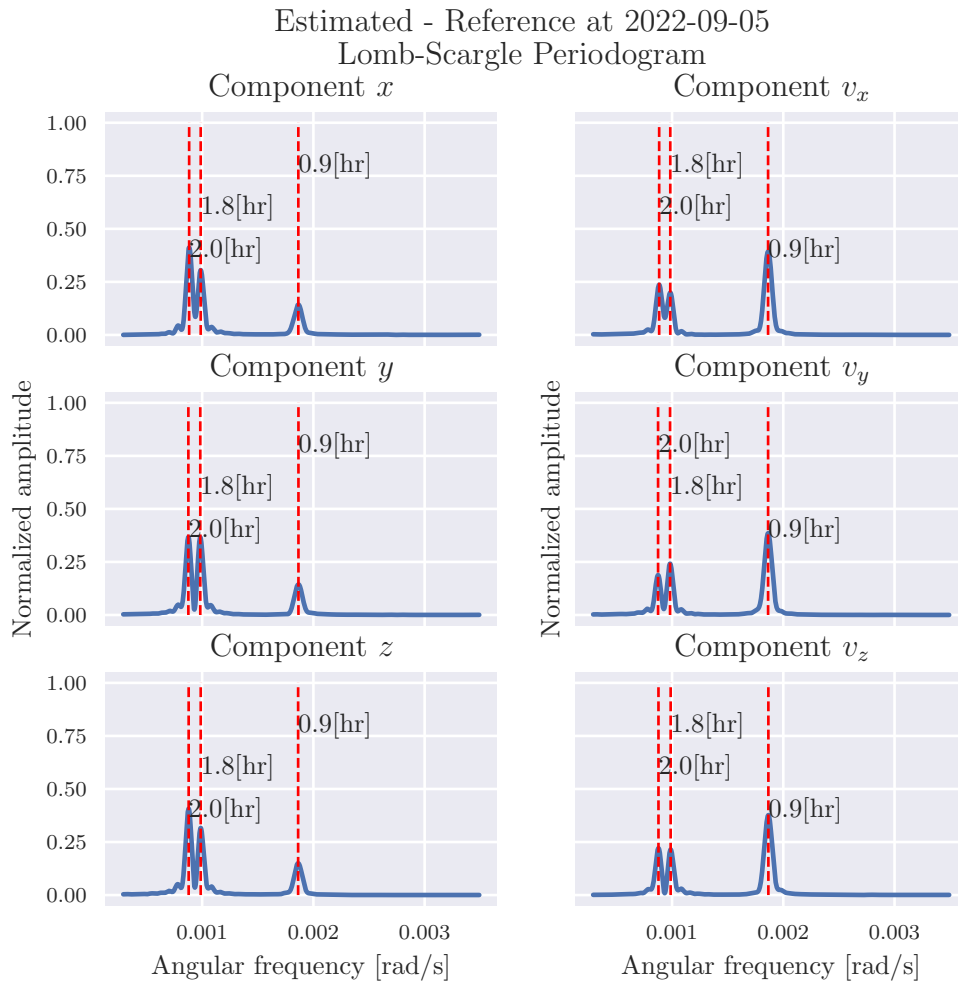
Figure 6.11: Lomb-Scargle periodogram for the differences between estimated and reference results for satellite state in GCRF.
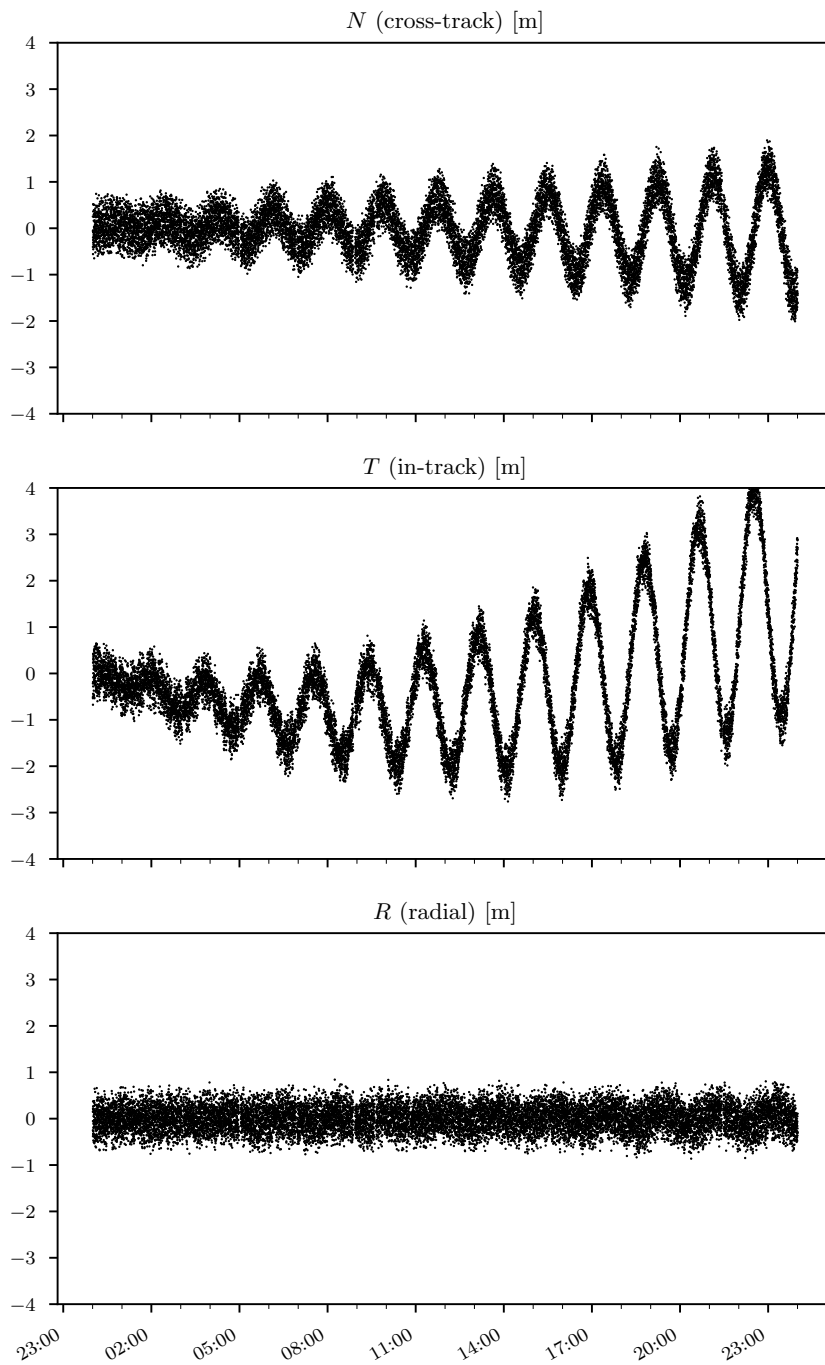
Figure 6.12: Discrepancies of estimated state against the orbits estimated at CNES/AALTO for one day of JASON-3 orbit (in radial, across-track and in-track RF).
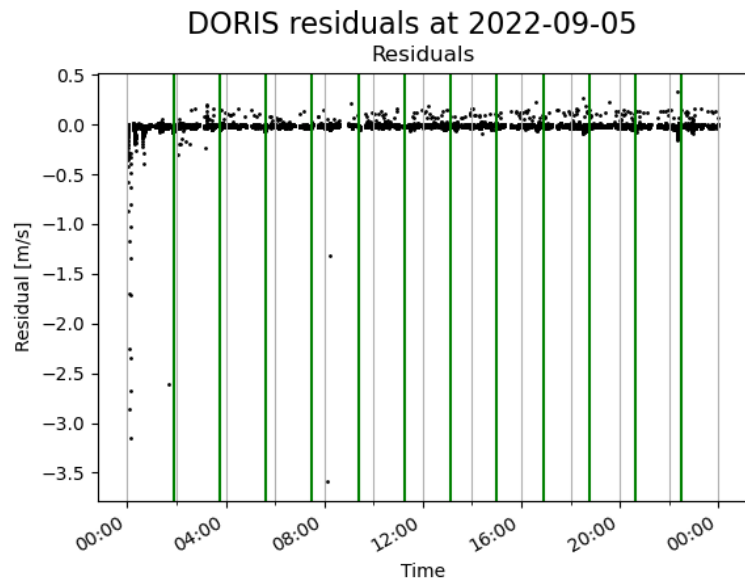
149

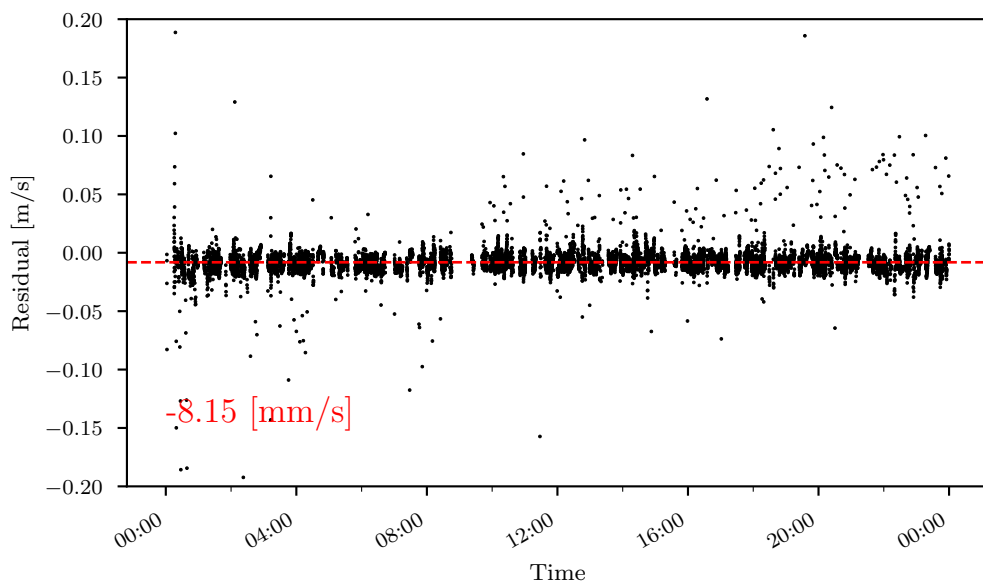Figure 6.13: DORIS residuals computed from one day of JASON-3 orbit determination.

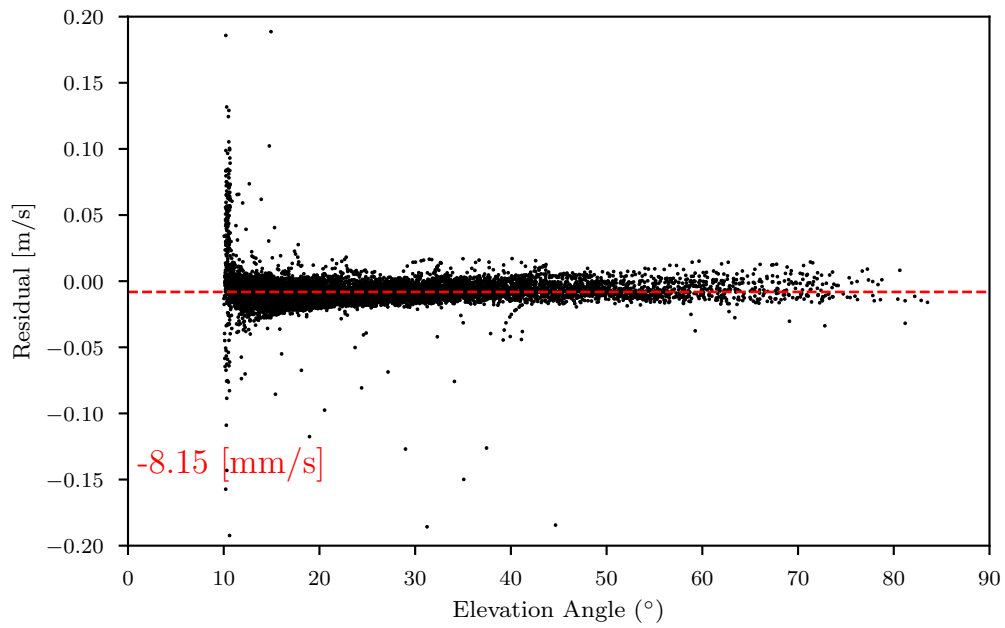Figure 6.14: DORIS residuals computed from one day of JASON-3 orbit determination.

Figure 6.15: DORIS residuals w.r.t. elevation angle computed from one day of JASON-3 orbit determination.

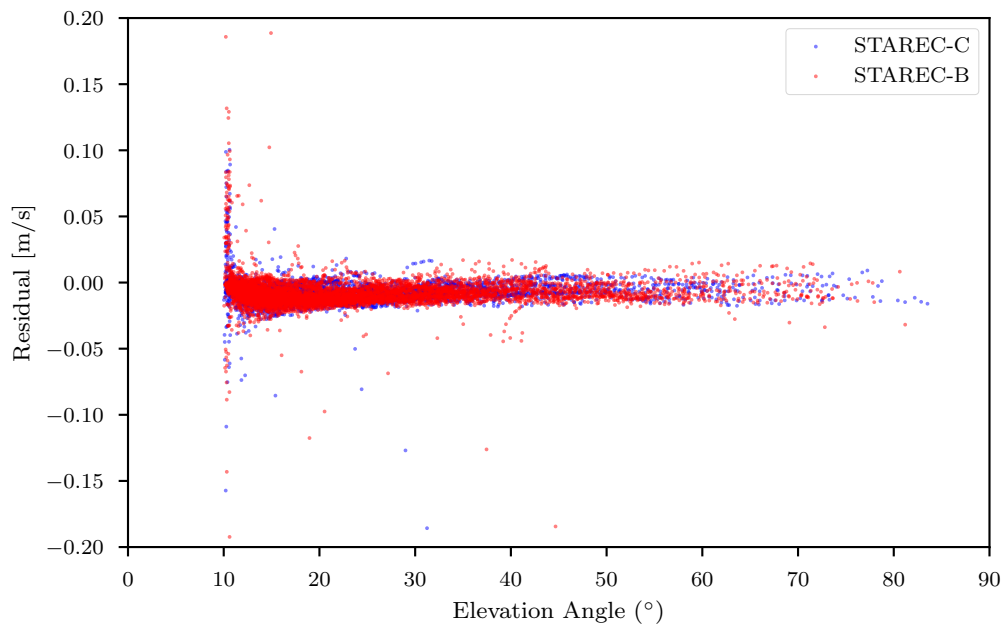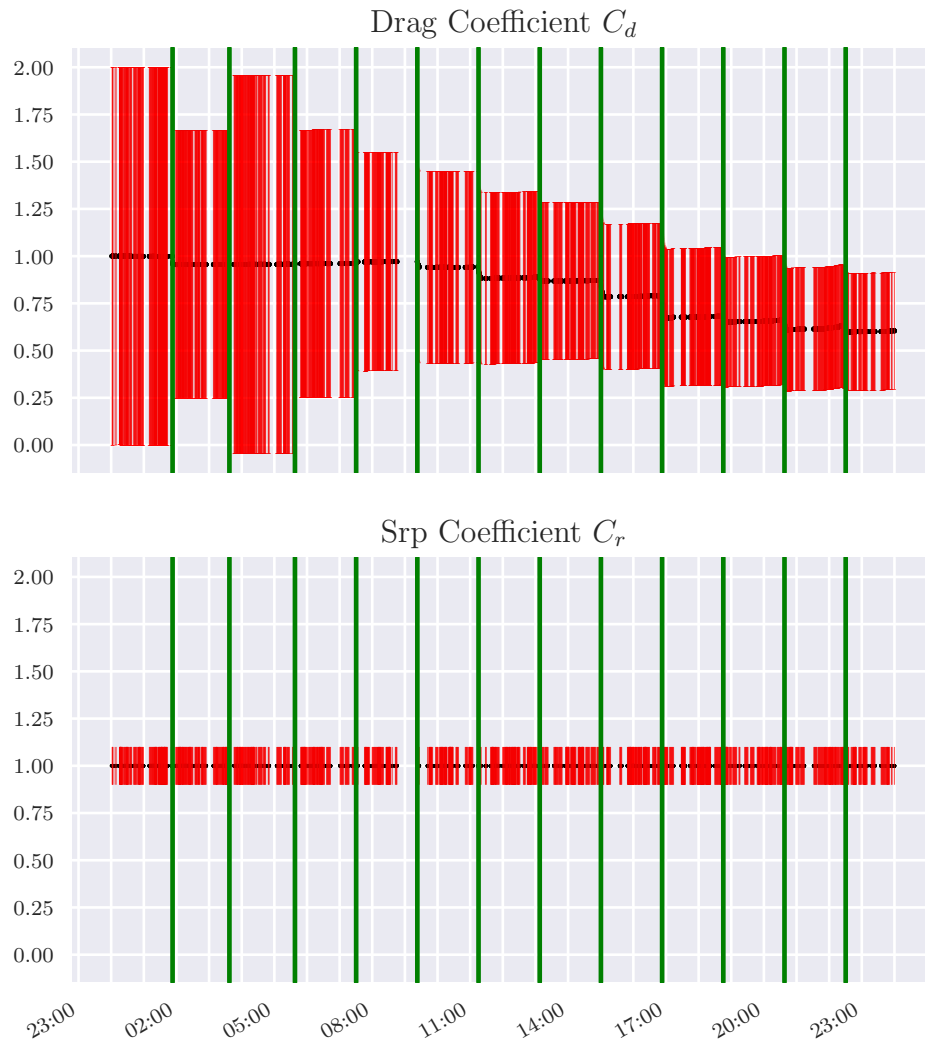Figure 6.16: DORIS residuals w.r.t. elevation angle computed from one day of JASON-3 orbit determination.

Figure 6.17: Estimated dynamic orbit parameters (drag and solar radiation pressure coefficients, C_d and C_r), for one day of JASON-3 orbit determination.

Chapter 7

Conclusions And Recommendations

7.1 Conclusions

DORIS is a fundamental technique in Satellite Geodesy that has been steadily contributing significant results, products, and insights in a wide range of geosciences and related fields since the early 1990s. It has played a crucial role in expanding the geodetic knowledgebase and enhancing our understanding of the Earth's dynamics. Together with GNSS, SLR, and VLBI, DORIS forms a fundamental pillar of reference frame maintenance. However, despite its importance, the scientific audience for DORIS is disproportionately limited, as evidenced by the small number of dedicated Analysis Centers compared to other space geodetic techniques. This lack of dedicated scientific software tools for a prominent space geodetic technique is a significant challenge that needs to be addressed. The absence of specialized, scientific software tools for a significant space geodetic method like DORIS served as the primary objective and motivation for this Thesis.

This Thesis presents the development and implementation of a software package that serves as a fundamental building block for a dedicated analysis tool to process DORIS observations at an IDS level. The software package was designed with two main principles in mind: efficiency and genericity/modularity. This architectural approach is expected to attract new users by promoting reusability, maintenance, and repurposing. The software package is free and open-source, aimed at fostering growth in the user community and stimulating interest in the DORIS technique for further development.

The software built amounts to approximately 100000 lines of source code, di-

vided into different modules/libraries (section 6.2). Using this design, it is trivial to create a DORIS analysis program to perform orbit determination (section 6.6), since all required functionality is delivered via the different modules. Adding yet another satellite in the processing chain, would only require the development of a dedicated attitude model (as e.g. done for JASON-3, subsection 6.4.1) and accommodating for the new state parameters in the filter.

As shown in earlier chapters, modeling of the fundamental conservative forces, i.e. Earth's gravity (c.f. section 2.2.3), third-body perturbations (computed here for Sun and Moon, c.f. section 2.2.3), solid earth tides (c.f. section 2.2.3) and ocean tides (c.f. section 2.2.3) is in close agreement with state-of-the-art scientific software (section 6.3). Additionally, given the accuracy of the results and validation tests obtained both in chapter 2 and section 6.6, intermediate but fundamental computations such as EOP interpolation (see subsection 2.3.4) and reference frames and time-scales transformations (see section 2.3 and section 2.4) seem to comply to high accuracy standards.

The results obtained from orbit determination using the JASON-3 satellite reveal average discrepancies, with position discrepancies amounting to a few meters and velocity estimates differing by a few millimeters per second compared to the CNES/SSALTO (multitechnique) solution. While these outcomes fall short of a POD result conforming to IDS quality standards, limitations of the current analysis pipeline are well recognized and easily surmountable:

- Limitations in the force model, including:

  - Currently only a few major ocean tidal constituents are considered. More can be added since the capacity is already there.

  - Account for earth pole tides and ocean pole tides. These tidal effects are less pronounced than the earth and ocean loading effects and simpler to model.

  - Apply more complex Earth radiation modeling (e.g. include albedo and empirical models)

  - Add dealiasing products (some gravity models were determined using this model)

  - Account for atmospheric loading effects

- Handle displacement of reference points (effects of tides on crustal deformation)

154

- Implement a more robust treatment of *proper time* (currently estimates extracted from RINEX)

- Discriminate between *zero tide* and *tide free* models and adopt a unified approach

Yet the most important step towards a more precise estimation process, would be the adoption of a more robust filtering design. Currently the *Extended Kalman Filter* algorithm is used as estimator (section 4.4). The more efficient and rigorous formulation of the Square Root Information Filtering (SRIF) algorithm could replace the current implementation. More crucially though, the introduction of stochastic properties via *process noise*. Currently, no process noise is introduced in the filter, meaning that the force model is considered "errorless", and the estimation is not allowed to deviate and account for mismodeled or even unmodeled effects. Process noise needs to be included in the model also due to modeling approximations and model integration errors. In a least squares sense, such effects are treated using stochastic accelerations.

It is noteworthy that the aforementioned improvements pertain to the enhancement of an existing software package. The majority of the work, aimed at achieving a state-of-the-art, scientific software tool, has already been accomplished and is now available to all interested parties through this Thesis. The majority of this tool has been implemented, extensively documented, and rigorously tested. Given that the limited number of software packages available for accurate processing of DORIS observations are either not free and/or not open-source, the tools presented in this Thesis represent a new and innovative alternative.

7.2 Recommendations

As discussed before, the software tools presented in this Thesis constitute a fundamental infrastructure for a state-of-the-art DORIS analysis software package. Incorporation of a few refinements (outlined in section 7.1) can result to analysis results meeting the highest standards. The basis of further development, should evolve around the following considerations:

- Adherence to a free and open source policy; this policy results in attraction of new users, which will pose new scientific questions, explore limitations and drawbacks, and eventually drive the development forward to meet new, wider

and higher demands. This cycle will in turn promote scientific knowledge and push for technological advance of the technique itself.

- Adherence to a modular design paradigm, favoring genericity and efficiency. Given that the software aims to be used by the scientific community, which by large is familiar with concepts such as programming, these two attributes should be preferred over e.g. user-friendliness.

- Upgrade the filtering process to a more robust estimator including the introduction of process noise (stochastic properties).

- Incorporate more space geodetic techniques. As said, most scientific software packages of high caliber, are not limited to one technique. This happens because once the groundwork is laid, the introduction of a new space geodetic technique is a matter of efficiently handling the corresponding observation equation model. Complex earth dynamics, reference and time frame transformations, filtering and adjustment, integration and linear algebra are all already in place. Additionally, the introduction other techniques, allows for validation and can further provide crucial scientific results and insight.

- Enhance the package to meet IDS standards and contribute to the community. This will require meeting high-precision demands while simultaneously drive updateting and refining, since it will necessitate adoption of the latest developments in geodesy.

Appendices

A   Variational Equations Differential Equations

A slightly different but enlighting approach is presented here for the formation and solution of the variational equation system of differential equations. The developments presented here can be found in Tapley et al. 2004b. The Φ matrix here will contain the combined state transition matrix and the sensitivity matrix $\boldsymbol{S}(t)$, see subsection 4.5.2.

The differential equation for the variational equations can be written in the form

$$\dot{\Phi}(t, t_0) = A(t)\Phi(t, t_0), \text{ with} \tag{1}$$

$$\Phi(t_0, t_0) = \boldsymbol{I} \tag{2}$$

The state transition matrix can be split in the following way

$$\Phi(t, t_0) \equiv \frac{\partial \boldsymbol{y}(t)}{\partial \boldsymbol{y}_0} \equiv \begin{pmatrix} \phi_1(t, t_0) \\ \phi_2(t, t_0) \\ \phi_3(t, t_0) \end{pmatrix} = \begin{pmatrix} \frac{\partial \boldsymbol{r}(t)}{\partial \boldsymbol{y}_0} \\ \frac{\partial \boldsymbol{v}(t)}{\partial \boldsymbol{y}_0} \\ \frac{\partial \boldsymbol{p}(t)}{\partial \boldsymbol{y}_0} \end{pmatrix} \tag{3}$$

where

$$\phi_3(t, t_0) = \begin{pmatrix} \boldsymbol{0}_{n_p \times 6} & \boldsymbol{I}_{n_p \times n_p} \end{pmatrix} \tag{4}$$

By differentiating Equation 3, Equation 1 in terms of a second order differential equation,

$$\dot{\Phi}(t, t_0) = \frac{\partial \dot{\boldsymbol{y}}(t)}{\partial \boldsymbol{y}_0} = \begin{pmatrix} \dot{\phi}_1(t, t_0) \\ \dot{\phi}_2(t, t_0) \\ \dot{\phi}_3(t, t_0) \end{pmatrix} = \begin{pmatrix} \frac{\partial \dot{\boldsymbol{r}}(t)}{\partial \boldsymbol{y}_0} \\ \frac{\partial \dot{\boldsymbol{v}}(t)}{\partial \boldsymbol{y}_0} \\ \boldsymbol{0}_{n_p \times 6} \end{pmatrix} = \begin{pmatrix} \frac{\partial \dot{\boldsymbol{r}}(t)}{\partial \boldsymbol{y}(t)} \\ \frac{\partial \dot{\boldsymbol{v}}(t)}{\partial \boldsymbol{y}(t)} \\ \boldsymbol{0}_{n_p \times 6} \end{pmatrix} \frac{\partial \boldsymbol{y}(t)}{\partial \boldsymbol{y}_0} \tag{5}$$

Note that $\dot{\phi}_2 = \ddot{\phi}_1$.

The second order differential equation could be solved to obtain $\Phi(t, t_0)$

$$\ddot{\phi}_1(t, t_0) = \frac{\partial \ddot{r}(t)}{\partial \boldsymbol{y}_0} = \frac{\partial \ddot{r}(t)}{\partial \boldsymbol{y}(t)} \frac{\partial \ddot{\boldsymbol{y}}(t)}{\partial \boldsymbol{y}_0}$$

$$= \begin{pmatrix} \frac{\partial \ddot{r}(t)}{\partial \boldsymbol{r}(t)} & \frac{\partial \ddot{r}(t)}{\partial \boldsymbol{v}(t)} & \frac{\partial \ddot{r}(t)}{\partial \boldsymbol{p}} \end{pmatrix} \begin{pmatrix} \frac{\partial \boldsymbol{r}(t)}{\partial \boldsymbol{y}_0} \\ \frac{\partial \dot{\boldsymbol{r}}(t)}{\partial \boldsymbol{y}_0} \\ \frac{\partial \boldsymbol{p}}{\partial \boldsymbol{y}_0} \end{pmatrix} \tag{6}$$

which reduces to

$$\ddot{\phi}_1(t, t_0) = \frac{\partial \ddot{r}(t)}{\partial \boldsymbol{r}(t)} \phi_1(t, t_0) + \frac{\partial \ddot{r}(t)}{\partial \boldsymbol{v}(t)} \dot{\phi}_1(t, t_0) + \frac{\partial \ddot{r}(t)}{\partial \boldsymbol{p}} \phi_3(t, t_0) \tag{7}$$

with initial conditions

$$\phi_1(t_0, t_0) = \begin{pmatrix} \boldsymbol{I} & \boldsymbol{0} \end{pmatrix} \tag{8}$$

$$\dot{\phi}_1(t_0, t_0) = \phi_2(t_0, t_0) = \begin{pmatrix} \boldsymbol{0} & \boldsymbol{I} & \boldsymbol{0} \end{pmatrix} \tag{9}$$

This second order ODE system can be transformed to a $n \times n$ first-order system (if the solution of first order ODE is preffered)

$$\dot{\phi}_1(t, t_0) = \phi_2(t, t_0)$$
$$\dot{\phi}_2(t, t_0) = \frac{\partial \ddot{r}(t)}{\partial \boldsymbol{r}(t)} \phi_1(t, t_0) + \frac{\partial \ddot{r}(t)}{\partial \boldsymbol{v}(t)} \phi_2(t, t_0) + \frac{\partial \ddot{r}(t)}{\partial \boldsymbol{p}} \phi_3(t, t_0) \tag{10}$$
$$\dot{\phi}_3(t, t_0) = \boldsymbol{0}$$

or $\dot{\Phi}_{(}t, t_0) = A(t)\Phi(t, t_0)$, or

$$\begin{pmatrix} \dot{\phi}_1(t, t_0) \\ \dot{\phi}_2(t, t_0) \\ \dot{\phi}_3(t, t_0) \end{pmatrix}_{n \times n} = \begin{pmatrix} \boldsymbol{0}_{3 \times 3} & \boldsymbol{I}_{3 \times 3} & \boldsymbol{0}_{3 \times m} \\ \left(\frac{\partial \ddot{r}(t)}{\partial \boldsymbol{r}(t)}\right)^*_{3 \times 3} & \left(\frac{\partial \ddot{r}(t)}{\partial \boldsymbol{v}(t)}\right)^*_{3 \times 3} & \left(\frac{\partial \ddot{r}(t)}{\partial \boldsymbol{p}}\right)^*_{3 \times m} \\ \boldsymbol{0}_{m \times 3} & \boldsymbol{0}_{m \times 3} & \boldsymbol{0}_{m \times m} \end{pmatrix}_{n \times n} \begin{pmatrix} \phi_1(t, t_0) \\ \phi_2(t, t_0) \\ \phi_3(t, t_0) \end{pmatrix}_{n \times n} \tag{11}$$

B   Short Introduction to Quaternion Algebra

This chapter is only a very short introduction to quaternions, focused on essential definitions required to use the quaternion as a representation of the attitude of an object. A more detailed review of the matter can be found in Markley and Crassidis 2019 and Diebel 2006.

A quaternion q consists of four elements q_0, q_1, q_2, q_3 and is defined as:

$$\boldsymbol{q} \equiv q_0 + iq_0 + jq_1 + kq_2 \tag{12}$$

where i, j and k are imaginary numbers satisfying following conditions

$$\begin{aligned}
i^2 + j^2 + k^2 &= -1 \\
ij &= -ji = k \\
jk &= -kj = i \\
ki &= -ik = j
\end{aligned} \tag{13}$$

q may be represented as a vector,

$$\boldsymbol{q} = \begin{pmatrix} q_0 & q_1 & q_2 & q_3 \end{pmatrix} = \begin{pmatrix} q_0 \\ \boldsymbol{q}_{1:3} \end{pmatrix} \tag{14}$$

where the component $q_0 \in \mathbb{R}$ represents the scalar (real) part and $\boldsymbol{q}_{1:3} \in \mathbb{R}^3$ the vector (imaginary) part. The four components of a quaternion can hold the axis $\boldsymbol{e}$ and angle θ of a rotation. In this case,

$$\begin{aligned}
q_0 &= \cos \frac{\theta}{2} \\
q_1 &= \boldsymbol{e}_1 \sin \frac{\theta}{2} \\
q_2 &= \boldsymbol{e}_2 \sin \frac{\theta}{2} \\
q_3 &= \boldsymbol{e}_3 \sin \frac{\theta}{2}
\end{aligned} \tag{15}$$

The following properties of a quaternion $\boldsymbol{q}$ are defined:

- The conjugate of a quaternion is:

$$\bar{q} = \begin{pmatrix} q_0 \\ -\boldsymbol{q}_{1:3} \end{pmatrix} \tag{16}$$

159

- The norm of a quaternion is:

$$\|q\| = \sqrt{q_0^2 + q_1^2 + q_2^2 + q_3^2} \tag{17}$$

- The normalized conjugate or inverse of a quaternion is:

$$q^{-1} = \frac{\bar{q}}{\|q\|} \tag{18}$$

- Multiplication of $\boldsymbol{q}$ with another quaternion $\boldsymbol{p}$ is defined as

$$\boldsymbol{q} = \boldsymbol{p} \odot \boldsymbol{q} = \begin{pmatrix} p_0 q_0 - \boldsymbol{p}_{1:3} \cdot \boldsymbol{q}_{1:3} \\ p_0 \cdot \boldsymbol{q}_{1:3} + q_0 \cdot \boldsymbol{p}_{1:3} + \boldsymbol{p}_{1:3} \times \boldsymbol{q}_{1:3} \end{pmatrix} \tag{19}$$

A rotation of a vector $\boldsymbol{r}$ from a coordinate system A to a system B can be expressed using quaternions as (Zeitlhöfler 2019):

$$\boldsymbol{r}_B^* = \hat{\boldsymbol{q}} \odot \boldsymbol{r}_A^* \odot \boldsymbol{q} \tag{20}$$

where $\boldsymbol{r}_B^*$ and $\boldsymbol{r}_A^*$ are the vectors $\boldsymbol{r}_B$ and $\boldsymbol{r}_A$ expressed as quaternions with a sclar part (q_0) equal to zero.

Bibliography

Acton, C., N. Bachman, B. Semenov, and E. Wright (2018). "A look towards the future in the handling of space science mission geometry". In: *Planetary and Space Science* 150. Enabling Open and Interoperable Access to Planetary Science and Heliophysics Databases and Tools, pp. 9–12. ISSN: 0032-0633. DOI: https://doi.org/10.1016/j.pss.2017.02.013. URL: https://www.sciencedirect.com/science/article/pii/S0032063316303129.

Anderson, P., F. Rich, and S. Borisov (2018). "Mapping the South Atlantic Anomaly continuously over 27 years". In: *Journal of Atmospheric and Solar-Terrestrial Physics* 177. Dynamics of the Sun-Earth System: Recent Observations and Predictions, pp. 237–246. ISSN: 1364-6826. DOI: https://doi.org/10.1016/j.jastp.2018.03.015. URL: https://www.sciencedirect.com/science/article/pii/S1364682617303887.

Askne, J. and H. Nordius (1987). "Estimation of tropospheric delay for microwaves from surface weather data". In: *Radio Science* 22.3, pp. 379–386. DOI: https://doi.org/10.1029/RS022i003p00379. eprint: https://agupubs.onlinelibrary.wiley.com/doi/pdf/10.1029/RS022i003p00379. URL: https://agupubs.onlinelibrary.wiley.com/doi/abs/10.1029/RS022i003p00379.

Atallah, A. M., A. Bani Younes, R. M. Woollands, and J. L. Junkins (June 2022). "Analytical Radial Adaptive Method for Spherical Harmonic Gravity Models". In: *The Journal of the Astronautical Sciences* 69.3, pp. 745–766. ISSN: 2195-0571. DOI: 10.1007/s40295-022-00321-3. URL: https://doi.org/10.1007/s40295-022-00321-3.

Atallah, A. M., R. M. Woollands, T. A. Elgohary, and J. L. Junkins (June 2020). "Accuracy and Efficiency Comparison of Six Numerical Integrators for Propagating Perturbed Orbits". In: *The Journal of the Astronautical Sciences* 67.2, pp. 511–538. ISSN: 2195-0571. DOI: 10.1007/s40295-019-00167-2. URL: https://doi.org/10.1007/s40295-019-00167-2.

Auriol, A. and C. L. Tourain (2010). "DORIS system: The new age". In: *Advances in Space Research* 46.12. DORIS: Precise Orbit Determination and Applications to Earth Sciences, pp. 1484–1496. ISSN: 0273-1177. DOI: https://doi.

org/10.1016/j.asr.2010.05.015. URL: https://www.sciencedirect.com/science/article/pii/S0273117710003479.

Bannoura, W., F. Parisot, P. Vaze, and G. Zaouche (Oct. 2011). "ASON–3 Mission Status3 Mission Sta". Presented at Ocean Surface Topography Science Team (OSTST) meeting, San Diego. URL: https://www.aviso.altimetry.fr/fileadmin/documents/OSTST/2011/oral/01_Wednesday/Plenary/Program%20Status/09%20OSTST_2011_Jason-3_mission_overview_gz_v3.pdf.

Barlier, F. (2005). "The DORIS system: a fully operational tracking system to get orbit determination at centimeter accuracy in support of Earth observations". In: *Comptes Rendus Geoscience* 337.14, pp. 1223–1224. ISSN: 1631-0713. DOI: https://doi.org/10.1016/j.crte.2005.07.007. URL: https://www.sciencedirect.com/science/article/pii/S1631071305002002.

Barthelmes, F. (2018). "Global Models". In: *Encyclopedia of Geodesy*. Ed. by E. Grafarend. Cham: Springer International Publishing, pp. 1–9. ISBN: 978-3-319-02370-0.

Barthelmes, F. and C. Förste (2011). *The ICGEM-format*. Tech. rep. GFZ Potsdam, Department 1 "Geodesy and Remote Sensing". URL: http://icgem.gfz-potsdam.de/ICGEM-Format-2011.pdf.

Battin, R. H. (June 1999). *An introduction to the mathematics and methods of astrodynamics*. Reston, VA: New York, American Institute of Aeronautics and Astronautics, Inc.

Beal, J. W. (Feb. 2015). "GEODYN Systems Description Volume 1". In: ed. by J. W. Beal, J. J. McCarthy, S. Rowton, D. Moore, D. E. Pavlis, S. B. Luthcke, and L. S. Tsaoussi. Prepared For: Space Geodesy Branch, Code 926. NASA GSFC, Greenbelt, MD. URL: https://space-geodesy.nasa.gov/techniques/tools/GEODYN/geodyn_vol1.pd%5Ccite%7B%7Df.

Beauducel, F. (2023). *Doodson tidal wave components*. Accessed: 2023-02-06. URL: https://github.com/beaudu/doodson (visited on 02/06/2023).

Bertiger, W., Y. Bar-Sever, A. Dorsey, B. Haines, N. Harvey, D. Hemberger, M. Heflin, W. Lu, M. Miller, A. W. Moore, D. Murphy, P. Ries, L. Romans, A. Sibois, A. Sibthorpe, B. Szilagyi, M. Vallisneri, and P. Willis (2020). "GipsyX/RTGx, a new tool set for space geodetic operations and research". In: *Advances in Space Research* 66.3, pp. 469–489. ISSN: 0273-1177. DOI: https://doi.org/10.1016/j.asr.2020.04.015. URL: https://www.sciencedirect.com/science/article/pii/S0273117720302532.

Beutler, G. (2005). *Methods of Celestial Mechanics*. 1st ed. Vol. Volume II: Application to Planetary System, Geodynamics and Satellite Geodesy. Astronomy and Astrophysics Library. Springer, Berlin, Heidelberg. ISBN: 978-3-642-42642-1.

Biancamaria, S., D. P. Lettenmaier, and T. M. Pavelsky (Mar. 2016). "The SWOT Mission and Its Capabilities for Land Hydrology". In: *Surveys in Geophysics* 37.2, pp. 307–337. ISSN: 1573-0956. DOI: 10.1007/s10712-015-9346-y. URL: https://doi.org/10.1007/s10712-015-9346-y.

Bierman, G. J. (May 1977). *Factorization methods for discrete sequential estimation.* en. Mathematics in Science and Engineering. San Diego, CA: Academic Press.

Bizouard, C., S. Lambert, C. Gattano, O. Becker, and J.-Y. Richard (Aug. 2019). "The IERS EOP 14C04 solution for Earth orientation parameters consistent with ITRF 2014". English. In: *Journal of Geodesy* 93.5, pp. 621–633. DOI: 10.1007/s00190-018-1186-3.

Bradley, B. K., A. Sibois, and P. Axelrad (2016). "Influence of ITRS/GCRS implementation for astrodynamics: Coordinate transformations". In: *Advances in Space Research* 57.3, pp. 850–866. ISSN: 0273-1177. DOI: https://doi.org/10.1016/j.asr.2015.11.006. URL: https://www.sciencedirect.com/science/article/pii/S0273117715007929.

Bruinsma, S. and C. Boniface (2021). "The operational and research DTM-2020 thermosphere models". In: *J. Space Weather Space Clim.* 11, p. 47. DOI: 10.1051/swsc/2021032. URL: https://doi.org/10.1051/swsc/2021032.

Butcher, J. C. (Aug. 2016). *Numerical methods for ordinary differential equations.* en. 3rd ed. Nashville, TN: John Wiley and Sons, Ltd.

Capdeville, H., J.-M. Lemoine, L. Soudarin, and A. Mezerette (May 2016a). *Are the Jason-2 and Jason-3 USO sensitive to the SAA?* IDS AWG meeting, Delft 26-27 May 2016. URL: https://ids-doris.org/images/documents/report/AWG201605/IDSAWG201605-Capdeville-SAA_Jason2&3.pdf.

Capdeville, H., P. Štěpánek, L. Hecker, and J.-M. Lemoine (2016b). "Update of the corrective model for Jason-1 DORIS data in relation to the South Atlantic Anomaly and a corrective model for SPOT-5". In: *Advances in Space Research* 58.12. Scientific Applications of DORIS in Space Geodesy, pp. 2628–2650. ISSN: 0273-1177. DOI: https://doi.org/10.1016/j.asr.2016.02.009. URL: https://www.sciencedirect.com/science/article/pii/S0273117716000909.

Capitaine, N., A. H. Andrei, M. R. Calabretta, V. Dehant, T. Fukushima, B. R. Guinot, C. Y. Hohenkerk, G. H. Kaplan, S. A. Klioner, J. Kovalevsky, and et al. (2006). "Proposed terminology in fundamental astronomy based on IAU 2000 resolutions". In: *Proceedings of the International Astronomical Union* 2.14, pp. 474–475. DOI: 10.1017/S1743921307011490.

Capitaine, N., J. Chapront, S. Lambert, and P. T. Wallace (2003). "Expressions for the Celestial Intermediate Pole and Celestial Ephemeris Origin consistent with the IAU 2000A precession-nutation model". In: *Astronomy and Astrophysics*

400.3, pp. 1145–1154. DOI: 10.1051/0004-6361:20030077. URL: https://doi.org/10.1051/0004-6361:20030077.

Capitaine, N. and P. T. Wallace (2006). "High precision methods for locating the celestial intermediate pole and origin". In: *Astronomy and Astrophysics* 450.2, pp. 855–872. DOI: 10.1051/0004-6361:20054550. URL: https://doi.org/10.1051/0004-6361:20054550.

Cerri, L., A. Couhert, and P. Ferrage (Feb. 2022). *DORIS satellites models implemented in POE processing*. Tech. rep. Centre National d'Etudes Spatiales, International DORIS Service. URL: https://ids-doris.org/documents/BC/satellites/DORISSatelliteModels.pdf.

Cerri, L. and F. Mercier (May 2011). "Processing of DORIS RINEX data and relationship with the "2.2" format". Presented at the DORIS AWG Meeting, Paris, France. URL: https://ids-doris.org/images/documents/report/AWG201105/IDSAWG1105-Cerri-RINEXProcessing.pdf.

Chen, J., A. Cazenave, C. Dahle, W. Llovel, I. Panet, J. Pfeffer, and L. Moreira (Feb. 2022). "Applications and Challenges of GRACE and GRACE Follow-On Satellite Gravimetry". In: *Surveys in Geophysics* 43.1, pp. 305–345. ISSN: 1573-0956. DOI: 10.1007/s10712-021-09685-x. URL: https://doi.org/10.1007/s10712-021-09685-x.

Chobotov, V. A. (2002). *Orbital mechanics*. 3rd ed. AIAA education series. Reston, Va.: American Institute of Aeronautics and Astronautics (AIAA). DOI: https://doi.org/10.2514/4.862250.

CNES (Dec. 2013). "Algorithmic Documentation of the GINS Software". In: ed. by C. national d'études spatiales and G. de Recherche de Géodésie Spatiale (GRGS). URL: https://www5.obs-mip.fr/wp-content-omp/uploads/sites/28/2017/11/GINS_Algo_2013.pdf.

Couderc, V. and G. Zaouche (2015). *Jason-3 Characteristics for POD Processing*. Tech. rep. Centre National d'Etudes Spatiales. URL: https://ids-doris.org/documents/BC/satellites/Jason-3_CharacteristicsForPODprocessing.pdf.

Cunningham, L. E. (June 1970). "On the Computation of the Spherical Harmonic Terms Needed during the Numerical Integration of the Orbital Motion of an Artificial Satellite". In: *Celestial Mechanics* 2.2, pp. 207–216. DOI: 10.1007/BF01229495.

Curtis, H. D. (2014). *Orbital Mechanics for Engineering Students (Third Edition)*. Third Edition. Boston: Butterworth-Heinemann. ISBN: 978-0-08-097747-8. DOI: https://doi.org/10.1016/B978-0-08-097747-8.00012-8. URL: https://www.sciencedirect.com/science/article/pii/B9780080977478000128.

Dach, R. (2015). "Bernese GNSS Software Version 5.2, User Manual". In: ed. by R. Dach, S. Lutz, P. Walser, and P. Fridez. Astronomical Institute, University of Bern, Bern Open Publishing. ISBN: 978-3-906813-05-9.

Dam, E. B., M. Koch, and M. Lillholm (2000). "Quaternions, Interpolation and Animation". In: ed. by U. o. C. Department of Computer Science. Technical Rep ort DIKU-TR-98/5. URL: https://web.mit.edu/2.998/www/QuaternionReport1.pdf.

VM-Data-Server (2020). *VMF Data Server; editing status 2020-12-14; re3data.org - Registry of Research Data Repositories*. DOI: 10.17616/R3RD2H. URL: http://doi.org/10.17616/R3RD2H.

Davis, J. L., T. Herring, I. I. Shapiro, A. E. E. Rogers, and G. Elgered (1985). "Geodesy by radio interferometry: Effects of atmospheric modeling errors on estimates of baseline length". In: *Radio Science* 20.6, pp. 1593–1607. DOI: https://doi.org/10.1029/RS020i006p01593. eprint: https://agupubs.onlinelibrary.wiley.com/doi/pdf/10.1029/RS020i006p01593. URL: https://agupubs.onlinelibrary.wiley.com/doi/abs/10.1029/RS020i006p01593.

Delva, P. et al. (Jan. 2023). "GENESIS: co-location of geodetic techniques in space". In: *Earth, Planets and Space* 75.1, p. 5. ISSN: 1880-5981. DOI: 10.1186/s40623-022-01752-w. URL: https://doi.org/10.1186/s40623-022-01752-w.

Dettmering, D., M. Limberger, and M. Schmidt (Dec. 2014). "Using DORIS measurements for modeling the vertical total electron content of the Earth's ionosphere". In: *Journal of Geodesy* 88.12, pp. 1131–1143. DOI: 10.1007/s00190-014-0748-2.

Diebel, J. (2006). *Representing Attitude: Euler Angles, Unit Quaternions, and Rotation Vectors*. URL: https://www.astro.rug.nl/software/kapteyn-beta/_downloads/attitude.pdf.

Doornbos, E., M. Förster, B. Fritsche, T. van Helleputte, J. van den IJssel, Georg, Koppenwallner, H. Lühr, D. Rees, P. N. Visser, and M. Kern (Jan. 2009). "ESTEC contract 21022/07/NL/HE air density models derived from multi-satellite drag observations - Final report". In: *Technical Report DEOS/TU Delft Scientific Report 01/2009*.

Estérie, P., J. Falcou, M. Gaunard, J.-T. Lapresté, and L. Lacassagne (2014). "The numerical template toolbox: A modern C++ design for scientific computing". In: *Journal of Parallel and Distributed Computing* 74.12. Domain-Specific Languages and High-Level Frameworks for High-Performance Computing, pp. 3240–3253. ISSN: 0743-7315. DOI: https://doi.org/10.1016/j.jpdc.2014.07.002. URL: https://www.sciencedirect.com/science/article/pii/S0743731514001245.

Fabian, R. (Sept. 2018). *Data-oriented design*. Stockport, England: Richard Fabian.

Ferrage, P. (June 2020). *Jason1&2&3 Descriptions of the Quaternion and Solar Panel Files*. Tech. rep. Centre National d'Etudes Spatiales, Service Altimetrie & Localisation Precise. URL: https://ids-doris.org/documents/BC/ancillary/quaternions/jason1_2_3_quaternion_solar_panel.pdf.

Folkner, W. M., J. G. Williams, and D. H. Boggs (Aug. 2009). "The Planetary and Lunar Ephemeris DE 421". In: *Interplanetary Network Progress Report* 42-178, pp. 1–34.

Förste, C., S. Bruinsma, O. Abrikosov, F. Flechtner, J.-C. Marty, J.-M. Lemoine, C. Dahle, H. Neumayer, F. Barthelmes, R. König, and R. Biancale (May 2014). "EIGEN-6C4 - The latest combined global gravity field model including GOCE data up to degree and order 1949 of GFZ Potsdam and GRGS Toulouse". In: *EGU General Assembly Conference Abstracts*. EGU General Assembly Conference Abstracts, 3707, p. 3707.

Fu, L.-L., E. J. Christensen, C. A. Yamarone Jr., M. Lefebvre, Y. Ménard, M. Dorrer, and P. Escudier (1994). "TOPEX/POSEIDON mission overview". In: *Journal of Geophysical Research: Oceans* 99.C12, pp. 24369–24381. DOI: https://doi.org/10.1029/94JC01761. eprint: https://agupubs.onlinelibrary.wiley.com/doi/pdf/10.1029/94JC01761. URL: https://agupubs.onlinelibrary.wiley.com/doi/abs/10.1029/94JC01761.

Gambis, D. (Nov. 2006). "DORIS and the Determination of the Earth's Polar Motion". In: *Journal of Geodesy* 80.8, pp. 649–656. ISSN: 1432-1394. DOI: 10.1007/s00190-006-0043-y. URL: https://doi.org/10.1007/s00190-006-0043-y.

Gao, F., B. Peng, Y. Zhang, N. H. Evariste, J. Liu, X. Wang, M. Zhong, M. Lin, N. Wang, R. Chen, and H. Xu (2015). "Analysis of HY2A precise orbit determination using DORIS". In: *Advances in Space Research* 55.5, pp. 1394–1404. ISSN: 0273-1177. DOI: https://doi.org/10.1016/j.asr.2014.11.032. URL: https://www.sciencedirect.com/science/article/pii/S0273117714007352.

Gawlik, I., S. Pałka, T. Pędzimąż, and B. Ziółko (July 2018). "Meta-Programming and Policy-Based Design as a Technique of Architecting Modular and Efficient DSP Algorithm Implementations". In: *Computing and Informatics* 37.2, pp. 269–290. URL: https://www.cai.sk/ojs/index.php/cai/article/view/2018_2_269.

Gelb, A., J. F. Kasper, R. A. Nash, C. F. Price, and A. A. Sutherland (1974). *Applied Optimal Estimation*. Ed. by A. Gelb, J. F. Kasper, R. A. Nash, C. F. Price, and A. A. Sutherland. Cambridge, MA: The MIT Press. ISBN: 0262570483.

Griffiths, D. F. and D. J. Higham (Nov. 2010). *Numerical methods for ordinary differential equations*. en. 2010th ed. Springer undergraduate mathematics series. London, England: Springer.

Guennebaud, G. and B. Jacob (2010). *Eigen v3*. http://eigen.tuxfamily.org.

Gurfil, P. and K. Seidelmann (June 2018). *Celestial mechanics and astrodynamics: Theory and practice*. en. Astrophysics and Space Science Library. Berlin, Germany: Springer.

Hairer, E., S. P. Norsett, and G. Wanner (Dec. 2009). *Solving ordinary differential equations I*. en. 2nd ed. Springer Series in Computational Mathematics. Berlin, Germany: Springer.

Hairer, E. and G. Wanner (Feb. 2010). *Solving ordinary differential equations II*. en. 2nd ed. Springer series in computational mathematics. Berlin, Germany: Springer.

Hilla, S. (Sept. 2010). "The Extended Standard Product 3 Orbit Format (SP3-c)". Silver Spring, MD 20910-6233, USA.

Hintz, G. R. (Oct. 2016). *Orbital mechanics and astrodynamics*. en. Cham, Switzerland: Springer International Publishing. ISBN: 978-3-319-09443-4. DOI: https://doi.org/10.1007/978-3-319-09444-1.

Hofmann-Wellenhof, B., N. Kuhtreiber, and H. Moritz (Apr. 2005). *Physical Geodesy*. en. 2nd ed. Vienna, Austria: Springer.

IAU Division 1 Working Group (n.d.). *Nomenclature for Fundamental Astronomy (NFA), Summary of the Work and Final Documents*. https://syrte.obspm.fr/iauWGnfa/. Accessed: 2023-01-30.

IAU SOFA Board (2021a). *IAU SOFA Software Collection*. URL: http://www.iausofa.org.

— (Apr. 2021b). *SOFA Time Scale and Calendar Tools*. URL: http://www.iausofa.org.

— (Apr. 2021c). *SOFA Tools for Earth Attitude*. URL: http://www.iausofa.org.

International DORIS Service (2020). *IDS Recommendations and suggestions for ITRF 2020 reprocessing*. https://ids-doris.org/images/IDS_RecommendationsITRF2020_04.02.2020.pdf. URL: https://ids-doris.org/analysis-coordination/itrf2020.html.

Jäggi, A., G. Beutler, and U. Hugentobler (2005a). "Efficient Stochastic Orbit Modeling Techniques using Least Squares Estimators". In: *A Window on the Future of Geodesy*. Ed. by F. Sansò. Berlin, Heidelberg: Springer Berlin Heidelberg, pp. 175–180. ISBN: 978-3-540-27432-2.

Jäggi, A., H. Bock, U. Hugentobler, and G. Beutler (2005b). "Comparison of Different Stochastic Orbit Modeling Techniques". In: *Earth Observation with CHAMP: Results from Three Years in Orbit*. Ed. by C. Reigber, H. Lühr, P. Schwintzer, and J. Wickert. Berlin, Heidelberg: Springer Berlin Heidelberg, pp. 89–94. ISBN: 978-3-540-26800-0. DOI: 10.1007/3-540-26800-6_14. URL: https://doi.org/10.1007/3-540-26800-6_14.

Jäggi, A., U. Meyer, M. Lasser, B. Jenny, T. Lopez, F. Flechtner, C. Dahle, C. Förste, T. Mayer-Gürr, A. Kvas, J.-M. Lemoine, S. Bourgogne, M. Weigelt, and A. Groh (2023). "International Combination Service for Time-Variable Gravity Fields (COST-G)". In: *Beyond 100: The Next Century in Geodesy*. Ed. by J. T. Freymueller and L. Sánchez. Cham: Springer International Publishing, pp. 57–65. ISBN: 978-3-031-09857-4.

Jalabert, E. and F. Mercier (2018). "Analysis of South Atlantic Anomaly perturbations on Sentinel-3A Ultra Stable Oscillator. Impact on DORIS phase measurement and DORIS station positioning". In: *Advances in Space Research* 62.1, pp. 174–190. ISSN: 0273-1177. DOI: https://doi.org/10.1016/j.asr.2018.04.005. URL: https://www.sciencedirect.com/science/article/pii/S0273117718302941.

Johannessen, J., G. Balmino, C. Provost, R. Rummel, R. Sabadini, H. Sünkel, C. C. Tscherning, P. Visser, P. Woodworth, C. Hughes, P. Legrand, N. Sneeuw, F. Perosanz, M. Aguirre-Martinez, H. Rebhan, and M. Drinkwater (July 2003). "The European Gravity Field and Steady-State Ocean Circulation Explorer Satellite Mission Its Impact on Geophysics". In: *Surveys in Geophysics* 24.4, pp. 339–386. ISSN: 1573-0956. DOI: 10.1023/B:GEOP.0000004264.04667.5e. URL: https://doi.org/10.1023/B:GEOP.0000004264.04667.5e.

Kim, E., S. Han, and A. M. A. Sayegh (2019). "Sensitivity of the Gravity Model and Orbital Frame for On-board Real-Time Orbit Determination: Operational Results of GPS-12 GPS Receiver". In: *Remote Sensing* 11.13. ISSN: 2072-4292. DOI: 10.3390/rs11131542. URL: https://www.mdpi.com/2072-4292/11/13/1542.

Klein, A. (Jan. 2006). "A Generalized Kahan-Babuška-Summation-Algorithm". In: *Computing* 76.3, pp. 279–293. ISSN: 1436-5057. DOI: 10.1007/s00607-005-0139-x. URL: https://doi.org/10.1007/s00607-005-0139-x.

Kong, Q., J. Guo, Y. Sun, C. Zhao, and C. Chen (Mar. 2017). "Centimeter-level precise orbit determination for the HY-2A satellite using DORIS and SLR tracking data". In: *Acta Geophysica* 65.1, pp. 1–12. ISSN: 1895-7455. DOI: 10.1007/s11600-016-0001-x. URL: https://doi.org/10.1007/s11600-016-0001-x.

Kur, T., H. Dobslaw, J. Śliwińska, J. Nastula, M. Wińska, and A. Partyka (Dec. 2022). "Evaluation of selected short-term predictions of UT1-UTC and LOD collected in the second earth orientation parameters prediction comparison campaign". In: *Earth, Planets and Space* 74.1, p. 191. ISSN: 1880-5981. DOI: 10.1186/s40623-022-01753-9. URL: https://doi.org/10.1186/s40623-022-01753-9.

Lambert, S. and C. Bizouard (Oct. 2002). "Positioning the Terrestrial Ephemeris Origin in the International Terrestrial Reference Frame". In: *Astronomy and Astrophysics* 394, pp. 317–321. DOI: 10.1051/0004-6361:20021139.

Landskron, D. and J. Böhm (Apr. 2018). "VMF3/GPT3: refined discrete and empirical troposphere mapping functions". In: *Journal of Geodesy* 92.4, pp. 349–360. ISSN: 1432-1394. DOI: 10.1007/s00190-017-1066-2. URL: https://doi.org/10.1007/s00190-017-1066-2.

Larson, K. M., N. Ashby, C. Hackman, and W. Bertiger (Dec. 2007). "An assessment of relativistic effects for low Earth orbiters: the GRACE satellites". In: *Metrologia* 44.6, pp. 484–490. DOI: 10.1088/0026-1394/44/6/007.

Lasser, M. (Jan. 2023). private communication.

Lasser, M., U. Meyer, A. Jäggi, T. Mayer-Gürr, A. Kvas, K. H. Neumayer, C. Dahle, F. Flechtner, J.-M. Lemoine, I. Koch, M. Weigelt, and J. Flury (2020). "Benchmark data for verifying background model implementations in orbit and gravity field determination software". In: *Advances in Geosciences* 55, pp. 1–11. DOI: 10.5194/adgeo-55-1-2020. URL: https://adgeo.copernicus.org/articles/55/1/2020/.

Lemoine, J.-M., R. Biancale, F. Reinquin, S. Bourgogne, and P. Gégout (Apr. 2019). *CNES/GRGS RL04 Earth gravity field models, from GRACE and SLR data*.

Lemoine, J.-M. and H. Capdeville (Nov. 2006). "A corrective model for Jason-1 DORIS Doppler data in relation to the South Atlantic Anomaly". In: *Journal of Geodesy* 80.8, pp. 507–523. ISSN: 1432-1394. DOI: 10.1007/s00190-006-0068-2. URL: https://doi.org/10.1007/s00190-006-0068-2.

Lemoine, J.-M., H. Capdeville, and L. Soudarin (Dec. 2016). "Precise orbit determination and station position estimation using DORIS RINEX data". In: *Advances in Space Research* 58.12, pp. 2677–2690. DOI: 10.1016/j.asr.2016.06.024.

Lemoine, J.-M. and P. Štěpánek (Sept. 2019). "Models and Standards for ITRF2020". Presented at the IDS AWG meeting, Paris. URL: https://ids-doris.org/images/documents/report/AWG201909/IDSAWG201909-JMLemoine-ModelsStandardsForITRF2020.pdf.

Lourme, E., V. Toumazou, and T. Guinle (May 2010). *RINEX DORIS 3.0 (Issue 1.3)*. URL: https://ids-doris.org/documents/BC/data/RINEX_DORIS.pdf.

Lyard, F. H., D. J. Allain, M. Cancet, L. Carrère, and N. Picot (2021). "FES2014 global ocean tide atlas: design and performance". In: *Ocean Science* 17.3, pp. 615–649. DOI: 10.5194/os-17-615-2021. URL: https://os.copernicus.org/articles/17/615/2021/.

Markley, F. L. and J. L. Crassidis (2019). "Fundamentals of spacecraft attitude determination and control". In: New York, NY: Springer New York.

Mercier, F., L. Cerri, and J.-P. Berthias (2010). "Jason-2 DORIS phase measurement processing". In: *Advances in Space Research* 45.12. DORIS: Scientific Applications in Geodesy and Geodynamics, pp. 1441–1454. ISSN: 0273-1177. DOI: https://doi.org/10.1016/j.asr.2009.12.002. URL: https://www.sciencedirect.com/science/article/pii/S0273117709007480.

Meyer, B. (2008). "Seven Principles of Software Testing". In: *Computer* 41.8, pp. 99–101. DOI: 10.1109/MC.2008.306.

Montenbruck, O., R. Schmid, F. Mercier, P. Steigenberger, C. Noll, R. Fatkulin, S. Kogure, and A. Ganeshan (2015). "GNSS satellite geometry and attitude models". In: *Advances in Space Research* 56.6, pp. 1015–1029. ISSN: 0273-1177. DOI: https://doi.org/10.1016/j.asr.2015.06.019. URL: https://www.sciencedirect.com/science/article/pii/S0273117715004378.

Montenbruck, O. (Mar. 1992). "Numerical integration methods for orbital motion". In: *Celestial Mechanics and Dynamical Astronomy* 53.1, pp. 59–69. ISSN: 1572-9478. DOI: 10.1007/BF00049361. URL: https://doi.org/10.1007/BF00049361.

Montenbruck, O. and E. Gill (2000). *Satellite Orbits Models, Methods and Applications*. Springer, Berlin, Heidelberg. ISBN: 978-3-642-63547-2. DOI: https://doi.org/10.1007/978-3-642-58351-3.

Moreaux, G. (2023). *DPOD2020 version 1.0*. Tech. rep. IDS Combination Center.

Moreaux, G., F. G. Lemoine, H. Capdeville, M. Otten, P. Štěpánek, J. Saunier, and P. Ferrage (2022). "The international DORIS service contribution to ITRF2020". In: *Advances in Space Research*. ISSN: 0273-1177. DOI: https://doi.org/10.1016/j.asr.2022.07.012. URL: https://www.sciencedirect.com/science/article/pii/S0273117722005865.

Nie, Y., Y. Shen, Q. Chen, and Y. Xiao (2020). "Hybrid-precision arithmetic for numerical orbit integration towards future satellite gravimetry missions". In: *Advances in Space Research* 66.3, pp. 671–688. ISSN: 0273-1177. DOI: https://doi.org/10.1016/j.asr.2020.04.042. URL: https://www.sciencedirect.com/science/article/pii/S0273117720302945.

Noll, C. E. (2010). "The crustal dynamics data information system: A resource to support scientific analysis using space geodesy". In: *Advances in Space Research* 45.12. DORIS: Scientific Applications in Geodesy and Geodynamics, pp. 1421–1440. ISSN: 0273-1177. DOI: https://doi.org/10.1016/j.asr.2010.01.018. URL: https://www.sciencedirect.com/science/article/pii/S0273117710000530.

Oberkampf, W. L. and C. J. Roy (2010). *Verification and Validation in Scientific Computing*. Cambridge University Press. DOI: 10.1017/CBO9780511760396.

Papanikolaou, T. D. and D. Tsoulis (Dec. 2016). "Assessment of numerical integration methods in the context of low Earth orbits and inter-satellite observation

analysis". In: *Acta Geodaetica et Geophysica* 51.4, pp. 619–641. ISSN: 2213-5820. DOI: 10.1007/s40328-016-0159-3. URL: https://doi.org/10.1007/s40328-016-0159-3.

Pavlis, E., V. Luceri, A. Basoni, D. Sarrocco, M. Kuzmicz-Cieslak, K. Evans, and G. Bianco (Jan. 2023). "ITRF2020: The ILRS Contribution and Operational Implementation". In: DOI: 10.22541/essoar.167327866.67198225/v1. URL: https://doi.org/10.22541%2Fessoar.167327866.67198225%2Fv1.

Petit, G. and B. J. Luzum, eds. (2010). *IERS Conventions (2010)*. Vol. 36. IERS Technical Note. International Earth Rotation and Reference Systems Service (IERS). International Earth Rotation and Reference Systems Service (IERS).

Picone, J., A. E. Hedin, D. P. Drob, and A. C. Aikin (2002). "NRLMSISE-00 empirical model of the atmosphere: Statistical comparisons and scientific issues". In: *Journal of Geophysical Research: Space Physics* 107.A12, SIA 15-1-SIA 15–16. DOI: https://doi.org/10.1029/2002JA009430. eprint: https://agupubs.onlinelibrary.wiley.com/doi/pdf/10.1029/2002JA009430. URL: https://agupubs.onlinelibrary.wiley.com/doi/abs/10.1029/2002JA009430.

Rebischung, P. (Apr. 2021). "Terrestrial frame solutions from the IGS third reprocessing". In: *EGU General Assembly Conference Abstracts*. EGU General Assembly Conference Abstracts, EGU21-2144, EGU21–2144. DOI: 10.5194/egusphere-egu21-2144.

Romero, I. (2020). *RINEX The Receiver Independent Exchange ICGEMFormat, Version 3.05*. Tech. rep. IGS/RTCM RINEX WG Chair, ESA/ESOC/Navigation Support Office.

Rothacher, M. and R. Schmid (2010). *ANTEX: The Antenna Exchange Format, Version 1.4*. Tech. rep. Forschungseinrichtung Satellitengeodäsie, TU München. URL: %7Bhttps://kb.igs.org/hc/en-us/articles/216104678-ANTEX-format-description%7D.

Rudenko, S., D. Dettmering, J. Zeitlhöfler, R. Alkahal, D. Upadhyay, and M. Bloßfeld (Feb. 2023). "Radial Orbit Errors of Contemporary Altimetry Satellite Orbits". In: *Surveys in Geophysics*. ISSN: 1573-0956. DOI: 10.1007/s10712-022-09758-5. URL: https://doi.org/10.1007/s10712-022-09758-5.

Saastamoinen, J. (1972). "Atmospheric Correction for the Troposphere and Stratosphere in Radio Ranging Satellites". In: *The Use of Artificial Satellites for Geodesy*. American Geophysical Union (AGU), pp. 247–251. ISBN: 9781118663646. DOI: https://doi.org/10.1029/GM015p0247. eprint: https://agupubs.onlinelibrary.wiley.com/doi/pdf/10.1029/GM015p0247. URL: https://agupubs.onlinelibrary.wiley.com/doi/abs/10.1029/GM015p0247.

Saunier, J., A. Auriol, and C. L. Tourain (2016). "Initiating an error budget of the DORIS ground antenna position: Genesis of the Starec antenna type C". In: *Advances in Space Research* 58.12. Scientific Applications of DORIS in Space

Geodesy, pp. 2717–2724. ISSN: 0273-1177. DOI: https://doi.org/10.1016/j.asr.2016.02.013. URL: https://www.sciencedirect.com/science/article/pii/S0273117716001125.

Scargle, J. D. (Dec. 1982). "Studies in astronomical time series analysis. II. Statistical aspects of spectral analysis of unevenly spaced data." In: *Astrophysical Journal* 263, pp. 835–853. DOI: 10.1086/160554.

Shampine, L. F. and M. K. Gordon (June 1975). *Computer solution of ordinary differential equations.* New York, NY: W.H. Freeman.

Shoemake, K. (July 1985). "Animating Rotation with Quaternion Curves". In: *SIGGRAPH Comput. Graph.* 19.3, pp. 245–254. ISSN: 0097-8930. DOI: 10.1145/325165.325242. URL: https://doi.org/10.1145/325165.325242.

Sinem, I., F. Barthelmes, S. Reißland, K. Elger, C. Förste, F. Flechtner, and H. Schuh (2019). "ICGEM – 15 years of successful collection and distribution of global gravitational models, associated services, and future plans". In: *Earth System Science Data* 11.2, pp. 647–674. DOI: 10.5194/essd-11-647-2019. URL: https://essd.copernicus.org/articles/11/647/2019/.

"Solution (Software/technique) INdependent EXchange Format Version 2.02" (Feb. 2006). URL: https://www.iers.org/SharedDocs/Publikationen/EN/IERS/Documents/ac/sinex/sinex_v202_pdf.pdf?__blob=publicationFile&v=2.

Somodi, B. and L. Földváry (2011). "Application of numerical integration techniques for orbit determination of state-of-the-art LEO satellites". In: *Periodica Polytechnica Civil Engineering* 55.2, pp. 99–106. URL: https://pp.bme.hu/ci/article/view/478.

Soudarin, L., J. Saunier, and P. Ferrage (Sept. 2019). "Presentation of the DORIS system and the International DORIS Service". Presented at the International Workshop for the Implementation of the Global Geodetic Reference Frame (GGRF) in Latin America. URL: https://www.sirgas.org/fileadmin/docs/GGRF_Wksp/26_Soudarin_et_al_2019_DORIS_and_IDS.pdf.

Štěpánek, P., J. Douša, and V. Filler (2013). "SPOT-5 DORIS oscillator instability due to South Atlantic Anomaly: Mapping the effect and application of data corrective model". In: *Advances in Space Research* 52.7, pp. 1355–1365. ISSN: 0273-1177. DOI: https://doi.org/10.1016/j.asr.2013.07.010. URL: https://www.sciencedirect.com/science/article/pii/S0273117713004225.

Štěpánek, P. and V. Filler (2022). "DORIS Alcatel ground antenna: Evaluation of the phase center variation models". In: *Advances in Space Research*. ISSN: 0273-1177. DOI: https://doi.org/10.1016/j.asr.2022.02.024. URL: https://www.sciencedirect.com/science/article/pii/S027311772200120X.

Štěpánek, P., V. Filler, U. Hugentobler, and D. Jan (2010). "DORIS at GOP: From Pilot Testing Campaign to Fully Operational Analysis Center". In: *Acta Geodyn*

Geomater 7.1, pp. 49–60. URL: http://www.irsm.cas.cz/materialy/acta_content/2010_01/6_Stepanek.pdf.

Štěpánek, P., G. Moreaux, U. Hugentobler, and V. Filler (2022). "The GOP analysis center: DORIS contribution to ITRF2020". In: *Advances in Space Research.* ISSN: 0273-1177. DOI: https://doi.org/10.1016/j.asr.2022.11.038. URL: https://www.sciencedirect.com/science/article/pii/S0273117722010626.

Tapley, B. D., S. Bettadpur, M. Watkins, and C. Reigber (2004a). "The gravity recovery and climate experiment: Mission overview and early results". In: *Geophysical Research Letters* 31.9. DOI: https://doi.org/10.1029/2004GL019920. eprint: https://agupubs.onlinelibrary.wiley.com/doi/pdf/10.1029/2004GL019920. URL: https://agupubs.onlinelibrary.wiley.com/doi/abs/10.1029/2004GL019920.

Tapley, B. D., B. E. Schutz, and G. H. Born (2004b). *Statistical Orbit Determination.* eng. Academic Press, Elsevier Inc. ISBN: 978-0-12-683630-1.

Tourain, C. L., G. Moreaux, A. Auriol, and J. Saunier (2016). "DORIS Starec ground antenna characterization and impact on positioning". In: *Advances in Space Research* 58.12. Scientific Applications of DORIS in Space Geodesy, pp. 2707–2716. ISSN: 0273-1177. DOI: https://doi.org/10.1016/j.asr.2016.05.013. URL: https://www.sciencedirect.com/science/article/pii/S0273117716301995.

Urban, S. and K. Seidelmann (2013). *Explanatory supplement to the astronomical almanac; 3rd ed.* Astronomical almanac for the year 2013 supplement. Mill Valley, CA: University Science Books. ISBN: 9781891389856.

Vallado, D. A. (2001). *Fundamentals of astrodynamics and applications.* eng. 2nd ed. Space technology library; v. 12. Dordrecht; Boston: Kluwer Academic Publishers. ISBN: 1881883124.

Vallado, D. A. and D. Finkleman (2014). "A critical assessment of satellite drag and atmospheric density modeling". In: *Acta Astronautica* 95, pp. 141–165. ISSN: 0094-5765. DOI: https://doi.org/10.1016/j.actaastro.2013.10.005. URL: https://www.sciencedirect.com/science/article/pii/S0094576513003755.

Vallado, D. A. and T. S. Kelso (Feb. 2013). "Earth Orientation Parameter and Space Weather Data for Flight Operations". In: *Proceedings of the 23rd AAS/AIAA Space Flight Mechanics Meeting held February 10–14, 2013, Kauai, Hawaii.* Vol. 148.

VanderPlas, J. T. (May 2018). "Understanding the Lomb–Scargle Periodogram". In: *The Astrophysical Journal Supplement Series* 236.1, p. 16. DOI: 10.3847/1538-4365/aab766. URL: https://doi.org/10.3847%2F1538-4365%2Faab766.

Vandevoorde, D., N. M. Josuttis, and D. Gregor (2017). *C++ Templates: The Complete Guide (2nd Edition)*. 2nd. Addison-Wesley Professional. ISBN: 0321714121.

Wang, N., A. Liu, D. Dettmering, Z. Li, and M. Schmidt (2022). *Using Near-Real-Time DORIS Data for Validating Real-Time GNSS Ionospheric Maps*. International DORIS Service Workshop.

Wilhelm, H., W. Zürn, and H.-G. Wenzel, eds. (1997). *Tidal Phenomena*. Springer-Verlag. DOI: 10.1007/bfb0011453. URL: https://doi.org/10.1007/bfb0011453.

Willis, P., B. J. Haines, Y. E. Bar-Sever, W. I. Bertiger, R. J. Muellerschoen, D. Kuang, and S. D. Desai (2003). "Topex/Jason combined GPS/DORIS orbit determination in the tandem phase". In: *Advances in Space Research* 31.8. Integrated Space Geodetic Systems and Satellite Dynamics, pp. 1941–1946. ISSN: 0273-1177. DOI: https://doi.org/10.1016/S0273-1177(03)00156-X. URL: https://www.sciencedirect.com/science/article/pii/S027311770300156X.

Willis, P., M. B. Heflin, B. J. Haines, Y. E. Bar-Sever, W. I. Bertiger, and M. Mandea (2016a). "Is the Jason-2 DORIS oscillator also affected by the South Atlantic Anomaly?" In: *Advances in Space Research* 58.12. Scientific Applications of DORIS in Space Geodesy, pp. 2617–2627. ISSN: 0273-1177. DOI: https://doi.org/10.1016/j.asr.2016.09.015. URL: https://www.sciencedirect.com/science/article/pii/S0273117716305282.

Willis, P., C. Jayles, and Y. Bar-Sever (2006). "DORIS: From orbit determination for altimeter missions to geodesy". In: *Comptes Rendus Geoscience* 338.14. La Terre observée depuis l'espace, pp. 968–979. ISSN: 1631-0713. DOI: https://doi.org/10.1016/j.crte.2005.11.013. URL: https://www.sciencedirect.com/science/article/pii/S1631071305003603.

Willis, P., F. G. Lemoine, G. Moreaux, L. Soudarin, P. Ferrage, J. Ries, M. Otten, J. Saunier, C. Noll, R. Biancale, and B. Luzum (2016b). "The International DORIS Service (IDS): Recent Developments in Preparation for ITRF2013". In: *IAG 150 Years*. Ed. by C. Rizos and P. Willis. Cham: Springer International Publishing, pp. 631–640. ISBN: 978-3-319-30895-1.

Xia, F., S. Ye, D. Chen, L. Tang, C. Wang, M. Ge, and F. Neitzel (2022). "Advancing the Solar Radiation Pressure Model for BeiDou-3 IGSO Satellites". In: *Remote Sensing* 14.6. ISSN: 2072-4292. DOI: 10.3390/rs14061460. URL: https://www.mdpi.com/2072-4292/14/6/1460.

Yang, Y. (2012). "Spacecraft attitude determination and control: Quaternion based method". In: *Annual Reviews in Control* 36.2, pp. 198–219. ISSN: 1367-5788. DOI: https://doi.org/10.1016/j.arcontrol.2012.09.003. URL: https://www.sciencedirect.com/science/article/pii/S1367578812000387.

Yang, Y., R. Maj, C. He, R. Norman, E. Kerr, B. Carter, J. Currie, and S. Gower (2022). "Comparison of Atmospheric Mass Density Models Using a New Data

Source: COSMIC Satellite Ephemerides". In: *IEEE Aerospace and Electronic Systems Magazine* 37.2, pp. 6–22. DOI: 10.1109/MAES.2021.3125101.

Zeitlhöfler, J. (June 2019). *Nominal and observation-based attitude realization for precise orbit determination of the Jason satellites*. PhD Thesis, Technical University of Munich, Department of Civil, Geo and Environmental Engineering, Deutsches Geodätisches Forschungsinstitut (DGFI-TUM).

Zhang, R., R. Tu, P. Zhang, J. Liu, and X. Lu (2019). "Study of satellite shadow function model considering the overlapping parts of Earth shadow and Moon shadow and its application to GPS satellite orbit determination". In: *Advances in Space Research* 63.9. Multi-GNSS: Methods, Benefits, Challenges, and Geosciences Applications, pp. 2912–2929. ISSN: 0273-1177. DOI: https://doi.org/10.1016/j.asr.2018.02.002. URL: https://www.sciencedirect.com/science/article/pii/S0273117718301157.

Zhang, Y., X. Wang, K. Xi, and Z. Li (Aug. 2022). "Comparison of shadow models and their impact on precise orbit determination of BeiDou satellites during eclipsing phases". In: *Earth, Planets and Space* 74.1, p. 126. ISSN: 1880-5981. DOI: 10.1186/s40623-022-01684-5. URL: https://doi.org/10.1186/s40623-022-01684-5.

Zhou, C., S. Zhong, B. Peng, J. Ou, J. Zhang, and R. Chen (2020). "Real-time orbit determination of Low Earth orbit satellite based on RINEX/DORIS 3.0 phase data and spaceborne GPS data". In: *Advances in Space Research* 66.7, pp. 1700–1712. ISSN: 0273-1177. DOI: https://doi.org/10.1016/j.asr.2020.06.027. URL: https://www.sciencedirect.com/science/article/pii/S0273117720304476.